Exoplanet Atmosphere Characterization with High-Resolution Doppler Spectroscopy

Dissertation zur Erlangung des mathematisch-naturwissenschaftlichen Doktorgrades
"Doctor rerum naturalium" der Georg-August-Universität Göttingen

im Promotionsprogramm PROPHYS
der Georg-August University School of Science (GAUSS)

vorgelegt von

David Cont

aus Bolzano/Bozen

Göttingen, 2023

Betreuungsausschuss

Prof. Dr. Ansgar Reiners
Institut für Astrophysik und Geophysik, Georg-August-Universität Göttingen

Dr. Fei Yan
Department of Astronomy, University of Science and Technology of China

Prof. Dr. Stefan Dreizler
Institut für Astrophysik und Geophysik, Georg-August-Universität Göttingen

Mitglieder der Prüfungskommission

Referent: Prof. Dr. Ansgar Reiners
Institut für Astrophysik und Geophysik, Georg-August-Universität Göttingen

Korreferent: Prof. Dr. Ignas Snellen
Leiden Observatory, Leiden University

Korreferent: Prof. Dr. Stefan Dreizler
Institut für Astrophysik und Geophysik, Georg-August-Universität Göttingen

Weitere Mitglieder der Prüfungskommission:

Dr. Miriam Rengel
Abteilung für Planetenwissenschaften, Max-Planck-Institut für Sonnensystemforschung

Prof. Dr. Jens Niemeyer
Institut für Astrophysik und Geophysik, Georg-August-Universität Göttingen

Prof. Dr. Andreas Tilgner
Institut für Astrophysik und Geophysik, Georg-August-Universität Göttingen

Tag der mündlichen Prüfung: 21. Februar 2023

Abstract

Ultra-hot Jupiters (UHJs) are a class of giant strongly irradiated exoplanets with dayside temperatures exceeding 2200 K. Due to their elevated temperatures, these objects are prime targets for atmospheric characterization by observing their thermal emission signal. In this context, high-resolution spectroscopy is a powerful tool since it offers the opportunity to resolve the individual spectral lines from exoplanet atmospheres. Studying the spectra of UHJs with this method allows measuring the composition of their atmospheres and thereby, insights into mechanisms of planet formation and migration can be provided. In addition, dynamical processes in the atmosphere are detected through excess Doppler-shifts of the spectral lines and rotational broadening affects the spectral line width. Hence, high-resolution spectroscopy enables analyzing the atmospheric circulation and investigating the rotation of exoplanets.

The presented work investigates the physical and chemical conditions in UHJ atmospheres by studying the emission spectra of the exoplanets WASP-33b and KELT-20b/MASCARA-2b. We employ a series of methods including principle component analysis, cross-correlation with model spectra, and a Bayesian retrieval framework for analyzing the high-resolution spectra from the daysides of these exoplanets. The signals of Ti I, V I, Fe I, the hydroxyl radical (OH), and strong evidence for Ti II and TiO lines are found in the emission spectrum of WASP-33b. In particular, the detection of Ti-bearing species is a remarkable result. These species are absent from the atmospheres of most UHJs and the underlying mechanisms of this depletion are not fully understood. Further, the Si I signature is detected in the high-resolution spectra of WASP-33b and KELT-20b/MASCARA-2b. Detection of silicon in the atmospheres of exoplanets has as of now been unprecedented. The spectral lines of all detected chemical species are emission shaped, which unambiguously proves the presence of inverted temperature profiles in the atmospheres of both investigated exoplanets. A detailed analysis of the WASP-33b emission spectrum is conducted to constrain the properties of the planetary dayside atmosphere. An offset in the Doppler-shift between different chemical species is interpreted as the presence of a three-dimensional chemical structure and super-rotational winds in the planetary atmosphere. We retrieve an increasing temperature with atmospheric altitude and super-solar elemental abundances. Moreover, we find a broadened spectral line profile that is likely caused by the fast rotation of the planet. Our analyses also comprise retrievals of the atmospheric conditions at different alignments between WASP-33b's dayside and the Earth-bound observer, which represents an advance in mapping local structures in exoplanet atmospheres.

Zusammenfassung

Ultraheiße Jupiter (englisch: Ultra-hot Jupiters) sind eine Klasse gasförmiger Exoplaneten, die so nahe um ihren Stern kreisen, dass ihre Atmosphären Temperaturen von über 2200 K erreichen. Die damit einhergehende starke thermische Emission macht diese Planeten zu erstklassigen Beobachtungsobjekten, um die Eigenschaften ihrer Atmosphären zu entschlüsseln. Die Technik der hochauflösenden Spektroskopie ermöglicht die Auflösung der einzelnen Spektrallinien von Exoplanetenatmosphären. Beobachtungen ultraheißer Jupiter mittels dieser Methode erlauben es, die Zusammensetzung ihrer Atmosphären zu bestimmen und liefern somit Einblicke in die Entstehungs- und Migrationsmechanismen von Planeten. Darüber hinaus ermöglicht die hochauflösende Spektroskopie eine Analyse der atmosphärischen Zirkulation und die Untersuchung der Rotation von Exoplaneten. Dynamische Prozesse in Exoplanetenatmosphären zeigen sich durch eine überschüssige Doppler-Verschiebung der Spektrallinien. Ebenso kann durch die Verbreiterung derselben die Rotation eines Exoplaneten nachgewiesen werden.

Die vorliegende Arbeit leistet einen Beitrag zur Erforschung der Eigenschaften von Atmosphären ultraheißer Jupiter. Zu diesem Zweck untersuchen wir die Emissionsspektren der Exoplaneten WASP-33b und KELT-20b/MASCARA-2b. Für die Analyse der hochauflösenden Spektren verwenden wir eine Reihe verschiedener Methoden wie Hauptkomponentenanalyse, Kreuzkorrelation mit Modellspektren und Regressionsanalyse. Im Spektrum von WASP-33b finden sich Emissionslinien von Ti I, V I, Fe I und dem Hydroxylradikal (OH) sowie deutliche Hinweise für Emissionslinien von Ti II und TiO. Die Entdeckung von Ti I, Ti II und TiO ist bemerkenswert, da diese Stoffe in den Atmosphären anderer ultraheißer Jupiter zumeist nicht nachweisbar und die zugrundeliegenden Mechanismen für deren Abwesenheit nicht vollständig geklärt sind. Des Weiteren finden wir Emissionslinien von Si I in den Spektren von WASP-33b und KELT-20b/MASCARA-2b. Es handelt sich dabei um den erstmaligen Nachweis von Silizium in den Atmosphären von Exoplaneten. In den Atmosphären beider untersuchten Planeten belegt die Anwesenheit von Emissionslinien das Vorhandensein einer thermischen Inversion. Wir führen eine detaillierte Analyse des Spektrums von WASP-33b durch. Die voneinander abweichenden Doppler-Verschiebungen der Spektrallinien unterschiedlicher Stoffe liefern Hinweise für eine dreidimensionale chemische Struktur und Superrotation in der Planetenatmosphäre. Zudem können wir eine Zunahme der Temperatur als Funktion der Höhe in der Atmosphäre und super-solare Elementhäufigkeiten nachweisen. Wir finden ein verbreitertes Spektrallinienprofil, das vermutlich durch die schnelle Rotation des Planeten verursacht wird. Unsere Forschung umfasst außerdem die Untersuchung der Atmosphäre von WASP-33b aus verschiedenen Sichtwinkeln. Dies stellt einen ersten Schritt zur Kartierung lokaler Strukturen der Atmosphären von Exoplaneten dar.

Contents

1. Introduction

The existence of planets around stars other than our Sun was hypothesized for centuries. However, it was not until 1992 that extrasolar planets (exoplanets) were discovered for the first time around the neutron star PSR 1257+12 (Wolszczan & Frail 1992). Three years later, Mayor & Queloz (1995) identified the close-in gas giant exoplanet 51 Pegasi b as the first planet around a main sequence star. The detection of other giant exoplanets soon followed this discovery (e.g., Butler & Marcy 1996; Butler et al. 1997). From then on, a new field of research in planetary astrophysics arose. In the early 2000s, the planet HD 209458b was identified as the first planet transiting in front of its host star with respect to the Earth-bound observer (Charbonneau et al. 2000; Henry et al. 2000), and the discovery of excess absorption of stellar light by the atmosphere of the said planet opened the era of exoplanet atmosphere characterization (Charbonneau et al. 2002).

Nearly three decades after the emergence of exoplanet science as an independent field of research, more than 5000 exoplanets have been discovered and confirmed[1]. As a result, in-depth characterization of individual planets and comparative studies of exoplanet populations have now become common practice (e.g., Sing et al. 2016; Hoeijmakers et al. 2019). A remarkable outcome of studying exoplanets is their vast diversity. Most of these objects are characterized by significantly different physical parameters compared to the planets of our own Solar System (Madhusudhan 2019). For example, a large variety of distances between exoplanets and their host stars have been observed, with both extremely close (~ 0.05 au) and widely separated orbits (> 10 au). The thermal conditions in exoplanet atmospheres can vary considerably as a function of the distance from the host star, enabling the existence of a variety of chemical regimes at different planetary equilibrium temperatures ($T_{\rm eq}$).

This thesis focuses on observing and characterizing the atmospheres of two strongly irradiated gas giant exoplanets. Gas giants with elevated temperatures are the most accessible objects for atmospheric studies, given their large radii and intense thermal fluxes. Investigation of their spectra allows us to constrain the physical and chemical conditions in the atmospheres of these targets. Such analyses provide us with information about the properties and history of planetary systems. In this chapter, we introduce gas giants with very high temperatures as an own class of exoplanets, define the orbital and radial velocity parameters relevant for observing their atmospheres, and explain the techniques that allow us to analyze their spectral signatures.

[1] NASA Exoplanet Archive; https://exoplanetarchive.ipac.caltech.edu/

1.1. Ultra-hot exoplanet atmospheres

Exoplanets with masses and radii similar to Jupiter, but with much smaller orbital distances from their stellar hosts, are the planetary objects best studied outside our Solar System. The orbital separations of these exoplanets from their host stars are typically on the order of a few percent of the Earth-Sun distance, thereby leading to short orbital periods ranging from a few hours to days. Consequently, these planets are exposed to extreme irradiation levels and have elevated temperatures in their atmospheres. Because of the small separation from their host stars, tidal circularization during the early evolution stage of these planetary systems caused very low or zero eccentricities of their orbits (e.g., Hut 1981). In addition, tidal forces caused a synchronization of the planetary rotation to the orbital period, resulting in permanent day- and nightsides. This so-called tidal locking leads to a strong temperature contrast between the day- and nightsides and hence, leads to significant differences in the atmospheric chemistry of the two planetary hemispheres (Komacek & Showman 2016).

Strongly irradiated gas giant exoplanets with dayside temperatures above 2200 K are referred to as ultra-hot Jupiters (UHJ; Parmentier et al. 2018). Given that the temperatures in the dayside atmospheres of these planets are close to the thermal regime of late-type stars, most of the molecular species are expected to thermally dissociate. Consequently, atomic and ionic species are predicted to dominate the composition of UHJ dayside atmospheres (Arcangeli et al. 2018), while significant concentrations of molecular species are likely restricted to the planetary nightsides and the regions near the day-night boundary, the so-called terminator (e.g., Helling et al. 2019). This prediction was confirmed by observations. Spectroscopic studies have found that atoms and ions are commonly present in the dayside atmospheres of UHJs (e.g., Ca, V, Cr, Fe, Ni; Yan et al. 2020; Kasper et al. 2021; Borsa et al. 2022; Hoeijmakers et al. 2022). On the other hand, only a limited number of molecular species were detected in the spectra emerging from the daysides of this class of exoplanets (e.g., TiO, CO; Nugroho et al. 2017; Yan et al. 2022a). These molecules are mostly characterized by strong chemical bonds that allow them to withstand extreme temperatures and elevated irradiation levels. Current research suggests that the presence of different chemical regimes between the day- and nightsides play an important role in the global heat redistribution of UHJs (Bell & Cowan 2018). This process comprises the thermal dissociation of molecular species on the dayside, and recombination back to molecules under the release of heat on the cooler planetary nightside.

Among the chemical species expected in the atmospheres of UHJs, metal atoms, their ions, oxides, and hydrates are particularly important for the atmospheric thermal structure. These species cause significant absorption of incoming stellar radiation, whereby an efficient heating mechanism in the upper planetary atmosphere is induced (Hubeny et al. 2003; Fortney et al. 2008; Arcangeli et al. 2018; Lothringer et al. 2018). The heating results in an increase of temperature toward higher altitude, a phenomenon that is generally referred to as thermal inversion or stratosphere, which can be identified by detecting emission lines in the spectra of UHJs (e.g., Nugroho et al. 2020a; Yan et al. 2020; Kasper et al. 2021). In addition, strong irradiation and atmospheric heating

can lead to atmospheres expanding beyond the Roche lobe, thereby causing UHJs to suffer from significant atmospheric escape (e.g., Yan & Henning 2018; Wyttenbach et al. 2020).

Finally, theoretical and observational work suggest the presence of significant atmospheric circulation with wind velocities in the order of a few $\mathrm{km\,s^{-1}}$ (e.g., Brogi et al. 2016; Komacek et al. 2017; Tan & Komacek 2019; Alonso-Floriano et al. 2019; Yan et al. 2022a). These winds are considered to be an important factor in shaping the global temperature distribution of UHJs. For example, super-rotational jets are suggested to be capable of shifting the hottest region in UHJ atmospheres from the substellar point toward the day-night terminator (e.g., Komacek et al. 2017). Such shifts are expected to affect the global distribution of various chemical species as the atmospheric chemistry is sensitive to the temperature (Kreidberg et al. 2018; Parmentier et al. 2018).

1.2. Orbital parameters and radial velocities

The position of an exoplanet relative to its host star seen by the observer varies due to the planetary orbital motion. Exoplanets at small distances from their host stars have orbital periods on the order of a few hours to days. Therefore, they can cover a large fraction of their orbit during a single observation. The position along the planetary orbit is described by the orbital phase (ϕ). Figure 1.1 shows a transiting and a non-transiting exoplanet system and provides an overview of the nomenclature of the orbital phase. During the so-called primary eclipse, the transiting exoplanet passes in front of the host star, and light shines through an atmospheric ring around the opaque planetary disk. During the secondary eclipse, the transiting exoplanet is occulted by its host star. For a non-transiting exoplanet system, the planetary day- and nightsides are aligned with the observer's line of sight at inferior and superior conjunction, respectively. Quadrature corresponds to the orbital phases where the planet has a geocentric angular separation of 90° from its host star. The orbital phase is defined as zero at transit or inferior conjunction, 0.5 during occultation by the host star or superior conjunction, as well as 0.25 and 0.75 at quadrature.

The orbital plane of an exoplanet around its host star can have different orientations with respect to the observer's line of sight. This orientation is described by the orbital inclination (i_p), which is defined as 0° and 90° if the planetary system is observed in face-on and edge-on geometry, respectively. Therefore, transiting exoplanets have an orbital inclination close to 90°. Figure 1.2 shows examples of exoplanet systems with different orbital inclinations. The maximum observable planetary radial velocity (RV) at a given orbital inclination is called orbital velocity semi-amplitude and is calculated in the assumption of a circular orbit as

$$K_\mathrm{p} = v_\mathrm{orb} \sin i_\mathrm{p}, \tag{1.1}$$

with v_orb being the velocity of the planet along its trajectory. The RV of the exoplanet orbiting its host star is calculated at each orbital phase as $K_\mathrm{p} \sin 2\pi\phi$.

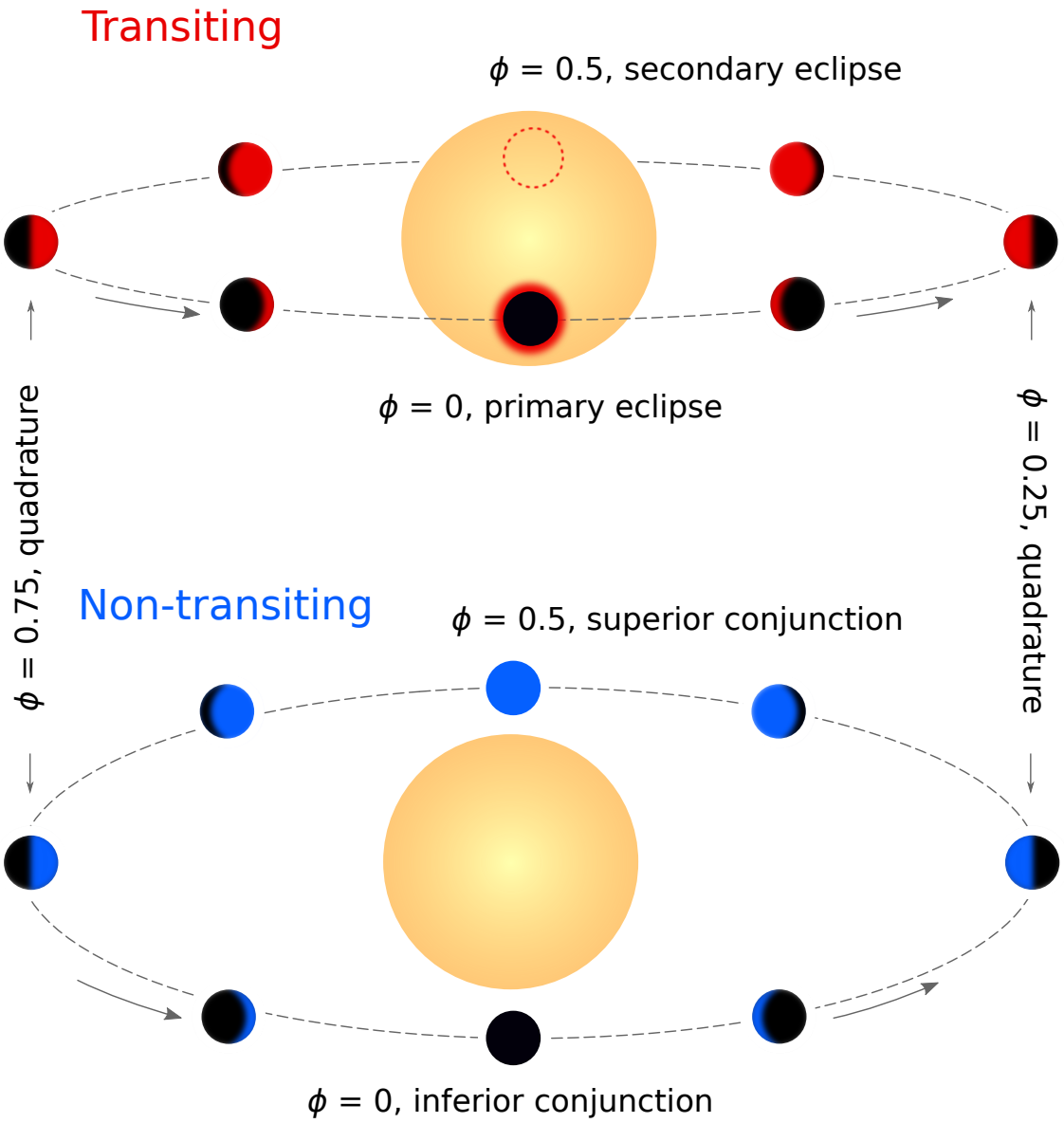

Figure 1.1.: Nomenclature for orbital phases of transiting and non-transiting exoplanet systems. The *top panel* illustrates a transiting exoplanet system. During the primary eclipse (ϕ = 0), the planet transits in front of the host star; light shines through an atmospheric ring around the opaque planetary disk. During the secondary eclipse (ϕ = 0.5), the planet is hidden behind its host star. The *bottom panel* shows a non-transiting exoplanet system. At inferior (ϕ = 0) and superior (ϕ = 0.5) conjunction the planetary day- and nightsides are aligned with the observer's line of sight, respectively. Quadrature corresponds to the orbital phases where the planet has a geocentric angular separation of 90° from its host star (ϕ = 0.25 and ϕ = 0.75). The planetary nightside is shown in black, the dayside in red and blue colors. We indicate the planetary orbital motion with gray arrows.

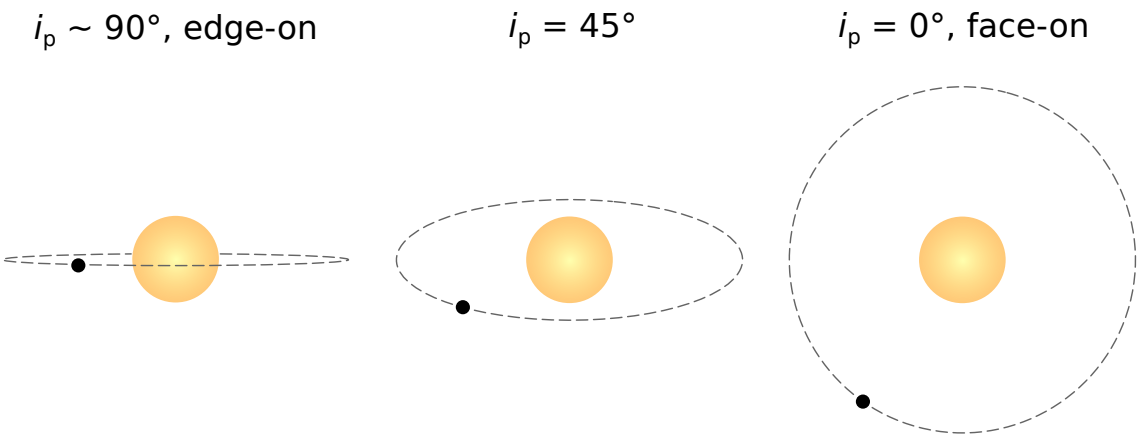

Figure 1.2.: Examples of orbital inclination. An exoplanet transits in front of its host star if the orbit is seen in edge-on geometry ($i_p \sim 90°$). No transits can be observed at orbital inclinations far from 90°. Observing an exoplanet system from the top is referred to as face-on geometry ($i_p = 0°$).

The spectral signature of an exoplanet is affected by a Doppler-shift resulting from the relative motion between the observer's rest frame and the planet. This Doppler-shift is described by the equation

$$\frac{\Delta\lambda}{\lambda} = \frac{v_p}{c}, \tag{1.2}$$

with $\Delta\lambda$ being the Doppler-shift at a wavelength of λ, c the speed of light, and v_p the RV between the planet and the observer. Figure 1.3 shows that v_p is the result of three RV contributions: the velocity of the planetary system relative to the Solar System v_{sys}, the Earth's barycentric correction v_{bary}, and the projected velocity of the exoplanet orbiting its host star $K_p \sin 2\pi\phi$. Consequently, we can describe an exoplanet's RV as

$$v_p = v_{sys} + v_{bary} + K_p \sin 2\pi\phi + \Delta v, \tag{1.3}$$

when assuming a circular orbit. The term Δv accounts for possible RV shifts caused by additional physical effects. For example, detecting Δv values that deviate from zero can indicate dynamical processes in exoplanet atmospheres or the presence of an eccentric orbit. Exoplanet characterization is usually performed on targets whose orbital and systemic velocities are well known from prior measurements. Thus, Eq. (1.3) allows us to estimate the Doppler-shift at which we can expect the planetary spectral signature.

1.3. Spectroscopy of exoplanets

In this thesis, we employ spectroscopy to investigate the atmospheres of exoplanets. In the following section, we give the definition of spectral resolution, compare low- versus high-spectral-resolution techniques, and give details on the theoretical background of the two spectroscopy methods most commonly used to study exoplanet atmospheres.

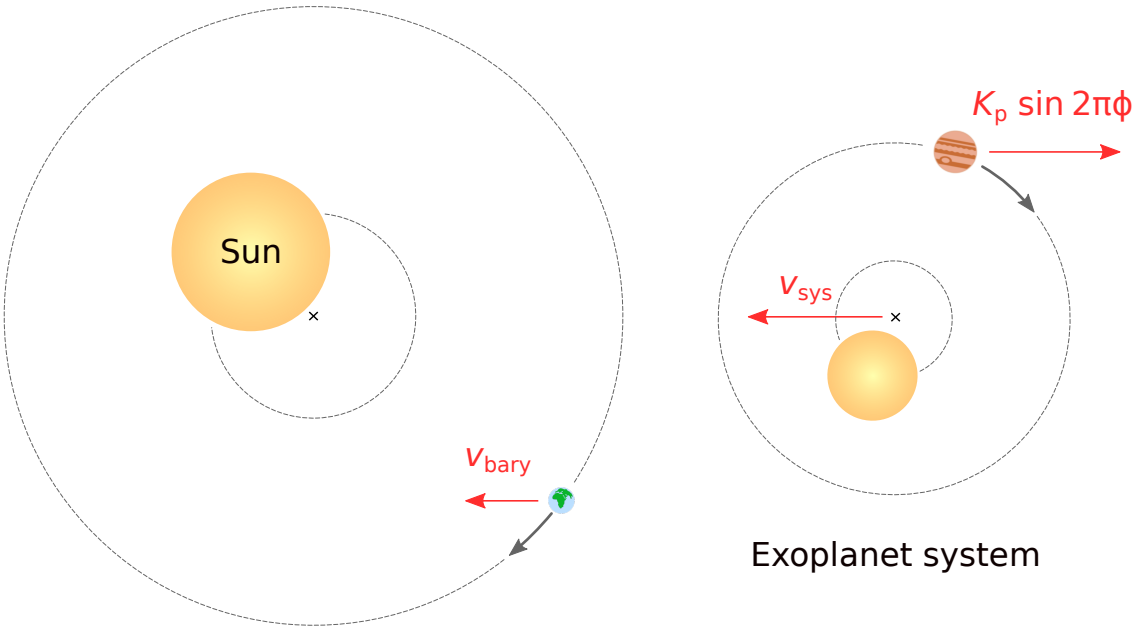

Figure 1.3.: Radial velocities relevant for exoplanet observations. The observed RV of an exoplanet corresponds to the sum of the systemic velocity (v_{sys}), the barycentric velocity correction (v_{bary}), and the projected orbital velocity of the exoplanet ($K_p \sin 2\pi\phi$). The barycentric velocity correction accounts for the Earth's rotation and orbital motion around the Sun. We indicate the orbital motions of the exoplanet and the Earth with gray arrows.

1.3.1. Low versus high spectral resolution

Spectroscopy of exoplanets is carried out by space- and ground-based observatories, which can significantly vary in their resolving power. The spectral resolution of an instrument is defined as

$$R = \frac{\lambda}{\Delta\lambda}, \tag{1.4}$$

with $\Delta\lambda$ being the smallest wavelength difference that can be distinguished at a wavelength λ. Low-spectral-resolution observations are typically carried out at a resolving power of $R < 4000$ (Birkby 2018), but can also reach considerably lower values on the order of 100 or below. On the other hand, high-resolution instruments operate at spectral resolutions of $R > 15\,000$ (van Sluijs et al. 2022) and can achieve values of 100 000 and beyond.

Space-based observations offer the advantage of not being affected by absorption lines and the thermal background of the Earth's atmosphere. Therefore, observing from space provides measurements of the absolute flux received from exoplanets. However, most space-based facilities deliver only low-spectral-resolution observations, which prevents resolving the individual lines of exoplanet spectra. For this reason, space-based low-resolution observations only allow us detecting bands of blended spectral lines, whereas bands of different chemical species in the same wavelength range are often hard to distinguish. In contrast, ground-based observations at high spectral resolution allow us to resolve the individual lines of exoplanet spectra and enable the unambiguous identification of individual chemical species. As a downside, ground-based high-resolution

spectra are affected by the absorption signature of the Earth's atmosphere. The presence of these so-called telluric lines limits spectral observations to restricted wavelength ranges with low contamination from the Earth's atmosphere. A further disadvantage of high-resolution spectroscopy is the lack of information from the spectral continuum level, which is lost during the correction for telluric lines when reducing the raw spectra. Therefore, this method only allows us to measure relative differences with respect to the local continuum. A detailed overview of the capabilities of high-resolution spectroscopy is given in Sect. 1.4.

In summary, space-based low-spectral-resolution observations are capable of measuring absolute flux levels, while ground-based high spectral resolution enables the identification of individual spectral lines. Therefore, the two methods provide complementary information, and combined analyses of low- and high-resolution spectra may offer the possibility of comprehensive studies of exoplanets (Brogi et al. 2017; Gandhi et al. 2019).

1.3.2. Transmission spectroscopy

If an exoplanet system is seen in edge-on geometry, the planetary orbit passes in front of the host star, leading to a primary eclipse or transit. During the primary eclipse, the planet blocks part of the stellar light, causing a dip at orbital phase zero in the measured light curve as shown in Fig. 1.4. The probability of an eclipse between a planet and its stellar host strongly depends on the orbital separation, wherein planets at low distances from their parent star are most likely to transit (Brown 2001). Therefore, the majority of transits can be attributed to exoplanets on close-in orbits. During a transit, stellar light passes through a thin atmospheric ring at the edge of the opaque planetary disk. This light carries the imprint of the conditions in the exoplanet atmosphere. Analyzing this light signature is referred to as transmission spectroscopy, allowing us to probe the atmosphere at the border between the planetary day- and nightsides.

During transit, the planet covers part of the stellar disk, which leads to a decrease in flux we can measure from the host star. The fraction of stellar light blocked by the exoplanet is called transit depth and calculated as $(R_t/R_*)^2$. We denote with R_t the radius of the planetary disk as seen by the transit observation, which is the so-called transit radius, and R_* is the radius of the host star. The fraction of stellar radiation passing through the thin atmospheric annulus around the planetary disk is attenuated by absorption and scattering with gas particles. The strength of these interactions, and hence, the attenuation of the stellar light, vary as a function of wavelength. Consequently, the transit radius R_t is also wavelength dependent. This provides us with the transmission spectrum $Tr(\lambda)$ of exoplanet atmospheres:

$$Tr(\lambda) = 1 - \left(\frac{R_t(\lambda)}{R_*}\right)^2 . \tag{1.5}$$

Transmission spectroscopy is a powerful tool for investigating the upper atmospheres of exoplanets (Flowers et al. 2019). Characterizing the spectral absorption lines or bands of individual species can provide information on the atmospheric chemistry at the location of the terminator. Moreover,

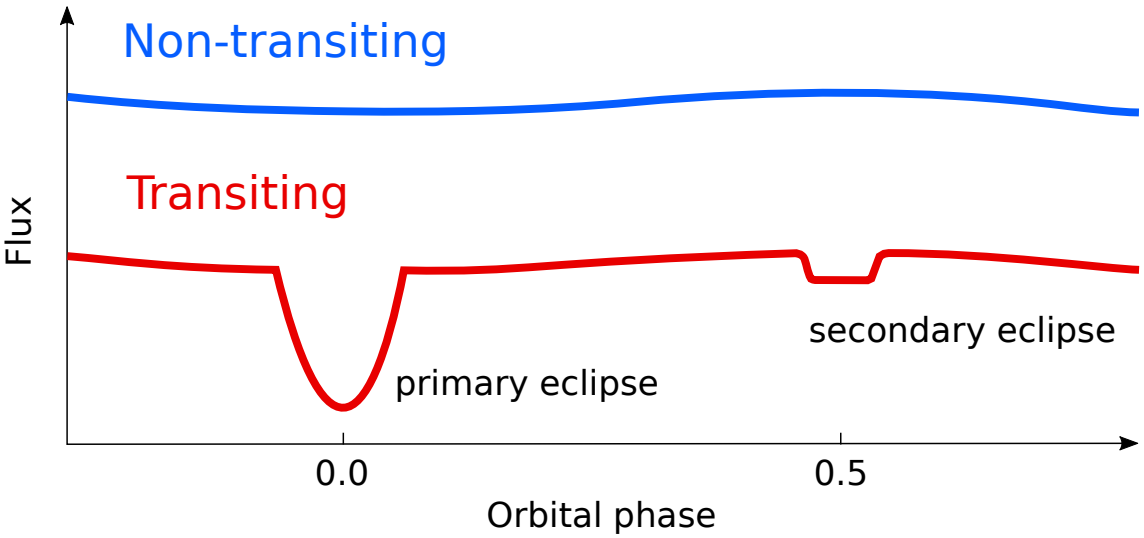

Figure 1.4.: Light curves of transiting (red) and non-transiting (blue) exoplanet systems as a function of the orbital phase. For a transiting system, the flux diminishes as the planet passes in front of the host star (primary eclipse); the flux also drops when the planet is occulted by its stellar host (secondary eclipse). The continuum modulation of the two light curves corresponds to the phase dependent contribution of the thermal emission signal from the planetary dayside. We added different offsets to the light curves for better visualization.

this method allows constraining the thermal conditions at the boundary between the planetary day- and nightsides. Excess Doppler-shifts of the detected transmission spectra can prove the presence of winds in the observed atmosphere. In addition, the presence of an optically thick cloud deck can obscure the transmission features of the underlying atmospheric layers. Therefore, the presence of clouds in exoplanet atmospheres can be inferred via the nondetection of significant spectral absorption lines (Fortney 2005). Also, atmospheric aerosols can be identified via the detection of slopes in exoplanet transmission spectra (Gao et al. 2021). In general, the characterization of the terminator as the transition zone between the permanent day- and nightsides of tidally locked gas giant planets is of particular interest because processes such as atmospheric rain-out or complex molecular chemistry are likely to occur in this region (e.g., Helling et al. 2019).

1.3.3. Thermal emission spectroscopy

The emission signal of an exoplanet can be observed at any point along its orbit except during the secondary eclipse, i.e. the situation when the exoplanet passes behind its host star. Hence, the thermal emission signal of a transiting exoplanet is depleted from the overall light flux during the secondary eclipse, which leads to a reduction in the light flux at orbital phase 0.5 as shown in Fig. 1.4. The contribution of the thermal emission to the overall signal of both transiting and non-transiting exoplanet systems can be recognized as the flux modulation of the illustrated light curves. For a transiting exoplanet, the planetary thermal emission signal can be isolated from the signal of the host star by comparing the out-of-eclipse flux with that during the secondary eclipse. Thus, the emission spectrum from an exoplanet is calculated as the ratio between the planetary flux and that of its host star as a function of wavelength $(F_p/F_*)(\lambda)$. The emission spectrum of

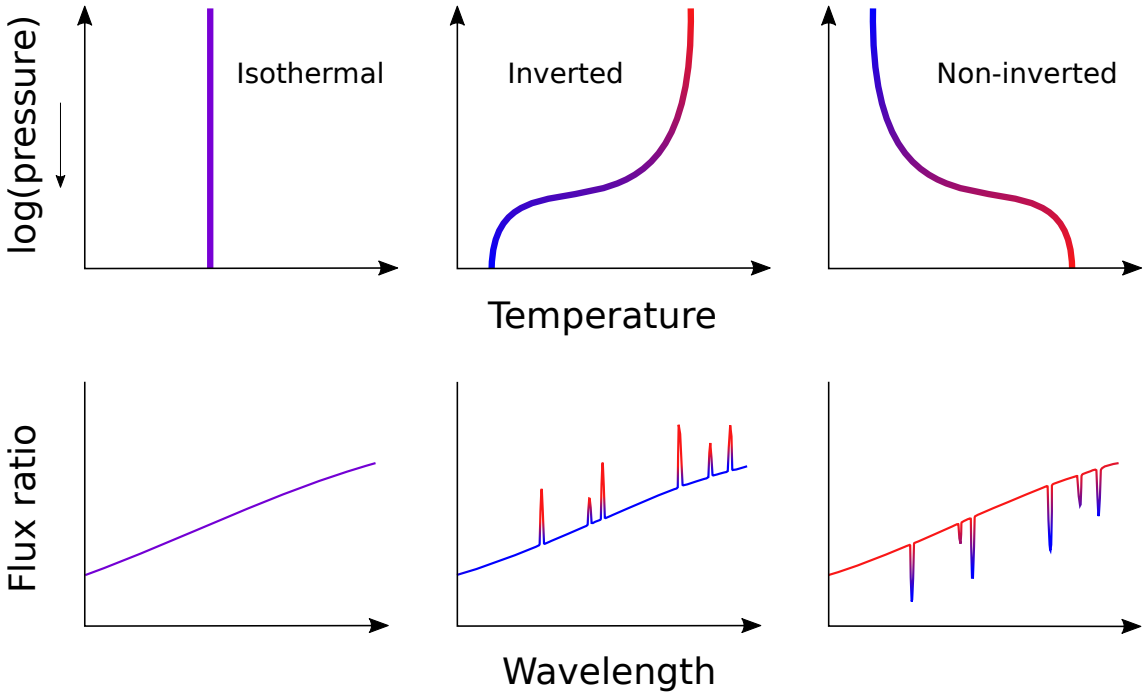

Figure 1.5.: Atmospheric thermal structures and resulting emission spectra. Spectral lines are absent in the emission spectrum of an isothermal atmosphere (*left panels*). Line features are present in the emission spectra resulting from atmospheres with an inverted (*middle panels*) or a non-inverted (*right panels*) temperature profile. The blue (low temperature) and red (elevated temperature) colors indicate the thermal conditions and the regions from where the features emerge in the planetary atmosphere.

a transiting exoplanet is usually measured at orbital phases close to the secondary eclipse when most of the planetary dayside is facing the observer and the contribution to the overall signal is largest. Alternatively, the emission spectrum of an exoplanet can be measured as the combination of the stellar and planetary spectral signature over an orbital phase interval without the need for observing the secondary eclipse. This approach is referred to as phase curve measurement and enables investigating the large sample of non-transiting exoplanets. Particularly, high-spectral-resolution phase curves offer the advantage that the stellar spectral contribution can be removed without the need for information on a secondary eclipse and therefore, are a powerful tool for studying the emission spectra of both transiting and non-transiting exoplanets. Details on the removal of the high-spectral-resolution stellar signature are given in Sect. 1.4. In general, emission spectroscopy is particularly well suited for characterizing exoplanets with elevated temperatures and large radii given their strong thermal fluxes.

The thermal structure of an exoplanet atmosphere strongly affects its thermal emission spectrum (Gandhi & Madhusudhan 2019). Figure 1.5 gives an overview of different atmospheric temperature profiles and the resulting emission spectra. When assuming an isothermal atmosphere, each atmospheric layer emits a blackbody spectrum with a constant temperature. Consequently, the resulting emission spectrum of the exoplanet atmosphere corresponds to that of a blackbody without spectral features as illustrated in the left panels in Fig. 1.5. On the other hand, line features are present in the emission spectrum under the assumption of a vertical temperature gradient in

an exoplanet atmosphere. These spectral features are a consequence of the wavelength dependency of the atmospheric opacity, which originates in the cross-sections of the different chemical species that can vary by orders of magnitude over a studied spectral range. The middle panels of Fig. 1.5 show the case of a so-called inverted temperature profile in which temperature increases with altitude. At wavelengths for which the atmospheric opacity is low, such an inverted temperature profile presents itself as a flux that originates mostly from lower layers in the atmosphere. At wavelengths for which the atmosphere is opaque, the flux emerges mostly from higher layers in the inverted atmosphere. Since the flux emitted at high atmospheric altitudes has a higher intensity than the flux emitted deep in the atmosphere due to the increased temperature, emission features are formed at the wavelengths where the atmospheric opacity is high. On the other hand, the right panels of Fig. 1.5 illustrate the situation for a non-inverted temperature profile in which temperature decreases with atmospheric altitude. For such a non-inverted temperature profile, the corresponding emission spectrum is affected by absorption features. At wavelengths for which the atmospheric opacity is low, such a non-inverted temperature profile presents itself as a flux that mostly originates from lower layers in the atmosphere where the temperature is high. At wavelengths for which the atmosphere is opaque, the cooler upper atmospheric layers block the spectral flux arising from the underlying atmospheric layers. This leads to a decrease in flux and hence, absorption features are formed at the wavelengths for which the atmosphere's opacity is elevated.

In summary, the spectral emission signature of an exoplanet is particularly sensitive to the thermal conditions in its atmosphere. Therefore, emission spectroscopy is suitable for studying the atmospheric thermal structure of planetary dayside atmospheres. In analogy to transmission spectroscopy, this method can also be used to study numerous additional atmospheric properties. For example, analyzing exoplanet emission spectra allows us to constrain the chemical conditions on the planetary dayside. Further, this method enables the investigation of global circulation and planetary rotation via the detection of excess Doppler-shifts of the spectral emission lines.

1.4. High-resolution Doppler spectroscopy

In recent years, high-resolution spectroscopy has become an increasingly successful observation method to investigate exoplanet atmospheres. Observations with this technique are typically carried out at spectral resolutions of $R > 15\,000$ (van Sluijs et al. 2022), enabling us to resolve the spectral signature of planetary atmospheres into a forest of individual lines. Exoplanets at low separations from their host star have elevated orbital velocities, which cause their spectral lines to undergo a significant, time-varying Doppler-shift. Taking a series of spectra with relatively short exposure times allows us to capture the rapidly changing Doppler-shift. The analysis of this so-called spectral time series enables us to separate the planetary signal from the almost stationary spectral contribution from the star and the Earth's atmosphere (e.g., Snellen et al. 2010; Birkby

et al. 2013; Alonso-Floriano et al. 2019; Sánchez-López et al. 2019). Moreover, an important advantage of high-resolution spectroscopy is the possibility of boosting the planetary signal by combining the information of numerous spectral lines (Snellen et al. 2015; Birkby 2018). This combination is typically achieved by computing the cross-correlation between high-spectral-resolution observations and a planetary model spectrum. The overall process of isolating planetary spectral lines by their Doppler-shift and extracting the spectral signature by cross-correlation is referred to as high-resolution Doppler spectroscopy.

The research presented in this thesis is based on high-resolution spectroscopy observations of exoplanet atmospheres. In this section, we give an overview of the high-resolution spectroscopy instrumentation used in our work and focus on the main data reduction steps applied to the observational data. Further, we provide details of the cross-correlation technique.

1.4.1. High-resolution spectrographs

This thesis is based on the observations obtained at three high-resolution echelle spectrographs, CARMENES, HARPS-N, and ESPaDOnS.

CARMENES (Calar Alto high-Resolution search for M dwarfs with Exoearths with Near-infrared and optical Échelle Spectrographs; Quirrenbach et al. 2016) is mounted at the 3.5 m telescope at the Calar Alto Observatory. The main science objective of the instrument is the detection of low mass planets around a sample of ∼ 300 main sequence stars. Consisting of two fiber-fed high-resolution spectrographs, the instrument covers the wavelength range 520–960 nm in the visible (VIS) and 960–1710 nm in the near-infrared (NIR) domain. CARMENES operates with a spectral resolution of $R \sim 94\,600$ in the VIS channel and $R \sim 80\,400$ in the NIR channel and consists of 61 and 28 spectral orders, respectively.

HARPS-N (High Accuracy Radial velocity Planet Searcher for the Northern hemisphere; Mayor et al. 2003; Cosentino et al. 2012) is a high-resolution spectrograph operated at the 3.6 m Telescopio Nazionale *Galileo* at the Roque de los Muchachos Observatory. The instrument's main objective is to characterize and search for terrestrial planets around bright stars. The instrument is fiber fed and covers the wavelength domain 383–690 nm, split into 69 spectral orders. HARPS-N has a spectral resolution of $R \sim 115\,000$.

ESPaDOnS (Echelle SpectroPolarimetric Device for the Observation of Stars; Donati 2003) is a high-resolution spectrograph at the Canada-France-Hawai'i telescope (CFHT) at the Mauna Kea Observatory. The flux is fed into the spectrograph via optical fibers. Its wavelength domain is 370–1050 nm across 40 spectral orders with a maximum resolving power of $R \sim 81\,000$. The spectra used in this work were obtained with an instrument setting corresponding to a resolution of $R \sim 68\,000$.

1.4.2. Extraction and pre-processing of the spectra

Echelle spectrographs use an echelle grating to diffract the light into separate spectral orders. This so-called cross-dispersion yields a two-dimensional spectrum, which is sampled by a CCD detector array. Figures 1.6a and 1.6b show a raw frame from a high-resolution echelle spectrograph. Each horizontal stripe pattern corresponds to an individual spectral echelle order. The wavelength of the spectrum increases from the left to the right and from the bottom to the top of the figures. Each spectral order is imaged twice, with a small wavelength offset between the two spectra. This technique is referred to as image slicing and aims to increase the resolution power of the spectrograph (Tala et al. 2017).

As a first data analysis step, the raw frames are transformed into a one-dimensional format. The extraction of the one-dimensional spectra from the raw data is performed by running the instrument-specific reduction pipelines. For the CARMENES spectra, this task is carried out by the software `caracal` v2.20 (Zechmeister et al. 2014; Caballero et al. 2016), yielding a one-dimensional spectrum for each echelle order. The same procedure is performed for HARPS-N by the `Data Reduction Software` (Cosentino et al. 2014) pipeline. This reduction software offers the possibility of providing the spectra for each echelle order individually or in an order-merged format. For ESPaDOnS, the extracted spectra are provided in an order-by-order format via the `Libre-ESpRIT` based `Upena` pipeline (Donati et al. 1997). Figure 1.6c shows an example spectrum extracted from the two-dimensional raw data.

After extraction, the one-dimensional spectra of a time series are sorted chronologically and stacked in a two-dimensional array for each echelle order, forming the so-called spectral matrix. Using the spectra in the order-merged format yields a single spectral matrix. In the next step, bad pixels flagged with NaN (not a number) values and outliers caused by cosmic rays are corrected. The details of the correction procedure vary slightly between the studies reported in the following chapters of this thesis. In Chapter 2, we fit a third-order polynomial to the time evolution of each pixel and thereafter, replace the outliers and the NaN-flagged pixels with the values of the polynomial function. On the other hand, in Chapters 3 and 4, we correct these pixel values by interpolating with the nearest neighbors. We refer the reader to the respective chapters for a more detailed description of the bad pixel correction.

In the following, each spectrum of the spectral matrix is normalized to the continuum level. This step is required to remove the contribution of the spectrograph's blaze function and the temporal variability of the spectral baseline caused by changing atmospheric conditions during the observation (e.g., Alonso-Floriano et al. 2019; Sánchez-López et al. 2019; Stangret et al. 2020). Figure 1.7 gives an overview of the normalization procedure. We apply a polynomial fit to the individual spectra. Subsequently, we divide the spectra with the fit function. We use a second-order and a seventh-order polynomial for the order-by-order and the order-merged spectra, respectively. Instead of including all data points in the fitting procedure, we divide the wavelength range into bins and take the 90th percentile value of each interval as the data points to be fitted. In this way,

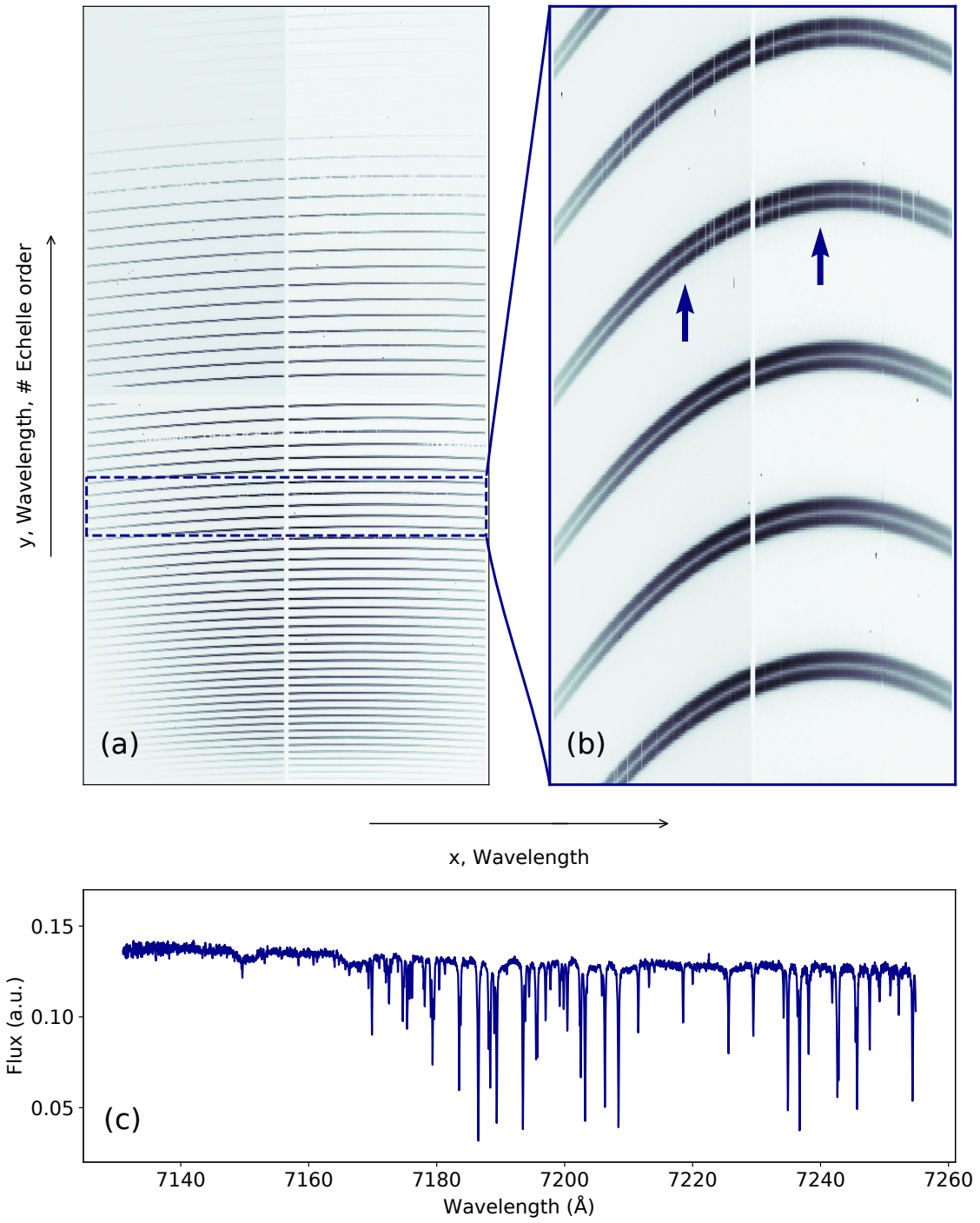

Figure 1.6.: Raw frame from a high-resolution echelle spectrograph. The illustrated spectrum is part of a WASP-33b observation taken with CARMENES VIS on 15 November 2017. *Panel a* shows the two-dimensional raw frame. The raw frame is subdivided into four segments, which causes the presence of a horizontal and a vertical gap. *Panel b* shows a zoom in on specific echelle orders indicated by the dark blue rectangle in *panel a*. The wavelength increases from the left to the right and from the bottom to the top of the image. Each echelle order is imaged twice to increase the resolving power of the spectrograph. Outliers due to cosmic rays and hot pixels can be recognized as artifacts in the detector array. In *panel c*, we show the one-dimensional spectrum resulting from the echelle order indicated with the dark blue arrows in *panel b*.

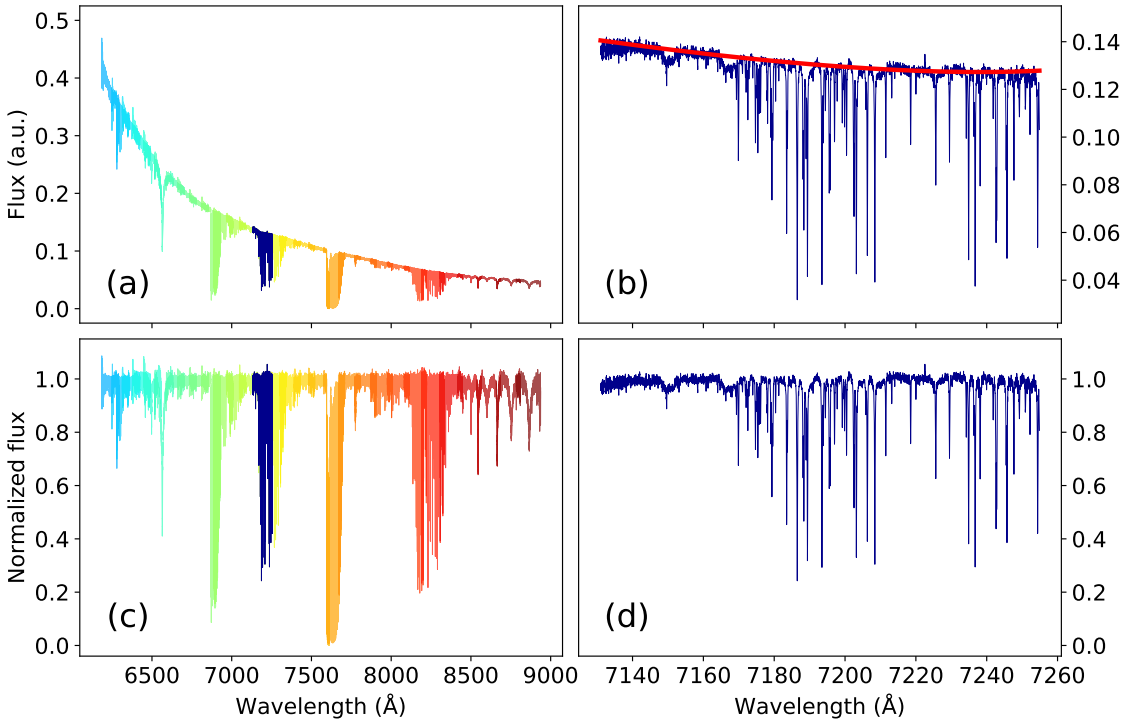

Figure 1.7.: Normalization of one-dimensional spectra to the continuum level. We present a selected range of spectral orders from the CARMENES VIS channel (echelle orders 98–68). *Panel a* shows the order-by-order spectra extracted from the raw images. *Panel b* shows a zoom in on a specific spectral order, which is illustrated in dark blue; the quadratic fit function used for normalization is shown in red. *Panel c* illustrates the order-by-order spectra after normalization; a zoom in on the normalized version of the selected spectrum, shown in dark blue color, is reported in *panel d*.

telluric and stellar lines can be prevented from impacting our fitting routine. An example of a normalized spectral matrix is reported in Fig. 1.8.

As a final pre-processing step, we mask the spectral regions that are affected by strong telluric absorption. This is done by masking wavelength intervals with a flux smaller than 20% of the continuum level. In particular, three spectral orders located in the CARMENES NIR channel are entirely discarded due to the almost total absence of detectable flux. These orders coincide with the telluric water absorption band at 1.4 μm, where the flux throughput of the Earth's atmosphere is drastically reduced. Not including wavelengths with a reduced flux is a reasonable choice since these intervals carry negligible information about the investigated exoplanet atmosphere but can introduce considerable noise into the analysis. In addition, strong sky emission lines are masked, which are mostly present at NIR wavelengths.

1.4.3. Correcting for systematic effects

To analyze the faint signal of an exoplanet atmosphere, we must first remove the contribution of systematic effects from the spectra. Telluric and stellar lines are the main systematic effects, but other sources of systematics such as instrumental effects can also bias the spectral data. Accurate

modeling of the systematics allows us to efficiently remove their contribution and therefore, is key to extract the signal of exoplanet atmospheres from high-resolution spectroscopy data.

The systematic contribution of the telluric lines to the spectral matrix can be recognized as vertical absorption patterns as demonstrated in Figs. 1.8a and 1.8b. These features are approximately stationary in wavelength space over the duration of the entire spectral time series. Analogously, most of the unknown systematics are supposed to undergo such a quasi-static behavior. In contrast, the planetary spectral lines are affected by a significant Doppler-shift that changes with time, allowing us to distinguish them from systematic spectral features. This property enables us to identify, model, and remove the systematic spectral contribution while leaving the planetary signal unaltered. Removing the modeled systematics from the data results in the so-called residual spectral matrix shown in Fig. 1.8c. This matrix exclusively contains the faint planetary signal that is dominated by noise. In Fig. 1.8d the same spectral matrix is shown, but with an enhanced planetary model spectrum injected into the data to render visible for the reader the Doppler-shifted spectral lines from the exoplanet atmosphere.

Different methods have been developed to model the systematic contribution from the telluric and stellar lines. An approach mostly applied in the early days of exoplanet atmosphere research with high-resolution Doppler spectroscopy is the use of polynomial regressions. This approach consists of fitting the flux evolution of each wavelength bin with a polynomial function for modeling the telluric lines (e.g., Snellen et al. 2010; Brogi et al. 2012, 2013; Schwarz et al. 2015). Alternatively, the Earth's atmosphere contamination can be removed by using synthetic telluric transmission spectra generated by software such as the European Southern Observatory's `MOLECFIT` tool (Smette et al. 2015). The correction for the spectral contribution of the host star can be carried out by using stellar model spectra. Although some of these methods have the advantage of preserving the continuum level of exoplanet spectra, it has proven difficult to account for unknown systematics. For this reason, methods based on principal component analysis (PCA) have recently gained acceptance.

Using PCA-based methods offers the opportunity to overcome the difficulty of unknown systematics. Following a blind approach, PCA searches for systematic features common to all wavelength bins without prior knowledge and regardless of their source. Consequently, unknown systematic features that are otherwise impossible or very difficult to identify and model are efficiently detected in addition to the telluric and stellar lines (e.g., Line et al. 2021; Giacobbe et al. 2021; Kasper et al. 2021; van Sluijs et al. 2022). In this thesis, we use `SYSREM` (Tamuz et al. 2005), a PCA algorithm that provides the possibility to weight the input data with the respective uncertainties. The algorithm was originally developed to detect and correct for systematic effects in light curve studies, but has proven to be particularly powerful when applied in exoplanet research (e.g., Birkby et al. 2013; Nugroho et al. 2017; Gibson et al. 2020; Herman et al. 2020; Yan et al. 2021). Each wavelength bin of the spectral matrix is considered as an independent light curve when the algorithm is applied to search for the signature of exoplanet atmospheres. `SYSREM` models the systematic

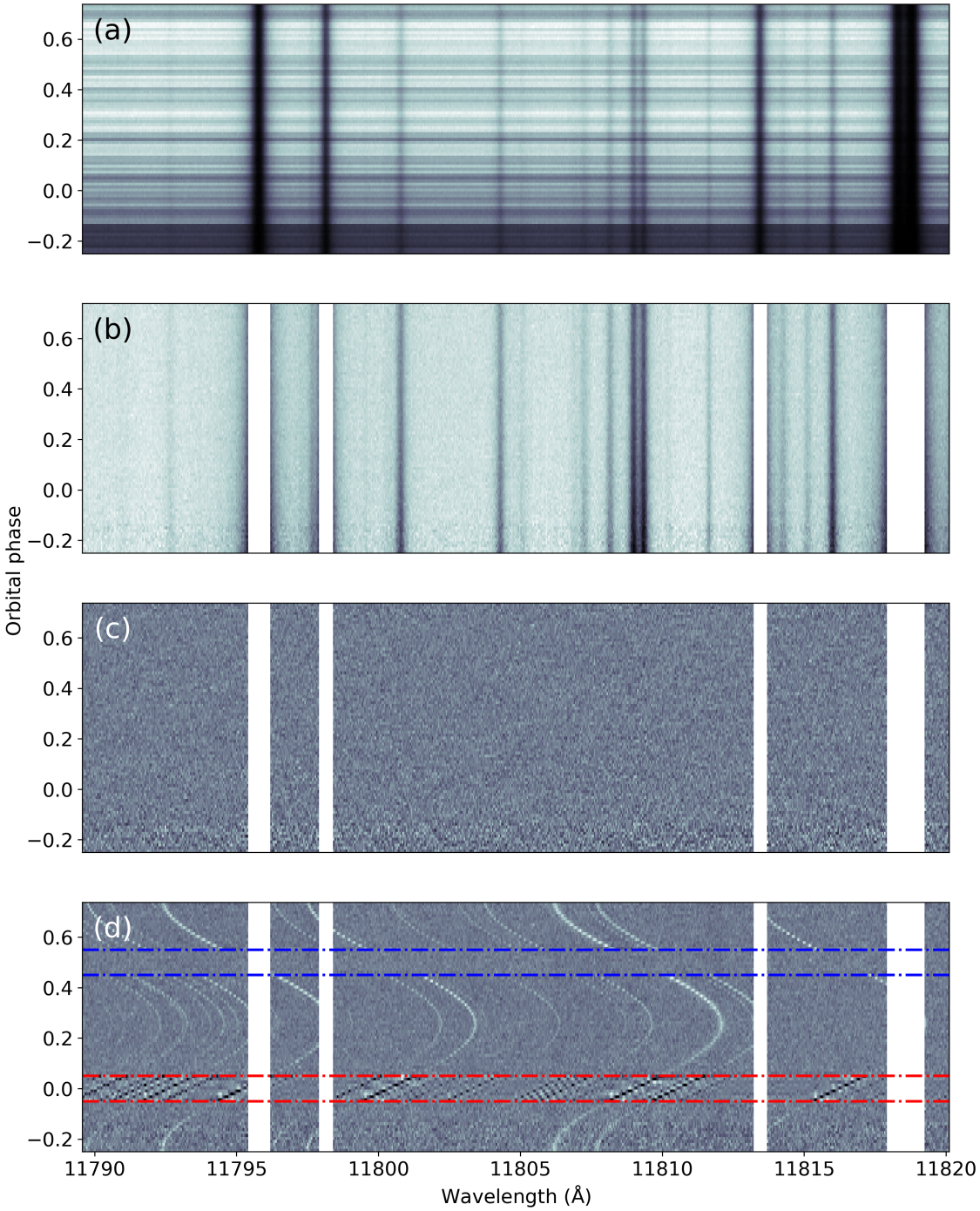

Figure 1.8.: Steps of data analysis including the use of `SYSREM`. The example data cover an entire planetary orbit. *Panel a* shows the spectral matrix after extraction from the raw data. *Panel b* illustrates the spectral matrix after normalization to the continuum level. The strongest telluric features are masked in this step. *Panel c* is the residual spectral matrix after applying `SYSREM` over several iterations. The systematic effects are removed, leaving behind the faint planetary signal that is buried in the noise. In *panel d*, we show the same residual spectral matrix, but with an enhanced synthetic model spectrum of an exoplanet atmosphere injected into the data. The Doppler-shift and the intensity of the planetary lines change as a function of time. The primary and the secondary eclipses are indicated by red and blue dash-dotted lines, respectively. During the primary eclipse, the planetary lines are in absorption shape, while outside primary eclipse the planetary emission lines can be recognized. The planetary spectral signature is absent during the secondary eclipse, when the planet is occulted by its host star.

features of the light curves by iteratively fitting their trends as a function of time. In the following, the modeled systematics are removed from the data.

The input data needed by SYSREM are the spectral matrix and the respective uncertainties. For most high-resolution spectrographs, these uncertainties are extracted from the instrument pipeline along with the spectra from the raw data. However, for specific instruments, the uncertainties are not provided by the instrument pipeline. For instance, this is the case for the spectra extracted from the HARPS-N data. A simple way to overcome the problem of missing uncertainties is to assign uniform errors to all data points of the spectral matrix. However, better performance of the SYSREM algorithm can be achieved by estimating the noise of the spectral matrix (Yan et al. 2020). In Chapter 4, we provide details about our method for quantifying the uncertainty of each data point of the HARPS-N spectral matrix.

To model the telluric and stellar lines, SYSREM is applied over multiple iterations. We use a maximum of ten consecutive iterations in this thesis depending on the number and intensity of the systematic features to correct for. After each iteration, the modeled systematic contribution is subtracted from the data. Most studies in the literature use this subtraction-based approach for applying SYSREM. However, subtraction of the modeled systematic effects comes with the disadvantage of not preserving the relative strength of the planetary spectral signature falling onto stellar and telluric lines. So-called retrieval frameworks used for fitting parametrized model spectra of planetary atmospheres to the residual spectra are sensitive to the strength of the exoplanet spectral lines. Thus, subtracting the modeled systematics from the data is not an appropriate procedure when using retrieval frameworks. An alternative method that preserves the amplitude of the planetary spectral lines has recently been proposed (Gibson et al. 2020). This method runs SYSREM in the classical way and thereafter, co-adds the models from all the iterations. The co-added SYSREM model is then divided out from the original data and unity is subtracted. This approach of correcting for systematics no longer alters the relative strength of the planetary lines at the location of strong systematic features.

After removing the systematic effects with SYSREM, the residual spectral matrix contains the spectral signature of the exoplanet atmosphere dominated by noise. In the case of transmission spectroscopy, the planetary signal corresponds to the transmission spectrum in Eq. (1.5) normalized to its continuum with unity subtracted (ΔF). When using emission spectroscopy, the planetary spectrum buried in the noise is equal to the continuum normalized planet-to-star contrast ratio (F_p/F_*).

1.4.4. Spectral modeling

An efficient procedure to extract the signature of an exoplanet atmosphere from the noisy spectral residual matrix is given by the cross-correlation method. This routine is widely used to investigate the atmospheres of exoplanets and comprises calculating the cross-correlation function between the residual spectra and a planetary model spectrum. The method combines the spectral lines of

the exoplanet atmosphere into a single detection peak that exceeds the noise, which provides a clear identification of the planetary signal (e.g., Snellen et al. 2010; Brogi et al. 2012; Rodler et al. 2012; Yan et al. 2020; Kasper et al. 2021).

In a first step, we need to define the atmospheric structure for calculating the model spectrum of an exoplanet atmosphere. Important parameters to describe the atmospheric structure are the temperature-pressure profile, the elemental abundances, and the surface gravity. Typically, several approximations are made in this step to achieve a relatively low complexity level of the model calculation. For example, temperature-pressure profiles that allow for a simple parametrization or equilibrium chemistry are assumed to describe the conditions in exoplanet atmospheres (e.g., Hoeijmakers et al. 2019; Ishizuka et al. 2021). In particular, the assumption of chemical equilibrium enables a relatively simple computation of the mixing ratios of the different chemical species present in the planetary atmosphere (e.g., Yan et al. 2020, 2022b). In most cases, assuming a plane-parallel atmospheric geometry is sufficient to successfully characterize exoplanet atmospheres. Alternatively, so-called general circulation models allow us to consider the three-dimensional atmospheric structure at the cost of an increased computational effort (e.g., Showman et al. 2013; Parmentier et al. 2018; Beltz et al. 2021).

Radiative transfer is calculated through the exoplanet atmosphere to obtain the model spectrum after setting up the atmospheric structure. This calculation considers the propagation of photons along different rays through the planetary atmosphere. Absorption, emission, and scattering of the photons with the gas particles are generally considered for solving for the radiative transfer equation. For details on radiative transfer in planetary atmospheres and the formal solution of the radiative transfer equation, we refer the reader to the literature (e.g., Lopez-Puertas & Taylor 2002). A number of tools and codes for radiative transfer are publicly available, for example `TAUREx` (Waldmann et al. 2015), `CHIMERA` (Line et al. 2017), or `petitRADTRANS` (Mollière et al. 2019). We use the latter radiative transfer code to compute the model spectra in this thesis. The `petitRADTRANS` radiative transfer code is available as `Python` package, allowing straightforward calculation of transmission and emission spectra at low ($R \sim 1000$) and high spectral resolution ($R \sim 10^6$). However, the accuracy of the model spectra critically depends on the quality of the opacity data of the atmospheric gas particles, which are needed as input for the radiative transfer calculation. For example, the limited precision of the TiO opacity database (Hoeijmakers et al. 2015; Nugroho et al. 2017) has led to conflicting results between several studies on UHJ atmospheres (e.g., Haynes et al. 2015; Nugroho et al. 2017; Herman et al. 2020; Serindag et al. 2021). Nevertheless, high precision opacity data is available for an increasing number of chemical species over a wide range of wavelengths, temperatures, and pressures (e.g., `HITRAN`, `HITEMP`, `EXOMOL` databases; Rothman et al. 2010; Tennyson et al. 2016; Gordon et al. 2017).

The radiative transfer code `petitRADTRANS` enables computing the transit radius and the exoplanet atmospheric flux as a function of the wavelength for transmission and emission spectroscopy, respectively. However, the scaling of these quantities is not consistent with that of the exoplanet signal in the residual spectral matrix. Therefore, the output of `petitRADTRANS` requires

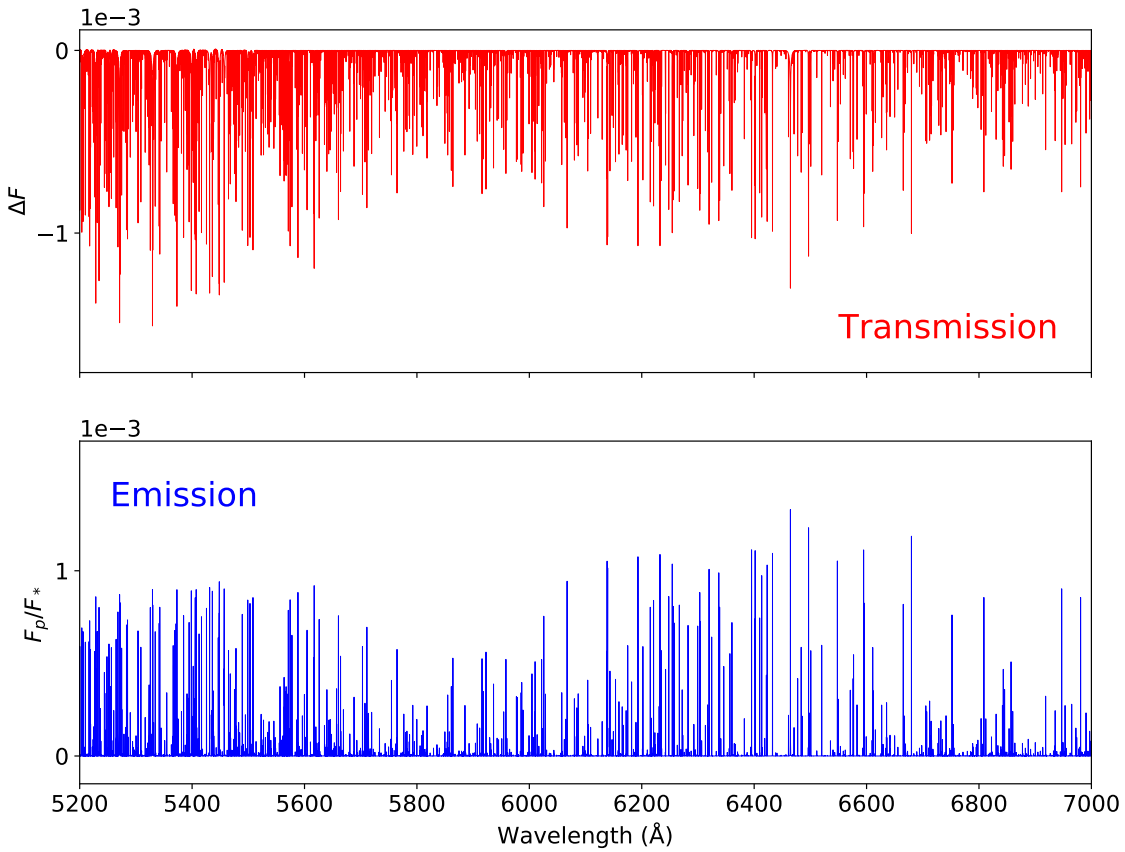

Figure 1.9.: Model spectra from an exoplanet atmosphere computed with `petitRADTRANS`. The *top* and *bottom* panels show examples of post-processed transmission (ΔF) and emission model spectra (F_p/F_*), respectively. The models are normalized to the spectral continuum level and convolved with the instrumental profile.

additional post-processing steps before computing the cross-correlation function with the residual spectra. Using Eq. (1.5), the transit radius modeled by `petitRADTRANS` is converted into the planetary transmission spectrum and thereafter, normalized to the spectral continuum level. On the other hand, for emission spectroscopy, we integrate the `petitRADTRANS` modeled flux from the exoplanet atmosphere over the planetary surface and normalize with the flux of the host star. The resulting planet-to-star flux ratio is then normalized to its continuum level. Finally, the normalized transmission and emission model spectra are convolved with the line-spread-function of the spectrograph to account for the intrinsic line broadening from the instrument. Figure 1.9 illustrates examples of `petitRADTRANS` model spectra resulting from the overall described post-processing procedure.

1.4.5. Cross-correlation analysis

Calculating the cross-correlation function between an exoplanet model spectrum and the residual spectra enables us to merge the information of the faint planetary spectral lines into a detectable signal. The cross-correlation function is computed separately for each residual spectrum of the time series. To this end, the model spectrum is shifted step-by-step over a predefined RV interval,

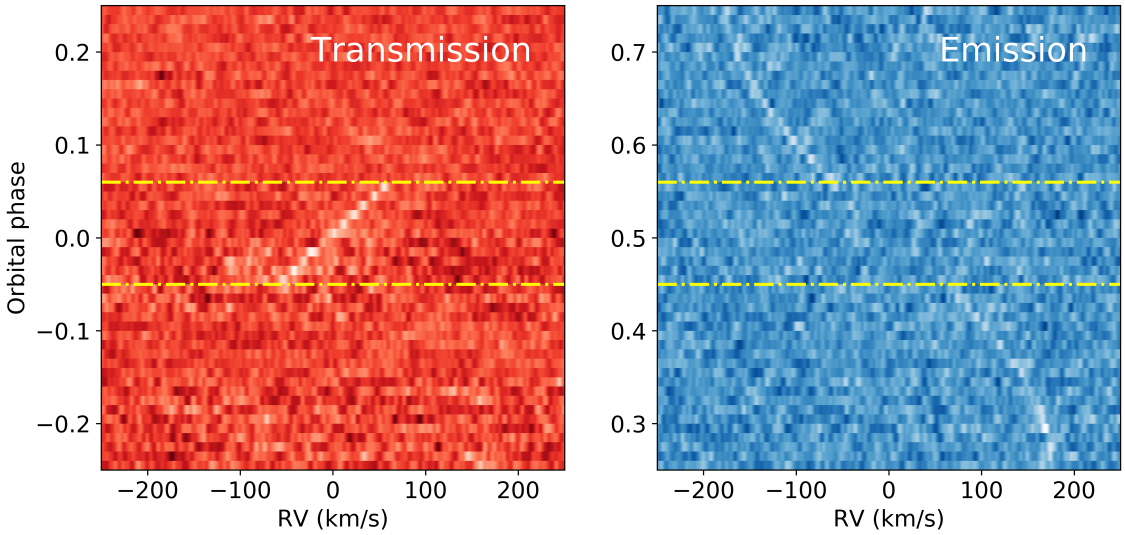

Figure 1.10.: Example CCF maps in the stellar rest frame. The *left panel* shows the transmission, and the *right panel* shows the emission cross-correlation signal from an exoplanet atmosphere. The yellow dash-dotted lines indicate the beginning and the end of the primary and secondary eclipse, respectively. The transmission signal is detectable exclusively during the primary eclipse, and the emission signal is absent during the secondary eclipse. We use synthetic data to generate the CCF maps.

which is typically centered on zero and extends over several hundred km s^{-1}. At each RV step, the model spectrum is multiplied with the residual spectrum under consideration. The so-obtained cross-correlation function (CCF) is defined as

$$\mathrm{CCF} = \sum r_i m_i(v), \tag{1.6}$$

with r_i being the residual spectrum and m_i the model spectrum shifted by v in the RV space. As an optional step, the data points of the residual spectra can be weighted with the inverse of the squared uncertainties, yielding the so-called weighted CCF (e.g., Yan et al. 2020, 2022a). Subsequently, if the spectra are provided in the order-by-order format, the information of the different echelle orders is combined by co-adding their CCFs. This step is not required if the CCFs are calculated from residual spectra in the order-merged format. In the following, the CCFs of the entire time series are arranged in a two-dimensional array, called CCF map. Figure 1.10 shows examples of CCF maps for transmission and emission spectroscopy, illustrating the moving Doppler-shift of the exoplanet signal that forms a tilted trail. Analyzing this CCF trail allows us to constrain the orbital and atmospheric parameters of the exoplanet under investigation.

Care must be taken when using the cross-correlation method as various effects can introduce spurious signals into the CCF map. Prominent examples of spurious signals are those caused by the Rossiter-McLaughlin effect (RME) and the center-to-limb variation (CLV), both originating in the distortion of the stellar line profile as the planet transits in front of its host star. The RME is caused by the stellar rotation (Rossiter 1924; McLaughlin 1924), while the CLV describes the variation of the stellar line depth from the center to the limb of the stellar disk (e.g., Czesla et al. 2015; Yan et al. 2015, 2017). Another example is the presence of artifacts in the CCF map caused by stellar

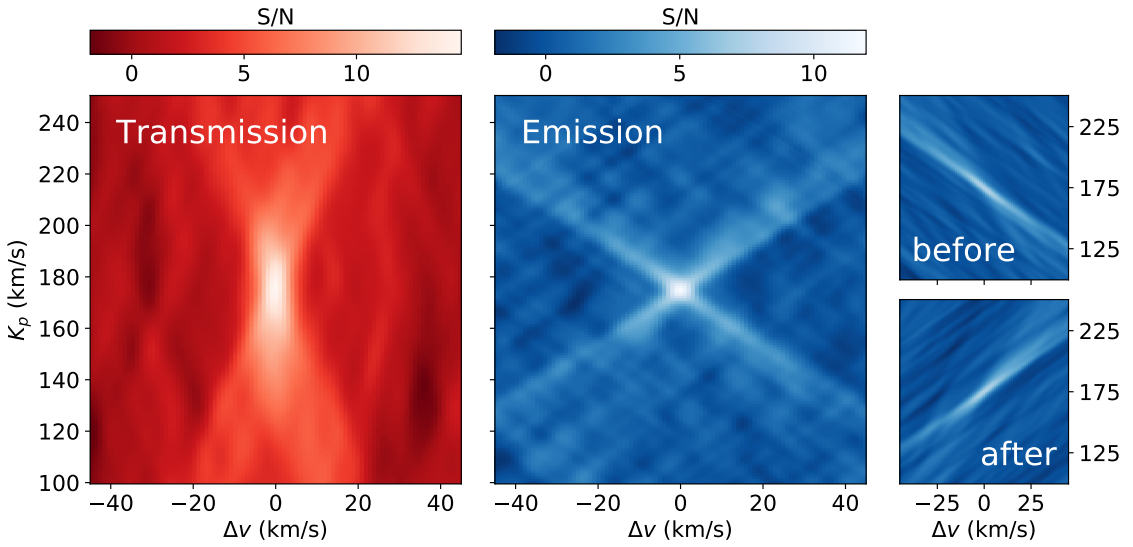

Figure 1.11.: Example S/N maps in the planetary rest frame computed from the CCF maps in Fig. 1.10. The *left panel* shows the transmission, the *middle panel* the emission S/N detection map. Particularly, emission spectroscopy enables us to get tight constraints on the location of the detection peak by combining the cross-correlation signal from orbital phases before and after the secondary eclipse. The contributions from orbital phases before and after the secondary eclipse to the overall emission S/N map are illustrated in the *right panels*.

pulsations, affecting both transmission and emission spectroscopy observations. These pulsations produce a variable stellar line profile and thereby, hinder an efficient removal of the lines from the host star during the correction for systematic effects (e.g., Nugroho et al. 2020a; Herman et al. 2022). For instance, artifacts of this type are found in the CCF maps of our WASP-33b observations, which are presented in Chapters 2, 3, and 4 of this thesis. In general, spurious signals of unwanted effects are either masked or modeled and then subtracted from the data (e.g., Yan et al. 2019; Kesseli et al. 2022).

In a next step, the cross-correlation signal is translated into a detection significance of the planetary atmosphere. Equation (1.3) is used to align the CCF map to the planetary rest frame over a range of different K_p values under the assumption of a circular orbit. Each shifted CCF map is collapsed into a one-dimensional CCF by computing the mean value over all orbital phases. Subsequently, the one-dimensional CCF of each alignment is stacked in a two-dimensional array. After normalizing the array by its standard deviation, we obtain a signal-to-noise detection map (S/N map) as a function of the orbital parameters K_p and Δv. If the planetary spectral signature is present in the data, the S/N map shows a significant peak at the expected K_p and close to a Δv of $0\,\mathrm{km\,s^{-1}}$. Typically, very faint planetary signals can be identified only after combining the aligned and collapsed CCF maps into the S/N map. Figure 1.11 shows example S/N maps from transmission and emission spectroscopy. The orientations of the S/N detection patterns between transmission and emission spectroscopy differ due to the distinct phase intervals probed by the two methods. In particular, emission spectroscopy offers the possibility of combining the differently oriented detection patterns measured at orbital phases before and after secondary eclipse, allowing us to precisely constrain the coordinates of the planetary signal in the K_p–Δv parameter space.

In addition, a number of alternative methods for extracting and characterizing an exoplanet signal from the CCF map are used in the literature. For example, the Welch t-test is applied to compare the distribution of pixel values inside and outside the planetary trail in the CCF map (Welch 1947). This test assesses the probability that the "in-trail" and "out-of-trail" pixel distributions result from the same parent distribution and thereafter, converts the resulting probability value into a detection significance (e.g., Cabot et al. 2019; Sánchez-López et al. 2019; Alonso-Floriano et al. 2019). Another successfully applied approach for extracting the exoplanet signal consists of directly fitting a parameterized model of the cross-correlation signal to the CCF map (Yan et al. 2020, 2022b).

1.5. Characterizing exoplanets at high spectral resolution

The use of high-resolution spectroscopy has become routine for detecting and resolving the individual spectral lines emerging from exoplanet atmospheres. Particularly, using the cross-correlation technique and fitting parameterized model spectra to high-resolution spectroscopy observations are promising methods for in-depth atmospheric characterization. This section provides an overview of the most important physical processes and properties of hot giant exoplanet atmospheres that can be inferred with high-resolution spectroscopy. We detail how this method enables us measuring the parameters of planetary systems and characterizing the atmospheric chemistry and dynamics of exoplanets. The effect of the thermal structure of exoplanet atmospheres on the spectral signature is discussed earlier in this thesis, and we refer the reader to Sects. 1.3.2 and 1.3.3 for the respective details.

1.5.1. Planetary and stellar parameters

High-resolution Doppler spectroscopy not only allows us to measure the planetary K_p and Δv values, but also enables the determination of additional parameters of exoplanet systems. In the following, we describe how these additional parameters can be determined and give the relevant equations.

The orbital semi-amplitude of an exoplanet's host star is given by

$$K_* = \left(\frac{2\pi G}{P}\right)^{1/3} \frac{M_\mathrm{p} \sin i_\mathrm{p}}{(M_\mathrm{p} + M_*)^{2/3}} \frac{1}{(1-e^2)^{1/2}}, \tag{1.7}$$

wherein M_p is the exoplanet mass, M_* is the stellar mass, G is the gravitational constant, P is the orbital period, e is the eccentricity, and i_p is the orbital inclination (Cumming et al. 1999). On the other hand, the orbital semi-amplitude of an exoplanet with a circular orbit is given by

$$K_\mathrm{p} = \frac{2\pi a}{P} \sin i_\mathrm{p} = \left(\frac{2\pi G M_*}{P}\right)^{1/3} \sin i_\mathrm{p}, \tag{1.8}$$

with a being the orbital semi-major axis (Birkby 2018). The combination of Eqs. (1.7) and (1.8) assuming $e = 0$ and $M_\mathrm{p} \ll M_*$ links the orbital motion of the exoplanet and its host star around the systemic barycenter to the masses of the two objects:

$$\frac{M_\mathrm{p}}{M_*} = \frac{K_*}{K_\mathrm{p}}. \tag{1.9}$$

The value of K_p is determined as described in Sect. 1.4.5, K_* is derived via RV measurements and M_* is calculated using stellar evolution models (Birkby 2018).

For non-transiting exoplanets, Eq. (1.8) enables us determining the orbital inclination i_p, which, in turn, can be used to estimate the exoplanet mass M_p via Eq. (1.7). In the presence of a transiting exoplanet, i_p can be directly derived from the transit light curve (e.g., Casasayas-Barris et al. 2019). In this case, the stellar mass M_* can be calculated model-independently via Eq. (1.8).

1.5.2. Elemental abundances and planetary formation

Planets form from the material of their surroundings in protoplanetary disks, which are rotating disks of gas and dust around young stars. The chemistry within these disks can strongly vary as a function of their evolutionary stage and the distance from the host star. Consequently, the formation and migration history of planets is encoded in their chemical composition (Madhusudhan 2019; Lothringer et al. 2021). Today, the core accretion model is thought to best explain the formation of gas giant planets. This scenario predicts the formation of a solid planetary core, followed by the accretion of significant amounts of gas (e.g., Pollack et al. 1996; Helled et al. 2014). Alternatively, the so-called disk instability model has been proposed, which predicts planet formation via fragmentation of the protoplanetary disk and eventual contraction of the fragments (e.g., Helled et al. 2014; Gargaud et al. 2015). Current models predict that planet formation occurs preferentially at large orbital separations from the host star, followed by migration to close-in orbits (e.g., Madhusudhan et al. 2014a; Hands & Helled 2022). However, theoretical work has shown that in-situ formation close to the host star may also be possible (Batygin et al. 2016; Boley et al. 2016). Consequently, one of the major goals of high-spectral-resolution observational studies is to constrain the present-day chemistry of exoplanet atmospheres and to compare the results with model predictions of planetary formation and migration.

The emission and absorption lines of a variety of chemical species have been discovered in the high-resolution spectra of exoplanet atmospheres. Spectral features of atomic species in their neutral and ionized form are most prominent in the spectra of UHJs as thermal dissociation mostly prevents the formation of more complex chemical species. Molecular lines, on the other hand, are commonly present in the spectra of planetary atmospheres with more moderate temperatures as compared to the atmospheric thermal conditions of UHJs. So-called retrieval frameworks have been developed that are employed to fit these spectral features with parameterized model spectra and to constrain the physical parameters and elemental abundances in the atmospheres of exoplanets (e.g., Brogi & Line 2019; Gibson et al. 2020). In particular, this method enables constraining

the exoplanet atmospheric carbon-to-oxygen (C/O) ratio and the abundances of metal[2] elements, which are quantities that are critically affected by the processes involved in planet formation (e.g., Madhusudhan 2012, 2019; Mordasini et al. 2016; Lothringer et al. 2021; Line et al. 2021). The C/O ratio is calculated as the ratio between the number of carbon and oxygen atoms per unit volume and defined by $\mathrm{C/O} = N_\mathrm{C}/N_\mathrm{O}$. The metallicity in an exoplanet atmosphere is the stellar- or solar-normalized logarithmic ratio between the number densities of the metal species in consideration and hydrogen and is calculated as $[\mathrm{M/H}] = \log\left(N_\mathrm{M}/N_\mathrm{H}\right)_\mathrm{p} - \log\left(N_\mathrm{M}/N_\mathrm{H}\right)_*$ (Nissen 2013).

Figure 1.12 gives a simplified picture of how the abundances of the most important volatile species (H_2O, CO_2, CO) in a protoplanetary disk affect the C/O ratio of a forming planet. The local temperature in the disk diminishes with increasing distance from the host star. At the distance where the disk temperature falls below the sublimation temperature of a specific volatile, the species in consideration passes from the gaseous to the solid state. This distance is referred to as snowline. Inside the snowline of the considered species, a volatile contributes to the gaseous component of the protoplanetary disk, while outside it is frozen out and contributes to the solid component. Among the most abundant volatile species, the innermost snowline is that of H_2O, followed by the snowlines of CO_2 and CO as shown in the top panel in Fig. 1.12 (Madhusudhan 2019). This freezing-out-sequence results in a C/O ratio of the disk gas that increases towards the outer regions of the protoplanetary disk. That of the solids is higher in the inner regions of the protoplanetary disk than in the outer regions. At distances beyond the CO_2 snowline, CO dominates the gaseous component of the disk, which leads to a C/O ratio close to unity as illustrated in the bottom panel in Fig. 1.12 (Öberg et al. 2011). In summary, the location relative to the different snowlines where a planet accreted gaseous or solid material during its formation critically affects the chemical abundances present in its atmosphere.

So far, measurements of the C/O ratio and metallicity have been performed mostly for short-period gas giant exoplanets. Elevated C/O ratios and low metallicity values are interpreted as an indication of planet formation outside the major snowlines, which is then followed by inward migration after the dissipation of the disk (Öberg et al. 2011; Madhusudhan et al. 2014a). On the other hand, low C/O ratios and elevated metal abundances hint towards the accretion of oxygen-rich planetesimals during migration through the protoplanetary disk before disk dissipation (Shibata et al. 2020, 2022; Lothringer et al. 2021). Other possible explanations for elevated metal abundances in exoplanet atmospheres consider the drift of pebbles with elevated metallicity from the outer to the inner regions of the protoplanetary disk where they undergo sublimation and accretion (Booth et al. 2017), or erosion and mixing of metal-rich material from the planetary core with the atmosphere (Madhusudhan et al. 2017). Expanding the sample of exoplanets accessible to measurements of elemental abundances and ratios, as well as advancing retrieval techniques in combination with theoretical work, will allow us to gain further insights into planet formation.

[2] In astronomy, all elements other than hydrogen and helium are referred to as metals. The metal abundance is called metallicity.

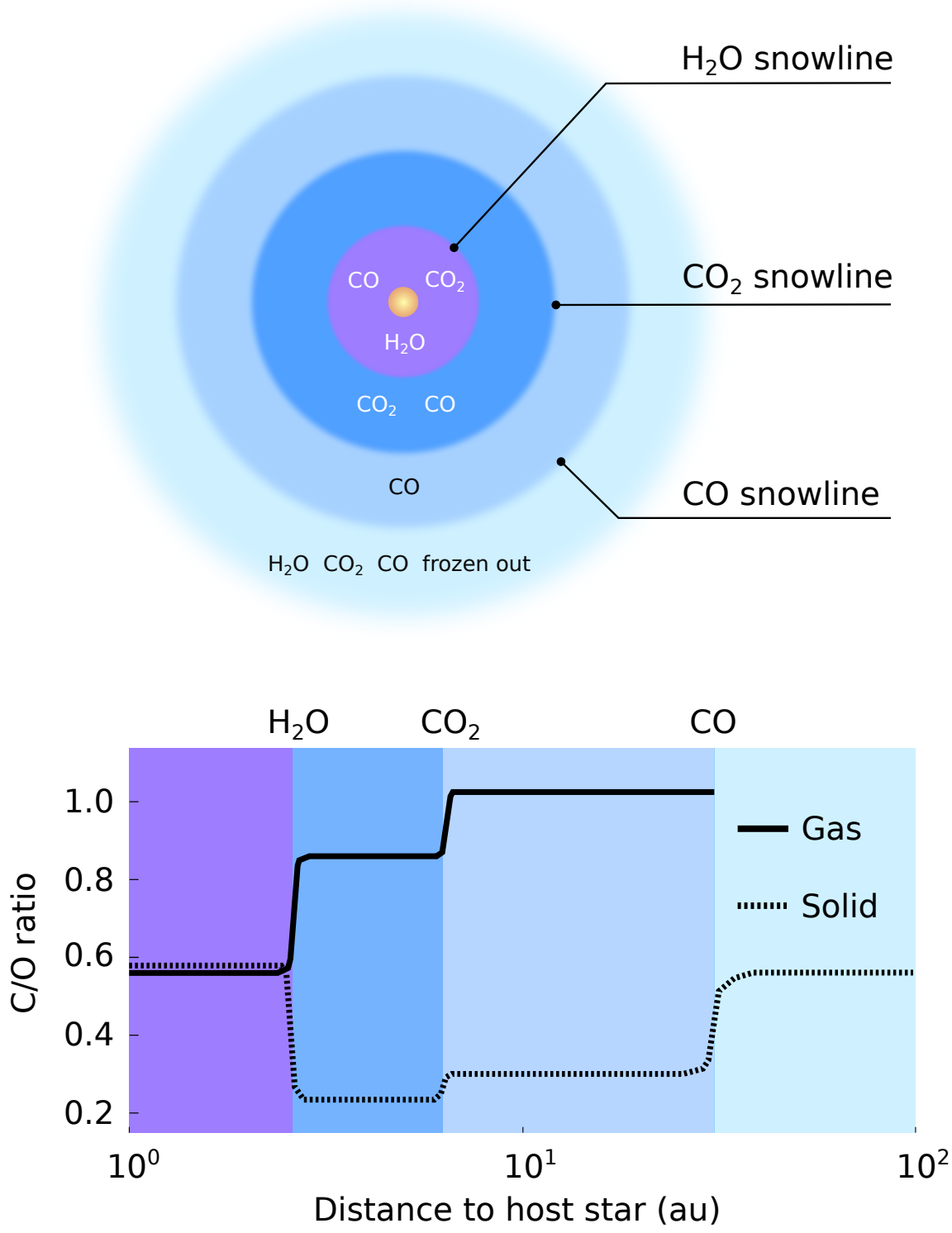

Figure 1.12.: Distribution of the main volatile species in the protoplanetary disk and C/O ratio. In the *top panel*, we report a simplified scheme of the protoplanetary disk with the snowlines of the main volatile species. In addition, we show the names of the main volatile species present in the gas phase at different orbital distances. The host star is the yellow sphere at the center of the disk. The image is not to scale. The *bottom panel* illustrates the C/O ratio of the gaseous and solid components of the disk as a function of the orbital distance from the host star (*Image credit:* Figure adapted from Madhusudhan 2019). At the specific snowlines, the species in consideration (H_2O, CO_2, and CO) freeze out. The C/O ratio of the gas increases outward in the disk; the C/O ratio of the solids is higher in the inner regions of the protoplanetary disk than in the outer regions.

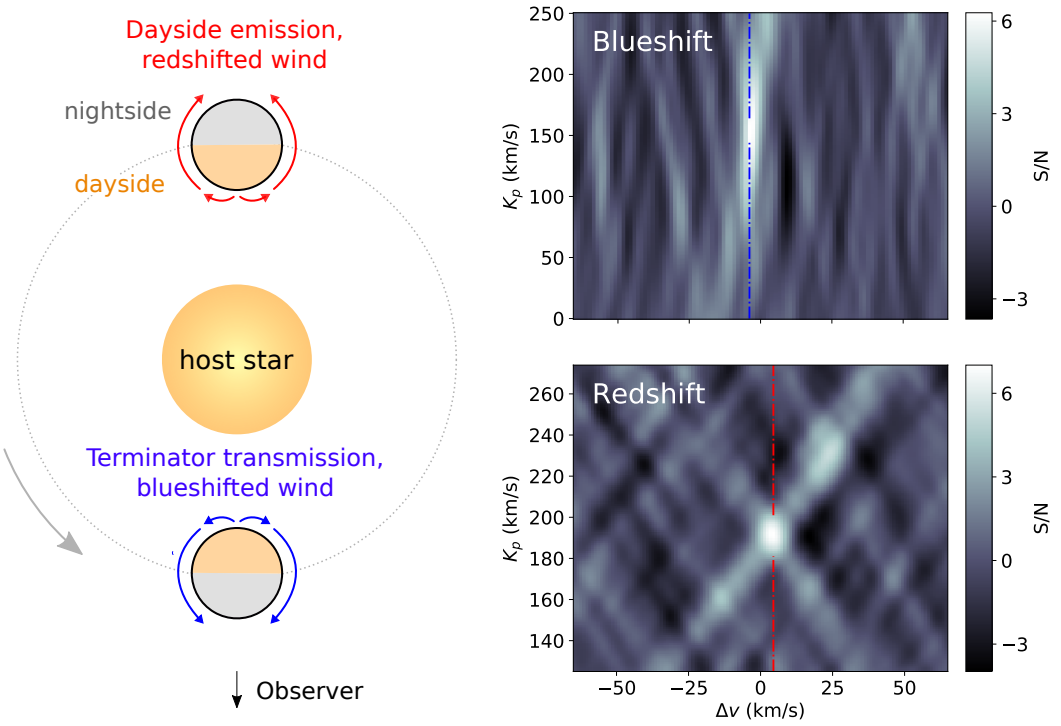

Figure 1.13.: Day- to nightside winds. The *left panel* shows a schematic of the day- to nightside winds for transmission and emission spectroscopy (*Image credit:* Figure adapted from Yan et al. 2022a). The *top right panel* shows the transmission spectroscopy S/N map obtained from the observation of the hot Jupiter HD 189733b (reanalysis of the H_2O detection by Alonso-Floriano et al. 2019; $\Delta v = -3.9\,\mathrm{km\,s^{-1}}$). When the planet passes in front of its host star, the atmospheric day- to nightside winds are oriented towards the observer, resulting in a blueshifted spectral signature. In the *bottom right panel*, we illustrate the emission spectroscopy S/N map from the observation of the UHJ WASP-189b (CO detection by Yan et al. 2022a; $\Delta v = 4.5\,\mathrm{km\,s^{-1}}$). The dayside of the planet is aligned with the observer's line of sight, resulting in a redshifted spectral signature as the wind is directed away from the observer. The red and blue dash-dotted lines indicate the blue- and redshifted signals from the planetary atmospheres.

1.5.3. Atmospheric dynamics

Theoretical work has explored the dynamics in the atmospheres of gas giant exoplanets with elevated temperatures. An important result of these studies is the existence of global winds with velocities on the order of a few $\mathrm{km\,s^{-1}}$ (Miller-Ricci Kempton & Rauscher 2012). Two classes of wind patterns dominating the atmospheric circulation are predicted: either day- to nightside airflows or super-rotational jet streams (Showman et al. 2013; Tan & Komacek 2019).

Day- to nightside winds can be identified in the atmospheres of hot giant exoplanets via the detection of significant Doppler-shifts at high spectral resolution. The left panel in Fig. 1.13 shows a simplified scheme of the day- to nightside winds. When the planet transits in front of its host star, the atmospheric day- to nightside airflow is oriented towards the observer. This results in a blueshifted transmission signal from the exoplanet atmosphere. Consequently, the detection peak in the S/N map is deviated to negative Δv values as illustrated in the top right panel of Fig. 1.13 (e.g., Snellen et al. 2010; Brogi et al. 2016, 2018; Alonso-Floriano et al. 2019). On the other hand, the atmospheric airflow is directed away from the observer when the planetary dayside is aligned with the observer's line of sight. This results in a redshifted emission signal from the dayside

atmosphere of the exoplanet. Such a redshift is detected as a deviation of the S/N peak toward positive Δv values as shown in the bottom right panel of Fig. 1.13 (Yan et al. 2020, 2022a).

Strong winds flowing at constant latitudes in the equatorial regions of hot giant exoplanets dominate the global circulation in the jet stream regime. In this scenario, the airflow moves toward the observer at one terminator and away from the observer at the other terminator when the planet transits across the front of its host star. Therefore, transmission spectroscopy can show a broadened spectral line profile or, in the case of very strong wind speeds, Doppler-shifted signals with opposite signs at ingress and egress. For instance, Salz et al. (2018) detected a redshifted and blueshifted signal at transit ingress and egress of HD 189733b, respectively. In this case, at ingress the absorption signal mostly originates from the leading planetary limb where super-rotation moves the material away from the observer. The atmospheric material at the trailing limb, which approaches the observer, mostly causes the blueshifted egress signal. On the other hand, the Doppler-shift of the emission spectroscopy signal caused by jet stream circulation corresponds to the integrated Doppler-velocity over the planetary disk. Measuring the integrated Doppler-shift results in a complex combination of winds and planetary rotation (Zhang et al. 2017). The detected values of $K_{\rm p}$ and Δv in the S/N map can significantly deviate from the expected coordinates. Hence, the interpretation of emission spectroscopy wind measurements is a challenging task. Moreover, the presence of equatorial jet streams causes the hottest region in giant exoplanet atmospheres to move downstream of the wind flow, away from the substellar point (Knutson et al. 2007). Attempts have been made to constrain the shifts of these so-called atmospheric hot spots at high spectral resolution. However, high-resolution observational studies as of now have not yielded conclusive results (e.g., Herman et al. 2022; van Sluijs et al. 2022).

In addition to atmospheric winds, other physical processes in the atmospheres of exoplanets can be characterized by high-resolution spectroscopy. For example, assessing the broadening of the detected cross-correlation signal allows for investigating the planetary rotation period (Snellen et al. 2014). On the other hand, an asymmetric CCF trail relative to the center of the primary or secondary eclipse can indicate thermal or chemical inhomogeneities in exoplanet atmospheres. These asymmetries usually translate into an offset of the detection peak from the expected position in the S/N map. Disentangling the Doppler-shifts originating from different atmospheric processes is difficult since the total Doppler-signature is a degeneracy of winds, rotation, thermal and chemical structure. Therefore, comparing the Doppler-offset and the line broadening measured at high spectral resolution with theoretical model predictions can improve our understanding of atmospheric dynamics, planetary rotation, and the structure of exoplanet atmospheres.

1.5.4. Atmospheric escape

Exoplanets on close-in orbits are exposed to elevated irradiation levels from their host stars. The intense stellar fluxes lead to strong heating in the atmosphere, which can cause a significant escape of gas from the planetary gravitational field. To date, two mechanisms are thought to best

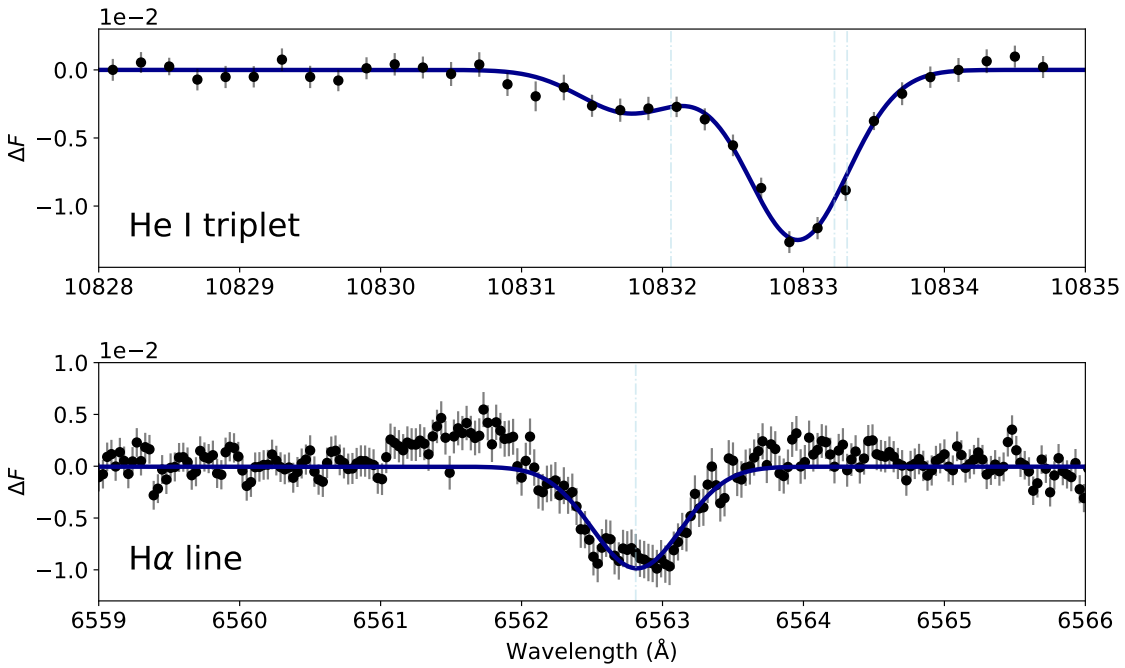

Figure 1.14.: High-spectral-resolution signature of atmospheric escape. The *top panel* shows the He I transmission spectrum, which is the combination of three distinct absorption lines (*Image credit:* Figure adapted from Lesjak et al. 2022). The *bottom panel* illustrates the transmission spectrum of the Hα line (*Image credit:* Figure adapted from Yan et al. 2021). We use black circles to denote the spectral data points with the respective uncertainties. The dark blue curves represent the best-fit Gaussian functions, which correspond to the superposition of three functions in the case of the He I spectral lines. The light blue dash-dotted lines indicate the centers of the respective absorption lines.

explain this so-called atmospheric escape. In the photoevaporation model, the absorption of X-ray and ultraviolet photons induces strong heating in the planetary atmosphere (Lammer et al. 2003). This heating mechanism results in the expansion of the planetary atmosphere, which leads to a significant gas outflow. Alternatively, the core-driven mass-loss model considers heating from the planetary interior in addition to the incoming stellar radiation as an energy source for atmospheric mass loss (Ginzburg et al. 2018; Gupta & Schlichting 2020). Hydrogen and helium are the chemical species that most easily overcome a planet's gravitational field given their low atomic weight, and strong outflows of these species can carry heavier atoms and molecules. This hydrodynamic drag enables species with masses significantly higher than hydrogen and helium, such as C II, O I, or Mg I, to escape from exoplanet atmospheres (Vidal-Madjar et al. 2004, 2013). Outside our Solar System, the outflow of atmospheric material has so far been observed in the spectra of gas giant planets and Neptune-sized objects (Owen 2019).

Atmospheric mass loss can be detected as strong excess absorption during transit events since the escaping material covers a significant fraction of the stellar disk. A key quantity in the observation of atmospheric escape is the so-called Roche lobe radius. The material within the Roche lobe radius is gravitationally bound to the planet, the material beyond this limit is no longer bound. Therefore, an observed transit radius of an exoplanet close to or greater than the Roche lobe radius indicates the presence of ongoing atmospheric escape and allows us to measure the planetary mass loss rate. Spectral features that are particularly sensitive to outflowing material include the

Lyman-α (Vidal-Madjar et al. 2003) and the Balmer Hα (Yan & Henning 2018) hydrogen absorption lines at ultraviolet and VIS wavelengths, as well as the He I line triplet in the NIR range (Oklopčić & Hirata 2018; Spake et al. 2018). Particularly, Hα and the three He I absorption lines are located at wavelengths accessible to present-day available high-resolution spectrographs and are therefore a suitable diagnostic to study the dynamical and spatial structure of escaping atmospheres (Yan & Henning 2018; Nortmann et al. 2018; Allart et al. 2019). Figure 1.14 illustrates transmission spectra of the Hα line and the He I line triplet. Since the spectral signature of atmospheric escape essentially consists of a few isolated spectral lines, their high-resolution transmission spectra are in most cases directly characterized rather than using the cross-correlation technique.

Theoretical work has shown that atmospheric mass loss is strongly affected by the properties of an exoplanet's host star (MacLeod & Oklopčić 2022). The interaction with the stellar wind can shape the outflowing material into a comet-like tail. For instance, excess absorption of the He I triplet in the spectra of WASP-69b beyond the primary eclipse has been interpreted as such a cometary outflow following the planet on its orbit (Nortmann et al. 2018). On the other hand, the planetary magnetic field can also affect the morphology of outflowing material and thus, influence the observable signature of atmospheric escape. Theoretical models predict a polar escape of material at strong magnetic field strengths, causing a double-tail outflow pattern that can be inferred from narrow band transit light curves (McCann et al. 2019; Carolan et al. 2021).

In addition, atmospheric escape is an important factor for planetary evolution and consequently for exoplanet populations. In particular, small exoplanets can be significantly affected by material outflows and lose a considerable fraction of the planetary mass over their lifetime. A well-known phenomenon showing how atmospheric escape can affect the population of exoplanets is the observed underpopulation of planets with radii between 1.5 and 2 times the Earth's radius, which is commonly known as "radius valley" (Fulton et al. 2017; Rogers et al. 2021). On the other hand, the evolution of giant exoplanets is suggested to be only marginally affected by atmospheric escape due to their elevated masses (Owen 2019).

1.6. Thesis outline

In this thesis, we present studies on the physical conditions in the atmospheres of the hottest exoplanets known to date, the UHJs. We use high-resolution spectroscopy observations obtained with the instruments CARMENES, HARPS-N, and ESPaDOnS for investigating the atmospheric properties of these planets.

In Chapter 2, we report the analysis of the emission spectrum of the UHJ WASP-33b in the VIS range. This study results in the detection of Fe I and provides evidence for the presence of TiO in the planetary atmosphere. A different strength of Doppler-shift between the spectra from the two chemical species indicates a three-dimensional chemical structure in the dayside hemisphere

of the planet. Chapter 3 presents the detection of Si I emission lines in the NIR spectra of the two UHJs WASP-33b and KELT-20b/MASCARA-2b. This study represents the first high-resolution detection of Si in any form in exoplanet atmospheres. Si-bearing species play a fundamental role for cloud formation and in the energy balance of hot giant exoplanets. Chapter 4 describes the study of the high-spectral-resolution signature of WASP-33b over an extended wavelength interval between the near-ultraviolet and the NIR range. The study yields the detection of the spectral emission lines of Si I, Ti I, Ti II, V I, Fe I, and the hydroxyl radical (OH). The emission lines of the detected species are used to perform a retrieval of the physical and chemical conditions in the planetary atmosphere, which reveals super-solar elemental abundances and an excess of spectral line broadening. The retrieval also shows that the nightside atmosphere of WASP-33b has significantly cooler temperatures than the dayside atmosphere. In Chapter 5, we summarize the studies presented in this thesis and provide conclusions. Finally, we present an outlook on the tasks and questions that future studies may address.

2. Detection of Fe and evidence for TiO in the dayside emission spectrum of WASP-33b

This chapter was published as the peer-reviewed article "Detection of Fe and evidence for TiO in the dayside emission spectrum of WASP-33b" (*Credit:* Cont et al., A&A, 651, A33, 2021, reproduced with permission ©ESO). The article was co-authored by F. Yan, A. Reiners, N. Casasayas-Barris, P. Mollière, E. Pallè, Th. Henning, L. Nortmann, M. Stangret, S. Czesla, M. López-Puertas, A. Sánchez-López, F. Rodler, I. Ribas, A. Quirrenbach, J. A. Caballero, P. J. Amado, L. Carone, J. Khaimova, L. Kreidberg, K. Molaverdikhani, D. Montes, G. Morello, E. Nagel, M. Oshagh, and M. Zechmeister. D. Cont performed the data reduction and the cross-correlation analysis, and implemented the toy model of a TiO-depleted hot spot in WASP-33b's atmosphere. F. Yan and N. Casasayas-Barris conducted the observations of WASP-33b. F. Yan contributed to the calculation of the volume mixing ratios of Fe and TiO. K. Molaverdikhani computed the high-resolution opacity data, which were used to generate the model spectra for cross-correlation. The other co-authors contributed to the interpretation of the results and provided comments to the manuscript. The layout of selected figures and tables has been slightly adapted for this thesis.

2.1. Abstract

Theoretical studies predict the presence of thermal inversions in the atmosphere of highly irradiated gas giant planets. Recent observations have identified these inversion layers. However, the role of different chemical species in their formation remains unclear. We search for the signature of the thermal inversion agents titanium oxide (TiO) and iron (Fe) in the dayside emission spectrum of the ultra-hot Jupiter WASP-33b. The spectra were obtained with CARMENES and HARPS-N, covering different wavelength ranges. Telluric and stellar absorption lines were removed with `SYSREM`. We cross-correlated the residual spectra with model spectra to retrieve the signals from the planetary atmosphere. We find evidence for TiO at a significance of 4.9σ with CARMENES. The strength of the TiO signal drops close to the secondary eclipse. No TiO signal is found with HARPS-N. An injection-recovery test suggests that the TiO signal is below the detection level at the wavelengths covered by HARPS-N. The emission signature of Fe is detected with both instruments at significance levels of 5.7σ and 4.5σ, respectively. By combining all observations, we obtain a significance level of 7.3σ for Fe. We find the TiO signal at $K_\mathrm{p} = 248.0^{+2.0}_{-2.5}\,\mathrm{km\,s^{-1}}$, which is in disagreement with the Fe detection at $K_\mathrm{p} = 225.0^{+4.0}_{-3.5}\,\mathrm{km\,s^{-1}}$. The K_p value for Fe is in

agreement with prior investigations. The model spectra require different temperature profiles for TiO and Fe to match the observations. We observe a broader line profile for Fe than for TiO. Our results confirm the existence of a temperature inversion layer in the planetary atmosphere. The observed K_p offset and different strengths of broadening in the line profiles suggest the existence of a TiO-depleted hot spot in the planetary atmosphere.

2.2. Introduction

Hot Jupiters are gas giant planets with close-in orbits, which exhibit strong spectral features due to their enhanced temperatures and sizes. So far, targets of atmospheric observations have been mostly among this class of exoplanets. Hubeny et al. (2003) and Fortney et al. (2008) predicted the existence of temperature inversion layers in highly irradiated gas planets due to the strong absorption of visible and ultraviolet radiation caused by TiO and VO in the upper atmosphere. Initial evidence for the presence of an atmospheric inversion was found in the spectrum of the hot Jupiter HD 209458b by Knutson et al. (2008). However, the claim of an inverted atmospheric temperature profile could not be confirmed (Hansen et al. 2014; Diamond-Lowe et al. 2014; Schwarz et al. 2015; Evans et al. 2015), and Hoeijmakers et al. (2015) did not find any signatures of TiO in high-resolution spectra of the planet. Moreover, Hoeijmakers et al. (2015) investigated the TiO line database and found several wavelength ranges with poor line list precision.

Producing high-resolution spectral line lists for transition metal diatomic molecules is computationally challenging, but the completeness and accuracy of line lists are critical for the detection of these chemical species (McKemmish et al. 2019; Merritt et al. 2020). Nevertheless, hints for the existence of TiO and VO were found in the atmospheres of WASP-33b and WASP-121b in secondary eclipse measurements by Haynes et al. (2015) and Evans et al. (2017), respectively. High-resolution Doppler spectroscopy led to the detection of TiO in the emission spectrum of WASP-33b (Nugroho et al. 2017). However, Herman et al. (2020) reported a nondetection of TiO at high spectral resolution. More recently, Serindag et al. (2021) reassessed the presence of TiO in the spectra from Nugroho et al. (2017) by using an improved TiO line list, but they could not find a detection at the same orbital parameters as the previous work. Also the existence of TiO and VO in WASP-121b could not be confirmed by high-resolution spectroscopy observations (Merritt et al. 2020). TiO was also detected in the low-resolution transmission spectrum of WASP-19b by Sedaghati et al. (2017), but the detection was not confirmed by Espinoza et al. (2019).

To explain these nondetections of metal oxides in the atmospheres of highly irradiated planets, a number of mechanisms have been proposed. A theoretical study by Spiegel et al. (2009) predicted the depletion of TiO and VO in the upper atmosphere of hot Jupiters, as gravitational settling moves the species into deeper layers of the atmosphere. Close-in giant planets are assumed to be tidally locked, with a permanent day- and nightside. Hence, the existence of a day-night cold-trap effect has been suggested. In this scenario, TiO and VO are moved by winds on a global scale to the

nightside of the planet (Parmentier et al. 2013), where they condense due to cooler temperatures and they are thus efficiently removed. According to the studies of Lothringer et al. (2018) and Lothringer & Barman (2019), temperature inversions are also sensitive to the spectral type of the host star. Their simulations predict the occurrence of thermal dissociation and ionization in planetary atmospheres around hot stars, which decrease molecular abundances in favor of atomic species and ions.

Although TiO and VO have not been widely detected in hot Jupiters, thermal inversions have been found in several planets, such as WASP-33b (Haynes et al. 2015; Nugroho et al. 2017, 2020a), WASP-121b (Evans et al. 2017), WASP-19b (Sedaghati et al. 2017), WASP-18b (Sheppard et al. 2017; Arcangeli et al. 2018), WASP-103b (Kreidberg et al. 2018), and HAT-P-7b (Mansfield et al. 2018). These planets are all ultra-hot Jupiters (UHJs), that is gas giant planets with dayside temperatures greater than 2200 K (Parmentier et al. 2018). Theoretical simulations (e.g., Lothringer et al. 2018) suggest that the absorption of atoms and ions can produce thermal inversion layers in UHJs. Extreme thermal conditions lead to the dissociation of molecules into their constituent elements, allowing us to characterize the elemental composition of UHJ atmospheres.

Recently, atomic hydrogen was found in the transmission spectra of UHJs (e.g., Yan & Henning 2018; Casasayas-Barris et al. 2018; Jensen et al. 2018; Cauley et al. 2021; Yan et al. 2021). Moreover, metals such as Fe, Mg, Na, Ca, Ti, or V and their ions were detected via transmission spectroscopy in the atmospheres of KELT-9b, KELT-20b, WASP-121b, WASP-12b, and WASP-33b (e.g., Fossati et al. 2010; Hoeijmakers et al. 2018, 2019, 2020a; Casasayas-Barris et al. 2019; Cauley et al. 2019; Sing et al. 2019; Yan et al. 2019; Stangret et al. 2020; Nugroho et al. 2020b; Gibson et al. 2020; Ben-Yami et al. 2020). For some planets, the detected spectral lines allowed for properties of their atmospheres to be analyzed in more detail, including atmospheric mass loss rate (e.g., Yan & Henning 2018; Wyttenbach et al. 2020) and nightside condensation (Ehrenreich et al. 2020; Kesseli & Snellen 2021). In addition to the transmission spectra, emission features of neutral iron consistent with the presence of an inversion layer were observed in the dayside spectra of the UHJs KELT-9b, WASP-189b, and WASP-33b (Pino et al. 2020; Yan et al. 2020; Nugroho et al. 2020a). These detections of atoms and ions, together with the absence of TiO and VO in the spectra of several UHJs suggest that metals are likely to play a key role in the formation of thermal inversions.

WASP-33b (planet and host star parameters are listed in Table 2.1) moves on a retrograde orbit around a δ Scuti A-type star with a period of 1.22 days. The host star has a visual magnitude of $V \sim 8$ mag, which makes WASP-33b a favorable target for observations. With an equilibrium temperature ($T_{\rm eq}$) of 2700 K and a dayside temperature of $T_{\rm day} \sim 3000$ K, WASP-33b is the second hottest exoplanet known so far. This makes the planet an ideal candidate for investigating the role of chemical species in thermal inversions, their effect on the energy budget, and global circulation of strongly irradiated atmospheres. WASP-33b shows evidence for the presence of an inversion layer (Haynes et al. 2015). In addition to the detection of TiO by Nugroho et al. (2017), Yan et al. (2019) found Ca II and Nugroho et al. (2020a) detected the presence of Fe as well as the existence

Table 2.1.: Parameters of the WASP-33 system used in this work.

Parameter	Symbol (Unit)	Value
Planet		
Radius [(a)]	R_p (R_J)	$1.679^{+0.019}_{-0.030}$
Orbital period [(b)]	P_orb (d)	1.219870897
Transit epoch (BJD) [(b)]	T_0 (d)	2 454 163.22449
Systemic velocity [(c)]	v_sys (km s^{-1})	-3.0 ± 0.4
RV semi-amplitude [(a)]	K_p (km s^{-1})	231 ± 3
Duration ingress [(d)]	T_ingress (d)	0.0124 ± 0.0002
Duration transit [(d)]	T_transit (d)	0.1143 ± 0.0002
Surface gravity [(d)]	$\log g$ (cgs)	3.46
Star		
Radius [(a)]	R_* ($R_\odot$)	$1.509^{+0.016}_{-0.027}$
Effective temperature [(e)]	T_eff (K)	7430 ± 100
Rotational velocity [(f)]	$v_\mathrm{rot} \sin i_*$ (km s^{-1})	$86.63^{+0.37}_{-0.32}$

References. [(a)] Lehmann et al. (2015) with parameters from Kovács et al. (2013), [(b)] Maciejewski et al. (2018), [(c)] Nugroho et al. (2017), [(d)] Kovács et al. (2013), [(e)] Collier Cameron et al. (2010), [(f)] Johnson et al. (2015).

of a thermal inversion via high-resolution Doppler spectroscopy. Hints for other high temperature absorption species were also found by von Essen et al. (2019) and Kesseli et al. (2020), who tentatively detected the spectral signature of AlO and FeH, respectively.

In this work, we report the detection of Fe and evidence for the presence of TiO on the dayside of WASP-33b. We use high-resolution Doppler spectroscopy with CARMENES (Calar Alto high-Resolution search for M dwarfs with Exoearths with Near-infrared and optical Échelle Spectrographs) and HARPS-N (High Accuracy Radial velocity Planet Searcher for the Northern hemisphere). The signature of both species is observed in emission, indicating the presence of an inverted temperature profile in the planetary atmosphere. We structure the paper as follows. In Sects. 2.3 and 2.4, we describe our observations and the data reduction procedures. Section 2.5 details the methodology used to find the signals of TiO and Fe. In Sect. 2.6, we present the results with discussions. Conclusions are drawn in Sect. 2.7.

2.3. Observations

We observed the thermal emission spectrum of WASP-33b on 15 November 2017 with the CARMENES spectrograph (Quirrenbach et al. 2016, 2018, 2020) at the 3.5 m Calar Alto telescope.

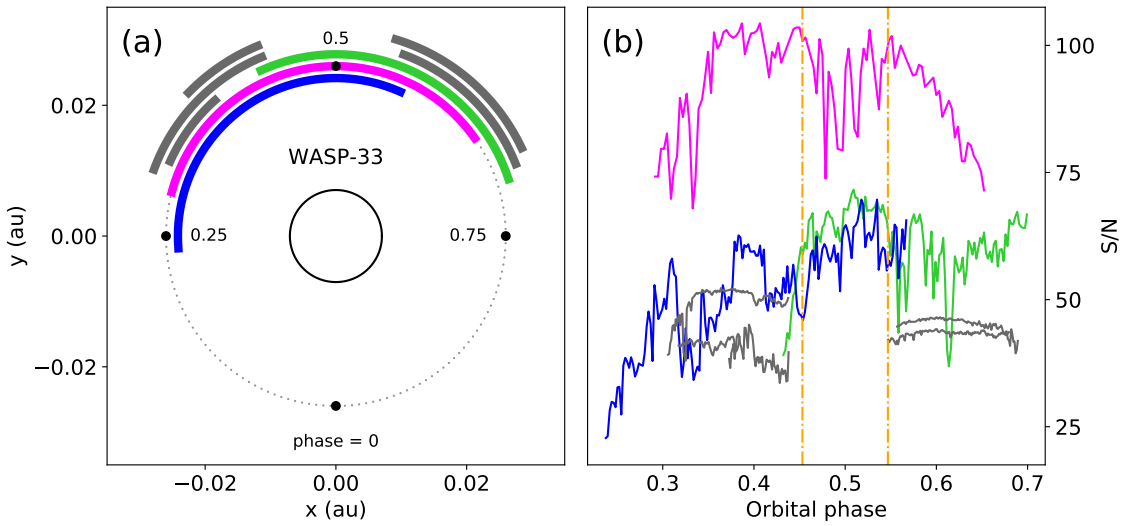

Figure 2.1.: Orbital phase coverage and S/N. Pink corresponds to CARMENES, blue/green to HARPS-N and gray to the ESPaDOnS observations (Herman et al. 2020). *Panel a*: WASP-33 system with the phase coverage of the observations. *Panel b*: S/N of each spectrum as a function of orbital phase. The begin and the end of the secondary eclipse are indicated by the orange dash-dotted lines.

CARMENES consists of two fiber fed high-resolution spectrographs covering the wavelength ranges from 520 to 960 nm (VIS) and from 960 to 1710 nm (NIR), which corresponds to 61 and 28 spectral orders, respectively. The resolution is $R \sim 94\,600$ in the VIS channel and $R \sim 80\,400$ in the NIR channel. In this work, only the data collected with the VIS channel are used. The CARMENES observation covered pre-eclipse, eclipse and post-eclipse of the planet, which corresponds to an orbital phase coverage of 0.29 to 0.65 (cf. Fig. 2.1a). In total, we gathered 105 spectra, each with an exposure time equal to 300 s. The airmass varied between 1.00 and 2.53. Except for one thick cirrus, the night was photometric with a seeing of about 1.5″. We discarded seven spectra for which the target was not centered onto the fiber due to bad guiding of the telescope. Moreover, we removed three spectra during the passing of the cirrus cloud, ending up with a total number of 95 spectra for further analysis.

Another two observations of the thermal emission spectrum of WASP-33b were obtained on 15 October 2020 and 7 November 2020 with the HARPS-N spectrograph (Mayor et al. 2003; Cosentino et al. 2012) at the Telescopio Nazionale *Galileo*. HARPS-N is a fiber fed high-resolution spectrograph that covers the wavelength range from 383 to 690 nm, corresponding to 69 spectral orders. The spectral resolution is $R \sim 115\,000$. Our observations covered the orbital phase range 0.43 to 0.70 in the first night and 0.24 to 0.57 in the second night (cf. Fig. 2.1a). We obtained 125 and 155 spectra, respectively. The exposure time of each spectrum was 200 s for both observations. The airmass varied between 1.01–1.99 and 1.01–2.03, respectively.

For all the observations, we observed the target with fiber A and used fiber B to record the sky background for considering the sky emission lines in the subsequent data analysis. Further details on the observations are reported in the observation log in Table 2.2.

Table 2.2.: Observation log.

Instrument	Date	Observing time (UT)	Airmass change	Phase coverage	Exposure time (s)	N_{spectra}
New data						
CARMENES	2017-11-15	17:59–04:47	1.87–1.00–2.53	0.29–0.65	300	105
HARPS-N	2020-10-15	21:06–04:55	1.99–1.01–1.27	0.43–0.70	200	125
HARPS-N	2020-11-07	19:39–05:18	1.96–1.01–2.03	0.24–0.57	200	155
Archival data						
ESPaDOnS	2013-09-15	09:09–13:00	1.75–1.05	0.30–0.44	90	110
ESPaDOnS	2013-09-26	10:35–12:29	1.16–1.05	0.37–0.44	90	55
ESPaDOnS	2014-09-04	10:49–14:42	1.39–1.05–1.07	0.56–0.69	90	110
ESPaDOnS	2014-09-15	10:00–13:53	1.42–1.05–1.06	0.55–0.68	90	110
ESPaDOnS	2014-11-05	08:51–10:49	1.08–1.05–1.08	0.31–0.38	90	55

Notes. The observations from CARMENES and HARPS-N are presented the first time in this work (new data). The observations with ESPaDOnS are archival data from Herman et al. (2020).

In addition to our data from CARMENES and HARPS-N, we also re-analyzed five archival observations from ESPaDOnS (Echelle SpectroPolarimetric Device for the Observation of Stars) at the Canada-France-Hawai'i telescope (Herman et al. 2020). Details of this analysis are provided in Sects. 2.6.5 and 2.6.6.

2.4. Data reduction

2.4.1. Pre-processing the spectra

The raw frames were processed by the data reduction pipelines `caracal` v2.20 for CARMENES (Zechmeister et al. 2014; Caballero et al. 2016) and the `Data Reduction Software` for HARPS-N. With CARMENES, we obtained a one-dimensional spectrum for each frame and spectral order (our numbering is 1–61, corresponding to the CARMENES echelle orders 118–58). We split the order-merged, one-dimensional spectra from HARPS-N into 69 order-like segments to conduct the same analysis steps for both instruments (hereafter spectral orders; for wavelength range of each segment see Fig. 2.12). The flux signal-to-noise ratio (S/N) of each spectral order and one-dimensional spectrum was calculated by the instrument pipelines. We report the mean S/N value of each spectrum in Fig. 2.1b.

We used `Python` to apply the following procedures to the spectra. After sorting the spectra chronologically, we obtained a two-dimensional matrix for each observation and spectral order (see an

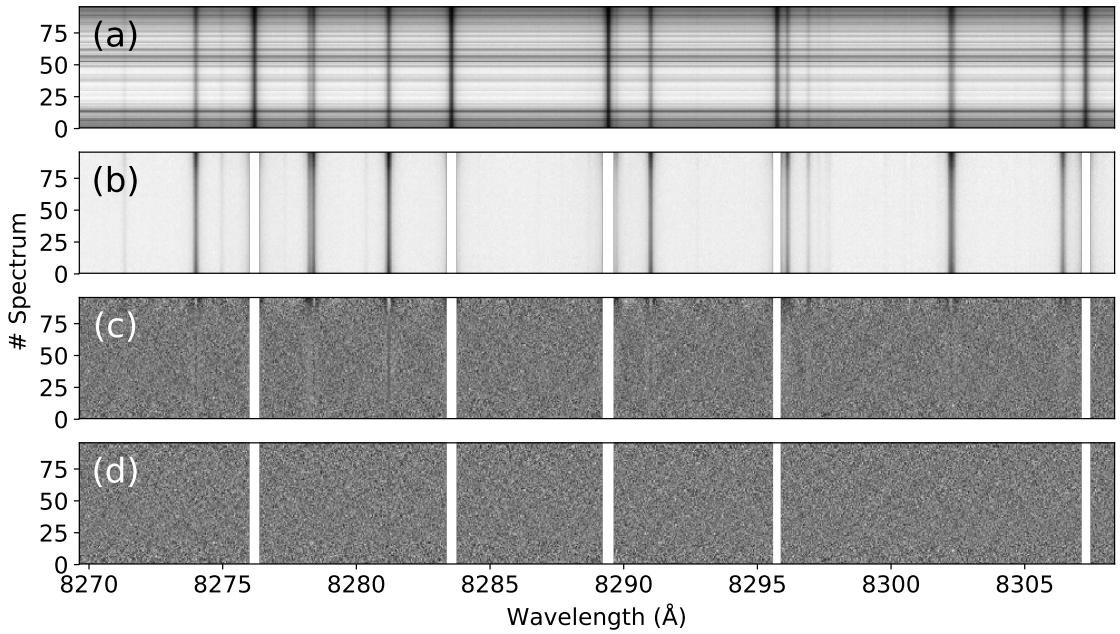

Figure 2.2.: Pre-processing steps for a selected wavelength range of CARMENES. *Panel a*: unprocessed spectral matrix; *panel b*: matrix after normalization, masking and outlier correction; *panels c* and *d*: spectral residuals after one and six `SYSREM` iterations, respectively. After one iteration, several telluric lines are still visible. At higher iteration numbers the telluric lines are almost entirely removed.

example of spectral matrix in Fig. 2.2a). We corrected pixels that the pipelines flagged as bad quality by linear interpolation to the nearest neighbors. Pixels that were flagged more than three times during the time series were masked. To correct 5σ outliers due to cosmic rays, we fitted a third-order polynomial to the time evolution of each pixel and replaced the affected pixels with the polynomial function values. Furthermore, we needed to remove the contribution of the grating blaze function and the different exposure levels of the spectra due to the varying atmospheric conditions (e.g., changing airmass) during the observations. Hence, we individually fitted a second-order polynomial to the pseudo-continuum of each spectrum and normalized it with the resulting fit function. Wavelength ranges with broad stellar absorption bands or strong emission lines in fiber B were excluded during the second-order polynomial fit. We masked wavelength ranges where the flux was below 20% of the continuum level. Due to almost no flux, the five spectral orders at the red end of the CARMENES wavelength range were entirely masked and excluded from further analysis. As a result, we obtained a normalized, masked and outlier corrected spectral matrix for each observation and spectral order (see example in Fig. 2.2b).

2.4.2. Removal of telluric and stellar lines

The Earth's telluric and stellar lines were removed from the spectra by using `SYSREM`, a detrending algorithm originally designed to remove systematic effects from sets of transit light curves (Tamuz et al. 2005). The algorithm iteratively performs linear fits of the stellar and telluric line evolution in time and then subtracts the linear contribution from the signal. We treated each wavelength

bin as an individual light curve to remove systematics from the spectral time series. The spectra were detrended by passing each two-dimensional spectral matrix as input to the algorithm. We assigned airmass as the starting fit parameter in order to improve the performance of SYSREM. We ran the algorithm for different iteration numbers, that is between one and ten consecutive iterations (see example of different iterations in Figs. 2.2c and 2.2d). To remove large-scale features, we filtered the resulting spectral residual matrices with a Gaussian high-pass filter (25 pixels for CARMENES; 75 pixels for HARPS-N) and divided each matrix column by its variance (Yan et al. 2019).

When assuming a circular orbit with a semi-amplitude velocity equal to 231 $\mathrm{km\,s^{-1}}$ (Lehmann et al. 2015; Kovács et al. 2013), the planet is expected to move at radial velocities between –220 $\mathrm{km\,s^{-1}}$ and +231 $\mathrm{km\,s^{-1}}$ during our observations (phase coverage 0.24–0.70). On the other hand, the telluric and stellar lines are approximately stationary. Therefore, at small iteration numbers, the SYSREM algorithm removes mostly the telluric and stellar lines while only slightly affecting the planetary signal. However, once telluric and stellar lines are fitted and removed to a certain degree, the algorithm begins to detrend also the planetary lines (e.g., Birkby et al. 2017; Nugroho et al. 2017; Alonso-Floriano et al. 2019; Sánchez-López et al. 2019). Hence, we expect the planetary signal to appear strongest after an optimal number of SYSREM iterations. This number should vary from order to order due to a different strength of telluric and stellar line contamination. However, we decided to use a conservative approach and assumed a common optimal iteration number for all spectral orders. The amplitude of the signal from the planetary atmosphere varies between different wavelength ranges and chemical species. Therefore, we assessed the optimal iteration number by maximizing the detection strength for each instrument and chemical species separately (see Sects. 2.6.1 and 2.6.2).

2.5. Methods

The planetary signal is buried in the noise of the residual matrices (see example in Fig. 2.2d). To extract the atmospheric emission signature, we employed the cross-correlation method, which has been successfully applied in a number of previous studies (e.g., Snellen et al. 2010, 2014; Brogi et al. 2012; Rodler et al. 2012; Birkby et al. 2013; Alonso-Floriano et al. 2019; Sánchez-López et al. 2019). This technique allows us to combine the numerous weak planetary lines into a detectable signal by computing the cross-correlation function (CCF) between the residual spectra and a planetary model spectrum. To this end, we computed model spectra for the chemical species we intended to search for (i.e., TiO and Fe).

2.5.1. Spectral models

Molecular species are affected by thermal dissociation in the dayside atmosphere of UHJs (e.g., Kreidberg et al. 2018; Parmentier et al. 2018; Arcangeli et al. 2019). As TiO may be depleted at

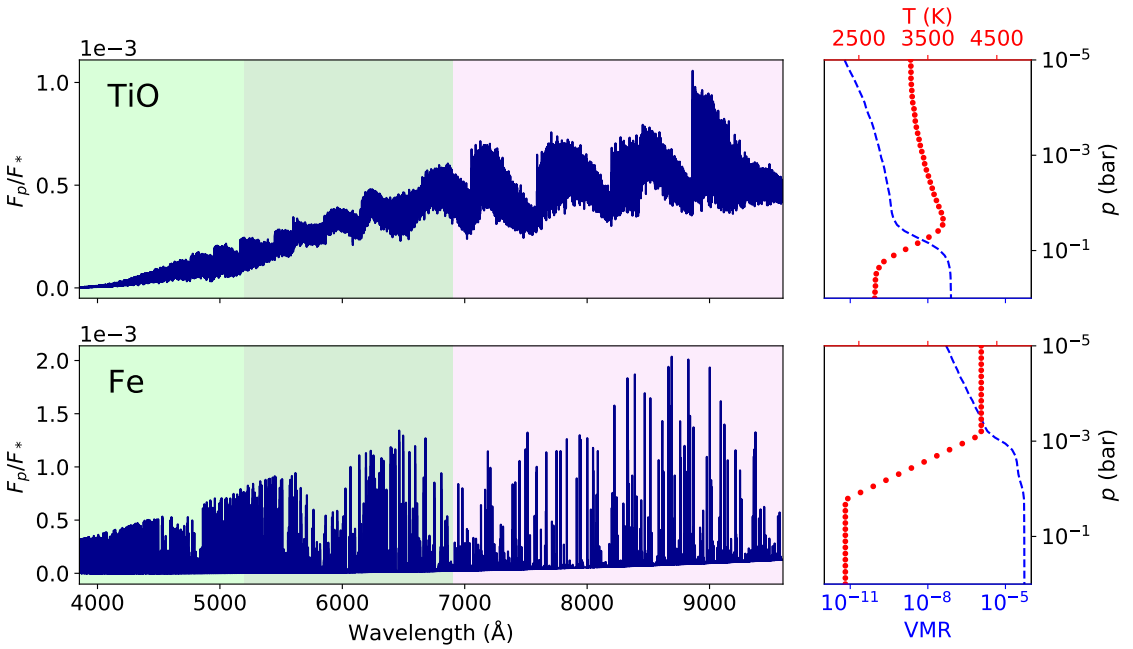

Figure 2.3.: Modeled planetary emission spectra (*left panels*) and the corresponding T-p profiles with volume mixing ratios (VMRs, *right panels*). We used different T-p profiles for the two species and computed the VMRs assuming equilibrium chemistry with solar elemental abundances. The *top* and the *bottom panels* refer to TiO and Fe, respectively. The CARMENES wavelength range is shaded in pink; the HARPS-N wavelength range is shaded in green; the ranges overlap. The spectral lines are stronger in the CARMENES range when compared to HARPS-N. A different scaling is applied to the planet-to-star flux contrast ratio on the y-axis of the spectra. The spectral lines of Fe are stronger when compared with the TiO model spectrum.

the locations where the temperature is highest (near the substellar point), we hypothesize that the spectral signatures of TiO and Fe may emerge from atmospheric regions with different thermal conditions. For this reason, we decided to model two different atmospheres, each with an individual thermal structure. Both atmospheres consist of 40 layers in a pressure range from 10^{-5} to 1 bar and are equispaced on a logarithmic scale. We assumed a moderate temperature for the TiO atmosphere (to avoid TiO to be significantly dissociated) and a higher temperature for Fe. In Sect. 2.6.3, we further discuss the usage of two different temperature profiles. For TiO, we took the inverted T-p profile found by Haynes et al. (2015). To model the Fe spectrum, we used the T-p profile of WASP-189b, which was retrieved by Yan et al. (2020) using the Fe emission lines. This planet has properties similar to WASP-33b (e.g., mass, radius, equilibrium temperature, and spectral type of the host star). Therefore, using this T-p profile is an appropriate approximation for studying the presence of Fe in the atmosphere of WASP-33b. We used `easyCHEM` (Mollière et al. 2017) to compute the volume mixing ratio (VMR) and the mean molecular weight for each layer under the assumption of equilibrium chemistry and solar elemental abundances. We calculated emission spectra for TiO and Fe using the radiative transfer code `petitRADTRANS` (Mollière et al. 2019). We used a blackbody spectrum with a temperature of 7430 K for the host star to compute the planet-to-star flux ratio. The flux normalized model spectra as well as the corresponding T-p profiles and VMRs are shown in Fig. 2.3. We convolved the normalized emission model spectra with the instrument profiles and applied the same high-pass filter as described for the residual

spectra in Sect. 2.4.2. This makes our analysis insensitive to the emission continuum level and consequently, allows us to only account for the relative strength of the spectral lines.

2.5.2. Cross-correlation

Our implementation of the cross-correlation is based on the `Python` routine `pyasl.crosscorrRV` from the `PyAstronomy` package (Czesla et al. 2019). We computed the CCFs over a range of Doppler-shifts from –364 km s^{-1} to +364 km s^{-1} and applied velocity steps of 1.3 km s^{-1} for CARMENES and 0.8 km s^{-1} for HARPS-N , which corresponds to the mean pixel spacing of the instruments. A CCF with the planet model spectrum was calculated for each residual spectrum. This resulted in a 95×561 cross-correlation matrix ($\overline{\mathrm{CCF}}$) for CARMENES and to a 125×911 and a 155×911 $\overline{\mathrm{CCF}}$ for HARPS-N. We subtracted the median value from each CCF to avoid any interference with leftover broadband features in the spectra. The $\overline{\mathrm{CCF}}$s were calculated independently for all spectral orders, chemical species and observations.

We co-added the $\overline{\mathrm{CCF}}$s for each chemical species and observation separately. This led to the final cross-correlation maps. Only the $\overline{\mathrm{CCF}}$s of the spectral orders that are selected in Sect. 2.5.3 were included in this step. This resulted in a final cross-correlation function map (CCF map) for each chemical species and observation (e.g., Fig. 2.4). Finally, we merged the CCF maps of the two HARPS-N observations into one single 280×911 CCF map, which led to one CCF map for each instrument and chemical species.

We found strong artifacts in the CCF map of Fe that originate from residual stellar lines (see Fig. 2.4). These lines are not efficiently removed by `SYSREM` as their strength varies with time due to the pulsation of the host star. The radial velocity (RV) domain of the residual stellar lines is determined by the stellar rotation velocity and is confined to the range between $\pm v_{\mathrm{rot}} \sin i_*$ (i.e., between roughly –87 km s^{-1} and +87 km s^{-1} in the stellar rest frame). To avoid any correlation with the model spectrum in the CCF map of Fe, we masked all velocities between –90 km s^{-1} and +90 km s^{-1} in the stellar rest frame (for comparison, the planetary RV during secondary eclipse is between –67 km s^{-1} and +67 km s^{-1}). Hence, the RV ranges from –90 km s^{-1} to –67 km s^{-1} and from +67 km s^{-1} to +90 km s^{-1} are lost as the planetary trail in the CCF map is masked. This represents 10% (CARMENES) and 16% (HARPS-N) of the observations outside eclipse. Consequently, the masking of the stellar line residuals will not strongly affect the detection in Sect. 2.6.1 and the resulting conclusions.

2.5.3. Exclusion of bad spectral orders

The precision of line lists is of critical importance when using the cross-correlation technique. However, the line lists of TiO suffer from inaccuracies, which reduce the detection sensitivity of the molecule (Hoeijmakers et al. 2015; Nugroho et al. 2017). The calculation of models leading to a detection of TiO in planetary atmospheres remains a challenging task (Herman et al. 2020;

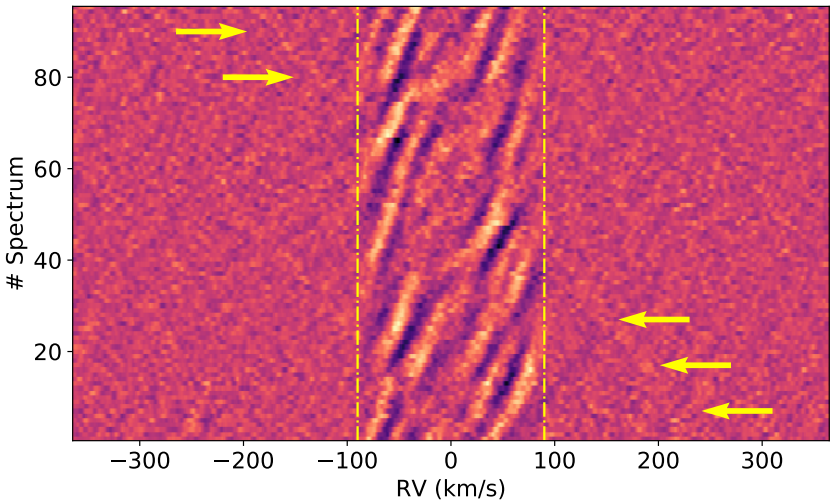

Figure 2.4.: CCF map of Fe obtained with CARMENES in the stellar rest frame. The strong residuals between the yellow dash-dotted lines are caused by residual Fe lines from the host star pulsation. We indicate the faint planetary trail with yellow arrows.

Serindag et al. 2021). We attempted to mitigate this issue by using the new line database `ToTo ExoMol` (McKemmish et al. 2019) to generate our TiO model spectrum. However, this line list is also expected to show inaccuracies in certain wavelength ranges (McKemmish et al. 2019). To exclude spectral orders with a poor line list from our analysis, we conducted an order-wise validation of the TiO line list. A detailed description of the TiO line list validation is provided in Sect. 2.8. As a result, we only included the $\overline{\text{CCF}}$s from spectral orders corresponding to wavelength ranges with a precise line list when generating the CCF map for TiO. In contrast, Fe line lists are considered to be precise (Kurucz 2011). Hence, we refrained from analyzing the line list precision of Fe and included the $\overline{\text{CCF}}$s of all orders to compute the CCF map of this species.

No prominent emission features are present in the TiO model spectrum blueward of about 6000 Å (see Fig. 2.3). To assess whether the molecular signature in the corresponding spectral orders is strong enough to contribute to a detection of TiO, we conducted an order-wise injection-recovery test (Sect. 2.9). Consequently, we included only the $\overline{\text{CCF}}$s that allow us to recover an injected model spectrum into the CCF map. We recovered the injected model spectrum in several spectral orders of CARMENES successfully (roughly between 6000 Å and 9000 Å). In contrast, only in one spectral order of HARPS-N the injected signal could be retrieved. This result suggests that even if present, the signature of TiO will be below the required level for a significant detection in the HARPS-N observations. On the other hand, all the spectral orders contribute to the detection of Fe due to the stronger emission features in the model spectrum when compared to TiO (cf. Fig. 2.3). Consequently, we included all the spectral orders when calculating the Fe CCF map.

In conclusion, only the spectral orders passing both the line list assessment and the injection-recovery test were included in our TiO analysis. All other spectral orders were excluded. In contrast, we included all spectral orders in the Fe analysis because of the availability of a precise line list and a strong spectral signature expected from the model spectrum in Fig. 2.3.

2.5.4. Searching for atmospheric features

We assumed that the planet moves on a circular orbit and expect its observed radial velocity to be described by the expression

$$v_{\rm p} = v_{\rm sys} + v_{\rm bary} + K_{\rm p} \sin 2\pi\phi + \Delta v, \tag{2.1}$$

where $v_{\rm sys}$ is the systemic velocity, $v_{\rm bary}$ is the observer's barycentric velocity, $K_{\rm p}$ is the orbital semi-amplitude velocity of the planet, ϕ is the orbital phase and Δv is the residual radial velocity in the planetary rest frame. By using Eq. (2.1) and linear interpolation, we aligned the CCF map to the planetary rest frame (see Fig. 2.5). To account for the varying flux level from atmospheric conditions and instrumental effects (e.g., telescope guiding, alignment with the instrument fiber), each row of the CCF map was weighted with the squared flux S/N (see Fig. 2.1b) of the corresponding spectrum (Brogi & Line 2019). We collapsed the aligned CCF map along the time axis by computing the mean value of each matrix column. If the model spectrum reflects the planetary signal and a Doppler-shift according to Eq. (2.1) is present, the collapsed CCF map will show a peak at Δv close to $0\,\mathrm{km\,s^{-1}}$ (see top panels in Fig. 2.6). Following the same procedure as previous studies (e.g., Birkby et al. 2017; Sánchez-López et al. 2019; Alonso-Floriano et al. 2019), we aligned with different $K_{\rm p}$ values and combined the resulting 1D plots of the collapsed CCF map in a 2D matrix. We used $K_{\rm p}$ values between $+150\,\mathrm{km\,s^{-1}}$ and $+310\,\mathrm{km\,s^{-1}}$ in steps of $0.5\,\mathrm{km\,s^{-1}}$. We considered a range of Δv from $-80.6\,\mathrm{km\,s^{-1}}$ to $+80.6\,\mathrm{km\,s^{-1}}$ in steps of $1.3\,\mathrm{km\,s^{-1}}$ for the CARMENES observation. The considered values for both HARPS-N observations ranged from $-80.0\,\mathrm{km\,s^{-1}}$ to $+80.0\,\mathrm{km\,s^{-1}}$ in steps of $0.8\,\mathrm{km\,s^{-1}}$. Under exclusion of the peak, we computed the standard deviation of the 2D matrix. The matrix was normalized with the standard deviation and a signal-to-noise map of the detection significance (S/N map) as a function of the orbital semi-amplitude $K_{\rm p}$ and the radial velocity deviation from the planetary rest frame Δv was obtained. To assess the strength and the position of the detection peaks, we computed the S/N map from each instrument and chemical species independently.

2.6. Results and discussion

2.6.1. Detection of Fe

We found a clear signature of Fe with both instruments. With CARMENES, we achieved a maximum peak value of $S/N = 5.7$ at $K_{\rm p} = 228.0^{+3.5}_{-5.0}\,\mathrm{km\,s^{-1}}$ and $\Delta v = 1.3^{+3.9}_{-3.9}\,\mathrm{km\,s^{-1}}$ after five consecutive `SYSREM` iterations (see Fig. 2.6 right panel). For HARPS-N the maximum peak value of $S/N = 4.5$ was found after eight iterations at $K_{\rm p} = 225.0^{+2.0}_{-5.0}\,\mathrm{km\,s^{-1}}$ and $\Delta v = -0.8^{+4.0}_{-2.4}\,\mathrm{km\,s^{-1}}$ (see Fig. 2.7b). A summary of all results is provided in Table 2.3. The detected Fe signal is strong enough to be clearly identified in the CCF maps (Figs. 2.5 and 2.7). Since we only used the sections of planetary trail that are located outside the region dominated by stellar iron lines (c.f. the

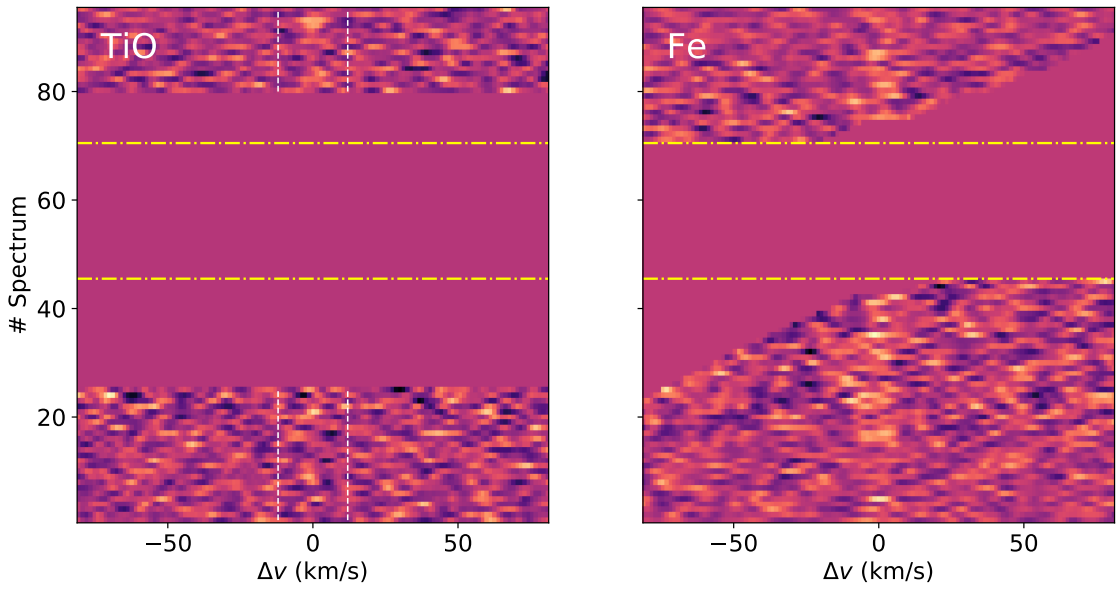

Figure 2.5.: CCF maps from CARMENES aligned to the rest frame consistent with the maximum K_p values (i.e., 248.0 km s^{-1} for TiO and 228.0 km s^{-1} for Fe; see Fig. 2.6). We indicate the TiO signature with the vertical dashed lines. The two horizontal dash-dotted lines indicate the beginning and end of the secondary eclipse. We masked the phase interval where the TiO signal is below the noise level (see Sect. 2.6.2). Also the radial velocity domain of residual stellar Fe lines was masked (see Sect. 2.5.2). The wider Fe trail when compared to TiO is likely caused by a different degree of rotational broadening, which hints at a global distribution of Fe and localized TiO in the atmosphere of WASP-33b.

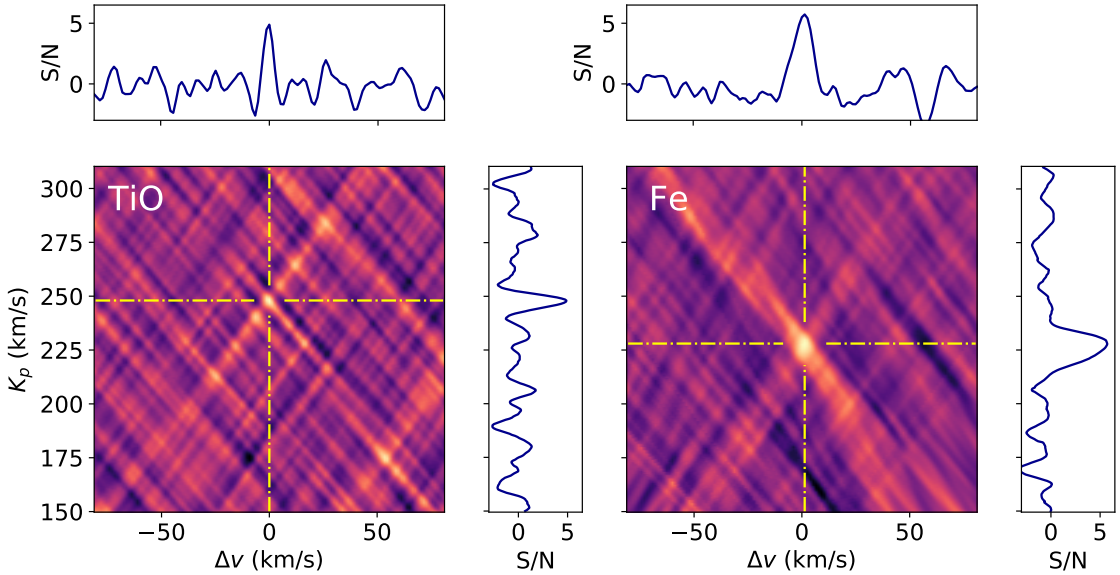

Figure 2.6.: S/N maps after six and five consecutive `SYSREM` iterations with CARMENES for TiO and Fe, respectively. We get S/N significance levels of 4.9 for TiO and 5.7 for Fe. The peak coordinates in the S/N map are indicated by the yellow dash-dotted lines. Cross-sections of the S/N peaks are reported in the horizontal and vertical panels. The horizontal panels also correspond to the collapsed CCF maps in Fig. 2.5. The Fe signal is consistent with the expected K_p value; the TiO peak is found with an offset of roughly +17 km s^{-1}.

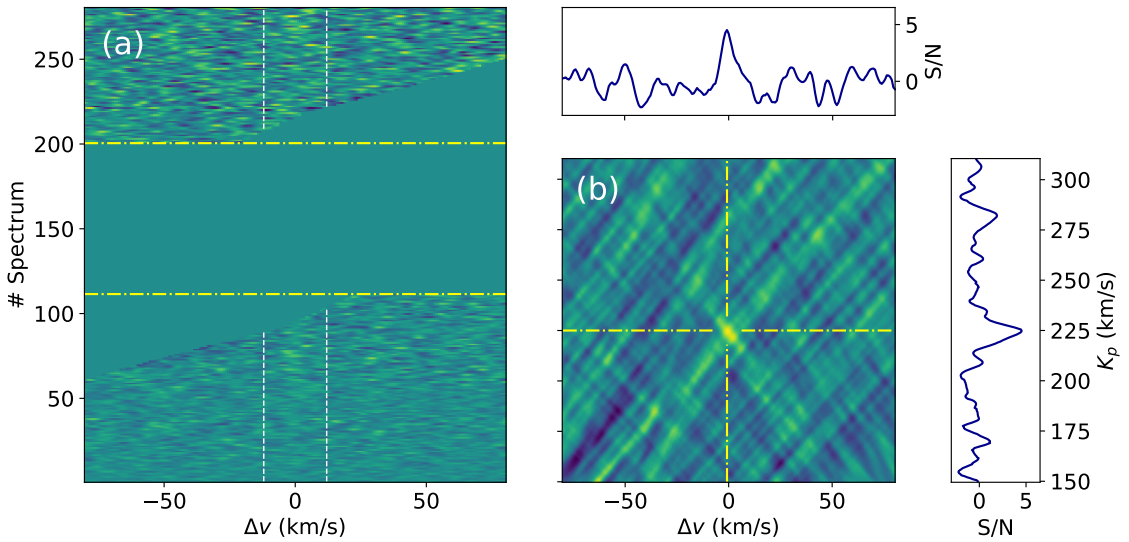

Figure 2.7.: Detection of Fe with HARPS-N. *Panel a*: CCF map in the planetary rest frame (aligned using $K_p = 225.0\,\mathrm{km\,s^{-1}}$). The vertical trail indicated with white lines is the planetary Fe signal. The two horizontal dash-dotted lines indicate the beginning and end of secondary eclipse. *Panel b*: signal-to-noise ratio map. The peak coordinates in the S/N map are indicated by the yellow dash-dotted lines. Cross-sections of the S/N map are shown in the horizontal and vertical panels.

CCF map in Fig. 2.4), the detected signal is not affected by the stellar line residuals from the pulsations. Moreover, we computed the S/N maps of Fe by using the non-inverted T-p profile from Nugroho et al. (2017) and observed negative S/N peaks with orbital parameters that are consistent with those found by using the inverted atmospheric profile (Fig. 2.16).

Our results confirm the recent report of neutral iron and an atmospheric inversion layer in the dayside of WASP-33b (Nugroho et al. 2020a). As the model spectrum used for cross-correlation is based on an inverted T-p profile, the detection of Fe is an unambiguous proof of a temperature inversion in the planetary atmosphere. The negative detection peaks obtained with a non-inverted T-p profile further substantiate the existence of a thermal inversion layer. The obtained K_p values are close to the expected K_p ($231 \pm 3\,\mathrm{km\,s^{-1}}$), which was calculated using the planetary orbital parameters. The strong detection of Fe strengthens the hypothesis that the species is significantly contributing to the heating of the upper planetary atmosphere (Lothringer et al. 2018; Lothringer & Barman 2019). However, additional atomic and molecular species (e.g., Ti, Mg, AlO, SiO, CaO, FeH) and ions (e.g., Fe II, Mg II) may also contribute to maintain the atmospheric temperature inversion (Lothringer et al. 2018; Lothringer & Barman 2019; Gandhi & Madhusudhan 2019).

2.6.2. Evidence for TiO

We find evidence for TiO in all ten S/N maps of CARMENES, with each map corresponding to a different number of `SYSREM` iterations (see Fig. 2.6 left panel). In contrast, no significant signature at physically realistic values of K_p was detectable with HARPS-N. This nondetection

is not surprising because the expected TiO emission feature is relatively weak in the HARPS-N wavelength range (Fig. 2.3).

The TiO signal found with CARMENES peaks after six consecutive iterations and when we excluded an orbital phase interval around secondary eclipse (i.e., between 0.37 and 0.60, which is masked in Fig. 2.5). This suggests that inside this orbital phase range the planetary signal is not detectable. A map of the detection strength when excluding different orbital phase ranges is provided in Fig. 2.17. We found the maximum S/N at $K_\mathrm{p} = 248.0^{+2.0}_{-2.5}\,\mathrm{km\,s^{-1}}$ and $\Delta v = 0.0^{+2.6}_{-2.6}\,\mathrm{km\,s^{-1}}$ with a significance level of $S/N = 4.9$ (cf. Table 2.3). The measured evidence for TiO is in line with prior detections (Haynes et al. 2015; Nugroho et al. 2017) and consistent with the systemic velocities calculated by Nugroho et al. (2017, 2020a). However, K_p is located $+17\,\mathrm{km\,s^{-1}}$ off from the expected value ($231\,\mathrm{km\,s^{-1}}$). In comparison, Nugroho et al. (2017) also found a deviation of about $+8\,\mathrm{km\,s^{-1}}$ from the expected K_p value.

Our detected signature of TiO is unlikely to originate from the host star. WASP-33 is an A-type star and hence, we expect the absence of significant stellar TiO concentrations (e.g., in stellar spots). Moreover, the planetary trail of TiO in Fig. 2.5 is located outside the RV range that could potentially be affected by residual stellar TiO lines (i.e., outside $\pm v_\mathrm{rot} \sin i_*$ in the stellar rest frame).

2.6.3. TiO-depleted hot spot region

The TiO signal is located at a K_p value deviating from the expected one, while the Fe signal is consistent with the expected value. To explain the K_p deviation, we propose the presence of a TiO-depleted hot spot region in the dayside atmosphere of WASP-33b. General circulation models predict a confined region with enhanced temperature, namely the hot spot, as a general feature in UHJ atmospheres (e.g., Komacek et al. 2017; Parmentier et al. 2018; Arcangeli et al. 2019). With an average dayside temperature of $T_\mathrm{day} \sim 3000\,\mathrm{K}$ (Zhang et al. 2018; von Essen et al. 2020), TiO is expected to be largely dissociated in the hot spot region. Consequently, the molecule will be more concentrated toward the terminator region of the planet. Moreover, theoretical studies predict Doppler-shifts of hot Jupiter atmospheres due to global-scale winds with predominant super-rotation (e.g., Showman et al. 2013; Zhang et al. 2017; Flowers et al. 2019; Beltz et al. 2021). Therefore, we propose that the combination of a TiO-depleted hot spot region, the planetary rotation, and atmospheric winds could cause the observed deviation of K_p.

To check the plausibility of this scenario, we implemented a simple toy model to compute the synthetic CCF map and the corresponding S/N map. In this toy model, we assumed that TiO is absent in the hot spot region and is only present in the regions close to the equator at both sides of the planetary limb. An example of the model setup is shown in Fig. 2.8. We divided the TiO regions into individual longitudinal grid points and assumed a Doppler-shifted Gaussian profile as the CCF of each point. The velocity of each grid point is determined by the planetary rotation, the super-rotation of the atmosphere, and the planetary orbital motion. The velocity at the equator due to rotation was set to $v_\mathrm{rot} = 7\,\mathrm{km\,s^{-1}}$, which corresponds to a tidally locked planet.

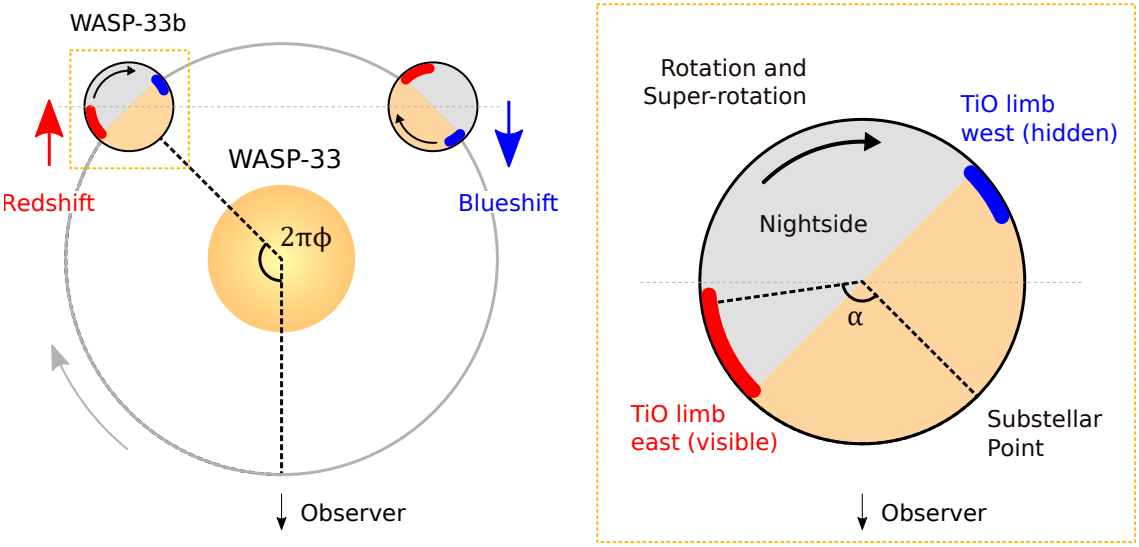

Figure 2.8.: Illustration of the toy model. The *left panel* represents the WASP-33 system; the *right panel* illustrates a zoom in on the planet. The curved black arrows indicate the rotation direction and the gray arrow indicates the orbital motion direction. We assumed the presence of TiO near the terminator (indicated as red and blue regions). Due to the planetary rotation, the TiO signature is redshifted before eclipse (red arrow) and blueshifted after eclipse (blue arrow). The orbital phase is ϕ and the geographical longitude is denoted with α (west limb at –90 °; east limb at +90 °; substellar point at 0 °).

To construct a model S/N map resembling that of the CARMENES observations, we defined a set of different combinations of the following parameters: geographical longitudes where TiO is present, velocities of the super-rotation and K_p values in the uncertainty range ($231 \pm 3\,\mathrm{km\,s^{-1}}$). We simulated the S/N map for each combination and assessed the locations of the peak values. As a result, we found several parameter configurations that led to a peak in the model S/N map at K_p values between $240\,\mathrm{km\,s^{-1}}$ and $250\,\mathrm{km\,s^{-1}}$. To produce a S/N peak in this range, our model tends to favor the presence of TiO on the night hemisphere or close to the terminator regions. However, the nightside atmosphere has a significantly lower average temperature than the dayside (von Essen et al. 2020). Hence, the nightside atmosphere is unlikely to possess a temperature inversion and we do not expect that the TiO emission originates from the nightside hemisphere. Instead, we hypothesize that the TiO emission signals are from the regions close to the planetary terminators. We also suggest that a super-rotating atmosphere may transport heated gas across the eastward terminator, leading to a significant presence of TiO in a restricted region of the nightside. Figure 2.9 shows a toy model solution for this scenario, adopting a super-rotating atmosphere with $v_\mathrm{wind} = 8\,\mathrm{km\,s^{-1}}$ and two TiO regions at longitudes 90 ° to 130 ° (east limb) and –70 ° to –90 ° (west limb; Fig. 2.8). This led to a maximum S/N located at $K_\mathrm{p} = 243.0\,\mathrm{km\,s^{-1}}$, which is close to the orbital parameters of the planet obtained with CARMENES from the TiO signal. In order to obtain a similar K_p as the CARMENES result, only one TiO region must be visible at a given phase, otherwise we would observe a double-peak CCF. Figure 2.8 shows that the region at the east planetary limb is only visible before the eclipse while the west limb region is only visible after the eclipse. Although the toy model can explain the observed TiO signal, we emphasize that the model is not constrained sufficiently well to retrieve the actual parameters of the global circulation and the TiO distribution. Due to the simplicity of the toy model, we also refrain from giving the

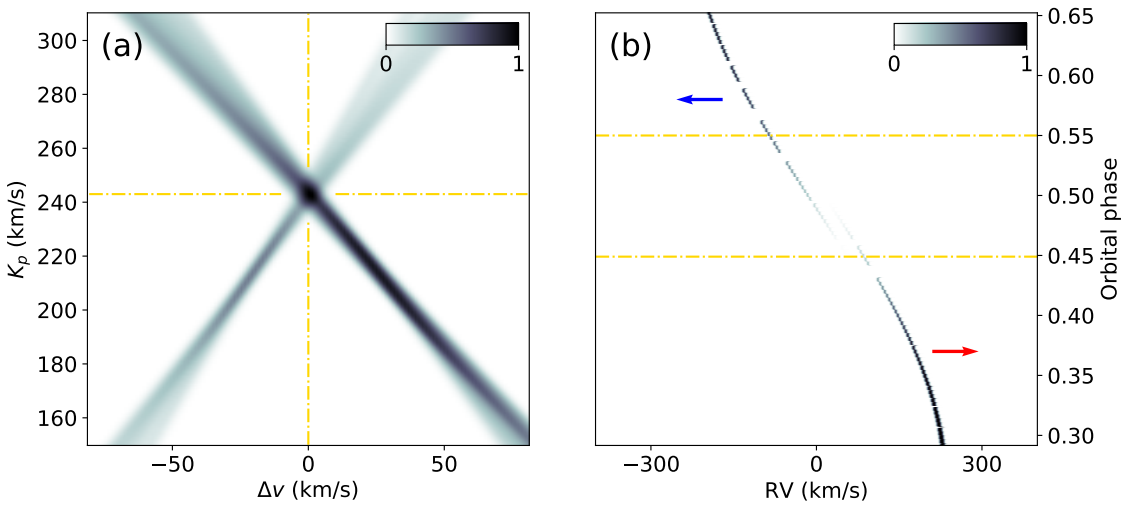

Figure 2.9.: Solution of the toy model for the TiO signal. *Panel a*: modeled S/N map. The yellow dash-dotted lines indicate the peak value at $K_p = 243.0\,\mathrm{km\,s^{-1}}$. *Panel b*: modeled CCF map in the stellar rest frame. The yellow dash-dotted lines indicate the begin and end of the secondary eclipse. We also show the continuation of the CCF trail during eclipse for a better understanding. Prior to the secondary eclipse only the terminator region at the east limb is visible to the observer, leading to a redshift of the TiO signature (shift indicated by red arrow). After eclipse only the blueshifted TiO signal from the terminator at the west limb is visible (shift indicated by blue arrow).

uncertainties of the parameters. The parameters of global circulation could probably be retrieved from a more comprehensive model of the atmosphere along with observations with higher S/N.

Our toy model also predicts that the TiO signal weakens at orbital phases close to the eclipse as the TiO-depleted hot spot faces toward the observer. This prediction is consistent with the observed results. We found the strongest TiO peak in the S/N map when excluding the orbital phases between 0.37 and 0.60 (Fig. 2.17). This indicates that the spectra inside this phase range probably carry a very weak TiO signal that is below the noise level. On the other hand, Fe is not depleted in the hot spot region but distributed more homogeneously over the planetary dayside. We emphasize that the suggested scenario of a TiO-free hot spot is consistent with our choice of using two different T-p profiles. We assumed atmospheric profiles with a higher temperature for Fe and a moderate temperature for TiO. Each profile may describe the average thermal conditions for the specific species. To verify this hypothesis, we reassessed the detection strengths by exchanging the two temperature profiles used to calculate the TiO and Fe model spectra. The coordinates of the S/N peaks do not change significantly (cf. Fig. 2.18). This indicates that the detection peaks are mainly caused by the presence of a thermal inversion layer. However, the detection strengths are lower than the results in Sects. 2.6.1 and 2.6.2, which is an additional hint toward TiO emission at moderate thermal conditions and Fe emission at higher temperatures.

2.6.4. Comparison of line profiles

We also assessed the width of the detected significance peaks by fitting a Gaussian function to the signals (Fig. 2.15). We found FWHM values of the Fe signal equal to $8.6 \pm 1.0\,\mathrm{km\,s^{-1}}$ and

$6.7 \pm 0.8\,\mathrm{km\,s^{-1}}$ for CARMENES and HARPS-N, respectively. The FWHM of the TiO signal is equal to $4.0 \pm 0.7\,\mathrm{km\,s^{-1}}$. The results are summarized in Table 2.3.

The CCF of Fe is significantly broader than that of TiO (cf. Figs. 2.6 and 2.15 for comparison; FWHM values in Table 2.3). This indicates that the line width of Fe is larger when compared to the TiO lines. Therefore, we suggest that the two chemical species experience a different level of rotational broadening, with Fe being affected more strongly than TiO. The narrow TiO line profile can be explained by the presence of the TiO-depleted hot spot, which produces a localized TiO concentration and a less rotational-broadened line profile. We checked this assumption by simulating two cross-correlation functions: the auto-correlation of the non-broadened TiO model spectrum; the cross-correlation between the non-broadened Fe model and a rotationally broadened Fe model, assuming a tidally locked rotational velocity (i.e., $7\,\mathrm{km\,s^{-1}}$ at the equator). The widths of the simulated CCFs are close to the widths of the observed CCFs (Fig. 2.19), indicating that the profile of the Fe lines is more strongly rotationally broadened than the profile of the TiO lines.

2.6.5. Comparison with previous work

In contrast to the results of this work and previous studies (Haynes et al. 2015; Nugroho et al. 2017), a recent investigation by Herman et al. (2020) does not report a significant detection of TiO in the atmosphere of WASP-33b. Their measurements with ESPaDOnS at the Canada-France-Hawai'i telescope (CFHT) are comparable to our data, as the authors use a cumulative exposure time equivalent to ~ 1.4 times of our observation with CARMENES. At $K_\mathrm{p} \sim 250\,\mathrm{km\,s^{-1}}$ and $v_\mathrm{sys} \sim 0\,\mathrm{km\,s^{-1}}$ in their Fig. 4 a weak pattern is visible, which resembles the peak region in the S/N map from our work (cf. left panel in Fig. 2.6). The orientation of the weak pattern (from upper left to lower right in their Fig. 4) indicates that most of the contribution to this feature is from the observations before the eclipse.

The authors use the Plez'12 (Plez 2012) database to compute the TiO model spectrum instead of the more precise `ToTo ExoMol` (McKemmish et al. 2019). Thus, we analyzed the data from Herman et al. (2020) to investigate whether the weak signature at $K_\mathrm{p} \sim 250\,\mathrm{km\,s^{-1}}$ is caused by a real TiO signal or by line list dependent effects (Merritt et al. 2020). We downloaded the spectra from the CFHT archive and applied the same data reduction procedures as for the CARMENES and HARPS-N spectra. We used the `ToTo ExoMol` TiO model spectrum (as in Fig. 2.3) to perform the cross-correlation. Our re-analyzed ESPaDOnS result shows a weak TiO signature with $S/N \sim 3$, which is similar to the weak pattern in Fig. 4 of Herman et al. (2020). The obtained S/N map of TiO is presented in Fig. 2.20. This weak feature is located close to our TiO detection with CARMENES. Therefore, this ESPaDOnS feature could be a real signature of TiO. However, the TiO signature in the ESPaDOnS spectra appears to be absent after the eclipse in contrast to the CARMENES observation. This could be due to the existence of temporal variability in global circulation (Komacek & Showman 2020).

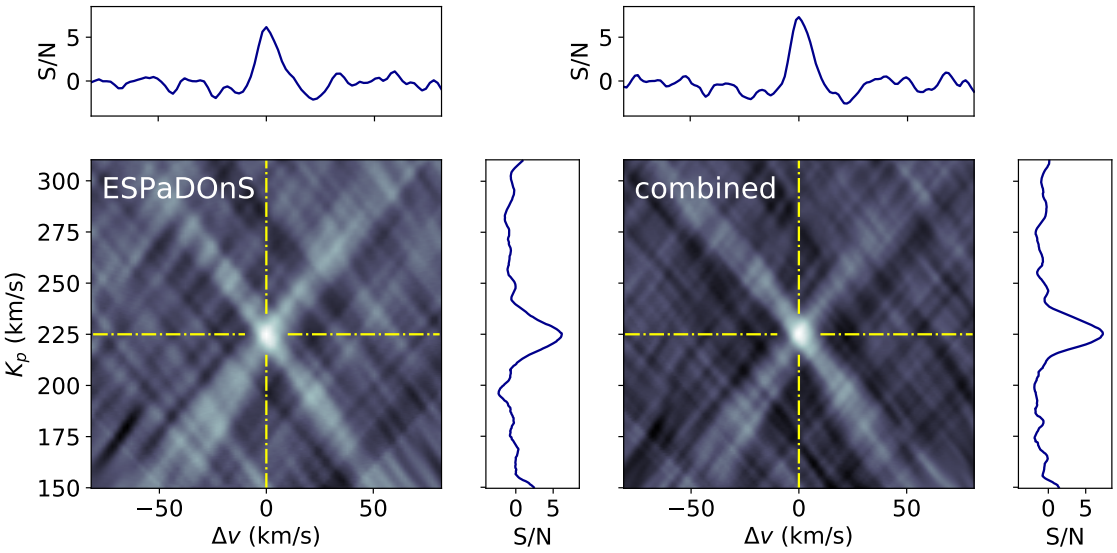

Figure 2.10.: S/N maps of Fe for ESPaDOnS (*left panel*) and a combination of all instruments (CARMENES, HARPS-N and ESPaDOnS; *right panel*). The detection significance peaks in both cases at $K_p = 225.0\,\mathrm{km\,s^{-1}}$ and $\Delta v = 0.0\,\mathrm{km\,s^{-1}}$ with a S/N value of 6.2 and 7.3, respectively. The peak coordinates in the S/N maps are indicated by the yellow dash-dotted lines; cross-sections of the S/N peaks are reported in the horizontal and vertical panels.

Very recently, Serindag et al. (2021) reassessed the TiO observation from Nugroho et al. (2017), but did not confirm the results from this previous study. In line with Serindag et al. (2021), we used the same line list `ToTo ExoMol` and adopted a similar approach by assuming a common optimal number of `SYSREM` iterations. They find a significant TiO detection with a K_p that is similar to our value, but different from the value published by Nugroho et al. (2017). In contrast, we identified the molecular signature at a Δv that is consistent with the planetary rest frame. We assumed the presence of a TiO-depleted hot spot to explain the K_p deviation of the detection peak, a hypothesis that has to be confirmed in future studies. Otherwise, we cannot exclude the presence of a spurious signal. This aspect is also discussed by Serindag et al. (2021), who suggest that previous claims of TiO may be false positives. The contradicting results of different studies on TiO in the atmosphere of WASP-33b (Haynes et al. 2015; Nugroho et al. 2017; Herman et al. 2020) highlight the critical role of accurate line lists and the potential need of different data reduction techniques and spectral models in further investigations.

2.6.6. Additional analysis of the Fe signal

In addition to TiO, we also searched for Fe features in the ESPaDOnS data. We applied the same reduction procedures as described in Sects. 2.4 and 2.5. The velocity steps were set to $1.8\,\mathrm{km\,s^{-1}}$, which corresponds to the mean pixel spacing of the instrument. The signature of Fe is clearly detected with a peak S/N of 6.2 after nine `SYSREM` iterations (Fig. 2.10). The signal is located at $K_p = 225.0^{+3.5}_{-5.0}\,\mathrm{km\,s^{-1}}$ and $\Delta v = 0.0^{+3.6}_{-3.6}\,\mathrm{km\,s^{-1}}$, which is in agreement with the results from CARMENES and HARPS-N. The FWHM of the peak CCF is measured as $11.1 \pm 1.1\,\mathrm{km\,s^{-1}}$.

Table 2.3.: Summary of results.

Instrument	S/N	K_p (km s^{-1})	Δv (km s^{-1})	FWHM (km s^{-1})
TiO				
CARMENES	4.9	$248.0^{+2.0}_{-2.5}$	$0.0^{+2.6}_{-2.6}$	4.0 ± 0.7
HARPS-N	no significant detection			
ESPaDOnS	no significant detection			
Fe				
CARMENES	5.7	$228.0^{+3.5}_{-5.0}$	$1.3^{+3.9}_{-3.9}$	8.6 ± 1.0
HARPS-N	4.5	$225.0^{+2.0}_{-5.0}$	$-0.8^{+4.0}_{-2.4}$	6.7 ± 0.8
ESPaDOnS	6.2	$225.0^{+3.5}_{-5.0}$	$0.0^{+3.6}_{-3.6}$	11.1 ± 1.1
Combined	7.3	$225.0^{+4.0}_{-3.5}$	$0.0^{+2.6}_{-2.6}$	9.2 ± 0.7

We further calculated a combined S/N map of Fe using the data from all three instruments (CARMENES, HARPS-N, ESPaDOns). For this purpose, we used a common velocity step equal to 1.3 km s^{-1}. We firstly merged the CCFs of all the spectra and then computed the S/N map following the description in Sect. 2.5.4. The final combined S/N map is presented in the right panel of Fig. 2.10. The resulting detection peak with $S/N = 7.3$ is located at $K_p = 225.0^{+4.0}_{-3.5}$ km s^{-1} and $\Delta v = 0.0^{+2.6}_{-2.6}$ km s^{-1}. The measured FWHM of the combined Fe peak CCF is 9.2 ± 0.7 km s^{-1}.

2.7. Conclusions

We observed the dayside of WASP-33b at high spectral resolution with the CARMENES and HARPS-N spectrographs. By using the cross-correlation technique, we detected Fe and found strong evidence for the presence of TiO. Both species show emission spectra, which confirms the presence of a temperature inversion claimed by prior studies (Haynes et al. 2015; Nugroho et al. 2017, 2020a). For TiO, we found the signal peak at $K_p = 248.0^{+2.0}_{-2.5}$ km s^{-1}, which deviates from the literature value by +17 km s^{-1} (Kovács et al. 2013; Lehmann et al. 2015; Nugroho et al. 2020a). In contrast, we detected Fe at $K_p = 225.0^{+4.0}_{-3.5}$ km s^{-1}, which is consistent with the literature values. The observed CCF of Fe is broader than that of TiO, indicating that the Fe lines are broader than the TiO lines.

We hypothesize that a TiO-depleted hot spot is present in the atmosphere of WASP-33b. Since TiO is suggested to be thermally dissociated in the hot spot region, we suppose that the observed TiO signal originates from locations close to the terminators. Our toy model suggests that this could lead to the observed deviation of K_p from the literature value. Such a scenario is also supported by the observed narrow line profile of TiO. Because TiO may be restricted to regions outside the hot spot while a homogeneous Fe distribution is expected in the dayside hemisphere, the TiO lines are less broadened by the planetary rotation compared to the Fe lines.

Although temperature inversions have been detected in a number of UHJs, the underlying formation mechanisms are still a matter of discussion. Our results suggest that atomic species and metal oxides are both involved in the heating mechanism, which is required to maintain a thermal inversion layer. Observations with higher S/N and the inclusion of 3D atmospheric structure into spectral modeling will be beneficial for further advances in exploring the atmospheres of extremely irradiated planets.

2.8. Appendix A) Validation of the TiO line list

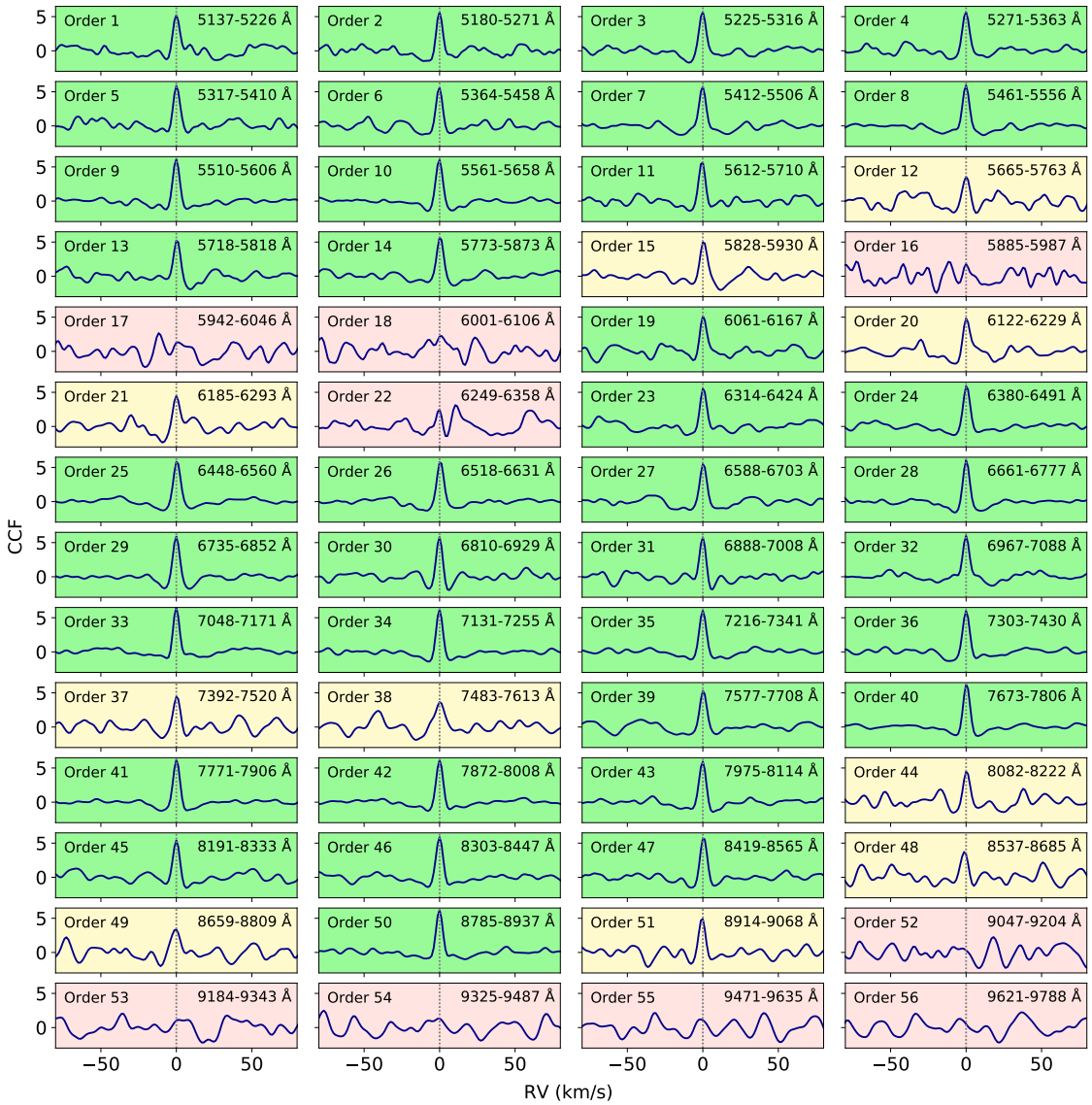

Figure 2.11.: CCFs between the TiO transmission model and the high-resolution spectrum of Barnard's star for CARMENES. The *x*-axis represents the radial velocity offset from the stellar rest frame; the *y*-axis measures the CCF in units of standard deviation. The yellow and green shaded panels indicate the spectral orders with a CCF peak greater than three and five standard deviations, respectively. Red shaded panels represent spectral orders not showing any correlation.

Figure 2.12.: Same as Fig. 2.11, but for wavelength segments (cf. Sect. 2.4.1) of HARPS-N.

We assessed the quality of the `ToTo ExoMol` line list via comparison of the line positions with the spectrum of Barnard's star (Reiners et al. 2018) that is dominated by TiO absorption features. The TiO transmission model spectrum was computed with `petitRADTRANS` by using the VMR and T-p profile from Sect. 2.5.1. The analysis covered both the CARMENES VIS channel and HARPS-N wavelength ranges. We convolved the transmission model spectrum with the instrument profiles and removed large-scale features with a Gaussian high-pass filter (25 pixels for

CARMENES; 75 pixels for HARPS-N). The filter was also applied to the high-resolution spectrum of Barnard's star. We then computed the CCF between the spectrum and the transmission model. The considered Doppler-shifts relative to the stellar rest frame were between –80.6 km s^{-1} and +80.6 km s^{-1} in steps of 1.3 km s^{-1} for CARMENES. We applied Doppler-shifts between –80.0 km s^{-1} and +80.0 km s^{-1} in steps of 0.8 km s^{-1} in the HARPS-N analysis. The line list was assumed to be accurate if a prominent CCF peak ($> 3\sigma$) was present at the systemic velocity of Barnard's star.

We found prominent cross-correlation signals for most of the spectral orders, except for CARMENES spectral orders [16:18, 22, 52:56] and HARPS-N spectral orders (segments) [1:9, 11:13, 29, 42, 47:51, 55, 56]. This is consistent with the line list analysis from McKemmish et al. (2019) and shows the improved precision of `ToTo` `ExoMol` at wavelengths shorter than 6000 Å in comparison to the line list Plez'98 (Plez 1998; Hoeijmakers et al. 2015). An order-wise plot of the CCF is given in Figs. 2.11 and 2.12 for CARMENES and HARPS-N, respectively. Spectral orders at wavelengths with a poor line list were not considered in the TiO analysis.

2.9. Appendix B) Injection-recovery test

After scaling the TiO model spectrum from Sect. 2.5.1 by a factor of 3, we convolved it with the respective instrument profiles of CARMENES and HARPS-N. We then shifted the convolved model spectrum with the planetary orbital RV and injected the model spectrum into the raw spectra (1D spectra from the instrument pipelines). The raw spectra with the injected model were subsequently processed in the same way as described in Sect. 2.4 and cross-correlated with the convolved TiO model spectrum in Fig. 2.3. This resulted in a cross-correlation matrix ($\overline{\mathrm{CCF}}_{\mathrm{inj}}$) for each observation and spectral order.

We computed a S/N map for all $\overline{\mathrm{CCF}}_{\mathrm{inj}}$s and identified the spectral orders that allowed us to recover the injected model spectrum (good orders). We assumed that only these spectral orders will give a contribution to the detection of the real planetary signature. In contrast, we assumed that spectral orders with no recovery of the injected model spectrum (bad orders) will not contribute to the detection of the real planetary signature. The following metric was applied to discriminate between good and bad orders. Good orders were supposed to detect the injected model spectrum ($S/N > 3$ at the injected K_{p} and Δv position) at least for one specific number of `SYSREM` iterations in the S/N map. Bad orders were supposed to not show a significant detection of the injected model spectrum ($S/N < 3$).

As a result, we found that the spectral orders number [1:20, 22, 24, 50, 51, 54:56] will not contribute to the detection of TiO in the CARMENES observation. For HARPS-N we recovered the injected model spectrum only in one order (segment) out of 69, that is order number 26. This suggests that the TiO signal will not be detectable with the HARPS-N data even if present in the data. The recovered detection strengths are shown for each spectral order in Figs. 2.13 and 2.14.

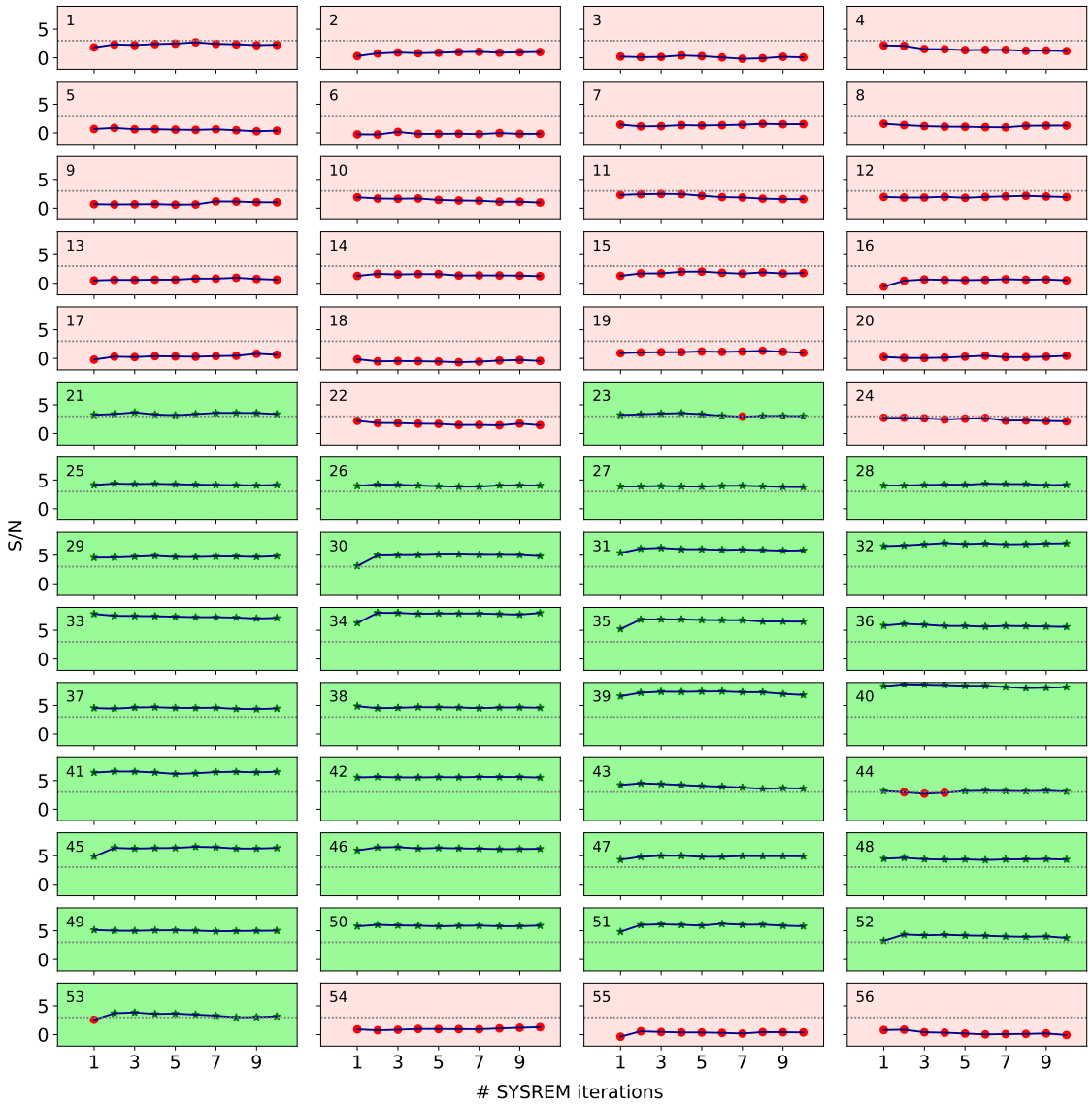

Figure 2.13.: Strength of the injected TiO model spectrum. The x-axis represents the number of consecutive `SYSREM` iterations; the y-axis measures the S/N detection strength of the injected model spectrum. Each panel is labeled with the number of the corresponding spectral order. Data points marked with green stars correspond to a detection, red circles to a nondetection of the injected model. The horizontal gray line corresponds to $S/N = 3$. We consider a spectral order to be good, if the injected model spectrum is detected at $S/N > 3$ for at least one specific number of `SYSREM` iterations. Spectral orders shaded with green are considered to be good orders, orders shaded with red to be bad orders. Although we got detections of the injected model in orders 50 and 51, we observed a strong enhancement of noise the in the final S/N detection map if we included them (cf. Sect. 2.5.4). We concluded that these orders have an increased noise level and excluded them from the list of good orders.

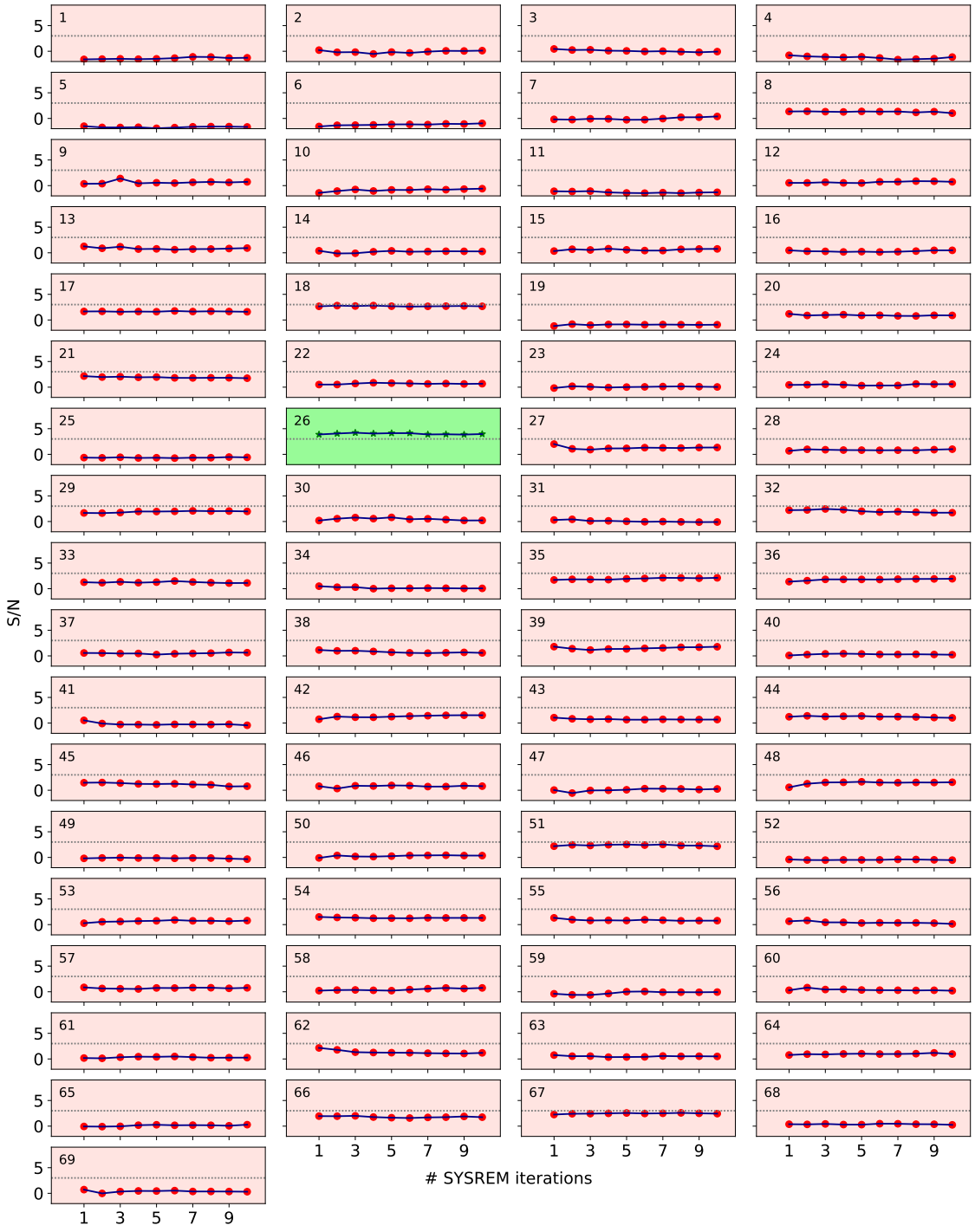

Figure 2.14.: Same as Fig. 2.13, but for wavelength segments (cf. Sect. 2.4.1) of HARPS-N. We retrieved the injected model planet spectrum only in one segment.

2.10. Appendix C) Additional figures

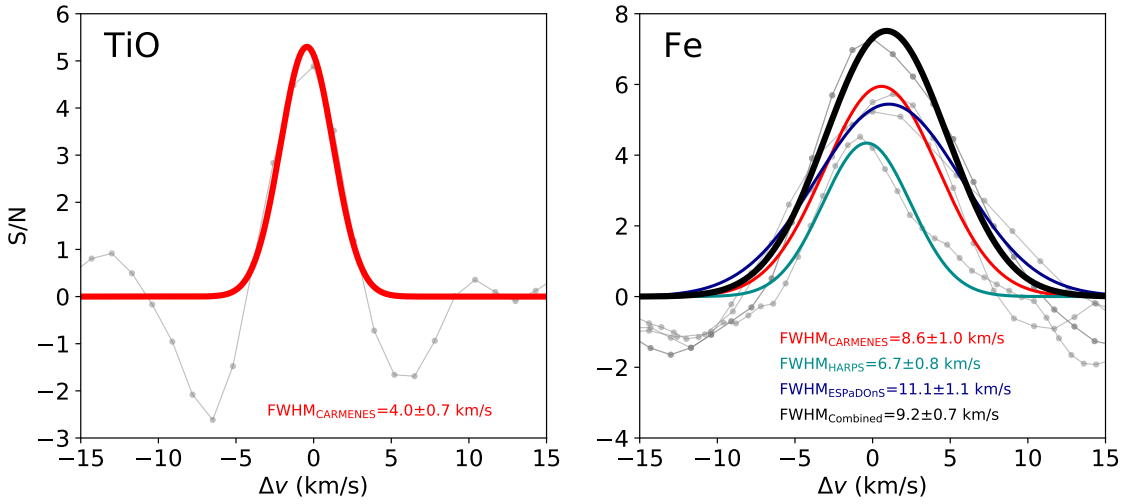

Figure 2.15.: Comparison between the CCF widths of the detection peaks of TiO and Fe. The Fe signal is broader when compared to TiO. The observed CCFs are represented by the gray circles. The Gaussian fit functions are presented by the thick solid lines with different colors denoting different instruments. Red: CARMENES; green: HARPS-N; blue: ESPaDOnS; black: combined signal of CARMENES, HARPS-N, and ESPaDOnS.

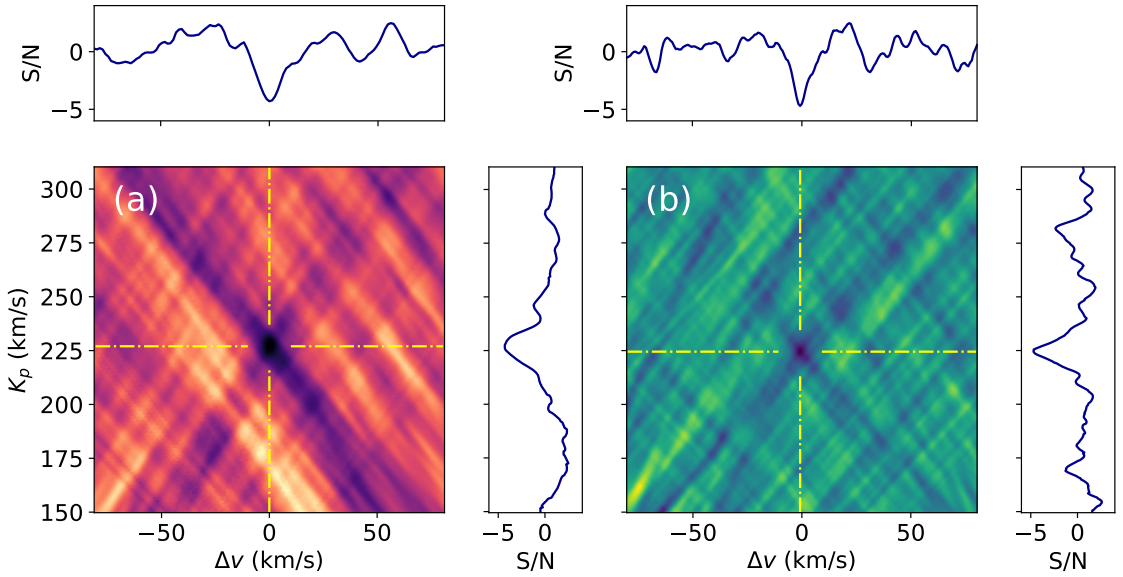

Figure 2.16.: S/N maps of Fe obtained by using a non-inverted T-p profile for cross-correlation (Nugroho et al. 2017). *Panel a*: anticorrelation signal of Fe in the CARMENES data ($S/N = -4.3$); *panel b*: anticorrelation with the HARPS-N data ($S/N = -4.6$). The coordinates of the negative S/N peaks are indicated by the yellow dash-dotted lines. The cross-sections of the negative S/N peaks are reported in the horizontal and vertical panels. Each S/N map corresponds to the `SYSREM` iteration number that maximizes the detection strength in Sects. 2.6.1 and 2.6.2.

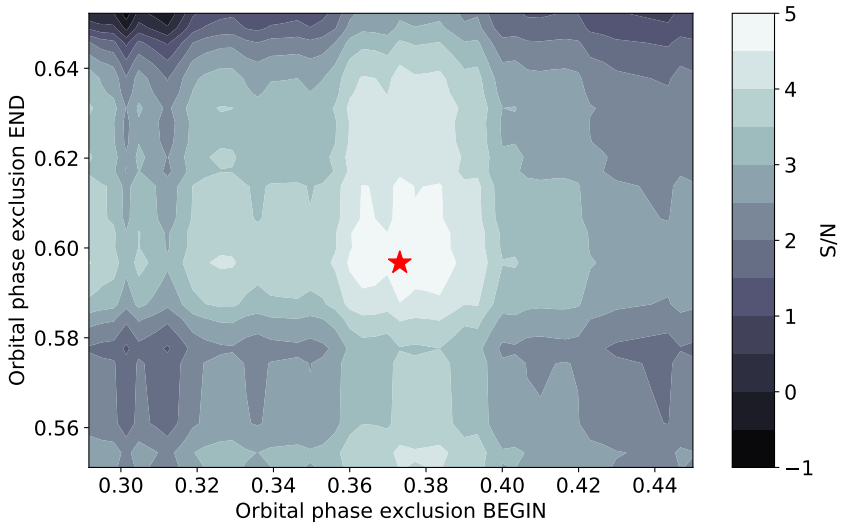

Figure 2.17.: Map of TiO S/N detection significance when excluding different orbital phase ranges around the secondary eclipse (measured at $K_p = 248.0\,\mathrm{km\,s^{-1}}$ and $\Delta v = 0.0\,\mathrm{km\,s^{-1}}$). The values on the x- and y-axis show the boundaries of the excluded phase intervals. The signal of TiO peaks when the orbital phase interval between ~ 0.37 and ~ 0.60 is excluded. The corresponding phase values are indicated with a red star. We checked the exclusion of all possible orbital phase intervals. Phase ranges that are entirely inside eclipse were not considered (between roughly 0.45 and 0.55).

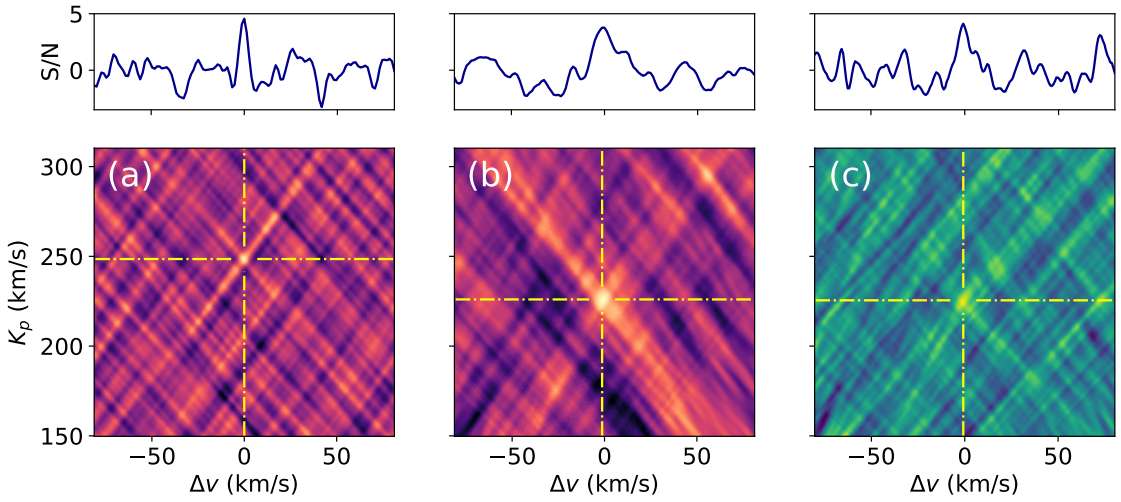

Figure 2.18.: S/N maps obtained by exchanging the T-p profiles of TiO and Fe to compute the model spectra for cross-correlation. All detection strengths are lower than those found in Sects. 2.6.1 and 2.6.2. *Panel a* corresponds to the TiO signal observed with CARMENES ($S/N = 4.6$); *panel b*: Fe detection with CARMENES ($S/N = 3.8$); *panel c*: Fe detection with HARPS-N ($S/N = 4.1$). The horizontal panels show the cross-sections of the S/N peaks. Each S/N map corresponds to the `SYSREM` iteration number that maximizes the detection strength in Sects. 2.6.1 and 2.6.2.

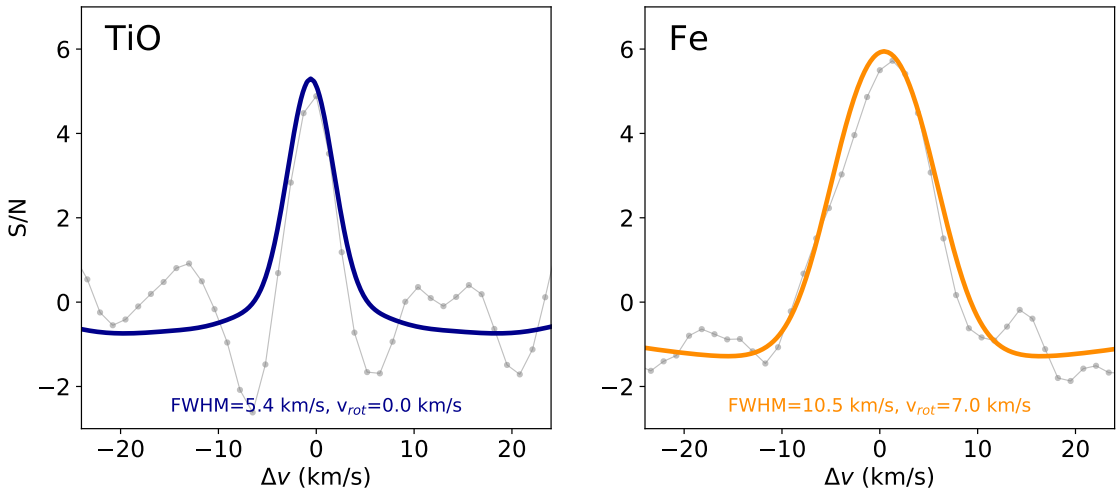

Figure 2.19.: Auto-correlation of the TiO model spectrum (*left panel*) and cross-correlation between the Fe model spectrum and a rotationally broadened version of itself ($v_{\rm rot} = 7\,{\rm km\,s^{-1}}$; *right panel*). For comparison, we plot the observed CCFs from the CARMENES observations in gray lines. The auto-correlation of the TiO model spectrum has a width of $5.4\,{\rm km\,s^{-1}}$. This is close to the FWHM value of the observed CCF ($4.0 \pm 0.7\,{\rm km\,s^{-1}}$). Also the FWHM of the cross-correlation with the broadened Fe model spectrum is close to the value of the observed CCF ($10.5\,{\rm km\,s^{-1}}$ and $8.6 \pm 1.0\,{\rm km\,s^{-1}}$, respectively).

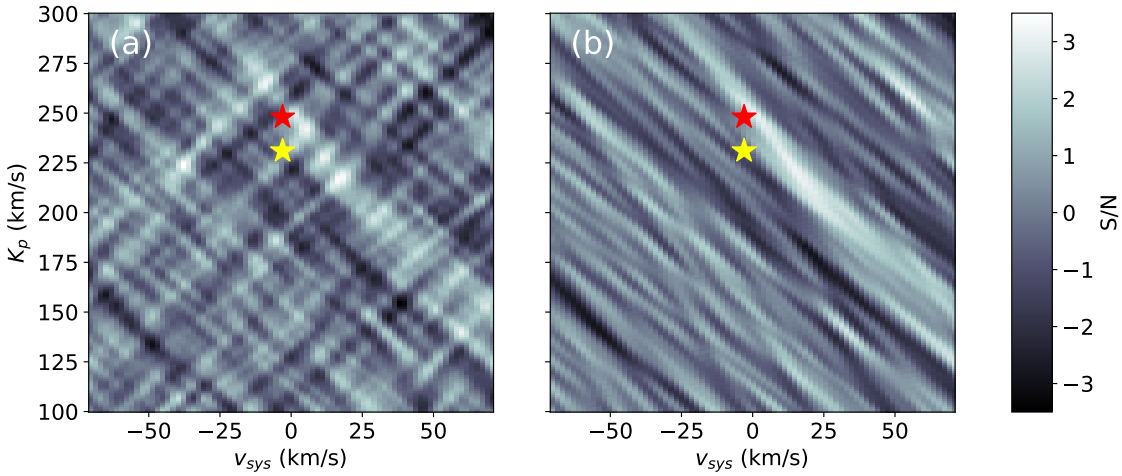

Figure 2.20.: S/N maps of TiO from the ESPaDOnS observations. *Panel a* represents the S/N map of all spectra; *panel b*: S/N map of the pre-eclipse TiO signature. The expected orbital parameters are indicated with the yellow star. A weak TiO signal is located close to the orbital parameters found with CARMENES, which is indicated with a red star. Only the spectra before eclipse contribute to the signal. The x-axis is presented in the systemic rest frame ($v_{\rm sys}$) in order to be consistent with Herman et al. (2020).

3. Silicon in the dayside atmospheres of two ultra-hot Jupiters

This chapter was published as the peer-reviewed article "Silicon in the dayside atmospheres of two ultra-hot Jupiters" (*Credit:* Cont et al., A&A, 657, L2, 2022, reproduced with permission ©ESO). The article was co-authored by F. Yan, A. Reiners, L. Nortmann, K. Molaverdikhani, E. Pallé, M. Stangret, Th. Henning, I. Ribas, A. Quirrenbach, J. A. Caballero, M. R. Zapatero Osorio, P. J. Amado, J. Aceituno, N. Casasayas-Barris, S. Czesla, A. Kaminski, M. López-Puertas, D. Montes, J. C. Morales, G. Morello, E. Nagel, A. Sánchez-López, E. Sedaghati, and M. Zechmeister. D. Cont conducted the data reduction, the cross-correlation analysis, and the null detection test. F. Yan conducted the observations of the two investigated exoplanets and contributed to the calculation of the volume mixing ratios. K. Molaverdikhani computed the high-resolution opacity data, which were used to generate the model spectra for cross-correlation. The other co-authors contributed to the interpretation of the results and provided comments to the manuscript. The layout of selected figures and tables has been slightly adapted for this thesis.

3.1. Abstract

Atmospheres of highly irradiated gas giant planets host a large variety of atomic and ionic species. Here we observe the thermal emission spectra of the two ultra-hot Jupiters WASP-33b and KELT-20b/MASCARA-2b in the near-infrared wavelength range with CARMENES. Via high-resolution Doppler spectroscopy, we searched for neutral silicon (Si) in their dayside atmospheres. We detect the Si spectral signature of both planets via cross-correlation with model spectra. Detection levels of 4.8σ and 5.4σ, respectively, are observed when assuming a solar atmospheric composition. This is the first detection of Si in exoplanet atmospheres. The presence of Si is an important finding due to its fundamental role in cloud formation and, hence, for the planetary energy balance. Since the spectral lines are detected in emission, our results also confirm the presence of an inverted temperature profile in the dayside atmospheres of both planets.

3.2. Introduction

Ultra-hot Jupiters (UHJs) are highly irradiated gas giant planets with equilibrium temperatures ($T_{\rm eq}$) close to the stellar regime ($T_{\rm eq} \geq 2200$ K; Parmentier et al. 2018). Planets in this regime are expected to be tidally locked to their host stars, given enough time for tidal forces to synchronize the rotation of the planet to its orbital motion. The extreme thermal conditions in combination with permanent day- and nightsides allow the existence of a large variety of chemical species. In the dayside atmospheres of UHJs, most of the molecules are expected to be dissociated, leading to the presence of atomic and ionic species (e.g., Lothringer et al. 2018; Arcangeli et al. 2018; Kitzmann et al. 2018). Molecules should be widely present in atmospheric regions other than the dayside, spanning from diatomic molecules at the terminators to more complex compounds on the planetary nightsides (Helling et al. 2019). To date, various chemical species have been detected in the transmission or emission spectra of UHJs. This includes atomic hydrogen and metals such as Ca, Cr, Fe, Mg, Mn, Na, Ti, Sc, V, and Y (e.g., Fossati et al. 2010; Jensen et al. 2018; Yan & Henning 2018; Casasayas-Barris et al. 2018, 2019; Hoeijmakers et al. 2018, 2019, 2020a; Sing et al. 2019; Cauley et al. 2019, 2021; Stangret et al. 2020; Nugroho et al. 2020a,b; Ben-Yami et al. 2020; Borsa et al. 2021a; Tabernero et al. 2021; Yan et al. 2021, 2022b) and molecules such as H_2O and OH[1] (e.g., Huitson et al. 2013; Edwards et al. 2020; Tsiaras et al. 2018; Mikal-Evans et al. 2020; Nugroho et al. 2021).

Inverted temperature-pressure (T-p) profiles have been measured in a number of UHJ atmospheres (e.g., Haynes et al. 2015; Evans et al. 2017; Sheppard et al. 2017; Arcangeli et al. 2018; Kreidberg et al. 2018; Mansfield et al. 2018; Nugroho et al. 2020a; Yan et al. 2020). The presence of these so-called temperature inversions (i.e., temperature increasing with altitude) was initially explained via strong absorption of the incoming stellar radiation by TiO and VO (Hubeny et al. 2003; Fortney et al. 2008). However, the presence of TiO is under debate due to the conflicting results of different studies (Evans et al. 2016; Nugroho et al. 2017; Herman et al. 2020; Edwards et al. 2020; Serindag et al. 2021; Cont et al. 2021). Besides, the search for VO remains elusive at high spectral resolution (Merritt et al. 2020). On the other hand, as various atoms and ions have been discovered in UHJs with an inverted atmosphere, atomic species have become promising candidates for causing and maintaining temperature inversions (Lothringer et al. 2018; Hoeijmakers et al. 2020b).

Theoretical simulations predict the presence of Si in the atmospheres of UHJs. Atomic Si is expected in planetary daysides, while Si-bearing molecules (e.g., SiO) should be prominent on the nightsides and in the terminator regions (Helling et al. 2019). Si is suggested to play a key role in cloud formation, which strongly impacts the atmospheric energy budget (Gao et al. 2020; Gao & Powell 2021). The abundance of Si is expected to be close to that of Fe for a solar atmospheric composition (Fossati et al. 2021).

[1] For a more complete list of detections, we refer the reader to the `Exoplanet Atmospheres Database` available at `http://research.iac.es/proyecto/exoatmospheres/`.

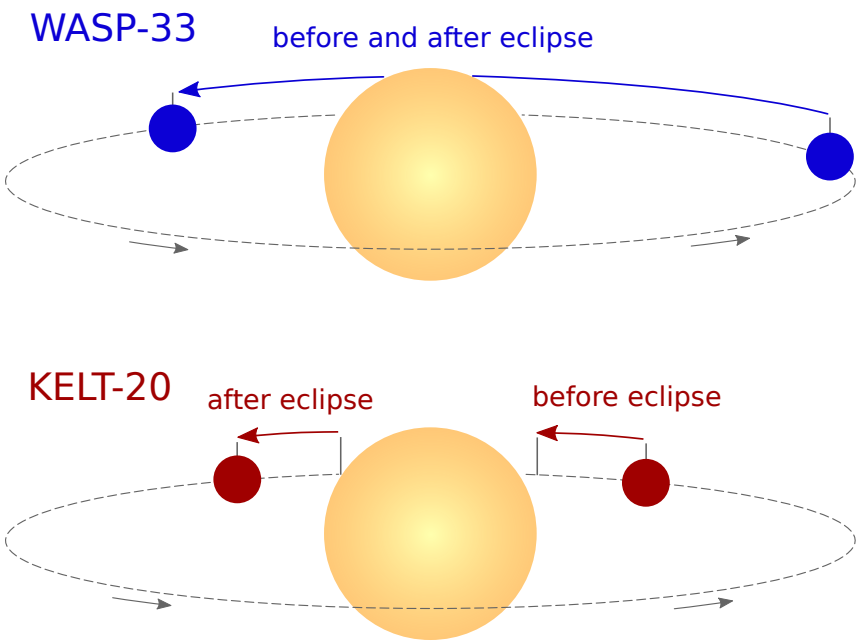

Figure 3.1.: Schematic of emission spectroscopy observations. The orbital phase coverage of WASP-33b is shown in the *top panel* (night of 15 November 2017) and that of KELT-20b in the *bottom panel* (before 21 May 2020 and after 9 July 2020). The orbital motion direction is indicated by the arrows.

Hints for atmospheric Si III absorption in the 1206.5 Å resonance line were found via transmission spectroscopy in HD 209458b (Linsky et al. 2010). However, Ballester & Ben-Jaffel (2015) later disproved this detection by identifying stellar flux variations as the cause for a false positive signal in the data. In addition to this specific spectral line, Fossati et al. (2021) proposed investigating the spectral features of Si II around 1530 Å as a further way of searching for this atomic species in planetary atmospheres. Hoeijmakers et al. (2019) searched for Si in KELT-9b via transmission spectroscopy at high spectral resolution but did not detect it. This non-detection is probably due to a low concentration of neutral Si in the atmosphere of KELT-9b that is, in turn, due to the strong ionization of the species. Ionized Si should be present, but its spectral signature is expected to be featureless in the investigated wavelength range.

In this Letter we report the first detection of neutral Si in exoplanet atmospheres. We detected Si I emission lines in the dayside atmospheres of WASP-33b and KELT-20b/MASCARA-2b via high-resolution emission spectroscopy in the near-infrared. WASP-33b (Collier Cameron et al. 2010) orbits an A-type star with δ Scuti pulsations (Herrero et al. 2011). With $T_{\rm eq} \sim 2700$ K, it is the second hottest planet known to date, showing a temperature inversion in its dayside atmosphere (Haynes et al. 2015). The spectral features of Ca II, Fe I, OH, TiO, and the hydrogen Balmer lines have been found at high spectral resolution (Nugroho et al. 2017, 2020a, 2021; Yan et al. 2019, 2021; Cauley et al. 2021; Borsa et al. 2021c; Cont et al. 2021), and AlO and FeH were tentatively detected (von Essen et al. 2019; Kesseli et al. 2020). KELT-20b/MASCARA-2b (Lund et al. 2017; Talens et al. 2018) is a UHJ with $T_{\rm eq} \sim 2300$ K that orbits an A-type star without pulsations. A number of metals, such as Ca, Cr, Fe, Na, and Mg, were found in the planetary transmission

Table 3.1.: Observation log.

Object	Date	Observing time (UT)	Airmass change	Phase coverage	Exposure time (s)	N_{spectra}
WASP-33b	2017-11-15	18:13–04:04	1.74–1.00–1.95	0.29–0.63	300	88 [(a)]
KELT-20b	2020-05-21	23:05–03:07	1.87–1.02	0.41–0.46	125	85
KELT-20b	2020-07-09	23:00–03:05	1.07–1.01–1.17	0.51–0.56	125	85

Notes. [(a)] Total number of spectra is 105; 17 spectra with insufficient quality were removed.

spectrum (Casasayas-Barris et al. 2018, 2019; Hoeijmakers et al. 2020a; Stangret et al. 2020; Nugroho et al. 2020b; Rainer et al. 2021). Recently, Yan et al. (2022b) used the spectral emission lines of Fe I to retrieve the atmospheric temperature profile, claiming the presence of a temperature inversion on the planetary dayside. The parameters of both planetary systems are summarized in Table 3.3.

3.3. Observations and data reduction

We observed the two planets over a total of three nights with the CARMENES (Calar Alto high-Resolution search for M dwarfs with Exoearths with Near-infrared and optical Échelle Spectrographs) spectrograph at the Calar Alto Observatory (Quirrenbach et al. 2014, 2020). The observation of WASP-33b took place on 15 November 2017, and KELT-20b was observed on two nights, 21 May 2020 and 9 July 2020 (see Fig. 3.1). To investigate the dayside atmospheres, we observed at orbital phases close to the secondary eclipse. These observations have already been utilized in previous studies (Cont et al. 2021; Yan et al. 2022b) to retrieve the Fe emission spectrum in the visible channel (5200–9600 Å; $R \sim 94\,600$). In this work we analyze the data collected with the near-infrared channel (9600–17 100 Å; $R \sim 80\,400$), for which the Si signal is expected to be stronger (see the model spectra with solar Si abundance in Sect. 3.4.1). For seven WASP-33b spectra, the star was not centered on the fiber, and for three spectra the flux dropped due to a passing cloud. For another seven spectra, the elevation of the target was too low (airmass > 2) to get a useful amount of flux in the near-infrared channel. Hence, we removed a total of 17 spectra from the WASP-33b observations. The targets were observed with fiber A, and fiber B was used to record the sky background. Details of the observations are given in the observation log in Table 3.1.

We used the reduction pipeline `caracal` v2.20 (Zechmeister et al. 2014; Caballero et al. 2016) to extract the order-by-order[2] one-dimensional spectra and the corresponding uncertainties from

[2] In the near-infrared channel, two detectors are located along the dispersion direction. The resulting spectra are therefore split into half-orders. For simplicity, we use the term "spectral order" to describe these "half-orders" in the following text.

the raw frames. The data of each night were reduced separately. We excluded the spectra from the echelle orders 45–43 due to an insufficient flux level. These orders correspond to the water absorption band around 1.4 μm, for which the Earth's atmosphere is almost entirely opaque. For each spectral order, we arranged the spectra chronologically to obtain the two-dimensional spectral matrix (Fig. 3.4a). To account for the variable continuum level, we fitted the individual spectra with a second-order polynomial and normalized them with the fit function. Wavelength ranges with strong emission lines in fiber B were excluded from the second-order polynomial fit. The outliers were removed by applying 5σ clipping to the time evolution of each pixel. We masked the wavelength bins with flux below 20 % of the continuum level (Fig. 3.4b).

To remove the telluric and stellar lines from the spectra, we used the detrending algorithm `SYSREM` (Tamuz et al. 2005). We passed the normalized spectral matrix and the corresponding uncertainties as an input to the algorithm (details in Sect. 3.8). The uncertainties were computed via error propagation. We ran `SYSREM` for ten consecutive times, resulting in a residual spectral matrix for each iteration. If present in the data, the signature of the planetary atmosphere is buried in the noise of the residual spectra (Fig. 3.4c).

3.4. Method

3.4.1. Model spectra

The model atmosphere of each planet was divided into 61 layers, evenly spaced on a logarithmic pressure scale from 1 to 10^{-6} bar. For WASP-33b, we adopted the T-p profile of WASP-189b from Yan et al. (2020), which was retrieved via the Fe I emission spectrum and by assuming a solar metallicity. This choice is motivated by the physical similarities between the two planets. The profile was also successfully used in a prior work to detect the Fe I signature in the atmosphere of WASP-33b (Cont et al. 2021). For KELT-20b, we took the T-p profile from a joint retrieval of CARMENES and TESS (Transiting Exoplanet Survey Satellite) by Yan et al. (2022b). We deployed `easyCHEM` (Mollière et al. 2017) to compute the volume mixing ratio (VMR) and the mean molecular weight of each atmospheric layer. To this end, we assumed equilibrium chemistry, at five different values of metallicity [M/H] between –2 dex and +2 dex in steps of 1 dex. We assumed that all metals vary with overall metallicity and, hence, [Si/H] = [M/H]. Figure 3.2 shows that under the assumption of equilibrium chemistry, neutral Si is most abundant at the location of the thermal inversion layers. Deeper in the atmospheres, SiO accounts for the majority of Si inventory. At higher altitudes, the VMR of the species decreases due to ionization.

We used the radiative transfer code `petitRADTRANS` (Mollière et al. 2019) to generate the model spectra. The continuum opacity of H^- was not taken into account, as it was found to only insignificantly affect the resulting model spectra (see Fig. 3.5). The Si opacities for the radiative transfer calculation were computed from the Kurucz line database (Kurucz 2018). For each planet, this resulted in five model emission spectra with different Si abundances (see Figs. 3.6 and 3.7).

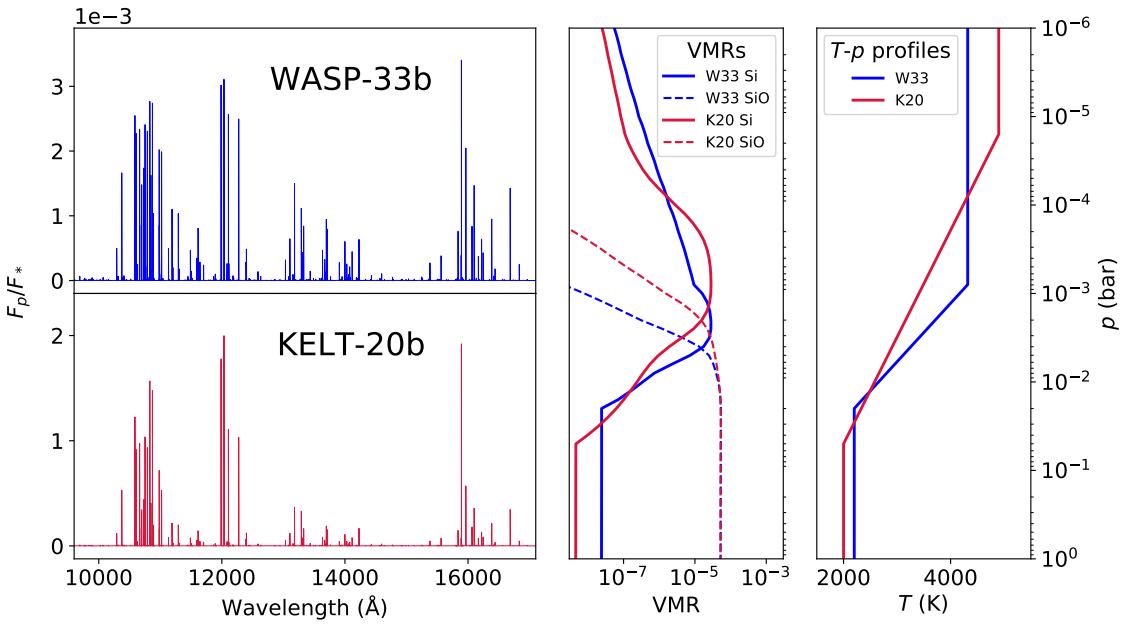

Figure 3.2.: Emission model spectra (*left panels*) for WASP-33b (W33, blue) and KELT-20b (K20, red) and their corresponding VMRs of Si and SiO (*middle panel*) and T-p profiles (*right panel*). We assumed equilibrium chemistry and [Si/H] = 0 to generate the presented model spectra (for sub- and super-solar metallicity values, see Figs. 3.6 and 3.7).

We computed the planet-to-star flux ratio of each model spectrum by dividing by the blackbody spectrum of the respective host star. As the reduced spectra were normalized, we also normalized the model spectra to the continuum. After convolving with the instrumental profile, we obtained the final emission model spectra for cross-correlation. The model spectra with [Si/H] = 0 are shown in Fig. 3.2.

3.4.2. Cross-correlation

The model spectra in Sect. 3.4.1 predict a planet-to-star flux ratio on the order of 10^{-3} or lower. Hence, the planetary signal is dominated by noise in the `SYSREM` reduced spectra. We applied the cross-correlation method to extract the emission signature of the planetary atmosphere (e.g., Snellen et al. 2010; Brogi et al. 2012; Alonso-Floriano et al. 2019; Sánchez-López et al. 2019). This technique maps the planetary emission lines onto a single peak, enabling the identification of the species in the planetary signal. We performed the cross-correlation analysis for each of the model spectra with different Si abundance separately.

The model spectrum was shifted over a radial velocity (RV) range from –520 km s^{-1} to +520 km s^{-1} with steps of 1 km s^{-1}. At each step, we multiplied the shifted model spectrum with the uncertainty-weighted residual spectra. As a result, we obtained the weighted cross-correlation function (CCF), defined as

$$\mathrm{CCF} = \sum r_i m_i(v), \tag{3.1}$$

for each observed spectrum and echelle order (Gibson et al. 2020). We denote with r_i the residual spectra weighted by the inverse of the squared uncertainties; m_i is the model spectrum shifted by v in the RV space. For each echelle order the CCFs were stacked into an individual array. Subsequently, we co-added the arrays from different echelle orders, leading to the final CCF map for each spectral model and observation night. Finally, we merged the CCF maps of the two KELT-20b observations.

The stellar line profile of WASP-33 undergoes time-dependent variations due to the pulsations of the star (Herrero et al. 2011). Lines of neutral Si are also present in the stellar spectrum and, consequently, not efficiently removed by `SYSREM`. This causes the pulsations of the star to appear as artifacts in the CCF map (Nugroho et al. 2020a; Cont et al. 2021). To exclude potential spurious signals from the pulsations of WASP-33, we masked the RV range between $\pm v_{\rm rot} \sin i_*$ (i.e., between –87 km s^{-1} and +87 km s^{-1}) in the stellar rest frame (Cont et al. 2021). In contrast, KELT-20 has no pulsations, which results in an efficient stellar line removal by `SYSREM`. No masking was therefore required in the CCF map of KELT-20b.

For each planet, we aligned the CCF map to the planetary rest frame over a range of different orbital velocity semi-amplitudes ($K_{\rm p}$). We assumed a circular orbit with a planetary RV of

$$v_{\rm p} = v_{\rm sys} + v_{\rm bary} + K_{\rm p} \sin 2\pi\phi + \Delta v \tag{3.2}$$

for shifting the CCF map, with $v_{\rm sys}$ the systemic velocity, $v_{\rm bary}$ the barycentric velocity of the observer, Δv the velocity deviation from the planetary rest frame, and ϕ the orbital phase. For each value of $K_{\rm p}$, we collapsed the CCF map into a one-dimensional CCF by calculating the mean value over all orbital phases. The CCFs from different $K_{\rm p}$ values were stacked in a two-dimensional array, which was further normalized by its standard deviation (excluding the region around the strongest signal peak). This resulted in a signal-to-noise mapping of the detection significance (S/N map), which enabled us to assess the presence of Si in the planetary atmospheres.

3.5. Results and discussion

We detected the spectral signature of neutral Si in the dayside atmospheres of the two exoplanets WASP-33b and KELT-20b. At `SYSREM` iterations higher than one and for all tested metallicity values ([Si/H] between –2 dex and +2 dex in steps of 1 dex; see Sect. 3.4.1), the signal is identified in the S/N maps. For each planet, the strongest signal was found assuming an atmosphere with a solar Si abundance. The respective S/N maps are shown in Fig. 3.3. For non-solar Si abundances, the detection peaks are less prominent. We show the S/N maps for non-solar abundances in Figs. 3.8 and 3.9. The evolution of the S/N with increasing `SYSREM` iterations is plotted in Fig. 3.10 and Fig. 3.11 shows the aligned planetary trails together with the profile of the detection peaks. In Sect. 3.10, we also show that our implementation of the cross-correlation technique does not lead to significant detection peaks when an inappropriate model spectrum is used.

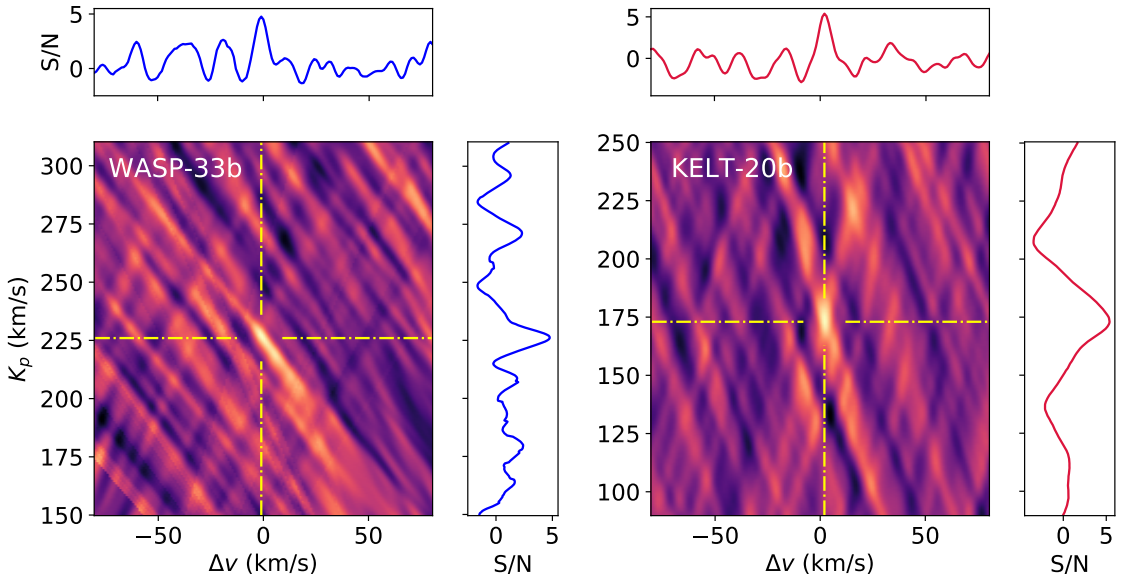

Figure 3.3.: S/N detection maps of neutral Si for WASP-33b (*left panel*) and KELT-20b (*right panel*). The signal of WASP-33b peaks with a S/N of 4.8 after three consecutive SYSREM iterations. For KELT-20b, we achieve the highest significance at $S/N = 5.4$ after four iterations. We indicate the peak coordinates by the yellow dash-dotted lines. The horizontal and vertical panels correspond to the cross sections of the S/N peaks.

For WASP-33b, we found the most significant detection after three SYSREM iterations at $S/N = 4.8$. The peak is located at $K_\mathrm{p} = 226.0^{+5.0}_{-11.5}$ km s^{-1}, which is close to the expected K_p of 231 ± 3 km s^{-1} calculated from the orbital parameters of the planet (Kovács et al. 2013; Lehmann et al. 2015). For Δv we find a small value of $-1.0^{+10.0}_{-4.0}$ km s^{-1}, which is consistent with zero. The K_p of our detection is slightly lower than the expected value, a trend that has also been found in prior studies of Fe (Nugroho et al. 2020a; Cont et al. 2021). We also detected the spectral signature of neutral Si in the atmosphere of KELT-20b. The strongest signal was found after four consecutive SYSREM iterations with a S/N of 5.4 at $K_\mathrm{p} = 173.0^{+6.5}_{-5.0}$ km s^{-1} and $\Delta v = 2.0^{+2.0}_{-2.0}$ km s^{-1}. This result agrees with the K_p values of $173.4^{+1.8}_{-1.5}$ km s^{-1} and $169.3^{+5.9}_{-4.6}$ km s^{-1} calculated from the system parameters of Talens et al. (2018) and Lund et al. (2017), respectively. The small value of Δv is also consistent with zero. All results are summarized in Table 3.2.

We also investigated whether the spectral lines of Si are affected by rotational broadening. For each planet, we simulated two CCFs: the auto-correlation of the non-broadened model spectrum and the cross-correlation between the non-broadened model and a rotationally broadened model. We assumed a tidally locked rotation, corresponding to rotation velocities of 7 km s^{-1} and 3 km s^{-1} at the equators of WASP-33b and KELT-20b, respectively. Figure 3.11 compares the profile of the measured CCF peaks with the simulated detection peaks. For WASP-33b, the observed CCF is best reproduced when no rotation is assumed, which hints toward a localized distribution of Si in the planetary atmosphere. However, for KELT-20b, the difference between the broadened and non-broadened simulations is marginal, and both of them are consistent with the observed CCF, which indicates that the rotational broadening probably makes a negligible contribution to the total line profile.

Table 3.2.: Summary of results.

Object	S/N	K_p (km s^{-1})	Δv (km s^{-1})
WASP-33b	4.8	$226.0^{+5.0}_{-11.5}$	$-1.0^{+10.0}_{-4.0}$
KELT-20b	5.4	$173.0^{+6.5}_{-5.0}$	$2.0^{+2.0}_{-2.0}$

We detected the spectral lines of the species in emission, which confirms the presence of thermal inversion layers in the dayside atmospheres of WASP-33b (Nugroho et al. 2017, 2020a; Cont et al. 2021) and KELT-20b (Yan et al. 2022b). Together with recent detections of neutral Fe (e.g., Pino et al. 2020; Yan et al. 2020; Nugroho et al. 2020a; Cont et al. 2021; Kasper et al. 2021), the presence of neutral Si also strengthens the assumption that atomic species play a key role in the energy balance of UHJ atmospheres. Due to a comparable ionization potential, we expect similar VMRs of Si and Fe in the upper atmosphere of UHJs (Fossati et al. 2021). However, the detection of Si is more challenging than that of Fe because of the smaller number of significant emission lines.

Although our detections are strongest when assuming a solar Si abundance, there is a degeneracy between the metallicity and the selected T-p profiles. Hence, our result of a solar metallicity in both planets is only valid for the specific T-p profiles that were selected. Considering the model spectra with [Si/H] = 0 in Figs. 3.6 and 3.7, we also conclude that the most prominent Si features in the planetary spectrum are probably restricted to the wavelength interval 10 000–13 000 Å and to a small region around 16 000 Å.

We note that in the S/N maps, detection peaks can even be observed at the lowest metallicity values investigated. This is due to the fact that the cross-correlation technique only takes the strength of the spectral lines relative to one another into account, not their absolute strength. The information about the absolute value of the CCFs is removed by the normalization step that is included in the calculation of the S/N maps (see Sect. 3.4.2). As shown in Figs. 3.6 and 3.7, the model spectra at [Si/H] ≤ 0 have spectral lines with a similar strength relative to one another. Therefore, it is plausible that the model spectra of sub-solar metallicities cause a similar S/N detection pattern compared to a solar metallicity despite their weak emission lines.

Neutral Si was not detected in the HARPS-N transmission spectra of KELT-9b (Hoeijmakers et al. 2019). This is not surprising, since Si is probably largely ionized due to the extreme thermal conditions in the atmosphere of this planet. In fact, Fossati et al. (2021) predicted that Si begins to get ionized at pressures around 10^{-2} bar in the atmosphere of KELT-9b. In addition, the transmission spectrum of ionized Si is expected to be featureless in the investigated wavelength range. Consequently, for planetary atmospheres with extreme thermal conditions such as KELT-9b, Si may be difficult to detect. For planets with more moderate thermal conditions, we suggest that the search for Si could be limited due to Si depletion. In this scenario, most of the Si would be bound in SiO and other Si-bearing molecules, which can also condense out of the gas phase. We

therefore posit that the thermal conditions in exoplanet atmospheres may be a crucial constraint for the search of Si.

Si is supposed to be an important element for cloud formation in exoplanet atmospheres, with silicates dominating the cloud composition over a wide range of planetary equilibrium temperatures. Our detections of Si in its gaseous phase indicate that the dayside atmospheres of UHJs are hotter than the condensation temperatures of Si-bearing condensates. This is in line with theoretical work that predicts the presence of silicate clouds primarily on the planetary nightsides (Gao et al. 2020; Gao & Powell 2021).

3.6. Conclusions

We used the CARMENES spectrograph to observe the dayside emission spectra of two UHJs – WASP-33b and KELT-20b. By using the cross-correlation technique, we detected the signature of neutral Si in the exoplanet atmospheres. For both planets, the Doppler-shifts of their Si spectra are consistent with the known orbital motion. We tested model spectra with different Si abundances and detected the strongest signals when assuming a solar abundance for the planetary atmospheres. From our Si model spectra, we conclude that the presence of prominent spectral features is probably restricted to two narrow regions in the near-infrared wavelength range. The spectral lines of Si were detected in emission, which is unambiguous evidence for the existence of temperature inversions in the two planetary atmospheres.

In combination with the presence of Fe, reported in prior studies, our detections of Si suggest that atomic species play a key role in the atmospheric heating process that is necessary to maintain a thermal inversion layer. Strong absorption lines of ionized Si should exist in the ultraviolet transmission spectra of UHJs and may be detectable with the *Hubble* Space Telescope and the upcoming World Space Observatory-Ultraviolet. Future observations over a wider wavelength range will provide further constraints on Si in planetary atmospheres, with the potential of shedding light on complex processes of cloud formation.

3.7. Appendix A) Parameters of planetary systems

Table 3.3.: Parameters of the WASP-33 and KELT-20/MASCARA-2 systems used in this work.

Parameter (Unit)	WASP-33b	KELT-20b/MASCARA-2b
Planet		
R_p (R_J)	$1.679^{+0.019}_{-0.030}$ [(a)]	1.83 ± 0.07 [(g)]
P_orb (d)	1.219870897 [(b)]	3.4741070 [(h)]
T_0 (d)	$2\,454\,163.22449$ [(b)]	$2\,457\,503.120049$ [(h)]
v_sys (km s^{-1})	-3.02 ± 0.42 [(c)]	-24.48 ± 0.04 [(i)]
K_p (km s^{-1})	231 ± 3 [(a)]	$173.4^{+1.8}_{-1.5}$ [(g)]
		$169.3^{+5.9}_{-4.6}$ [(h)]
T_ingress (d) [(*)]	0.0124 ± 0.0002 [(d)]	$0.01996^{+0.00080}_{-0.00077}$ [(h)]
T_transit (d) [(*)]	0.1143 ± 0.0002 [(d)]	$0.14898^{+0.00091}_{-0.00088}$ [(h)]
$\log g$ (cgs)	3.46 [(d)]	< 3.42 [(h)]
Star		
R_* ($R_\odot$)	$1.509^{+0.016}_{-0.030}$ [(a)]	1.60 ± 0.06 [(g)]
T_eff (K)	7430 ± 100 [(e)]	8980^{+90}_{-130} [(g)]
$v_\mathrm{rot} \sin i_*$ (km s^{-1})	$86.63^{+0.37}_{-0.32}$ [(f)]	114 ± 3 [(g)]

Notes. [(*)] WASP-33b is subject to a rapid orbital precession. The transit chord, transit duration, and ingress duration therefore change with time (Johnson et al. 2015; Watanabe et al. 2020; Cauley et al. 2021). [(a)] Lehmann et al. (2015) with parameters from Kovács et al. (2013), [(b)] Maciejewski et al. (2018), [(c)] Nugroho et al. (2017), [(d)] Kovács et al. (2013), [(e)] Collier Cameron et al. (2010), [(f)] Johnson et al. (2015), [(g)] Talens et al. (2018), [(h)] Lund et al. (2017) - we assumed a value of $\log g = 3.0$ to compute the model spectra because only an upper limit is reported, [(i)] Rainer et al. (2021).

3.8. Appendix B) Removal of telluric and stellar lines with SYSREM

SYSREM is a detrending algorithm that was originally designed to remove systematic effects from transit light curves (Tamuz et al. 2005). In its application to the search for exoplanet atmospheres, each wavelength bin of the spectral matrix is treated as an individual light curve. The algorithm models the systematics by iteratively fitting the trend of each wavelength bin as a function of time. Subsequently, the model is subtracted from the data. Systematic effects can have multiple causes, such as variations in airmass, atmospheric water vapor along the line of sight, seeing, or instrumental effects.

We implemented SYSREM following the method described by Gibson et al. (2020), which runs the algorithm in flux space instead of magnitude space (Tamuz et al. 2005). In a first step, we ran

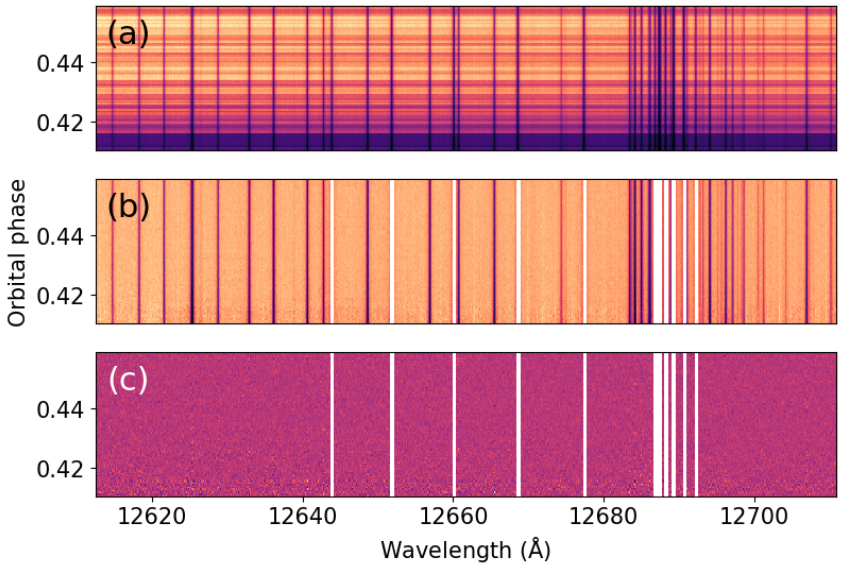

Figure 3.4.: Example of data reduction steps for a selected CARMENES wavelength range (observation on 21 May 2020). *Panel a* shows the unprocessed one-dimensional spectra. *Panel b* illustrates the spectra after normalization and outlier correction; the strongest telluric lines are masked in this step. *Panel c* shows the SYSREM reduced spectra after telluric and stellar line removal.

the algorithm in the traditional way, which resulted in a model-subtracted residual matrix for each SYSREM iteration. Then we divided the original spectral matrix by the sum of the models from each SYSREM iteration. We also divided the uncertainties by the final model for error propagation.

The SYSREM implementation proposed by Gibson et al. (2020) comes with the advantage of preserving the strength of the planetary spectral signature falling onto stellar and telluric lines. The mathematical description of the normalized spectra is $1+F_p/F_*$, where F_p/F_* is the planet-to-star flux ratio.

3.9. Appendix C) Additional figures

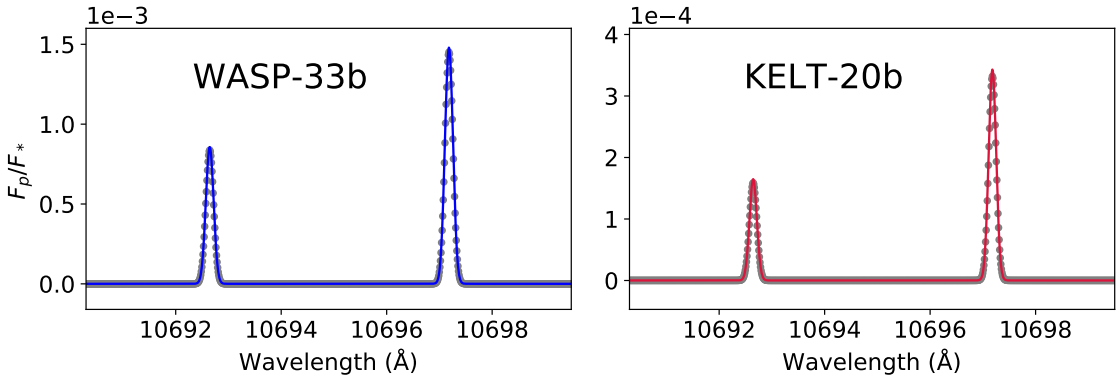

Figure 3.5.: Comparison between model spectra with (gray data points) and without (solid lines) H^- opacity. The difference between the models is insignificant, and hence the H^- continuum opacity can be neglected.

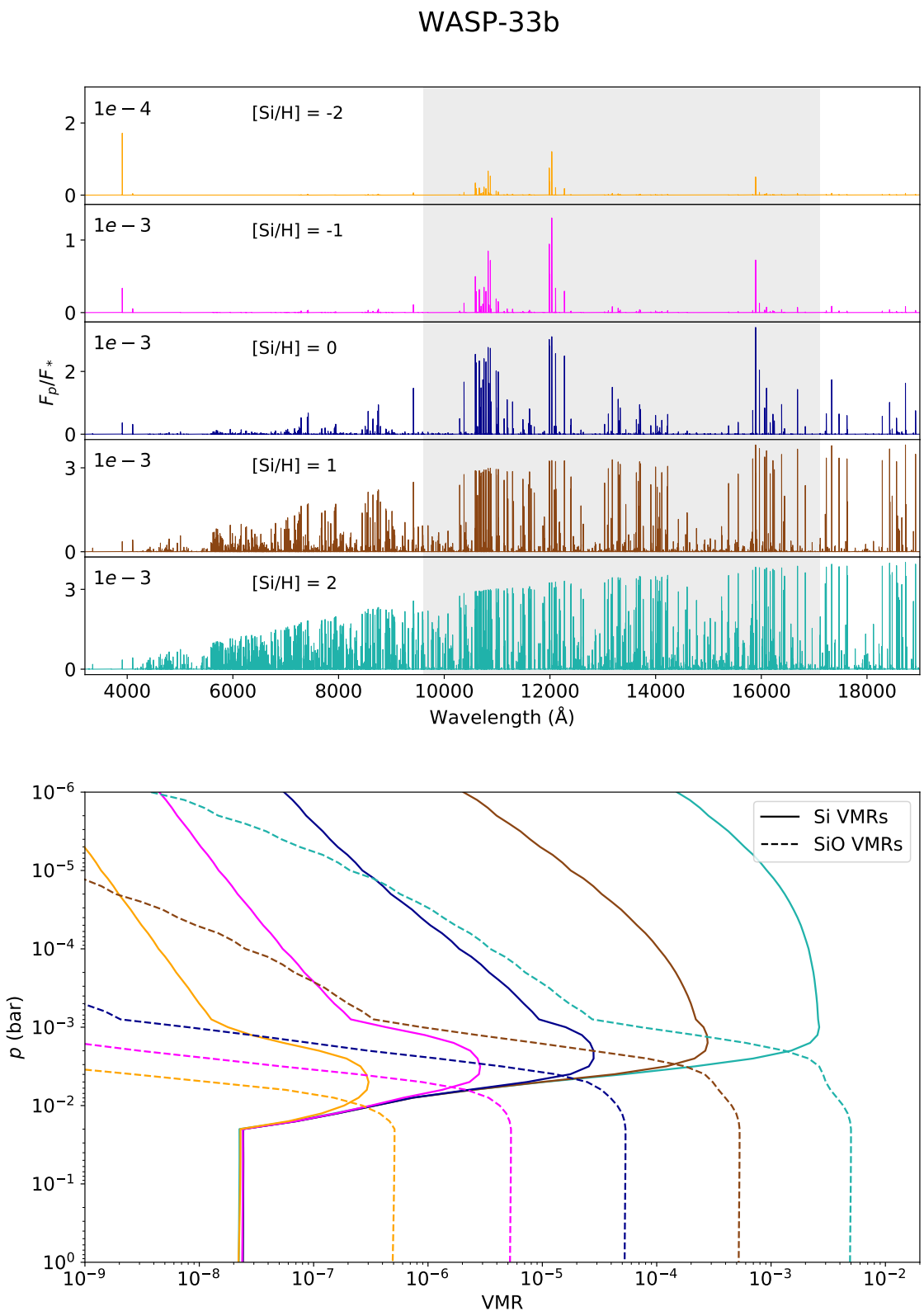

Figure 3.6.: Model spectra and VMRs at different metallicity values. *Top panel*: Model spectra for WASP-33b over a wide wavelength range (3000–19 000 Å). The gray shaded area corresponds to the CARMENES near-infrared channel. The spectra were calculated for VMRs with [Si/H] between –2 dex and +2 dex in steps of 1 dex. The model with [Si/H] = 0 is also shown in Fig. 3.2. *Bottom panel:* VMRs computed by assuming chemical equilibrium. We also plot the VMRs of SiO (dashed lines) to allow for a comparison with the VMRs of Si (solid lines).

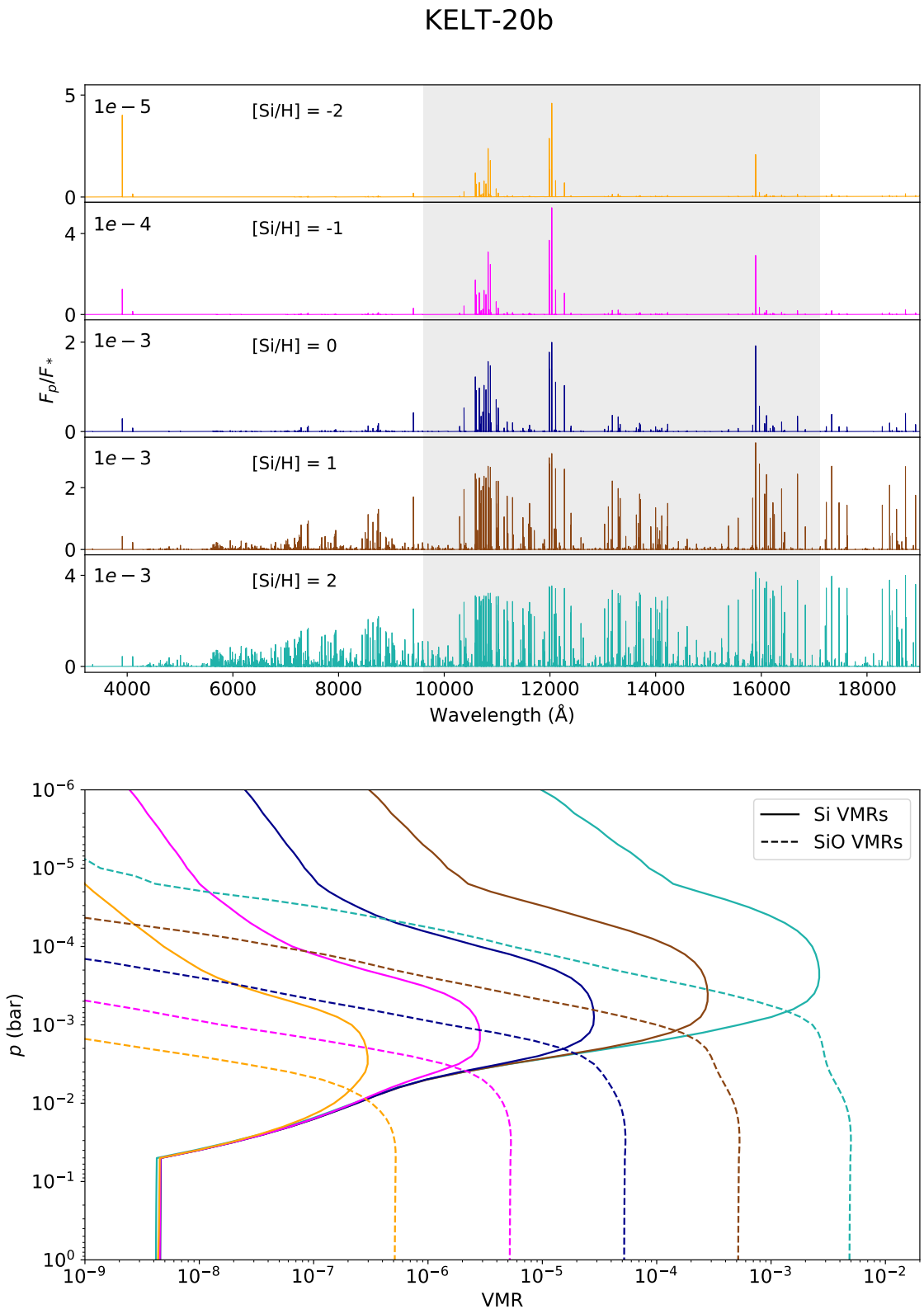

Figure 3.7.: Same as Fig. 3.6, but for KELT-20b.

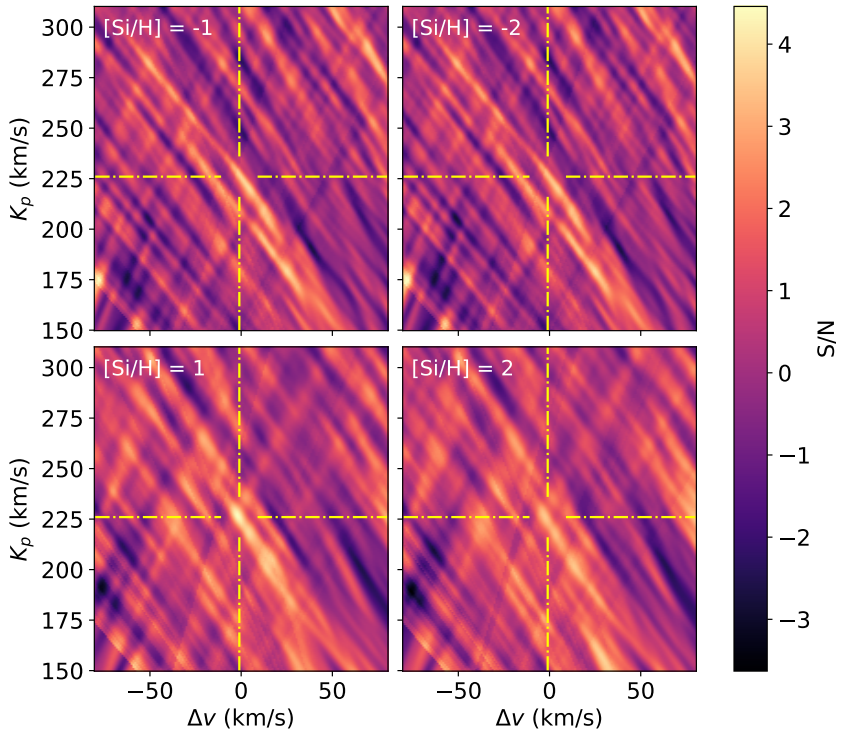

Figure 3.8.: S/N maps of WASP-33b after three SYSREM iterations from model spectra with non-solar Si abundances. The *top panels* and *bottom panels* correspond to sub-solar and super-solar [Si/H] ratios, respectively. The yellow dash-dotted lines indicate the location of the most significant detection peak, described in Sect. 3.5. The detection significance obtained with non-solar [Si/H] ratios is below the peak value obtained under the assumption of solar elemental abundances.

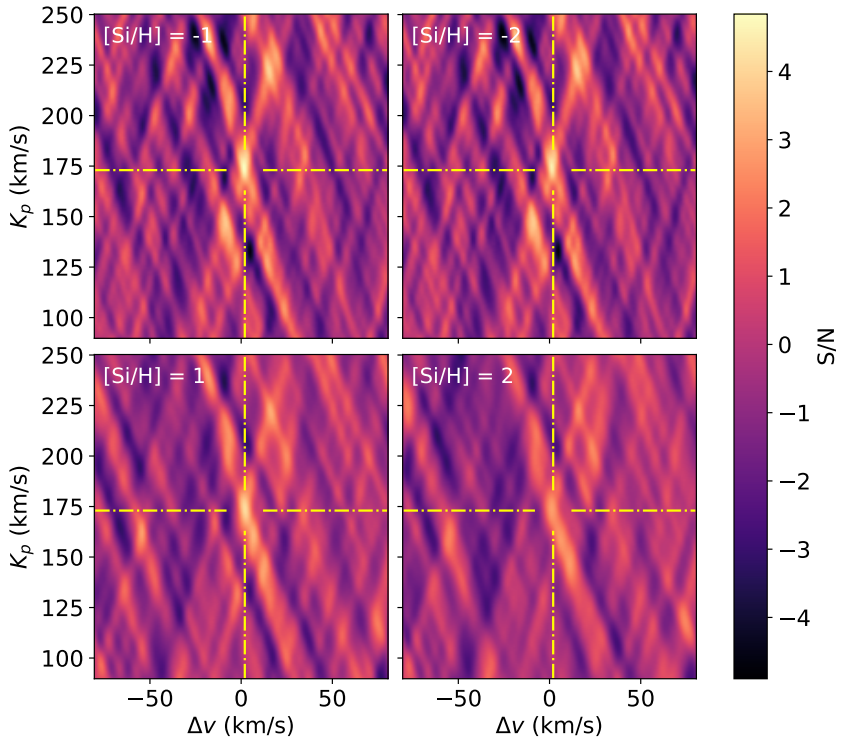

Figure 3.9.: Same as Fig. 3.8, but after four SYSREM iterations for KELT-20b.

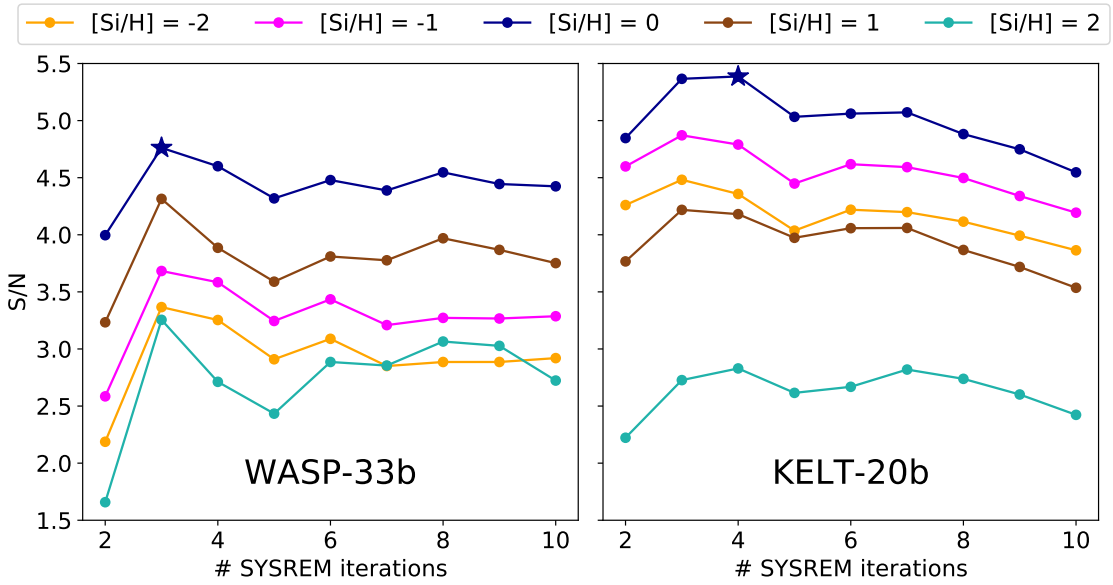

Figure 3.10.: Evolution of the S/N detection strength (measured at the position of the strongest peak; see Sect. 3.5) with increasing `SYSREM` iteration. We show the S/Ns of WASP-33b and KELT-20b in the *left* and *right panels*, respectively. The different Si abundances are indicated by different colors. The strongest S/N peaks are found for both planets at [Si/H] = 0 and are indicated by the blue stars.

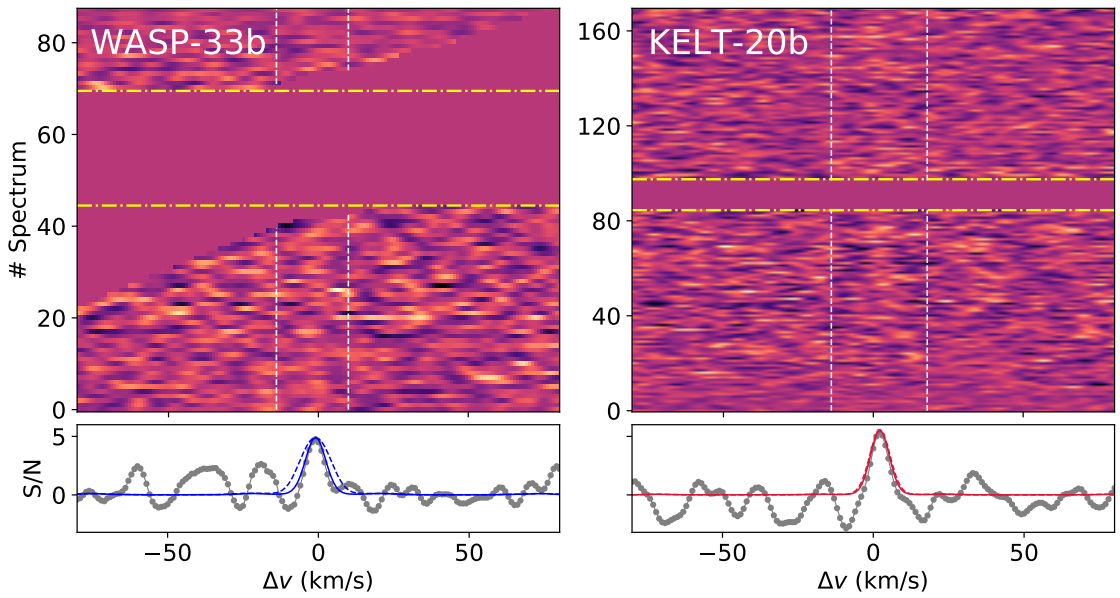

Figure 3.11.: CCF maps of WASP-33b (*left panels*) and KELT-20b (*right panels*). The aligned CCF maps are shown in the *top panels* (assuming K_p values of 226.0 km s^{-1} and 173.0 km s^{-1} for WASP-33b and KELT-20b, respectively). The vertical dashed lines indicate the planetary trail; the horizontal dash-dotted lines indicate ingress and egress from secondary eclipse. As described in Sect. 3.4.2, we masked the RV range of residual stellar Si lines in the CCF map of WASP-33b. In the *bottom panels* the collapsed CCF maps (gray lines) are compared to simulated CCFs (blue and red lines). The simulated CCFs that are rotationally broadened (by 7 km s^{-1} and 3 km s^{-1}, respectively) are represented by the dashed lines. Those without broadening are represented by the solid lines. We note that in the case of KELT-20b, the simulated CCFs with and without broadening differ only marginally and therefore lie on top of each other.

3.10. Appendix D) Null detection test

To further increase confidence in the detected Si signals, we tested how the use of an inappropriate model spectrum for cross-correlation affects the S/N maps. We chose to use a shifted Fe model spectrum, since the amplitude and density of the Fe emission lines are similar to those of Si in the near-infrared wavelength range of CARMENES (see Fig. 3.12). To avoid detecting a Fe signal (Fe is present in the atmosphere of WASP-33b and KELT-20b; Nugroho et al. 2020a, Cont et al. 2021, Yan et al. 2021), the wavelength solution of the Fe model spectrum was shifted by a constant value of 500 Å. By shifting the wavelength axis, the Fe lines are no longer located at the right position. Hence, we reached a situation that corresponds to that of a model with random lines. We also tested shifts other than 500 Å, all of which led to the same conclusions.

We computed the CCFs and the S/N detection maps by using the shifted Fe model spectrum. The resulting S/N maps show a noise pattern without any strong detection peaks (see Fig. 3.13). We conclude that our implementation of the cross-correlation technique does not lead to significant detections when an inappropriate model spectrum is used.

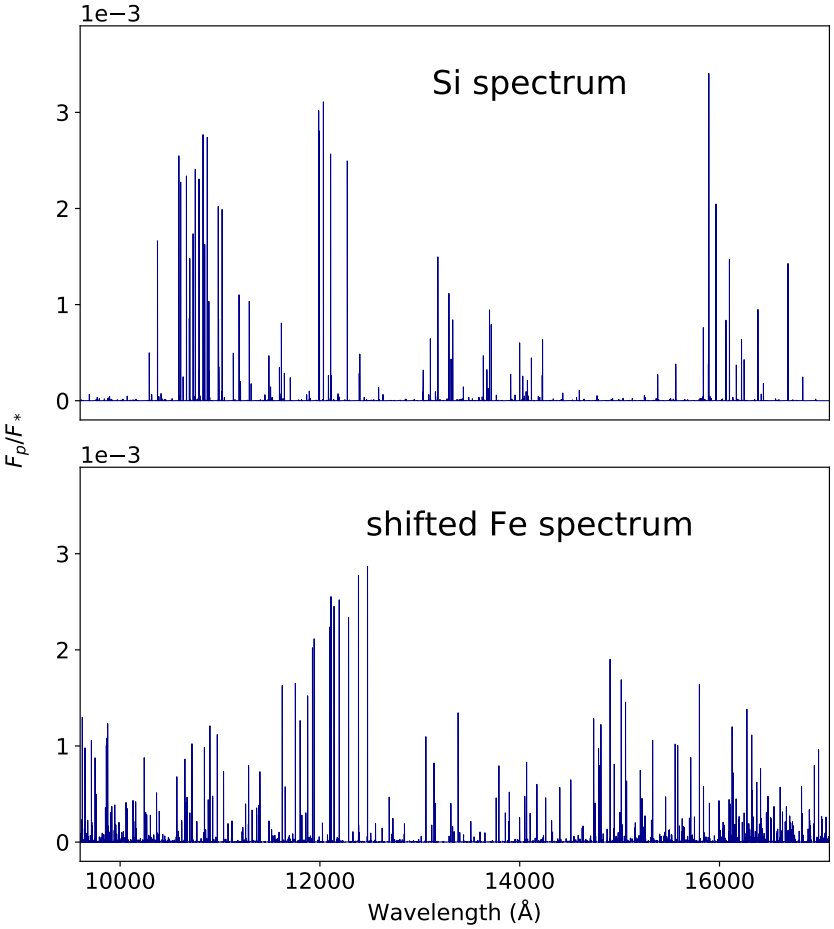

Figure 3.12.: Comparison between the Si model spectrum of WASP-33b (*top panel*) and the wavelength-shifted Fe model (*bottom panel*). We note that the density and amplitude of the emission lines in the two models are similar.

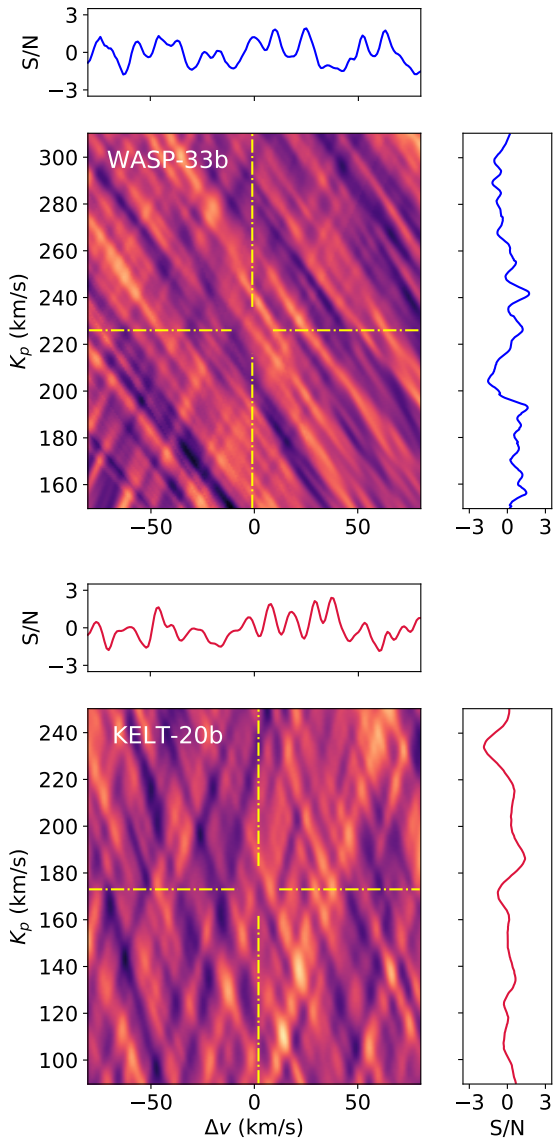

Figure 3.13.: S/N detection maps of WASP-33b (*top panel*) and KELT-20b (*bottom panel*), obtained from cross-correlation with the shifted Fe model spectrum. A random noise pattern without any significant detection peaks is found. The detection coordinates of Si are indicated by the yellow dash-dotted lines. The horizontal and vertical panels correspond to the cross sections at the location of the Si S/N peaks and do not show any detection signal.

4. Atmospheric characterization of the ultra-hot Jupiter WASP-33b

This chapter was published as the peer-reviewed article "Atmospheric characterization of the ultra-hot Jupiter WASP-33b. Detection of Ti and V emission lines and retrieval of a broadened line profile" (*Credit:* Cont et al., A&A, 668, A53, 2022). The article was co-authored by F. Yan, A. Reiners, L. Nortmann, K. Molaverdikhani, E. Pallé, Th. Henning, I. Ribas, A. Quirrenbach, J. A. Caballero, P. J. Amado, S. Czesla, F. Lesjak, M. López-Puertas, P. Mollière, D. Montes, G. Morello, E. Nagel, S. Pedraz, and A. Sánchez-López. D. Cont performed the data reduction, the cross-correlation analysis, and the retrieval of the atmospheric parameters. F. Yan conducted the CARMENES observations of WASP-33b, contributed to the calculation of the volume mixing ratios, and provided his retrieval code. K. Molaverdikhani computed the high-resolution opacity data, which were used to generate the model spectra for cross-correlation and the retrieval analysis. The other co-authors contributed to the interpretation of the results and provided comments to the manuscript. The layout of selected figures and tables has been slightly adapted for this thesis.

4.1. Abstract

Ultra-hot Jupiters are highly irradiated gas giant exoplanets on close-in orbits around their host stars. The dayside atmospheres of these objects strongly emit thermal radiation due to their elevated temperatures, making them prime targets for characterization by emission spectroscopy. We analyzed high-resolution spectra from CARMENES, HARPS-N, and ESPaDOnS taken over eight observation nights to study the emission spectrum of WASP-33b and draw conclusions about its atmosphere. By applying the cross-correlation technique, we detected the spectral signatures of Ti I, V I, and a tentative signal of Ti II for the first time via emission spectroscopy. These detections are an important finding because of the fundamental role of Ti- and V-bearing species in the planetary energy balance. Moreover, we assessed and confirm the presence of OH, Fe I, and Si I from previous studies. The spectral lines are all detected in emission, which unambiguously proves the presence of an inverted temperature profile in the planetary atmosphere. By performing retrievals on the emission lines of all the detected species, we determined a relatively weak atmospheric thermal inversion extending from approximately 3400 K to 4000 K. We infer a super-solar metallicity close to 1.5 dex in the planetary atmosphere, and find that its emission signature undergoes significant line broadening with a Gaussian full width at half maximum of about 4.5 km s^{-1}. Also,

we find that the atmospheric temperature profile retrieved at orbital phases far from the secondary eclipse is about 300 K to 700 K cooler than that measured close to the secondary eclipse, which is consistent with different day- and nightside temperatures. Moreover, retrievals performed on the emission lines of the individual chemical species lead to consistent results, which gives additional confidence to our retrieval method. Increasing the number of species included in the retrieval and expanding the set of retrieved atmospheric parameters will further advance our understanding of exoplanet atmospheres.

4.2. Introduction

In-depth characterization of exoplanet atmospheres is an emerging field in astronomy. Most known exoplanets have no analogs in our Solar System and therefore challenge our understanding of their formation and evolution. In recent years, observations and theoretical work have increased our knowledge about the subclass of ultra-hot Jupiters (UHJs; Parmentier et al. 2018), which are gas giant planets with the highest equilibrium temperatures identified to date ($T_{\rm eq} \geq 2200$ K). Located on close-in orbits, they are expected to be tidally locked to their host stars with highly irradiated daysides. The extreme irradiation regime in combination with a synchronous rotation causes a strong temperature contrast between the permanent day- and nightsides. Therefore, the atmospheric composition is significantly different between the two planetary hemispheres (e.g., Arcangeli et al. 2018; Bell & Cowan 2018; Komacek & Tan 2018; Tan & Komacek 2019; Molaverdikhani et al. 2020). UHJ daysides are likely dominated by atomic species with a high degree of ionization, while most of the molecules are predicted to dissociate (Kitzmann et al. 2018; Lothringer et al. 2018). In contrast, the planetary nightsides harbor a large variety of molecules and can be covered by clouds with complex molecular chemistry (Helling et al. 2019; Gao et al. 2020; Gao & Powell 2021).

The atmospheric composition of UHJs has been extensively studied in recent years. For instance, neutral or ionic species of H, Li, O, Na, Mg, Si, K, Ca, Sc, Ti, V, Cr, Mn, Fe, Sr, and Y have been identified in the atmospheres of several UHJs, including KELT-9b (Yan & Henning 2018; Hoeijmakers et al. 2018, 2019; Wyttenbach et al. 2020; Borsa et al. 2021b), WASP-33b (Yan et al. 2019, 2021; Nugroho et al. 2020a; Borsa et al. 2021c; Cont et al. 2021, 2022b; Herman et al. 2022), WASP-189b (Yan et al. 2020; Stangret et al. 2022; Prinoth et al. 2022), WASP-76b (Seidel et al. 2019; Ehrenreich et al. 2020; Tabernero et al. 2021; Deibert et al. 2021; Casasayas-Barris et al. 2021; Kesseli et al. 2022), and KELT-20b/MASCARA-2b (Casasayas-Barris et al. 2018, 2019; Stangret et al. 2020; Nugroho et al. 2020b; Hoeijmakers et al. 2020a; Rainer et al. 2021; Yan et al. 2022b; Borsa et al. 2022). Also, the spectral signatures of an increasing number of molecular species such as CO, HCN, H_2O, OH, SiO, or TiO have been identified in UHJ atmospheres (e.g., Nugroho et al. 2021; Cont et al. 2021; Landman et al. 2021; Fu et al. 2022; Prinoth et al. 2022; Sánchez-López et al. 2022; Yan et al. 2022a; van Sluijs et al. 2022; Lothringer et al. 2022). Detecting the spectral lines of different species not only allows for the characterization of atmospheric chemistry, but also provides the opportunity to constrain additional properties of

UHJs. For example, strong day-to-night winds (e.g., Louden & Wheatley 2015; Brogi et al. 2016; Alonso-Floriano et al. 2019), atmospheric mass loss (e.g., Yan & Henning 2018; Wyttenbach et al. 2020), or rain-out from the gas phase on the planetary nightside (Ehrenreich et al. 2020) have been identified. Moreover, the composition of exoplanet atmospheres can provide insights into the planetary formation and migration history, especially if the concentrations of the most important carbon- and oxygen-bearing species are well determined (Mordasini et al. 2016; Madhusudhan 2019).

Ultra-hot Jupiters are prime targets for atmospheric characterization by observing their thermal emission signal, given the elevated dayside temperatures of these objects. Various techniques have been used to study the emission signals from UHJ atmospheres, such as space-based photometric light curves (e.g., Zhang et al. 2018; von Essen et al. 2020; Deline et al. 2022), low-spectral-resolution observations (e.g., Arcangeli et al. 2018; Changeat & Edwards 2021), and ground-based high-resolution spectroscopy. In particular, emission spectroscopy has proven to be a powerful tool for identifying thermal inversions in the atmospheres of UHJs (e.g., Haynes et al. 2015; Nugroho et al. 2017; Kreidberg et al. 2018; Yan et al. 2020; Kasper et al. 2021). In these atmospheres, strong absorption of visible and ultraviolet radiation from the host star causes the temperature to increase with altitude. The presence of TiO and VO was initially proposed to cause this heating mechanism in upper planetary atmospheres (Hubeny et al. 2003; Fortney et al. 2008). However, theoretical work and more recent observations at high spectral resolution suggest that atomic metal species may also be fundamental for maintaining thermal inversion layers (e.g., Arcangeli et al. 2018; Lothringer et al. 2018). Neutral Fe is the species most commonly detected in thermal inversion layers, and is therefore thought to play an important role in the temperature structure of UHJ atmospheres (Pino et al. 2020; Nugroho et al. 2020a; Yan et al. 2020, 2021; Kasper et al. 2021; Cont et al. 2021; Herman et al. 2022).

Another significant result of UHJ high-spectral-resolution observations is the frequent nondetection of Ti, V, and their oxides, although their signature should be present in the planetary spectra when assuming equilibrium chemistry (e.g., Merritt et al. 2020; Hoeijmakers et al. 2020b; Tabernero et al. 2021; Yan et al. 2022b). This result suggests that depletion mechanisms may limit the presence of these species in the upper atmospheres of UHJs. Theoretical work has explored different mechanisms that may remove Ti- and V-bearing species from the atmospheres of hot giant exoplanets. For example, Spiegel et al. (2009) proposed the depletion of Ti and V in the upper part of planetary atmospheres via gravitational settling of TiO and VO. Cold trapping of Ti- and V-bearing molecules on the planetary nightsides has been suggested as another possible depletion scenario (Parmentier et al. 2013). However, these theoretical studies are mostly limited to the temperature range below that of UHJs. Further theoretical and observational work is therefore needed to better understand the circumstances under which Ti- and V-bearing species are depleted in UHJ atmospheres and how this impacts the planetary energy balance.

Several UHJs have been characterized using high-resolution Doppler spectroscopy. This technique uses the Doppler-shift of a planet's orbital motion relative to the telluric and stellar lines to

Table 4.1.: Parameters of the WASP-33 system.

Parameter	Symbol (Unit)	Value
Planet		
Radius [(a)]	R_p (R_J)	$1.679^{+0.019}_{-0.030}$
Orbital period [(b)]	P_orb (d)	1.219870897
Transit epoch (BJD) [(b)]	T_0 (d)	2 454 163.22449
Systemic velocity [(c)]	v_sys (km s^{-1})	-3.0 ± 0.4
RV semi-amplitude [(a)]	K_p (km s^{-1})	231 ± 3
Ingress duration [(d)]	T_ingress (h)	0.298 ± 0.005
Transit duration [(d)]	T_transit (h)	2.743 ± 0.005
Surface gravity [(d)]	$\log g$ (cgs)	3.46
Star		
Radius [(a)]	R_* ($R_\odot$)	$1.509^{+0.016}_{-0.027}$
Effective temperature [(e)]	T_eff (K)	7430 ± 100
Rotational velocity [(f)]	$v_\mathrm{rot} \sin i_*$ (km s^{-1})	$86.63^{+0.37}_{-0.32}$

References. [(a)] Lehmann et al. (2015) with parameters from Kovács et al. (2013), [(b)] Maciejewski et al. (2018), [(c)] Nugroho et al. (2017), [(d)] Kovács et al. (2013), [(e)] Collier Cameron et al. (2010), [(f)] Johnson et al. (2015) - other studies (e.g., Collier Cameron et al. 2010) report larger uncertainties; hence, we have also performed our calculations with a $v_\mathrm{rot} \sin i_*$ that deviates by ± 10 km s^{-1}, but could not find any significant differences in the results.

identify its spectral signature (e.g., Snellen et al. 2010; Brogi et al. 2012). However, constraining the atmospheric parameters from the observed spectra remains a difficult task. For example, the elemental abundances and ratios or the atmospheric temperature structure cannot be accurately determined using high-resolution Doppler spectroscopy alone. To overcome this difficulty, atmospheric retrieval frameworks have been developed to fit high-resolution spectroscopy observations with parameterized model spectra. These retrievals result in statistical estimates of the physical parameters in the exoplanet atmosphere. Most of these retrievals rely on a likelihood function that compares the observed data to a forward model. A Bayesian estimator is then used to optimize the forward model parameters (e.g., Brogi et al. 2017; Brogi & Line 2019; Yan et al. 2020; Gibson et al. 2020). The use of alternative techniques for retrievals, such as supervised machine learning, has also been explored recently (Fisher et al. 2020).

In this study, we investigate the dayside emission spectrum of the UHJ WASP-33b. We report the first detection of atomic Ti and V via emission spectroscopy. Also, we present the physical parameters of the planetary atmosphere obtained from a Bayesian retrieval. WASP-33b orbits an A5-type star undergoing δ Scuti pulsations. Its bright host star ($V \sim 8$ mag), high equilibrium temperature ($T_\mathrm{eq} \sim 2700$ K), and short orbital period ($P_\mathrm{orb} \sim 1.22$ d) make WASP-33b a prime target for emission spectroscopy. Different studies have shown that the planet possesses a temperature

inversion in its dayside hemisphere (e.g., Haynes et al. 2015; Nugroho et al. 2017; Cont et al. 2021). To date, the hydrogen Balmer lines, Si I, Ca II, Fe I, OH, CO, H_2O, and TiO have been identified via transmission or emission spectroscopy in the planetary atmosphere (Nugroho et al. 2017, 2020a, 2021; Yan et al. 2019, 2021; Cont et al. 2021, 2022b; Herman et al. 2022; van Sluijs et al. 2022). The WASP-33 system parameters used in this work are summarized in Table 4.1.

This work is organized as follows. We describe the observations and our data reduction routine in Sects. 4.3 and 4.4. The technique to search for individual species in the planetary atmosphere and the resulting detections are presented in Sect. 4.5. Our retrieval method and the inferred atmospheric parameters are described in Sect. 4.6. The conclusions of our work are given in Sect. 4.7.

4.3. Observations

The thermal phase curve of WASP-33b was observed at high spectral resolution over a total of eight visits. We observed the planetary emission spectrum on 15 November 2017 with CARMENES at the 3.5 m Calar Alto telescope (Quirrenbach et al. 2014, 2020). Both the visible (VIS) and near-infrared (NIR) wavelength channels of CARMENES were used. We consider the CARMENES channels independently as two different instruments. We also observed the spectrum of WASP-33b during the two nights of 15 October 2020 and 7 November 2020 with HARPS-N at the Telescopio Nazionale *Galileo* (Mayor et al. 2003; Cosentino et al. 2012). Another five observations were obtained between September 2013 and November 2014 by Herman et al. (2020) with ESPaDOnS at the Canada-France-Hawai'i telescope (Donati 2003). The combined set of nine observation datasets (two datasets from the CARMENES VIS and NIR observations, one dataset from each of the other seven observations) has already been used in previous studies to investigate the emission signature of TiO, Fe I, and Si I in the dayside atmosphere of WASP-33b (Herman et al. 2020, 2022; Cont et al. 2021, 2022b). Details of the observations and the main characteristics of the used spectrographs are summarized in Table 4.2.

Prior to the data reduction, we discarded a number of spectra due to poor data quality. All the discarded spectra belong to the CARMENES observation night on 15 November 2017. For seven spectra, the star was not aligned with the telescope fiber, and for three spectra the flux drastically dropped due to a passing cloud. Another seven spectra were removed due to the insufficient flux level in the NIR channel caused by the low elevation of the target towards the end of the observation night (airmass > 2). Consequently, we removed a total of 10 VIS channel spectra and 17 NIR channel spectra from the CARMENES observation. As no data quality issues were identified for the HARPS-N and ESPaDOnS observations, we included all spectra from the two instruments in the further analysis.

Table 4.2.: Observation log and instrument characteristics.

Instrument	Spectral resolution (R)	Wavelength range (Å)	Date	Phase coverage	Exposure time (s)	N_{spectra}
CARMENES	94 600 (VIS)	5200–9600	2017-11-15	0.29–0.65	300	95 [(a)]
	80 400 (NIR)	9600–17 100	2017-11-15	0.29–0.63	300	88 [(a)]
HARPS-N	115 000	3830–6900	2020-10-15	0.43–0.70	200	125
			2020-11-07	0.24–0.57	200	155
ESPaDOnS	68 000	3700–10 500	2013-09-15	0.30–0.44	90	110
			2013-09-26	0.37–0.44	90	55
			2014-09-04	0.56–0.69	90	110
			2014-09-15	0.55–0.68	90	110
			2014-11-05	0.31–0.38	90	55

Notes. [(a)] Total number of CARMENES spectra was 105; due to their poor quality ten spectra were removed from the time series of the VIS channel and 17 spectra were removed from the time series of the NIR channel.

4.4. Data reduction

4.4.1. Pre-processing the spectra

The extraction of the one-dimensional spectra from the raw frames was performed with the data reduction pipelines of the respective instruments. We extracted the order-by-order spectra of CARMENES using the instrument pipeline `caracal` v2.20 (Zechmeister et al. 2014; Caballero et al. 2016) and obtained the order-merged spectra of HARPS-N by running the `Data Reduction Software` (Cosentino et al. 2014). The order-by-order ESPaDOnS spectra were extracted by the observatory using the `Upena` pipeline, which relies on the data reduction package `Libre-ESpRIT` (Donati et al. 1997). Except for the echelle orders 45–43 in the CARMENES NIR channel, we included the entire wavelength range of all instruments in our analysis. The three excluded CARMENES NIR orders coincide with the telluric absorption band of water at 1.4 μm and therefore suffer from an insufficient flux level.

Each of the nine observation datasets was reduced separately. To normalize all the spectra to the same continuum level, we applied a polynomial fit to the individual spectra and divided them by the fit function. We used a second-order polynomial for the order-by-order spectra of CARMENES and ESPaDOnS and a seventh-order polynomial for the order-merged spectra of HARPS-N. Outliers were removed by applying a 5σ clip to the time evolution of each pixel. Wavelength bins with the absorption level larger than 80 % of the spectral continuum were masked. We also masked the strong sky emission lines, which are present in the CARMENES NIR channel.

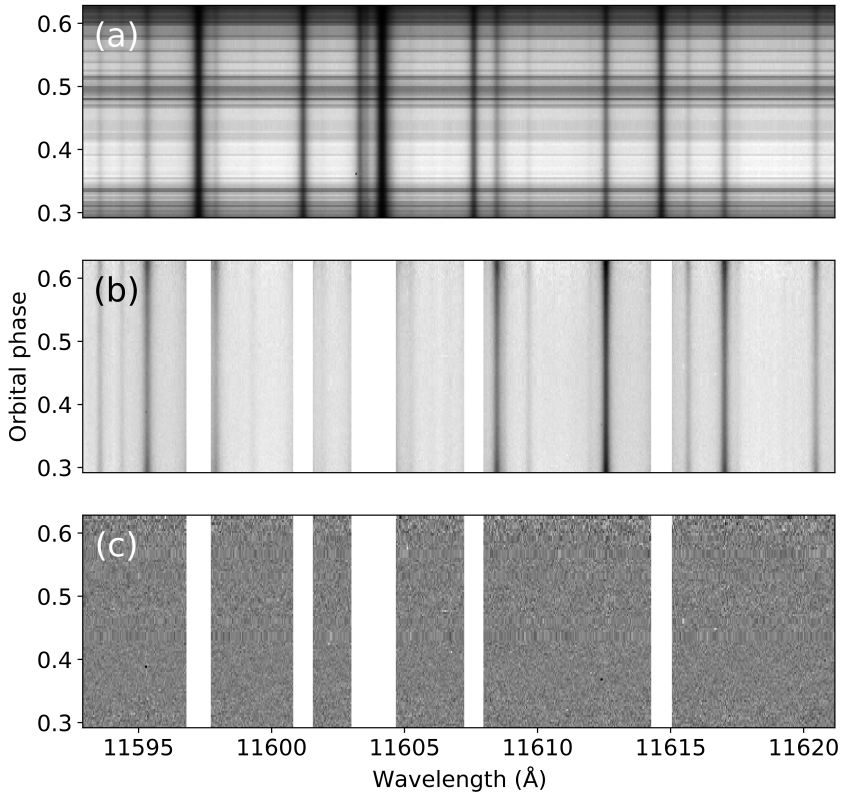

Figure 4.1.: Data reduction steps for a representative CARMENES NIR wavelength range. *Panel a*: unprocessed spectral matrix. *Panel b*: spectral matrix after normalization and outlier correction; we mask the strongest telluric lines in this step. *Panel c*: spectra reduced with `SYSREM` after telluric and stellar line removal.

4.4.2. Removal of telluric and stellar features

We applied the detrending algorithm `SYSREM` to the spectral matrix of each observation to correct for the contribution of telluric and stellar lines. The algorithm was originally proposed for the removal of systematic effects from large sets of photometric light curves (Tamuz et al. 2005). `SYSREM` models the common systematic features of the light curves by iteratively fitting their trends as a function of time. Subsequently, the modeled systematics are subtracted from the data. When applied to the search for exoplanets, each wavelength bin of the spectral matrix is considered as an independent light curve. This procedure results in the so-called residual spectral matrix, which is the spectral matrix after removal of the systematics.

The input data for `SYSREM` are the spectral matrix and its uncertainties. For the CARMENES and ESPaDOns data, we used the propagated uncertainties from the instrument pipelines. As the HARPS-N pipeline does not compute uncertainties, we estimated them according to the procedure described by Yan et al. (2020). This method consists of running `SYSREM` in a first step with five iterations and uniform uncertainty values. The resulting residual matrix is dominated by noise. We then calculated the average noise row by row and column by column. Finally, the uncertainty values of each data point are calculated as the mean of the respective row and column average noise.

We followed the approach from Gibson et al. (2020) and ran SYSREM in flux space instead of magnitude space (Tamuz et al. 2005). This method allows the relative strength of the planetary spectral lines to be preserved during the correction for the telluric and stellar contamination. First, we used the algorithm in the standard way to calculate a model of the systematic features. This model corresponds to the sum of the models from each SYSREM iteration. We then divided the model of the systematic features out of the original spectral matrix. Also, the uncertainties were divided by the model.

We ran the algorithm over ten consecutive iterations. This results in a residual spectral matrix for each iteration. For the CARMENES and ESPaDOnS observations, we created the order-merged residual spectral matrix by combining the order-by-order SYSREM reduced spectral matrices. This step was not necessary for the HARPS-N data, because the spectra were already provided by the instrument pipeline in an order-merged format. An overview of the data reduction including SYSREM is provided in Fig. 4.1.

4.5. Detection of the planetary emission lines

We used the cross-correlation technique (e.g., Snellen et al. 2010; Brogi et al. 2012; Sánchez-López et al. 2019; Prinoth et al. 2022) to extract the weak emission signature of WASP-33b from the noise-dominated residual spectra. This method combines numerous spectral lines and translates them into a single peak via calculating the cross-correlation function (CCF) between the residual spectra and model spectra as described below. We searched for the emission lines of the metal species Ti I, Ti II, V I, and V II. Also, we aimed to confirm the presence of the hydroxyl radical (OH), which was recently detected by Nugroho et al. (2021). Moreover, we reassessed the detections of Fe I and Si I in previous studies (Cont et al. 2021, 2022b) and investigated the presence of Fe II and Si II in the planetary atmosphere.

4.5.1. Model spectra

We modeled a planetary atmosphere with 61 layers equispaced in log pressure from 1 to 10^{-6} bar. As the atmospheric temperature profile of WASP-33b is not yet known in detail, we adopted the T-p profile of WASP-189b, which was measured by Yan et al. (2020) via the Fe I emission signature (Fig. 4.2). We believe that using the T-p profile of WASP-189b is a reasonable approximation because the planet has similar properties to WASP-33b. This temperature profile has also been used successfully in previous work to characterize the atmosphere of WASP-33b (Cont et al. 2021, 2022b). The T-p profile is parametrized by a low pressure point (T_1, p_1) and a high pressure point (T_2, p_2). An isothermal atmosphere is assumed at pressures below p_1 or higher than p_2. Between these two isothermal layers, we assumed a temperature that changes linearly as a function of log p. We used easyCHEM (Mollière et al. 2017) to calculate the mean molecular weight and the volume mixing ratios (VMRs) of the investigated chemical species (Fig. 4.2). For

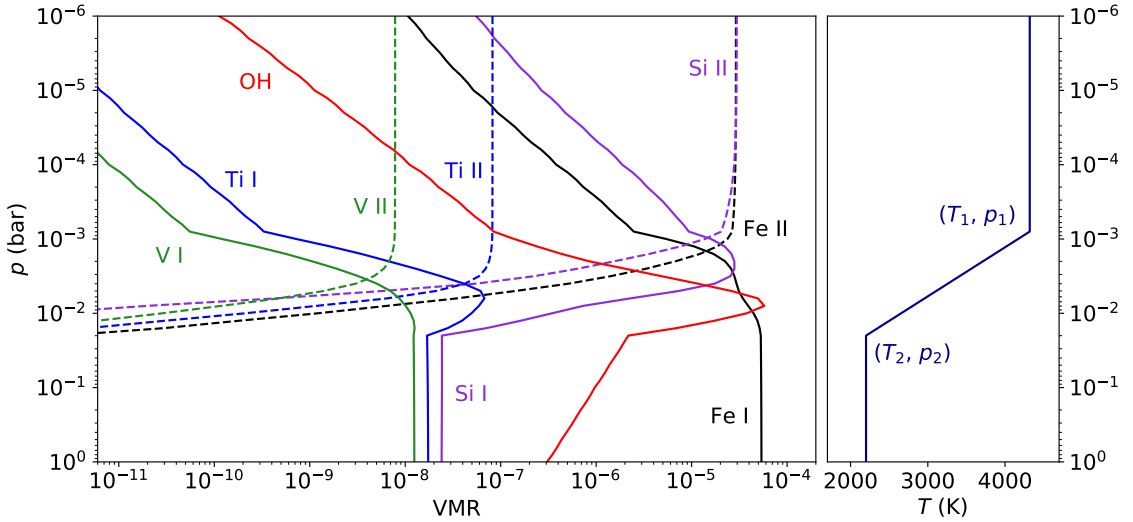

Figure 4.2.: Volume mixing ratios (VMRs; *left panel*) and T-p profile (*right panel*) used to generate the model spectra. We assumed equilibrium chemistry and solar elemental abundances for computing the VMRs. As the T-p pattern is not known in detail, we assumed the two-point profile that was retrieved for WASP-189b by Yan et al. (2020).

this purpose, we assumed equilibrium chemistry and a solar elemental abundance. An opacity grid of each species was computed for modeling the planetary spectra. The metal opacities were calculated from the Kurucz line list (Kurucz 2018) and the OH opacities were obtained from the `MoLLIST` line database (Brooke et al. 2016; Yousefi et al. 2018; Bernath 2020). Eventually, we ran the radiative transfer code `petitRADTRANS` (Mollière et al. 2019) to compute the model spectrum of each species.

As the reduced spectra were continuum normalized, a normalization of the model spectra was also required. First, we calculated the planet-to-star flux ratio of the model spectra by dividing with the blackbody spectrum of the host star. The result was then normalized to the planetary continuum. As a last step, we convolved each model spectrum with the instrument profiles, obtaining the final model spectra for cross-correlation. The normalized model spectra of all investigated species are illustrated in Figs. 4.3 and 4.4.

4.5.2. Cross-correlation method

The cross-correlation method was applied to each species independently. We Doppler-shifted the model spectrum from $-520\,\mathrm{km\,s^{-1}}$ to $+520\,\mathrm{km\,s^{-1}}$ with steps of $1\,\mathrm{km\,s^{-1}}$. Each order-merged residual spectrum was multiplied with the shifted model spectrum and weighted by the uncertainties. This resulted in the weighted CCF, defined as

$$\mathrm{CCF} = \sum r_i m_i(v). \tag{4.1}$$

The data points of the residual spectra weighted by the inverse of the squared uncertainties are denoted by r_i, and m_i is the model spectrum as a function of the Doppler-shift velocity v. By

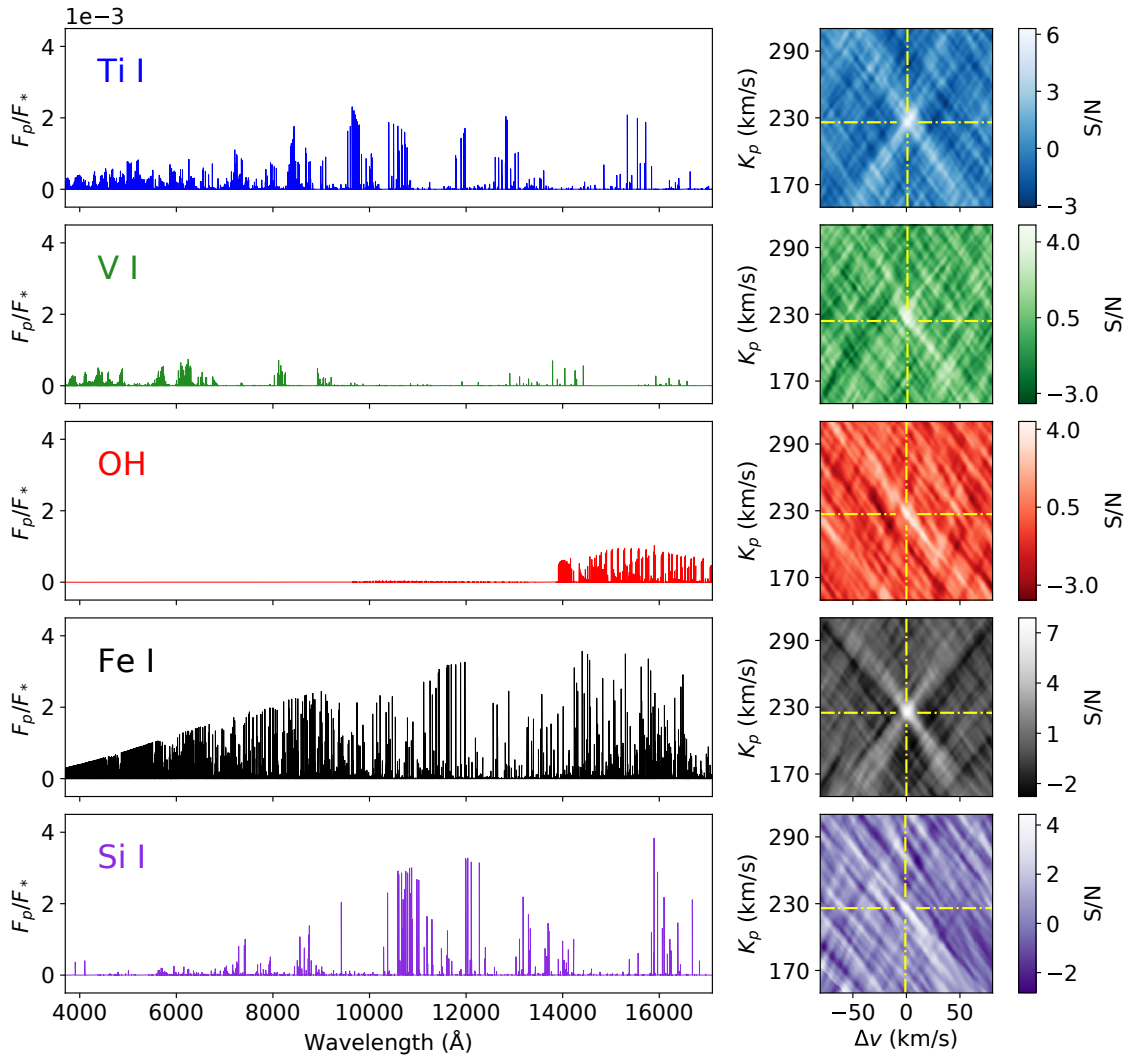

Figure 4.3.: Model spectra and S/N maps of the neutral chemical species investigated. *Left panels*: normalized model spectra of the detected species. The presented interval 3700–17 100 Å corresponds to the combined wavelength coverage of the instruments used. *Right panels*: S/N maps of the neutral species that we searched for. For each species, the S/N map corresponds to the specific `SYSREM` iteration that maximizes the detection. The detection peaks are indicated by the yellow dash-dotted lines.

combining the CCFs from the different datasets in a two-dimensional array, we obtained the final CCF map. In this step, we included the CCFs of those instruments that cover the wavelength ranges with significant emission features of the species in consideration. In contrast, we did not include the data of the instruments for which the model spectra predicted insignificant spectral features. The instruments and wavelength ranges included in the analysis and the corresponding chemical species are listed in Table 4.3.

WASP-33 is a δ Scuti variable star, showing time-dependent luminosity variations and a variable stellar line profile (Herrero et al. 2011). Given that `SYSREM` corrects only efficiently for stationary features, the variable stellar lines are not entirely removed by the algorithm from the observed spectra. The presence of residual stellar lines of the same species as the one under investigation can lead to artifacts in the CCF map. In this case, the affected radial velocity (RV) range in the

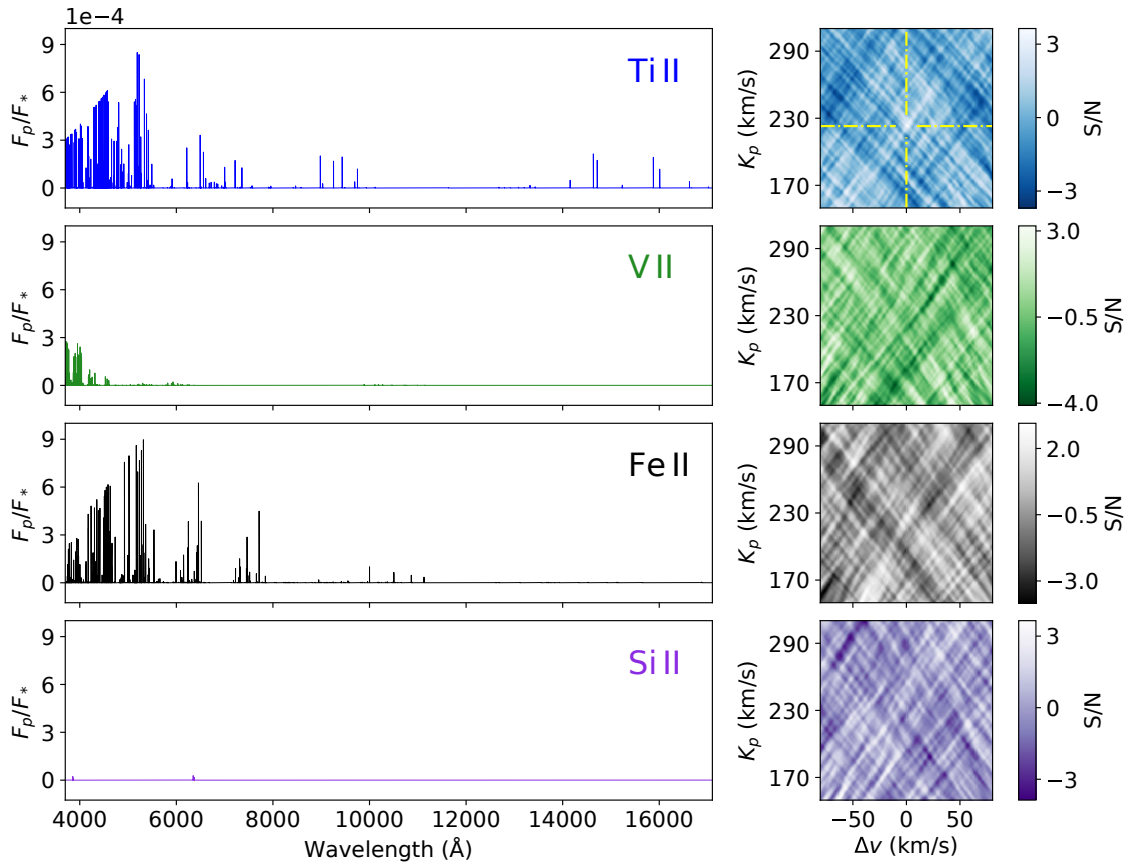

Figure 4.4.: Same as Fig. 4.3, but for the investigated ionic species. Only for Ti II a tentative detection peak that agrees with the planetary orbital motion is obtained. For V II, Fe II, and Si II, which are not detected at any SYSREM iteration, the S/N maps are the result of five consecutive iterations.

CCF map depends on the stellar rotation velocity and lies between $\pm v_{\rm rot} \sin i_*$ in the stellar rest frame (i.e., $\pm 87\,{\rm km\,s^{-1}}$ for WASP-33). We find these artifacts to be present in the CCF maps of Ti II, V II, Fe I, Fe II, Si I, and Si II, and therefore masked the affected RV range in the CCF maps of these species. For Ti I, V I, and OH, we find no residual stellar lines present because there are no artifacts in their CCF maps, nor is a substantial change in the detections of these species with or without masking achieved. No masking is therefore applied to the CCF maps of these three species. In Fig. 4.5 we show two example CCF maps, one with artifacts, the other without.

We assumed a circular orbit for shifting the CCF map of each species to the planetary rest frame. For this purpose, the CCFs were Doppler-shifted with a planetary RV of

$$v_{\rm p} = v_{\rm sys} + v_{\rm bary} + K_{\rm p} \sin 2\pi\phi + \Delta v, \tag{4.2}$$

with $K_{\rm p}$ the orbital velocity semi-amplitude, $v_{\rm sys}$ the velocity of the WASP-33 system, $v_{\rm bary}$ the barycentric correction, Δv the velocity deviation from the planetary rest frame, and ϕ the orbital phase. We repeated the alignment over a range of different $K_{\rm p}$ values. For each alignment, the CCF map was collapsed into a one-dimensional CCF by calculating the mean value over all out-of-eclipse CCFs. The one-dimensional CCFs were then combined in a two-dimensional array. This

Table 4.3.: Summary of cross-correlation results.

Species	S/N	K_p (km s^{-1})	Δv (km s^{-1})	SYSREM iteration	Instruments included	Wavelength range (Å)
Ti I	6.3	$226.0^{+7.5}_{-3.5}$	1^{+5}_{-3}	3	CV, CN, H, E	3700–17 100
V I	4.8	$224.0^{+9.0}_{-3.0}$	1^{+2}_{-5}	3	CV, H, E	3700–9600
OH	4.4	$227.0^{+6.0}_{-23.0}$	0^{+18}_{-4}	3	CN	9600–17 100
Fe I	7.9	$225.0^{+3.5}_{-3.0}$	0^{+3}_{-2}	10	CV, CN, H, E	3700–17 100
Si I	4.4	$226.0^{+5.0}_{-17.5}$	-1^{+14}_{-10}	4	CN	9600–17 100
Ti II	3.6	$223.0^{+5.5}_{-2.5}$	0^{+4}_{-2}	1	H	3830–6900
V II	No detection				H, E	3700–10 500
Fe II	No detection				H, E	3700–10 500
Si II	No detection				H, E	3700–10 500
Combined	8.5	$225.0^{+3.0}_{-2.5}$	0^{+3}_{-2}	9	CV, CN, H, E	3700–17 100

Notes. For each species, only those instruments predicted to have prominent emission lines in their wavelength range were included. We use the following abbreviations: CARMENES VIS (CV), CARMENES NIR (CN), HARPS-N (H), and ESPaDOnS (E).

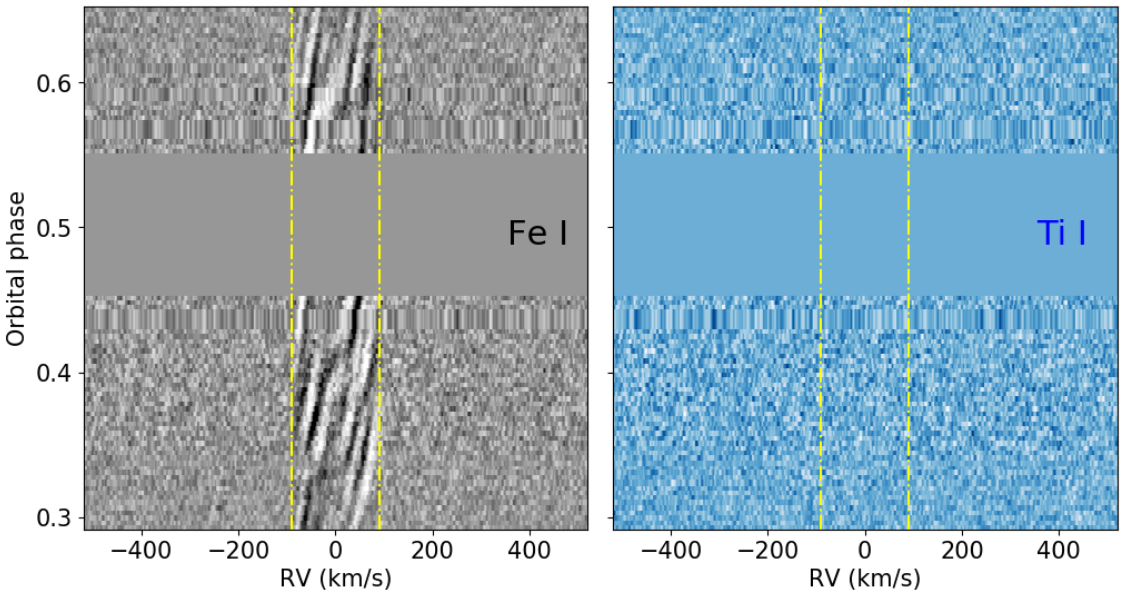

Figure 4.5.: Example CCF maps from CARMENES VIS data. The RV region between $\pm v_{\rm rot} \sin i_*$ is indicated by the yellow dash-dotted lines. In the *left panel* this region is dominated by artifacts from residual stellar Fe I lines. Stellar artifacts are absent in the CCF map of Ti I in the *right panel*. The in-eclipse CCFs are masked in both panels.

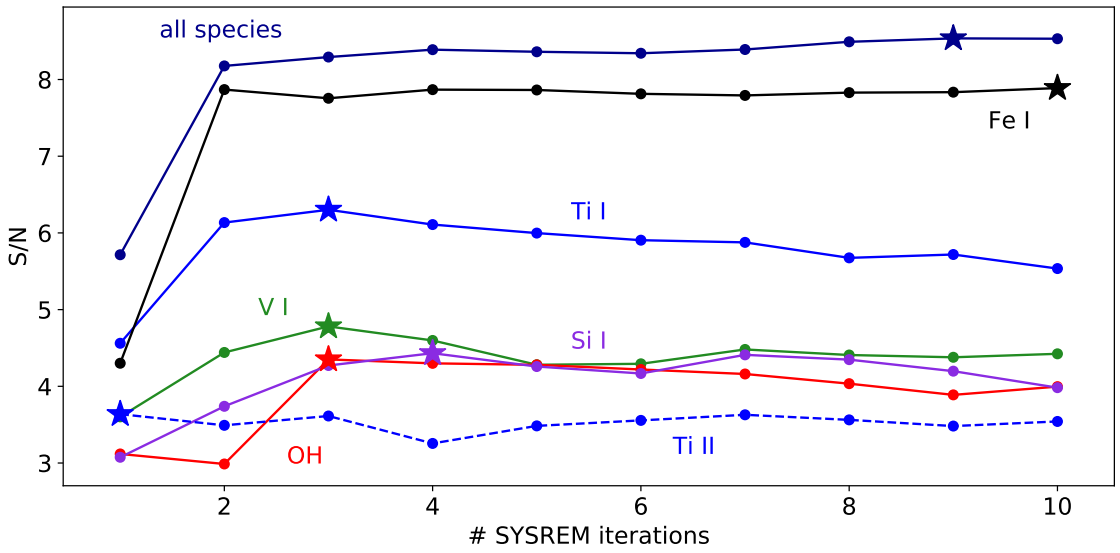

Figure 4.6.: S/N detection strength as a function of SYSREM iteration. We show the pattern for Ti I, V I, OH, Fe I, Si I, the tentatively detected signature of Ti II, and the spectral feature of all species together. The iteration with the most significant S/N peak is indicated by the star symbol.

array was normalized by its standard deviation under exclusion of the region around the strongest signal peak. In this way, we obtained a signal-to-noise map (S/N map) of the investigated chemical species. If the spectral signature is present in the data, the S/N map shows a significant peak at the location of the expected K_p and close to $\Delta v = 0\,\mathrm{km\,s^{-1}}$.

4.5.3. Cross-correlation results and discussion

We find significant detections ($> 4\sigma$) of Ti I, V I, OH, Fe I, and Si I that correspond to the Doppler-velocity of WASP-33b's orbital motion. A clear peak is seen for all SYSREM iterations greater than one in the S/N maps at the location of the expected orbital parameters (Fig. 4.6). Figure 4.3 shows the S/N maps and the corresponding model spectra used for cross-correlation. We summarize the S/N of the detections and the measured orbital parameters in Table 4.3.

This is the first detection of Ti I and V I in the atmosphere of WASP-33b. Previously, these two species were detected exclusively in transmission, making this their first detection in an exoplanet atmosphere using emission spectroscopy (Ben-Yami et al. 2020; Stangret et al. 2022; Ishizuka et al. 2021; Gibson et al. 2022; Kesseli et al. 2022; Bello-Arufe et al. 2022; Prinoth et al. 2022). Moreover, our results confirm the recent report of OH in the dayside atmosphere of WASP-33b (Nugroho et al. 2021). The detections of Fe I and Si I are a re-evaluation of earlier work (Cont et al. 2021, 2022b) and are shown here for completeness. We note that the orbital parameters found for the individual species differ slightly, but within the one-sigma range. Detecting the emission signature from multiple species also unambiguously proves the existence of a temperature inversion layer in the planetary atmosphere, which is in agreement with the predictions from theoretical work (Hubeny et al. 2003; Fortney et al. 2008; Lothringer & Barman 2019).

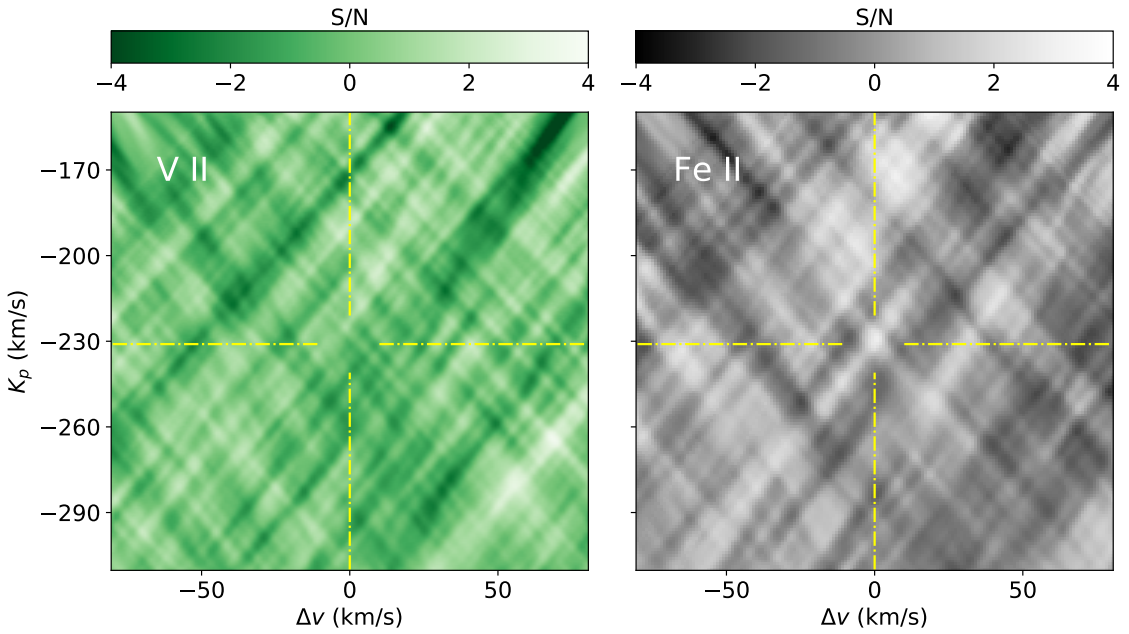

Figure 4.7.: S/N maps of injection-recovery tests for V II and Fe II. The position of the injected signal is indicated by the yellow dash-dotted lines. The injected V II signal cannot be detected, and that of Fe II causes a negligible peak in the S/N map. We conclude that the two species are not detectable even if they are present in the planetary atmosphere, given that the injected signals are poorly recovered.

Figure 4.4 illustrates the cross-correlation results for the ionic species Ti II, V II, Fe II, and Si II. Emission lines of Ti II, Fe II, and, to a lesser extent, V II are expected to be present near the blue end of the observed wavelength range. Only in the specific case of Ti II and when considering the data from HARPS-N alone do we find tentative evidence for emission lines consistent with the planetary rest frame. Given the strong detection of Ti I and the higher spectral resolution of HARPS-N in comparison to the other instruments used, we consider the tentative Ti II peak as a real signal. On the other hand, no significant detections of V II and Fe II are achieved. We ran an injection-recovery test to investigate the nondetections of the two species. To this end, we Doppler-shifted the convolved model spectra used to attempt the detection of V II and Fe II with the reversed K_p of WASP-33b (Merritt et al. 2020). Subsequently, we injected the shifted model spectra into the raw data and performed the pre-processing and cross-correlation analysis as described in Sects. 4.4 and 4.5.2. Doppler-shifting the injected signal with the reversed K_p value of –231 km s^{-1} prevents interference with potentially undetected V II and Fe II signals from the planetary atmosphere. No recovery could be achieved for V II, and the injected Fe II model spectrum resulted in a negligible peak in the S/N map. We show the results of the injection-recovery test in Fig. 4.7. Given the poor recovery of the injected V II and Fe II signals, we conclude that our nondetections of these species are likely due to the relatively small number of prominent emission lines rather than resulting from their absence in the planetary atmosphere. Our nondetection of the Si II signal was expected because the emission lines are very weak over the considered wavelength range. In summary, obtaining a cross-correlation signal of the metal ions studied is more challenging than detecting the corresponding neutral species because of the smaller number and strength of their emission lines, which are restricted to a relatively narrow wavelength range.

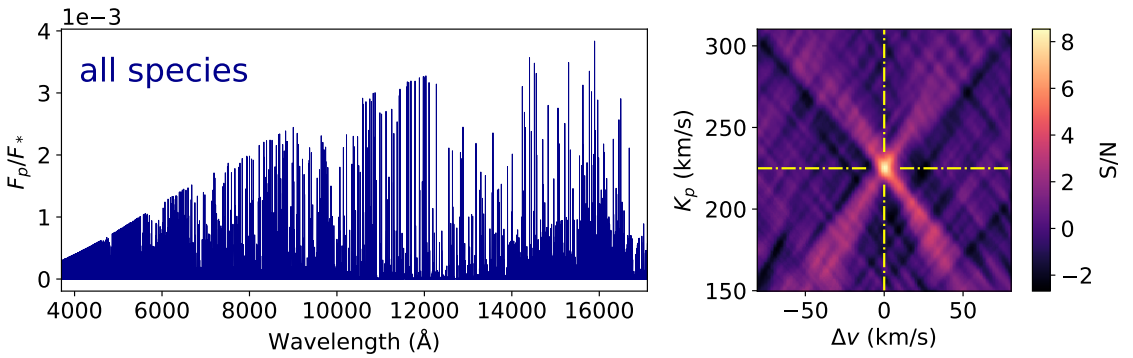

Figure 4.8.: Model spectrum and detected signature from combining the emission lines of all the detected chemical species. *Left panel*: normalized model spectrum that includes the spectral lines of Ti I, V I, OH, Fe I, Si I, and Ti II. *Right panel*: resulting S/N map. The detection peak coordinates are indicated by the yellow dash-dotted lines.

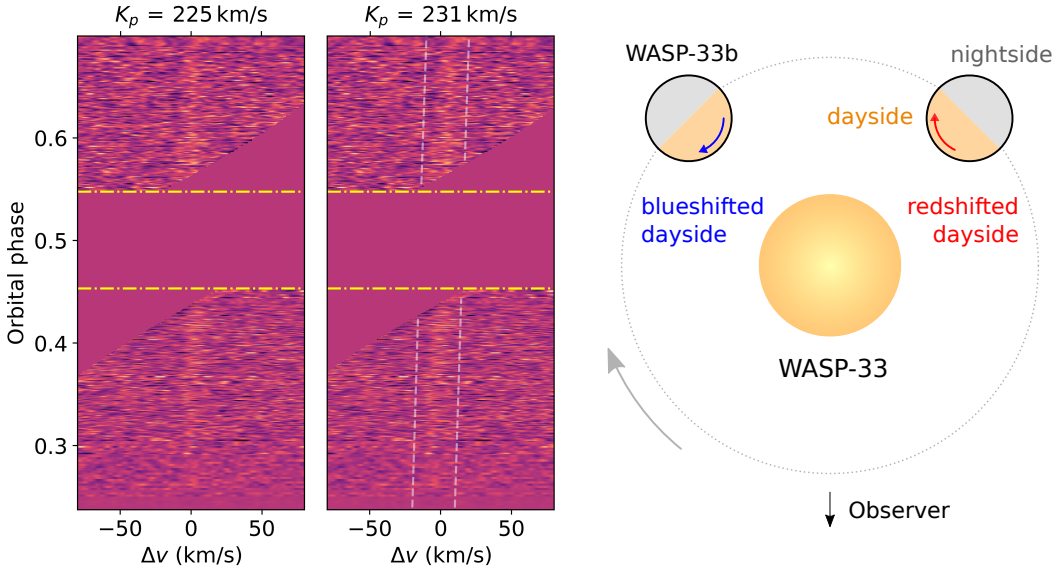

Figure 4.9.: CCF maps including all the detected chemical species and Doppler-shift induced by planetary rotation. The two CCF maps are aligned using the K_p values of 225 km s^{-1} (*left panel*; detected K_p) and 231 km s^{-1} (*middle panel*; expected K_p), respectively. When shifting the CCFs with the detected K_p, no offset from the planetary rest frame is found. The alignment with the expected K_p yields a blueshift before and a redshift after secondary eclipse, which is indicated by the white dashed lines. We indicate the secondary eclipse with the yellow dash-dotted lines. The masked regions in the CCF map outside eclipse correspond to the location of residual stellar lines. *Right panel*: WASP-33 system. The curved blue and red arrows indicate the planetary rotation direction, and the gray arrow indicates the orbital motion. Due to the planetary rotation, the signature from the planetary dayside experiences an additional blueshift before eclipse and redshift after eclipse.

Our results show that atomic Ti and V are not rained out, cold trapped, or otherwise depleted in the hot atmosphere of WASP-33b. Moreover, the detections of Ti I, V I, and the tentative signal of Ti II are consistent with the identification of these species in the atmospheres of a number of other strongly irradiated exoplanets (e.g., Hoeijmakers et al. 2018; Stangret et al. 2022; Prinoth et al. 2022; Bello-Arufe et al. 2022; Kesseli et al. 2022). We therefore conclude that the presence of significant Ti and V concentrations is favored at elevated temperatures. Because emission spectroscopy preferentially probes spectral lines emerging from the hot planetary dayside, we

propose this method to be particularly suitable for the search for refractory species such as Ti and V in exoplanet atmospheres. However, some observations suggest that the presence or absence of refractory species may not be determined by the atmospheric temperature alone. For example, Ti I was detected in the planetary atmosphere of HD 149026b (Ishizuka et al. 2021), the temperature of which is significantly below that of UHJs. On the other hand, the signature of the same species was not identified in the very hot atmosphere of KELT-20b/MASCARA-2b (Yan et al. 2022b). These observations suggests that physical parameters other than the temperature may also be important for the presence of Ti and V in the atmospheres of gas giant exoplanets.

We further applied the cross-correlation method to the datasets with a model spectrum that includes all the detected species (i.e., Ti I, V I, OH, Fe I, Si I, and Ti II). The S/N map and the model spectrum are shown in Fig. 4.8. We find that using the model spectrum of all the species together results in an overall detection strength of $S/N = 8.5$ after eight `SYSREM` iterations (Fig. 4.6). A comparison with the S/N values from the individual species in Table 4.3 shows that the spectral signature of Fe I is driving the detection. This is a reasonable finding, because the Fe I lines are expected to dominate the planetary emission spectrum over the entire wavelength range of our observations. The retrieved orbital parameters result in K_p and Δv values of $225.0^{+3.0}_{-2.5}$ km s^{-1} and 0^{+3}_{-2} km s^{-1}, respectively. Our K_p is slightly lower than the expected value of 231 ± 3 km s^{-1} (Kovács et al. 2013; Lehmann et al. 2015), but is consistent with the results of previous studies (Nugroho et al. 2020a; Cont et al. 2021, 2022b). The retrieved Δv value is consistent with the orbital motion of the planet. This indicates that the planet may not have a strong dayside to nightside wind at the altitudes probed by these emission lines, which would cause a deviation of the detection peak of the order of a few km s^{-1} from the planetary rest frame.

Figure 4.9 shows two versions of the CCF map, one aligned with the detected K_p of 225 km s^{-1}, the other with the expected value of 231 km s^{-1}. The emission signal aligned with the detected K_p value appears as a vertical trail with zero offset from the planetary rest frame. However, aligning the CCFs with the expected K_p results in a tilted trail that is blue- and redshifted by a few km s^{-1} before and after secondary eclipse, respectively. Assuming that the expected K_p reflects the true orbital velocity of the planet, we propose that these Doppler-shifts are caused by the fast rotation velocity of WASP-33b of ~ 7 km s^{-1} and the possible presence of super-rotation. In this scenario, the signature of the dayside atmosphere undergoes a spectral blueshift before eclipse and a redshift after eclipse (Fig. 4.9).

4.6. Retrieval of the atmospheric properties

We used the retrieval method developed by Yan et al. (2020) to constrain the properties of WASP-33b's atmosphere. This method has already been successfully used to determine the thermal structure in the atmosphere of two other UHJs, WASP-189b and KELT-20b/MASCARA-2b (Yan et al. 2020, 2022b; Borsa et al. 2022). In our implementation, we further developed this method for use with data from multiple instruments with different wavelength coverage.

Table 4.4.: Summary of instrument-specific results from cross-correlation.

Instrument	S/N	K_p (km s^{-1})	Δv (km s^{-1})	SYSREM iteration
CARMENES VIS	5.9	$227.0^{+5.0}_{-5.0}$	0^{+4}_{-3}	2
CARMENES NIR	6.4	$227.0^{+3.5}_{-18.0}$	-1^{+15}_{-3}	7
HARPS-N	6.7	$223.0^{+3.5}_{-3.0}$	1^{+2}_{-3}	3
ESPaDOnS	6.7	$225.0^{+5.5}_{-3.0}$	0^{+4}_{-2}	4

Notes. We used the spectral lines of all the detected chemical species (i.e., Ti I, V I, OH, Fe I, Si I, and Ti II).

4.6.1. Retrieval method

First, we calculated an individual master residual spectrum for each instrument. We used Eq. (4.2) to shift the residual spectra to the planetary rest frame. For aligning the spectra, we used the values of K_p and Δv measured for each instrument individually. The measurements were performed using the spectral model that consists of all the detected species. The corresponding S/N maps are reported in Fig. 4.10; the orbital parameters and SYSREM iterations used are summarized in Table 4.4. To obtain the master residual spectrum, we computed the average of the shifted residual spectra, weighted by the squared S/N of each exposure frame. As each spectrum corresponds to a different orbital phase value, the final result of our retrieval reflects the average atmospheric conditions over the observed phase interval. The master residual spectrum is still dominated by noise and contains the continuum normalized planet-to-star flux ratio.

In a second step, we defined the model spectrum for fitting with the master residual spectra from the four instruments. To this end, we used the radiative transfer code petitRADTRANS (Mollière et al. 2019). Our opacity grid covers a temperature range up to 25 000 K for all metal species. In the specific case of OH, the available partition function limited the opacity calculations to 5000 K. All OH opacities above this temperature were approximated with the 5000 K value. This limitation is caused by the fact that most of the OH molecules are thermally dissociated beyond this temperature. The planetary atmosphere was modeled with 25 layers equally spaced over a logarithmic scale between 1 and 10^{-8} bar. A two-point T-p parametrization, as described in Sect. 4.5.1, was used. We used the chemical equilibrium code easyCHEM (Mollière et al. 2017) to compute the VMRs as a function of the atmospheric elemental abundance, assuming that for all metals it varies with the overall metallicity. Moreover, we included the effect of spectral line broadening to account for the presence of atmospheric turbulence and bulk motion. To this end, we assumed a Gaussian as the line broadening function and set the standard deviation as $v_{\rm broad}$. We then convolved the model spectrum with the Gaussian function in velocity space to account for the line broadening. Following our description in Sect. 4.5.1, the model spectrum was further converted to the planet-to-star flux ratio and convolved with the instrument profile. The model spectrum was then interpolated to the wavelength solution of the master residual spectrum of each instrument.

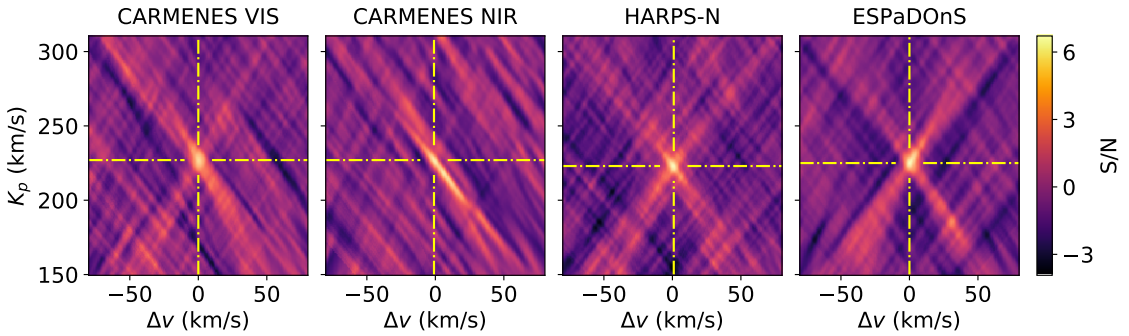

Figure 4.10.: Instrument-specific S/N maps including all the detected chemical species (i.e., Ti I, V I, OH, Fe I, Si I, and Ti II). The orbital parameters and the optimal number of `SYSREM` iterations from this analysis are used for aligning the spectra. The detection peaks are indicated by the yellow dash-dotted lines.

Finally, we fitted the spectral model to the master residual spectra. For each instrument, we used a standard Gaussian log likelihood function

$$\ln L = -\frac{1}{2}\sum_i \left[\frac{(R_i - m_i)^2}{(\beta\sigma_i)^2} + \ln 2\pi(\beta\sigma_i)^2\right], \tag{4.3}$$

with R_i the data points of the residual spectrum, σ_i their uncertainties, β a scaling term to correct for possible overestimation or underestimation of the uncertainties, and m_i the spectral model. We co-added the functions of the different instruments to get the combined log likelihood function of all the data. This results in an independent noise scaling factor for each instrument. For evaluating the combined likelihood function and estimating the fit parameters, we ran the Markov chain Monte Carlo (MCMC) method from the `emcee` software package (Foreman-Mackey et al. 2013). Our retrieval includes the following free parameters: the temperature profile T_1, p_1, T_2, p_2; a noise scaling parameter for each instrument $\beta_{\rm CV}$, $\beta_{\rm CN}$, $\beta_{\rm H}$, $\beta_{\rm E}$[1]; the overall metallicity [M/H]; the average broadening velocity $v_{\rm broad}$. For each free parameter, we used 24 walkers with 4000 steps in the sampling.

4.6.2. Retrieval results and discussion

4.6.2.1. Retrieval including all the detected species

We included the emission lines of all the detected chemical species from Sect. 4.5 into the retrieval (i.e., Ti I, V I, OH, Fe I, Si I, and Ti II). Only the spectra with a planetary Doppler-velocity outside the RV interval $\pm v_{\rm rot}\sin i_*$ were used. In this way, we can be sure that the residual stellar lines do not overlap with the planetary spectral signature. The excluded spectra correspond to $\sim 10\%$ of the cumulative exposure time. Table 4.5 summarizes the best-fit parameters resulting from the retrieval. The posterior distributions of the best-fit parameters are well constrained and are

[1] Each instrument has an independent noise scaling factor. We use the following abbreviations: CARMENES VIS (CV), CARMENES NIR (CN), HARPS-N (H), and ESPaDOnS (E).

shown in Fig. 4.14. Also, the retrieved noise scaling terms have values close to one, indicating an appropriate error estimation.

Figure 4.11 illustrates the retrieved T-p profile. A more exhaustive presentation is provided in Fig. 4.21. We find that the inversion layer extends over the pressure range $10^{-5.1}$ bar to $10^{-3.1}$ bar, with temperatures of 3981^{+213}_{-108} K and 3424^{+107}_{-111} K in the upper and lower planetary atmosphere, respectively. The thermal inversion layer is weaker when compared to the retrieval results of similar UHJs (Yan et al. 2020, 2022b). This implies that the emission lines of WASP-33b are relatively shallow. We investigated whether or not the presence of H^- opacity could explain the relatively low intensity of the emission lines, but found that the species has a negligible impact on our results (Fig. 4.12). To our knowledge, we performed the first retrieval of the thermal profile of WASP-33b's atmosphere using high-resolution spectroscopy. Similar work was recently carried out by van Sluijs et al. (2022), who maximized the S/N detection strengths of the CO emission lines to study the atmosphere of the same planet. We retrieve temperatures that are consistent with their results at low atmospheric pressures, but are able to get tighter constraints on the thermal profile at higher pressures.

The retrieval is mainly driven by the spectral signature of the neutral chemical species, which we assume are mostly ionized in the upper atmospheric layers due to the elevated temperatures. Nevertheless, we suggest that the emission lines of neutral species emerging from these layers are strong enough to allow the determination of the temperature T_1 at the upper limit of the thermal inversion. This suggestion is motivated by the fact that the posterior distribution of T_1 is well constrained in Fig. 4.14. In contrast, undetectable emission lines would cause a flat pattern toward higher temperatures in the posterior distribution, which is inconsistent with our results.

Our retrieval constrains the atmospheric metallicity to $[\mathrm{M/H}] = 1.49^{+0.82}_{-0.76}$ dex, which corresponds to a super-solar elemental abundance in the upper planetary atmosphere. This is in line with the results of van Sluijs et al. (2022), who obtain their strongest CO detection at abundances of ~ 1 dex in the atmosphere of WASP-33b. Moreover, our result is consistent with previous studies that measured atmospheric abundances greater than solar for a number of hot giant exoplanets (e.g., Madhusudhan et al. 2014b; Sedaghati et al. 2017; Nikolov et al. 2018). A correlation of the inferred [M/H] with the pressure parameters p_1 and p_2 can be recognized as diagonal distribution patterns in Fig. 4.14. This is consistent with the expected degeneracy between [M/H] and the atmospheric temperature profile. The VMRs of the investigated species are computed by assuming that the elemental abundances all vary with the same metallicity value. The reason for this approximation is that spectra with very high S/N would be needed to successfully determine the abundances of individual species, a task that may be addressed in future studies.

We point out that our forward model approximates the VMRs of the different species by assuming equilibrium chemistry. Fossati et al. (2021) on the other hand suggested that nonlocal thermodynamic equilibrium (NLTE) may play an important role in the upper atmospheres of UHJs. NLTE is expected to alter the population levels and thus the VMRs of different chemical species. For example, NLTE is predicted to strongly affect the population levels of Fe by lowering the VMR of

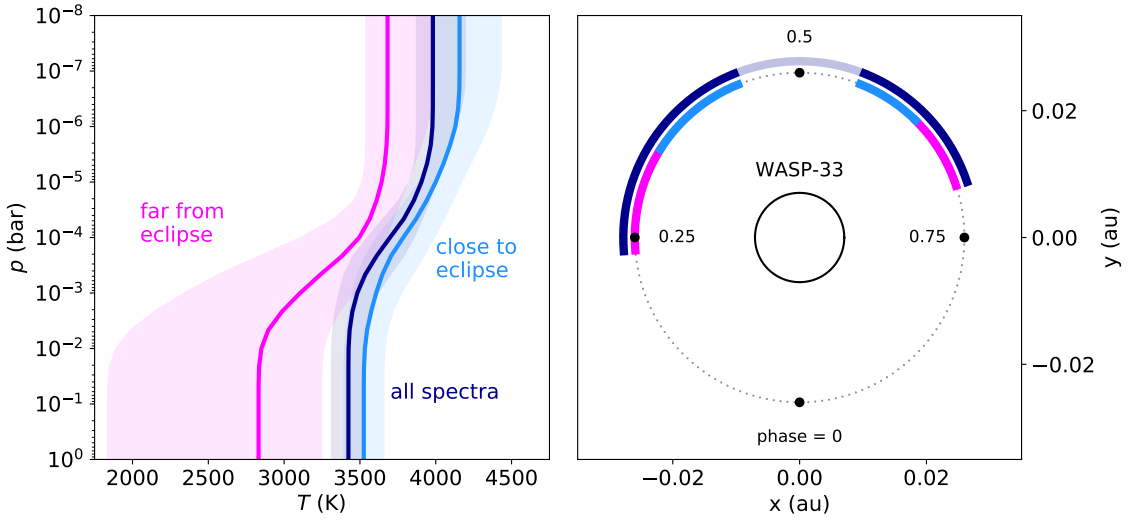

Figure 4.11.: Temperature curves from the retrievals including all the detected chemical species and orbital phase coverage. *Left panel*: median of the sampled temperature profiles with the 1σ interval. The dark blue line indicates the temperature profile computed using all the spectra outside the RV interval $\pm v_{\rm rot} \sin i_*$. We also measured the temperature profiles by running the retrieval on two subsets of the spectral time series. The T-p profile inferred from the spectra far from secondary eclipse is indicated in pink, while that inferred from the spectra close to eclipse is in light blue. *Right panel*: orbital phase intervals used to compute the different T-p profiles (orbital phases in the RV range $\pm v_{\rm rot} \sin i_*$ in transparent dark blue).

Fe I in favor of Fe II. The alteration of the population levels has important consequences for the amplitude of the planetary emission spectrum, the strength of atmospheric absorption of incoming stellar light, and therefore on the atmospheric T-p profile. Given the great importance of Fe in the thermal inversion layers of UHJ atmospheres, future consideration of NLTE effects will increase the reliability of atmospheric retrievals.

We find that the spectral emission lines are significantly broadened. The retrieved Gaussian broadening profile has a standard deviation of $v_{\rm broad} = 1.9 \pm 0.3\,{\rm km\,s^{-1}}$, corresponding to a full width at half maximum (FWHM) of $4.5 \pm 0.7\,{\rm km\,s^{-1}}$. The thermal and pressure broadening information is already included in the forward model via the opacities of the radiative transfer calculation. Therefore, $v_{\rm broad}$ is expected to account only for the broadening effects from atmospheric dynamics and the rotation of the planet. In particular, rotational broadening is supposed to affect the spectral line width, given the high rotational velocity of $\sim 7\,{\rm km\,s^{-1}}$ at WASP-33b's equator when assuming tidal locking. The line broadening from our retrieval is lower than that expected from a planetary sphere where the flux is emitted homogeneously over its entire surface, which would yield a FWHM of $\sim 9\,{\rm km\,s^{-1}}$. We calculated this rotational broadening value with the `PyAstronomy` software package (Czesla et al. 2019). The retrieved line broadening therefore suggests that most of the contribution to WASP-33b's emission spectrum may originate from the hottest region of the planetary atmosphere, which is located close to the substellar point.

We tested whether our method is capable of detecting the presence of spectral line broadening. To this end, we applied our retrieval method to synthetic data. We first took the model spectrum without additional broadening as shown in Fig. 4.8. We then broadened the spectrum with

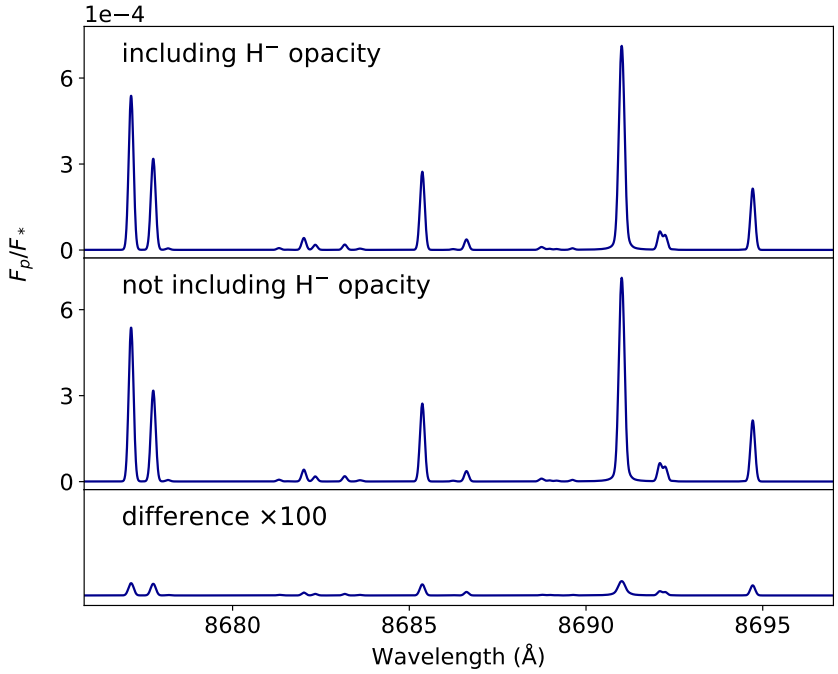

Figure 4.12.: Comparison between model spectra including (*top panel*) and not including (*middle panel*) H^- opacity. We used the emission lines of all the detected chemical species (i.e., Ti I, V I, OH, Fe I, Si I, and Ti II). The difference between the models is insignificant (*bottom panel*). Therefore, including H^- in the calculations would not affect our results significantly.

$v_{\rm broad} = 2\,{\rm km\,s^{-1}}$. Sequentially, we injected random white noise with different uncertainty levels to the model spectrum and performed the retrieval. We found that the correct broadening velocity can be retrieved even with the noise level of ten times the uncertainties of our observations (Fig. 4.15). We therefore conclude that the quality of the observational data used is good enough to allow an appropriate determination of the spectral line broadening with our retrieval method.

4.6.2.2. Phase resolved retrieval

The observer's line of sight aligns with different geographical longitudes of the planet as a function of the orbital phase. Consequently, different regions of the planetary atmosphere are expected to contribute to the observed signal during our observations. Performing the retrieval on subsets of the spectral time series that correspond to different orbital phase intervals will allow us to study the physical conditions at different longitudes in the planetary atmosphere.

To perform a phase resolved retrieval, we subdivided the spectral time series into two subsets for calculating the master residual spectra. One subset corresponds to the spectra close to the secondary eclipse when the dayside hemisphere faces the observer. The other subset consists of the spectra far from the secondary eclipse, and therefore contains the information from regions of both the planetary day- and nightsides. The orbital phase coverage of the two subsets is illustrated in Fig. 4.11. To avoid any interference with residual stellar lines, only the spectra at orbital phases outside the RV interval $\pm v_{\rm rot} \sin i_*$ were used.

Table 4.5.: Atmospheric retrieval results on WASP-33b.

Parameter	All spectra	Close to eclipse	Far from eclipse	Fe I	Ti I + Ti II	V I	Unit
T_1	3981^{+213}_{-108}	4157^{+274}_{-162}	3682^{+302}_{-142}	3985^{+167}_{-131}	4386^{+333}_{-278}	4985^{+714}_{-722}	K
$\log p_1$	$-5.12^{+0.93}_{-1.06}$	$-5.66^{+1.10}_{-0.93}$	$-4.54^{+1.03}_{-1.38}$	$-4.62^{+0.36}_{-0.69}$	$-6.41^{+0.69}_{-0.43}$	$-5.26^{+0.58}_{-0.82}$	log bar
T_2	3424^{+107}_{-111}	3525^{+131}_{-131}	2831^{+415}_{-997}	3459^{+205}_{-203}	3497^{+255}_{-315}	1949^{+972}_{-648}	K
$\log p_2$	$-3.08^{+0.67}_{-0.54}$	$-3.05^{+0.94}_{-0.63}$	$-2.71^{+0.67}_{-0.77}$	$-3.31^{+0.35}_{-0.33}$	$-2.93^{+0.35}_{-0.39}$	$-3.02^{+0.95}_{-0.51}$	log bar
[M/H]	$1.49^{+0.83}_{-0.76}$	$1.46^{+1.13}_{-1.01}$	$1.23^{+0.98}_{-0.81}$	1.49 (fixed)	1.49 (fixed)	1.49 (fixed)	dex
v_{broad}	1.9 ± 0.3	$2.1^{+0.3}_{-0.4}$	$1.7^{+0.5}_{-0.6}$	$2.4^{+0.3}_{-0.4}$	1.6 ± 0.8	$1.7^{+1.0}_{-0.9}$	$\mathrm{km\,s^{-1}}$
β_{CV}	0.841 ± 0.002	0.842 ± 0.002	0.842 ± 0.002	0.842 ± 0.002	0.842 ± 0.002	0.844 ± 0.002	...
β_{CN}	0.641 ± 0.002	0.639 ± 0.002	$0.639^{+0.002}_{-0.001}$	0.641 ± 0.002	0.641 ± 0.002	0.640 ± 0.002	...
β_{H}	0.795 ± 0.001	0.800 ± 0.001	0.789 ± 0.001	0.795 ± 0.001	0.795 ± 0.001	0.798 ± 0.001	...
β_{E}	1.122 ± 0.002	1.101 ± 0.002	1.155 ± 0.002	1.122 ± 0.002	1.122 ± 0.002	1.124 ± 0.002	...

Notes. In total, we ran six different retrievals. Three retrievals were performed with the spectral lines of all the detected species (i.e., Ti I, V I, OH, Fe I, Si I, and Ti II). We used (i) all the spectra, (ii) a subset of spectra at orbital phases close to the secondary eclipse, and (iii) a subset of spectra far from the secondary eclipse. Another three retrievals were performed by including all the spectra, but only with the emission lines of (iv) Fe I, (v) Ti I + Ti II combined, and (vi) V I, respectively. We conducted the retrievals by using uniform priors with the boundaries as follows. T_1 and T_2: 1000 to 6000 K; p_1 and p_2: 10^{-7} to 1 bar; [M/H]: –3 to 3 dex; v_{broad}: 0 to 10 $\mathrm{km\,s^{-1}}$; β_{CV}, β_{CN}, β_{H}, and β_{E}: 0 to 3.

The posterior distributions of the fit parameters are shown in Figs. 4.16 and 4.17. Figure 4.11 compares the T-p curves obtained from the two subsets with the thermal profile obtained from all the spectra. A more detailed overview on the T-p profiles is also shown in Fig. 4.21. Depending on the pressure level, the thermal profiles calculated from the two spectral subsets differ by about 300 K to 700 K, and the profile determined from all the spectra lies between the two. We find that the spectra close to the eclipse deliver a hotter temperature profile in comparison to those far from the eclipse. As the retrieved temperature profile corresponds to the average T-p curve of the visible hemisphere, this is consistent with the expectation of a temperature gradient away from the substellar point. Close to the secondary eclipse, mainly the dayside is facing the observer, leading to a hot average temperature profile. However, for spectra far from the secondary eclipse, the terminator region and a significant fraction of the cooler nightside are aligned with the observer's line of sight, resulting in lower atmospheric temperatures being measured.

The values of [M/H] and v_{broad} obtained for the two spectral subsets are consistent. We note a trend that spectra far from the secondary eclipse are less affected by line broadening than spectra near the eclipse. This is a reasonable result because far from the secondary eclipse, a significant fraction of the planetary disk that faces the observer is not illuminated by the host star. The nonilluminated planetary atmosphere is not expected to significantly contribute to the emission signal, decreasing the impact of the rotational line broadening. The dependence of the line broadening from the orbital phase can also be recognized when considering the CCF trail in Fig. 4.9, showing an increased width of the CCF toward the secondary eclipse. However, we note that the retrieved v_{broad} values should be compared with caution because of the relatively large uncertainties. All results of the phase resolved retrieval are listed in Table 4.5.

4.6.2.3. Retrieval of individual species

To compare the temperature profiles probed by individual chemical species, we ran retrievals for Ti, V, and Fe. These are the species with the most prominent detections in Sect. 4.5.3. Retrieving the T-p profile for the individual species also allows us to test the consistency of the results of our method. We set [M/H] to the previously determined value of 1.49 dex (cf. Sect. 4.6.2.1), because the metallicity was poorly constrained when leaving it as a free parameter. For the Ti retrieval, we included the opacities of both Ti I and Ti II. As we were not able to constrain the presence of V II and Fe II by cross-correlation, only V I and Fe I were included in the other two retrievals, respectively. We used the spectra with a planetary RV outside $\pm v_{\mathrm{rot}} \sin i_*$ for the retrievals including Ti II and Fe I, which are affected by residual stellar lines. For V I, we included all the out-of-eclipse spectra because we did not find any significant residuals of stellar V I lines. The posterior distributions of the fit parameters are shown in Figs. 4.18–4.20. Figure 4.13 compares the retrieved T-p profiles and a detailed overview is provided in Fig. 4.22. All results are summarized in Table 4.5.

For Fe I, the parameters are well constrained and almost perfectly match the results from the retrieval that uses all the species in Sect. 4.6.2.1. We attribute this similarity to the larger number

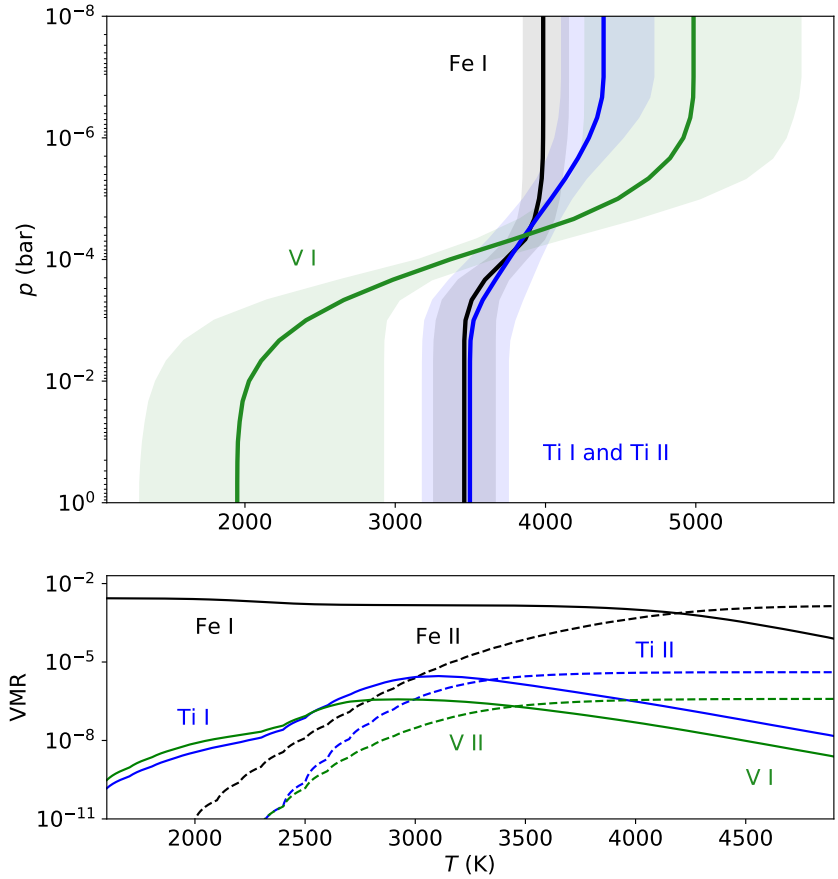

Figure 4.13.: T-p profiles retrieved with the lines from individual chemical species and VMRs as a function of temperature. *Top panel*: temperature profiles retrieved from the Ti I and Ti II, V I, and Fe I emission lines. We report the median of the sampled temperature profiles and the 1σ interval. *Bottom panel*: chemical equilibrium VMRs of Ti I, Ti II, V I, V II, Fe I, and Fe II as a function of temperature. We set [M/H] to the retrieved value of 1.49 dex; the pressure is set to 10^{-4} bar. Ti and V are expected to undergo stronger ionization than Fe.

of Fe I lines when compared to that of all the other species. This also suggests that the retrieval that includes all the species is mainly driven by the Fe I lines. Also, the T-p profile from Ti I and Ti II is in agreement with the retrieval result of all the species. The retrieval yielded a well constrained set of fit parameters, albeit at a somewhat lower precision than for Fe I. This is probably caused by the lower number and decreased strength of the Ti I and Ti II spectral lines in comparison to the Fe I emission signature. The fact that retrievals for independent species achieve consistent results demonstrates the reliability of our method and gives confidence to the calculated parameter values.

The posterior distributions of the V I retrieval provide a significantly poorer constraint of the atmospheric parameters. This results in extended uncertainties of the T-p profile in the lower and upper planetary atmosphere. In view of the relatively low detection significance and the scarce number of features in the V I model spectrum in Fig. 4.3, this agrees with our expectations. While the temperature profile inferred from V I is close to that derived from Ti I/Ti II and Fe I in the upper planetary atmosphere, we find a deviation at pressures higher than 10^{-3} bar. Apart from the large uncertainties, the interpretation of this difference is unfortunately difficult, because both physical

and method-dependent effects can cause the observed discrepancy. One possible scenario could be that the individual species are confined to different regions in the planetary atmosphere, and each has its own temperature profile. Figure 4.13 shows the chemical equilibrium VMRs of Ti I, Ti II, V I, V II, Fe I, and Fe II as a function of temperature. We consider a pressure level of 10^{-4} bar, which corresponds to the location of the thermal inversion layer. The VMRs of Ti I and Ti II show a similar pattern when compared to that of V I and V II, respectively. The colder temperatures probed by V I at higher pressure levels could therefore be explained by a lower abundance of the species than assumed by our method. In this case, the hottest region of the planetary atmosphere would be depleted by V I due to ionization and the hypothesized low abundance. Therefore, the V I signature would encode mainly the information from the coolest regions of the planetary dayside, leading to a more moderate T-p profile. The nominal abundance of Ti I and the inclusion of Ti II would instead allow information from the entire dayside atmosphere to be considered, resulting in a hotter T-p profile. Alternatively, the use of oversimplified modeling of the VMRs could prevent an accurate estimation of the temperature profile for individual species. If the equilibrium chemistry assumption is not met, this could result in a poorly constrained temperature curve due to the degeneracy between temperature and VMR. Also, an oversimplification of the T-p model used and the presence of horizontal variations of the temperature profile from the substellar point to the nightside could explain the discrepancy measured. Spectra with increased S/N, the inclusion of nonequilibrium chemistry, and the use of a more comprehensive T-p model will enable us to better understand the information encoded in the spectral signature of individual species.

4.7. Conclusions

We used observations from the high-resolution spectrographs CARMENES, HARPS-N, and ESPaDOnS to analyze the thermal emission spectrum of the UHJ WASP-33b. A joint analysis of the data from the three instruments allowed us to investigate the planetary emission spectrum over an extended wavelength range from the near-ultraviolet to the NIR (3700–17 100 Å). We applied the cross-correlation technique to extract the faint spectral signature of the planetary atmosphere from the observations. This analysis led to the first detection of the emission signature of Ti I and V I in an exoplanet atmosphere, as these two species had previously been detected exclusively by transmission spectroscopy. Also, we detected a tentative emission signal of Ti II. These detections are an important finding, given the frequently observed depletion of Ti- and V-bearing species in the atmospheres of UHJs. Moreover, we confirmed the presence of OH, Fe I, and Si I detected by previous studies. No significant signature from the ionic species V II, Fe II, or Si II could be found in our spectral time series. The identification of spectral emission lines unambiguously proves the presence of a thermal inversion layer in the dayside atmosphere of WASP-33b, which is in line with theoretical work on highly irradiated planetary atmospheres.

We conducted a retrieval for the atmospheric T-p profile, the elemental abundances, and the spectral line broadening. The retrieval was performed using the data from all three instruments to-

gether. For this purpose, we forward modeled the emission lines of all the detected species via the radiative transfer code `petitRADTRANS` and assumed equilibrium chemistry. Compared to other UHJs (e.g., WASP-189b, KELT-20b/MASCARA-2b), our retrieval results in a relatively weak thermal inversion that extends roughly from 3400 K to 4000 K at pressures near 10^{-3} bar and 10^{-5} bar. We determined super-solar elemental abundances around 1.5 dex in the upper planetary atmosphere and found a spectral line broadening with a Gaussian FWHM of about 4.5 km s^{-1}. By running the retrieval on two distinct subsets of the spectral time series, we obtained temperature profiles that differ by 300 K to 700 K. This confirms the expectation that the temperature is higher on the planetary dayside than on the nightside. We also performed the retrieval for different chemical species individually. The temperature profiles from Ti I/Ti II and Fe I are in good agreement with the overall result from all the species. However, the T-p profile of the V I signature slightly deviates from that of the other species. We suggest that a V I-depleted planetary atmosphere could explain the measured discrepancy between the T-p profiles.

Our work shows that high-resolution emission spectroscopy offers the possibility to study the physical conditions in UHJ atmospheres in great detail. Further progress on atmospheric retrievals will be achieved by deploying more sophisticated spectral forward models, increasing the number of species included, and expanding the orbital phase coverage of UHJ observations.

4.8. Appendix A) Posterior distributions

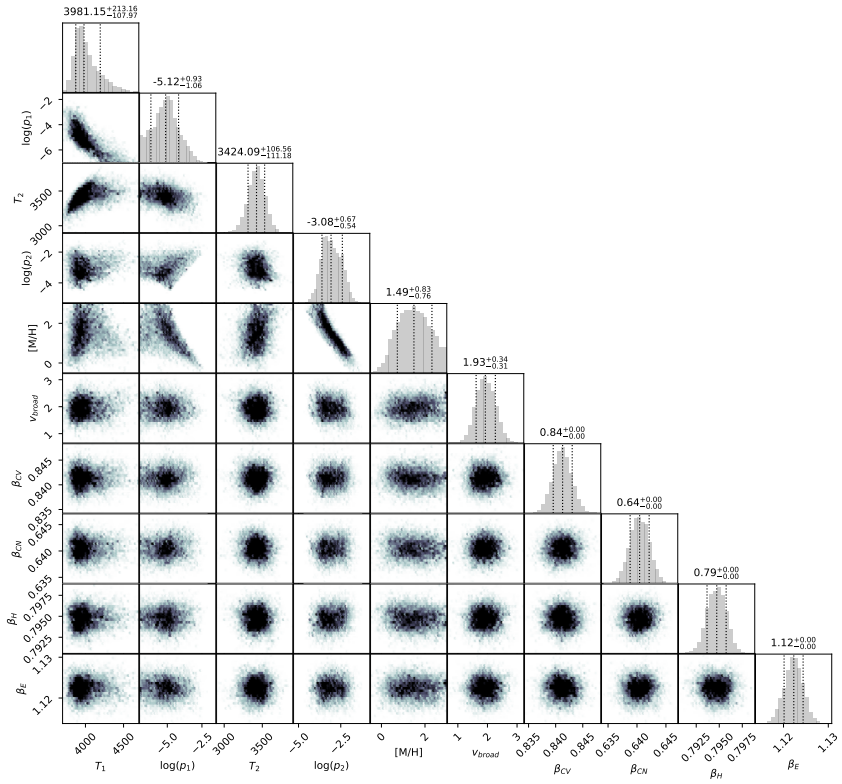

Figure 4.14.: Posterior distributions of the atmospheric parameters from our retrieval. We used the emission lines of all the detected species (i.e., Ti I, V I, OH, Fe I, Si I, and Ti II).

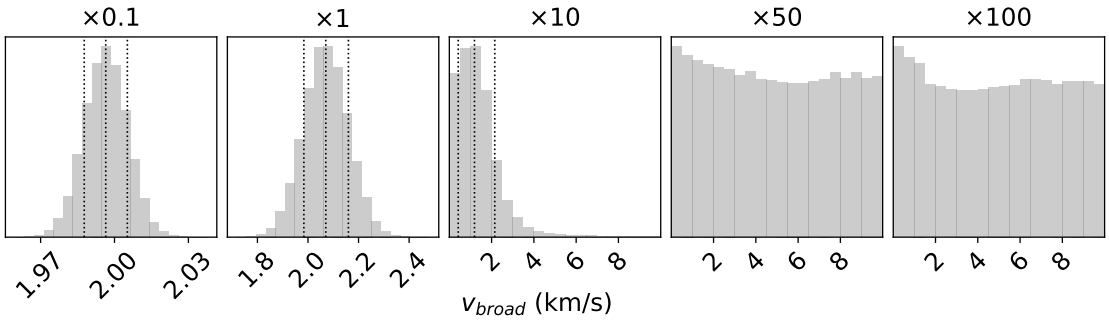

Figure 4.15.: Posterior distributions of $\upsilon_{\rm broad}$ from simulated data with different noise levels. The noise level corresponds to that of the observed spectra multiplied by the factor that is reported at the top of each panel. The simulated broadening of $2\,{\rm km\,s^{-1}}$ can be retrieved for noise levels up to ten times that of the simulated observation data. The median and 1σ percentiles of the distributions that retrieve the simulated line broadening are indicated by the dashed vertical lines.

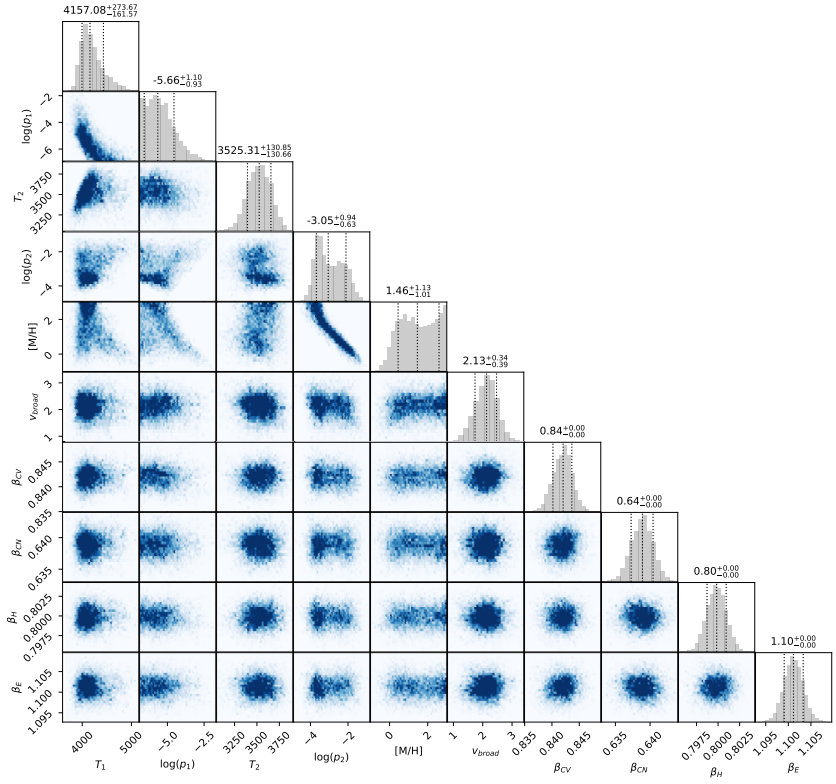

Figure 4.16.: Same as Fig. 4.14, but considering only the spectra close to the secondary eclipse.

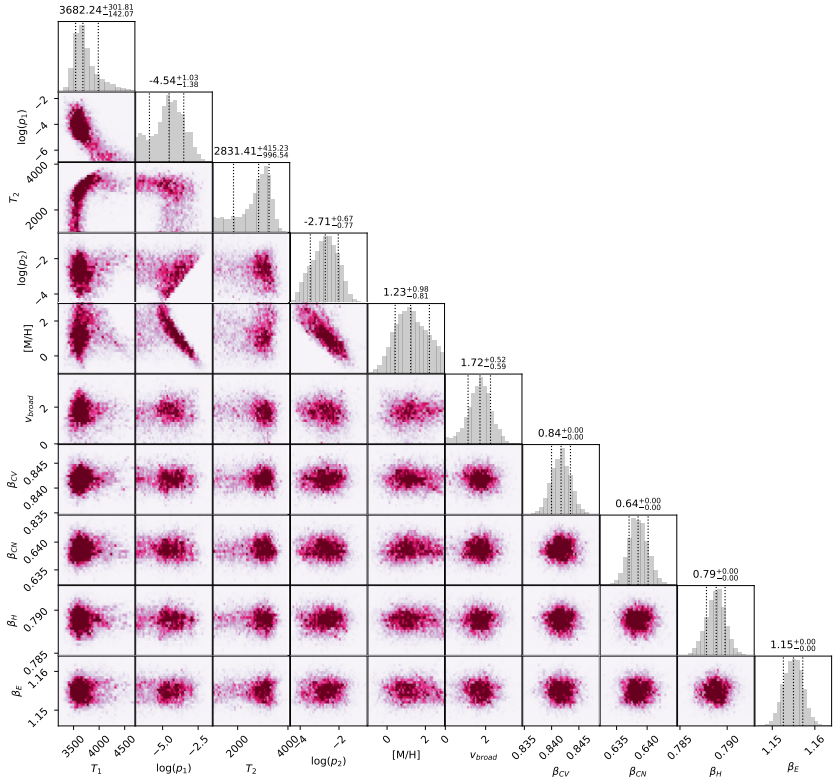

Figure 4.17.: Same as Fig. 4.14, but considering only the spectra far from the secondary eclipse.

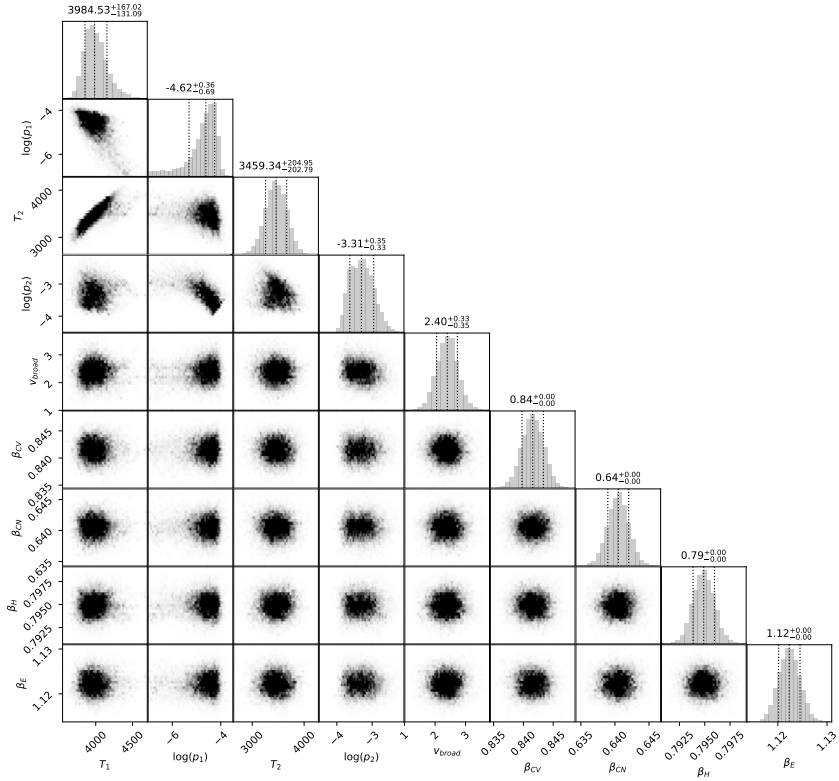

Figure 4.18.: Same as Fig. 4.14, but computed with the opacities from Fe I only. The metallicity was fixed to [M/H] = 1.49 dex.

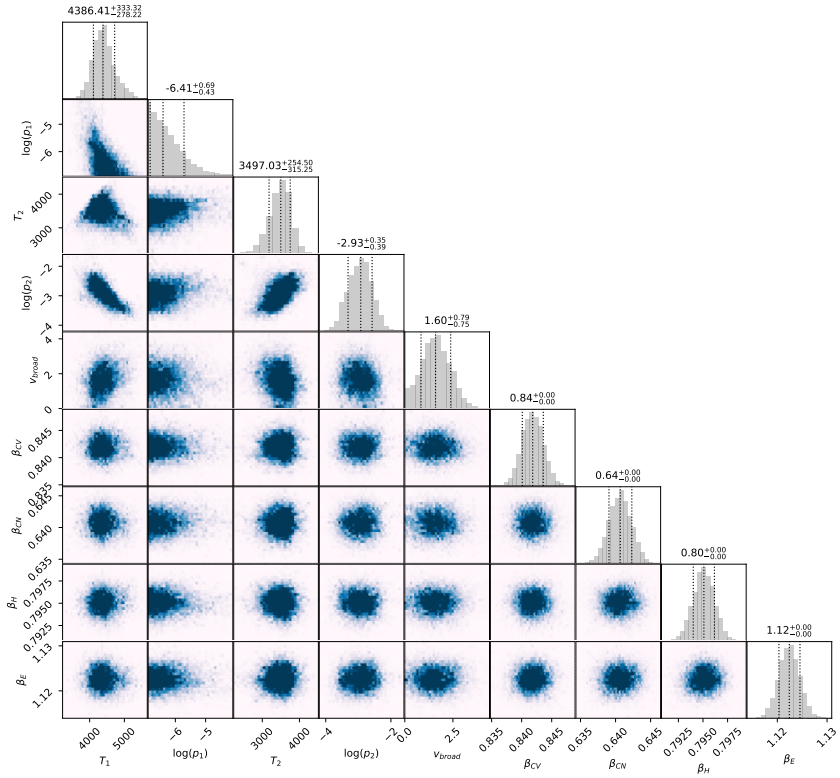

Figure 4.19.: Same as Fig. 4.14, but computed with the opacities from Ti I and Ti II only. The metallicity was fixed to [M/H] = 1.49 dex.

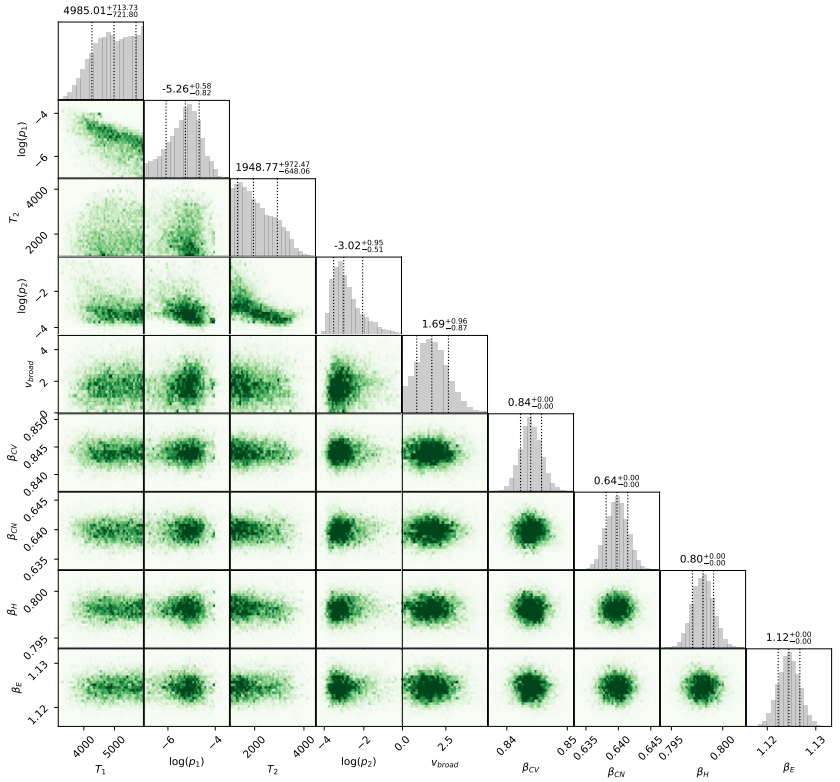

Figure 4.20.: Same as Fig. 4.14, but computed with the opacities from V I only. The metallicity was fixed to [M/H] = 1.49 dex.

4.9. Appendix B) Thermal profiles

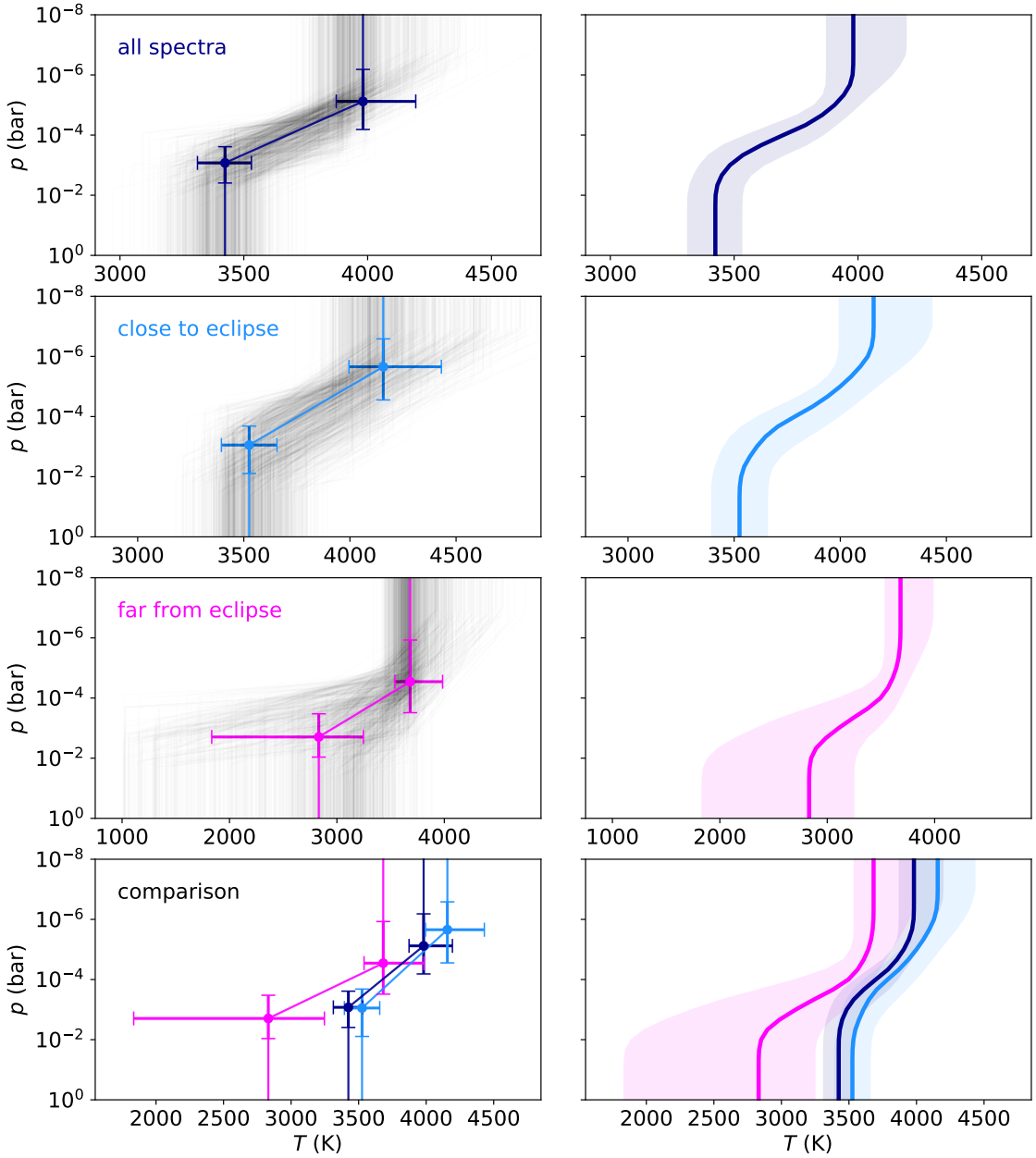

Figure 4.21.: Retrieved T-p profiles using the spectral lines of all the detected chemical species (i.e., Ti I, V I, OH, Fe I, Si I, and Ti II). The *left panels* show the retrieved two-point T-p profiles with the respective uncertainties. Examples of the T-p profiles that were sampled when running the MCMC method are indicated in gray. The *right panels* show the median of the sampled temperature profiles and the 1σ interval. The panels from top to bottom show the temperature profiles obtained using all the spectra, a subset of spectra close to the secondary eclipse, a subset of spectra far from the secondary eclipse, and a comparison of the three T-p curves.

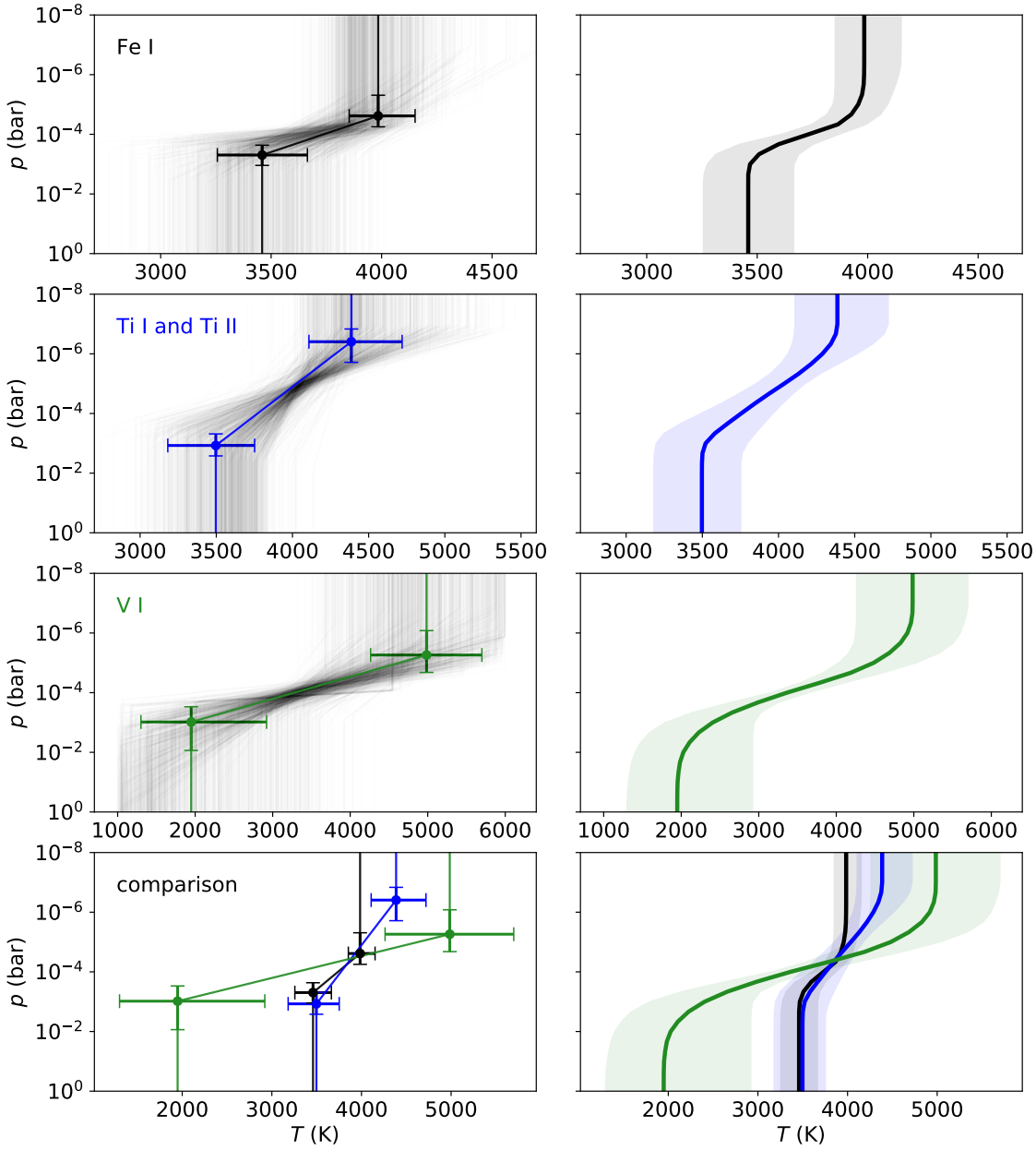

Figure 4.22.: Same as Fig. 4.21, but for individual chemical species. The panels from top to bottom show the temperature profiles obtained with the emission lines of Fe I, Ti I and Ti II, V I, and a comparison of the three T-p curves.

5. Conclusions

We used high-resolution Doppler spectroscopy to investigate the physical and chemical conditions in the atmospheres of the two UHJs WASP-33b and KELT-20b/MASCARA-2b. In this chapter, we summarize the main results and conclusions of our work and provide an outlook for future studies on strongly irradiated exoplanet atmospheres.

5.1. Summary

In this thesis, we present studies on the signature of different chemical species in the thermal emission spectra of exoplanets. The outcome of our studies enables us to draw conclusions about the physical and chemical conditions in their atmospheres. Most of the identified species are considered as strong absorbers of incoming stellar radiation that promote the formation of so-called temperature inversion layers in highly irradiated planetary atmospheres. These types of temperature profiles in which temperature increases with altitude have been predicted by theoretical work (e.g., Hubeny et al. 2003; Fortney et al. 2008; Lothringer et al. 2018; García Muñoz & Schneider 2019) and were recently observed in a number of UHJs (e.g., Pino et al. 2020; Yan et al. 2020; Kasper et al. 2021). In our studies, we employed a custom reduction pipeline based on the cross-correlation technique to extract the emission signature of the planetary atmosphere from our spectral observations. This technique maps the planetary emission lines onto a single peak, enabling the identification of the faint spectral signature from the planetary atmosphere. Moreover, we implemented a retrieval framework to fit the planetary spectral signature with parametrized model spectra.

In Chapter 2, we investigated the dayside emission spectrum of the UHJ WASP-33b using high-resolution spectra from CARMENES VIS and HARPS-N. The study led to the detection of Fe I, evidence for TiO, and proved the presence of a thermal inversion layer in the dayside atmosphere of the planet. The signals of Fe I and TiO were found to require distinct atmospheric temperature profiles and differ in their line broadening. Also, we found an offset in the measured Doppler-shift between the Fe I and TiO signals. A toy model was able to explain the observed differences between the signals of the two species when assuming the presence of a TiO-depleted hot spot and a super-rotating atmosphere. Hence, an important finding of this study is the indication of a three-dimensional chemical structure in the dayside atmosphere of WASP-33b.

In Chapter 3, we show a study of the high-resolution thermal emission spectra of the two UHJs WASP-33b and KELT-20b/MASCARA-2b in the NIR range with CARMENES. Applying the cross-correlation technique allowed detecting the signature of atmospheric Si I in the spectra of both planets, thereby leading to the first discovery of this species in exoplanet atmospheres. The detection of Si I is an important finding since Si plays a fundamental role for cloud formation in exoplanet atmospheres (Gao & Powell 2021).

Chapter 4 presents an in-depth analysis of the high-resolution emission spectrum of WASP-33b. We used observations from CARMENES VIS and NIR, HARPS-N, and ESPaDOnS, covering an extended wavelength range from the near-ultraviolet to the NIR. The study led to the first detection of the Ti I, Ti II, and V I signatures via emission spectroscopy. Detecting these species is a significant discovery as Ti- and V-bearing species have been found to be depleted in the atmospheres of several other UHJs (Merritt et al. 2020; Hoeijmakers et al. 2020b; Yan et al. 2022b). Our analysis further revealed the presence of OH, which is likely produced by H_2O photolysis in the strongly irradiated planetary atmosphere. Moreover, the prior detections of Fe I and Si I presented in Chapters 2 and 3 were confirmed. In our study, we ran a Bayesian retrieval for measuring the atmospheric temperature profile, the chemical abundances, and the spectral line broadening. The retrieval detected the presence of a thermal inversion layer and super-solar elemental abundances in the planetary atmosphere. In addition, we proved the presence of a significantly broadened line profile that is likely caused by the fast planetary rotation. By performing a phase resolved retrieval, we found a temperature profile that is cooler when the planetary terminator region is aligned with the observer's line of sight in comparison to the temperature profile measured when the planetary dayside faces the observer. Finally, we conducted individual retrievals for different chemical species, each resulting in temperature profiles that mostly agree with the overall retrieval result.

5.2. Discussion and conclusions

5.2.1. Methodology

In this work, we used several methods to reduce the data and extract information on exoplanet atmospheres from the high-resolution spectra. In the studies presented in Chapters 2, 3, and 4, these routines comprise removing the telluric and stellar lines from the normalized and outlier-corrected raw spectra and thereafter, mapping the weak planetary spectrum to a single peak using the cross-correlation method. Moreover, in Chapter 4 a Bayesian retrieval framework is used to fit the high-resolution exoplanet spectra to a parametrized model spectrum. Similar routines and methods are widely used in the literature on exoplanet atmospheres and have been improved considerably in recent years. In the following, we summarize the challenges and give the main conclusions related to the methodology used in this thesis.

5.2.1.1. Sensitivity of the detected signal to masking routines

Wavelength intervals of the high-resolution spectra with strong contamination by telluric absorption and sky emission lines are masked in the pre-processing step of the data analysis as these features cannot be efficiently removed by SYSREM. In the studies presented in this thesis, we masked all pixels with a flux smaller than 20% of the spectral continuum level. Other studies in the literature apply alternative flux thresholds to mask the telluric contamination (e.g., flux level of 40%; Landman et al. 2021). Analogously, a variety of different criteria can be applied to identify and mask prominent sky emission lines, which are mostly present at NIR wavelengths.

Different routines for masking the sky emission lines were employed in Chapters 3 and 4 in order to detect the spectral signature of Si I in the CARMENES NIR data. In Chapter 3, the masking routine was based on a fixed threshold (e.g., Stangret et al. 2020). On the other hand, in Chapter 4 the sky emission lines were visually identified and masked (e.g., Nugroho et al. 2021). These two different methods resulted in masked wavelength regions that overlap but comprise a different number of wavelength bins. Overall, we masked $\sim 9\%$ and $\sim 17\%$ of the total pixel number to remove the strongest telluric absorption and sky emission lines, respectively. The number of masked wavelength bins affects the number of detectable spectral lines of the exoplanet atmosphere. Therefore, the smaller number of masked wavelength bins in Chapter 3 causes the slightly higher detection strength of Si I in comparison to Chapter 4. The S/N values are measured as 4.8 and 4.4 in Chapters 3 and 4, respectively.

The deviating detection strengths of Si I obtained from the same dataset with different masking routines show that cross-correlation analyses are sensitive to the applied data reduction methods. Apart from the different detection strengths, the S/N maps of Si I in Chapters 3 and 4 are consistent as they show an identical noise pattern and a S/N peak at the same coordinates. Hence, we conclude that the results of our Si I analyses are robust. Apart from the example of the Si I detection presented here, the validation of cross-correlation results with different pre-processing settings can generally increase the reliability of exoplanet atmosphere studies.

5.2.1.2. Removal of telluric and stellar lines

A challenging data reduction step of high-resolution spectroscopy is the removal of the absorption lines from the Earth's atmosphere and the spectral features from an exoplanet's host star. In our implementation of this step, we used SYSREM, a PCA algorithm (Tamuz et al. 2005). When applying this algorithm, the telluric and stellar lines are efficiently removed from the spectra. In a first step, this procedure comprises computing a forward model of the telluric and stellar lines with SYSREM. Subsequently, the forward model is used to remove the information of the telluric contamination and the stellar lines from the data. In our work, we have tested two approaches for removing the telluric and stellar lines. In Chapter 2, we applied SYSREM in the standard way, which consists of subtracting the forward model from the spectra (e.g., Nugroho et al. 2017; Alonso-Floriano et al. 2019). Alternatively, in Chapters 3 and 4, we divided our forward model out of the high-resolution

spectral data (e.g., Merritt et al. 2020; Yan et al. 2020). We found that dividing the spectra with the SYSREM model or subtracting the model from the data yielded comparable cross-correlation peaks in the S/N maps when the same spectral template was used. For example, the Fe I detection strengths[1] obtained with the two methods in Chapters 2 and 4 are close to each other. We note, however, that the relative depth of the planetary spectral lines is preserved in the presence of strong telluric contamination only by division with the SYSREM model. The preservation of the relative line depth is required when using retrieval frameworks (e.g., Gibson et al. 2020) and thus, we stress the use of this procedure in future applications.

Since the SYSREM algorithm is applied iteratively, another critical aspect is the selection of the optimal iteration number. At small iteration numbers, the algorithm mainly models the telluric and stellar lines, and only slightly considers the presence of the planetary spectral signal. However, at higher iteration numbers, SYSREM increasingly accounts for the faint planetary spectral lines. Consequently, at an optimal iteration number, the telluric and stellar contamination is most efficiently removed, while the planetary signal is insignificantly affected. Several works, including the studies presented in Chapters 2, 3, and 4, have assumed that the SYSREM iteration with the optimal removal of telluric and stellar lines corresponds to the one with the highest detection strength (e.g., Stangret et al. 2020; Nugroho et al. 2020a). Alternatively, also signal-independent procedures for obtaining the optimal iteration number have been applied. For instance, Herman et al. (2022) have determined the optimal SYSREM iteration number as the value after which the root mean square of the spectral matrix does not decrease noticeably with additional iterations. On the other hand, Kesseli et al. (2020) have applied injection-recovery tests and selected the optimal iteration number as the one that maximizes the recovered signal from an injected model spectrum. In this thesis, we followed a conservative approach and assumed a common optimal iteration number for all spectral orders. Alternatively, some studies optimize the iteration number for each spectral order independently (e.g., Nugroho et al. 2017; Sánchez-López et al. 2019). This approach has the advantage of taking into account the wavelength dependency of contamination with telluric and stellar lines. However, we caution that the order-by-order optimization of the SYSREM iteration number, if not done carefully, may artificially enhance the detection strength by maximizing well-placed noise patterns in the S/N map.

In summary, various approaches of using SYSREM enable the removal of telluric and stellar lines from high-resolution spectra. The different procedures of applying SYSREM offer the possibility to increase the robustness of exoplanet studies as consistent outcomes of the different approaches are an indicator for appropriate removal of the telluric and stellar lines. The exploration of other techniques, such as fitting with Molecfit (Smette et al. 2015) and stellar model spectra, may provide additional approaches for isolating exoplanet spectra from the signal of the Earth's atmosphere and the stellar host.

[1] The detection of Fe I in Chapter 2 includes data from CARMENES VIS, HARPS-N, and ESPaDOnS ($S/N = 7.3$). In Chapter 4, the detection of Fe I results from the same data but with additional spectra from CARMENES NIR ($S/N = 7.9$). Exclusion of the CARMENES NIR spectra from the analysis in Chapter 4 results in an insignificant change in the results ($S/N = 7.5$), but allows comparison of the two methods of applying SYSREM.

5.2.1.3. Spectral line lists

Spectral line lists play a fundamental role for calculating the model spectra used in the cross-correlation analysis and for atmospheric retrievals. Our study in Chapter 2 suggests that the precision of these lists is critical for the correctness of conclusions drawn from high-resolution observations of planetary atmospheres as inaccurate line positions can falsely indicate the absence or depletion of chemical species (Flowers et al. 2019). Particularly, the line lists of diatomic transition metal molecules, such as TiO and VO, suffer from significant inaccuracies as their calculation is computationally difficult (McKemmish et al. 2019). Resolving and studying the spectral lines of these molecular species with high-resolution spectroscopy, however, is needed to further improve our understanding of the thermal structure, chemistry, and dynamics in UHJ atmospheres.

Validating the high-resolution line lists prior to their use for recovering the signal of chemical species can mitigate the limitations caused by inaccuracies in the line positions. A frequently used method for validation is cross-correlating a spectral model based on the line list in question with an observed high-resolution stellar spectrum that is known to exhibit the modeled spectral features (e.g., Hoeijmakers et al. 2015). Consequently, wavelength ranges with an insufficient accuracy of the line positions can be excluded from studies on exoplanet atmospheres. For example, the validation of the TiO line list and the subsequent removal of biased wavelength ranges from our analysis in Chapter 2 represents a critical step in finding evidence for the presence of this species in the atmosphere of WASP-33b. A similar approach was also applied by other studies for detecting TiO and OH in the spectrum of the same planet (Nugroho et al. 2017, 2021). We suggest that line list dependent effects may be an explanation for the rare detections and conflicting results of studies focusing on diatomic transition metal molecules with high-resolution spectroscopy. To date, only a few detections of TiO have been made, and other metal oxides and hydrates could not so far be detected at all using high-resolution spectroscopy. Theoretical work suggests the presence of these species in the atmospheres of strongly irradiated exoplanets and identifies them as key players for the planetary energy balance (Hubeny et al. 2003; Fortney et al. 2008).

5.2.1.4. Model spectra

Retrieving the faint signature of exoplanet atmospheres from spectral observations requires the calculation of planetary model spectra. The most advanced procedure for computing these models includes the use of so-called general circulation models (e.g., Komacek et al. 2017; Flowers et al. 2019). These models are capable of incorporating fluid dynamics, radiative transfer, and atmospheric chemistry, and can simulate the three-dimensional structure of exoplanet atmospheres. The atmospheric structure assessed by general circulation models is subsequently processed by a radiative transfer code. The main disadvantage of using these self-consistent models is the elevated computational effort required for their calculation. On the other hand, an exoplanet model spectrum can also be computed with a fixed underlying atmospheric structure that is described by a restricted number of parameters (e.g., Mollière et al. 2019). The calculation of these spectral

models requires a significantly lower amount of computing time, which is why these models are widely used.

We have applied the latter method in Chapters 2, 3, and 4 to model the planetary atmosphere and the corresponding emission spectra. However, the low computational effort comes with the trade-off that the atmospheric conditions cannot be captured as detailed as with general circulation models due to the use of a limited number of parameters and a simplified atmospheric structure. Further, the parameters used in this approach are usually average quantities such as the mean temperature profile, the mean chemical abundances, or the planetary surface gravity. Therefore, it is challenging to use these models for in-depth studies of planetary atmospheres, for instance, to analyze the variation of physical properties as a function of the location in the planetary atmosphere. Using rather simple models also often ignores chemical disequilibrium effects, and the potential presence of atmospheric clouds and hazes. We caution that oversimplification of the complex physical reality in exoplanet atmospheres can bias the measured planetary signal. For example, Beltz et al. (2022) showed that the high-resolution spectra of UHJ atmospheres can vary strongly between different orbital phases as a result of the three-dimensional atmospheric structure of an exoplanet, thereby leading to significant offsets in the recovered Doppler-shift. Consequently, a careful evaluation of the applied simplifications is crucial when using exoplanet atmosphere models for the interpretation of observational data. In addition, the use of more sophisticated spectral models may represent an appropriate approach for in-depth atmospheric characterization.

5.2.1.5. Atmospheric retrievals

Retrieval frameworks derive quantitative constraints on the physical and chemical conditions of exoplanet atmospheres by fitting parameterized model spectra to observational data. The atmospheric retrieval presented in Chapter 4 of this thesis shows the feasibility of combining observations from multiple high-resolution spectroscopy instruments. This combination offers the advantage of covering a wide wavelength range and thus, including the spectral lines of multiple chemical species into the retrieval. Owing to the broad spectral coverage of the instruments included, we were able to retrieve the spectral signature of ions, neutral atoms, and molecules, which typically cover different wavelength ranges and are expected to probe distinct regions of the planetary atmosphere. By targeting specific chemical species, their individual temperature profiles can be determined, which in principle, allows for reconstructing their location in planetary atmospheres. Including the spectral signature of a variety of chemical species can therefore advance studying the chemical structure in exoplanet atmospheres.

Retrievals in the current literature focus on recovering the atmospheric temperature profile and the mixing ratios of a number of chemical species (e.g., Brogi & Line 2019; Line et al. 2021). However, a variety of additional parameters can be included into the spectral models used for retrievals. This allows for a more comprehensive description of exoplanet atmospheres. For instance, we included a parameter that accounts for excess broadening of the spectral line profile

into our retrieval analysis in Chapter 4. In the current literature, spectral line broadening has not been extensively investigated with retrievals, although this may allow the study of planetary rotation (Snellen et al. 2014) and atmospheric circulation. Moreover, we have shown for the first time the feasibility of using a retrieval for measuring the atmospheric temperature profile, spectral line broadening, and elemental abundances at different orbital phases of an exoplanet. We detected phase dependent changes in the atmospheric temperature profile and found indications for a variable width of the spectral line profile. Our phase resolved retrieval therefore represents a first step toward the exploration of the physical conditions as a function of the geographical longitude and thus, in characterizing the three-dimensional atmospheric structure of exoplanets. Consequently, retrieval studies range from simple investigations of the average thermal and chemical conditions to more complex analyses, which can account for variable atmospheric conditions at different geographical longitudes or involve global circulation. However, such in-depth characterizations require a high degree of complexity in spectral modeling, which, in turn, puts a higher demand on the available computational resources. Therefore, computationally efficient implementations of the spectral models are a major advantage for successfully employing retrieval codes in interpreting high-resolution spectra of exoplanet atmospheres.

Finally, we point out that partial removal and distortion of the planetary spectral lines by `SYSREM` must be considered when computing the spectral models used in atmospheric retrievals (e.g., Brogi & Line 2019). These effects are expected when the change of the planetary RV between consecutive exposure frames is smaller than the velocity resolution of the detector pixels of the spectrograph used (Birkby 2018). However, in this thesis `SYSREM` was applied exclusively to high-resolution spectra of UHJs. These planets exhibit a rapid change in velocity along the observer's line of sight due to their short orbital periods. The rapid velocity change of UHJs allowed us to choose spectral integration times such that the velocity shift between consecutive exposures exceeded the pixel spacing of the spectrograph. The `SYSREM` algorithm was therefore not able to identify the planetary spectral signature as a stationary feature in the observational data. Consequently, the planetary spectral lines in our observations were mostly not affected by `SYSREM`, and mimicking the effect of the algorithm was not required when computing the spectral models. However, we caution that `SYSREM` may interfere with the planetary spectral signature in the more general case of investigating exoplanets with a slower RV change than UHJs. In this case, post-processing of the modeled spectra may be required after their generation with a radiative transfer code.

5.2.2. Science

In this thesis, we present the detection of the emission lines of several chemical species in the atmospheres of two UHJs. The analyses of their emission spectra allowed us to study the thermal and chemical properties in the atmospheres of strongly irradiated exoplanets. In the following, we draw conclusions and provide discussions on the scientific results of this work.

5.2.2.1. Dominance of atomic Fe lines

In Chapters 2 and 4 of this thesis, we report the detection of Fe I in the atmosphere of WASP-33b. The signature of Fe I presents the most prominent detection peak among the chemical species investigated in this work. This finding is in line with the significant detections of both neutral and ionized Fe in the atmospheres of several other strongly irradiated planets (e.g., Hoeijmakers et al. 2018; Stangret et al. 2020; Yan et al. 2020). Moreover, Fe I represents the most frequently detected species in the thermal emission spectra of UHJs (e.g., Pino et al. 2020; Nugroho et al. 2020a; Yan et al. 2022b; Herman et al. 2022). The frequent detection is likely caused by the enhanced chemical equilibrium abundance of Fe I, combined with its prominent signature consisting of a dense forest of spectral lines. Consequently, the detected signal and retrieved atmospheric parameters of UHJ atmospheres are mostly determined by the spectral Fe I lines (e.g., Kasper et al. 2021).

The spectra of UHJs exhibit strong emission lines, which unambiguously prove the existence of thermal inversion layers in their dayside atmospheres. The frequent observation of Fe I emission lines suggests that the species is strongly involved in the heating mechanism required to maintain these inversion layers. Theoretical work confirms this hypothesis and suggests that Fe I in combination with other atomic and ionic species plays an important role in the energy balance of UHJ atmospheres (Lothringer et al. 2018; Fossati et al. 2021). Therefore, investigating the spectral signature of Fe I allows us to constrain the thermal structure in the atmospheres of UHJs.

The abundance of atomic Fe is commonly used as a proxy for the stellar metallicity. In an analogous way, measuring the Fe I abundance of UHJ atmospheres can provide an estimate of the planetary metallicity. In Chapter 4, we derived the metallicity for the atmosphere of WASP-33b via a retrieval that is mainly driven by the strong Fe I spectral signature. We derived a super-solar metallicity, which is in line with studies on other strongly irradiated planets (e.g., Sedaghati et al. 2017; Nikolov et al. 2018). The metallicity of an exoplanet is an important observational parameter because the comparison with the metallicity of the host star can provide insight into the mechanisms of planet formation.

5.2.2.2. Discovery of Si as a novel chemical species

In Chapter 3, we present the discovery of Si I emission lines in the spectra of the two UHJs WASP-33b and KELT-20b/MASCARA-2b. This study adds Si I as a novel chemical species to the known atmospheric composition of UHJs. Our spectral models used for cross-correlation suggest that the spectral features of the species are predominantly present at NIR wavelengths. This restriction to a specific wavelength range is probably the reason why Si I has been overlooked in previous spectral studies on atomic and ionic species, whose spectral lines are mostly limited to wavelengths shorter than the NIR. Our chemical equilibrium calculations suggest that Si-bearing species other than Si I are widely present in the atmospheres of UHJs. Among these species, Si II and SiO are likely the most abundant representatives. However, in view of the almost featureless Si II model spectrum of

WASP-33b in Chapter 4, we caution that studying the signature of this species at near-ultraviolet, VIS, and NIR wavelengths in UHJ atmospheres may be a challenging task. In contrast, a recent low-spectral-resolution study on the exoplanet WASP-178b at shorter wavelengths provided strong evidence for the presence of SiO in UHJ atmospheres (Lothringer et al. 2022).

Theoretical work predicts that Si-bearing species play a fundamental role in the formation of silicate clouds on planetary nightsides (Gao et al. 2020). Also, the relatively low nightside temperatures measured in the atmospheres of several strongly irradiated planets and the observation of muted spectral features hint toward the presence of these clouds (Gao & Powell 2021). Consequently, silicate clouds are expected to critically influence heat transport processes and thus, the energy balance in exoplanet atmospheres. Future measurements of the occurrence and abundance of the most important Si-bearing cloud precursor species in UHJ atmospheres may therefore improve our understanding of clouds and rain-out processes of refractory species on planetary nightsides.

5.2.2.3. Depletion of Ti and V

Observational studies at high spectral resolution have led to the nondetection of Ti- and V-bearing species in the spectra of several UHJs (e.g., Merritt et al. 2020; Tabernero et al. 2021). This is a remarkable result, given that the presence of these species is predicted by theoretical work (e.g., Hubeny et al. 2003; Fortney et al. 2008) and other refractory species, such as atomic Fe, are present in their gaseous form in the atmospheres of the same planets (e.g., Yan et al. 2022b). The lack of detection of TiO and VO can be partially attributed to inaccuracies in the line lists of these species (e.g., McKemmish et al. 2019; Merritt et al. 2020). However, biased line lists cannot explain the absence of the Ti I, Ti II, V I, and V II spectral signatures from UHJ observations as the line positions of atomic and ionic metal species are known with high precision (Kurucz 2018). Consequently, depletion mechanisms likely remove significant amounts of these species from the atmospheres of several UHJs. Cold trapping has been proposed as a possible explanation for the observed depletion. This mechanism hypothesises nightside condensation and gravitational settling, which leads to the removal of Ti and V in any form from the upper atmospheres of strongly irradiated exoplanets (Spiegel et al. 2009; Parmentier et al. 2013).

The detections of Ti I, Ti II, and V I in Chapter 4 show that cold trapping of these species does not significantly affect the atmospheric chemistry of WASP-33b. Together with the limited number of detections of Ti- and V-bearing species reported in the literature, this result suggests that elevated atmospheric temperatures favor the occurrence of refractory species. For example, our discovery of Ti I and Ti II in the atmosphere of WASP-33b ($T_{\rm eq} \sim 2700$ K) is consistent with the identification of Ti II in the ultra-hot atmosphere of KELT-9b (Hoeijmakers et al. 2018; $T_{\rm eq} \sim 4000$ K) and the detection of Ti I, Ti II, and TiO in the very hot atmosphere of WASP-189b (Prinoth et al. 2022; $T_{\rm eq} \sim 2600$ K). On the other hand, the presence of the Ti I signal in the spectrum of the significantly cooler planet HD 149026b (Ishizuka et al. 2021; $T_{\rm eq} \sim 1700$ K) presents a deviation from this trend.

This indicates that physical parameters other than the temperature may also be relevant for the occurrence of refractory species in the atmospheres of gas giant exoplanets. Further theoretical and observational studies focusing on the role of Ti and V in the composition of hot giant exoplanets will benefit our understanding of depletion mechanisms in highly irradiated atmospheres.

Finally, we point out that our work represents the first discovery of Ti I, Ti II, and V I using high-resolution emission spectroscopy. Previous high-resolution detections of these species were obtained exclusively via transmission spectroscopy (e.g., Kesseli et al. 2022; Bello-Arufe et al. 2022; Prinoth et al. 2022). Transmission spectroscopy probes the day-night terminators of exoplanets, while emission spectroscopy mostly probes the spectral signature emerging from the hotter planetary dayside. We therefore suggest that emission spectroscopy is particularly suitable for searching the spectral signature of Ti- and V-bearing species, whose presence is probably favored by elevated temperatures.

5.2.2.4. Structure of exoplanet atmospheres

In this thesis, we have shown that emission spectroscopy is a powerful tool for characterizing the thermal structure of exoplanet atmospheres. In particular, emission lines in the spectra of strongly irradiated exoplanets provide unambiguous evidence for the presence of inverted temperature profiles in their atmospheres. Absorption of the incoming stellar radiation by metal atoms and their ions, oxides, and hydrates is assumed to cause such inverted atmospheric profiles (e.g., Hubeny et al. 2003; Fortney et al. 2008; Lothringer et al. 2018; Fossati et al. 2021). Our studies presented in Chapters 2, 3, and 4 report the detection of the emission lines from atomic and ionic species as well as molecules in the thermal inversion layers of two UHJs, which confirms this hypothesis.

Studying the spectral signature of individual chemical species allows drawing conclusions about their distribution over the surface of an exoplanet. For instance, in Chapter 2 we present our finding of a significant offset between the Doppler-shifts of the Fe I and TiO signals in the dayside spectrum of WASP-33b. Moreover, our cross-correlation model spectra require a hotter temperature profile for Fe I than for TiO to match the observational data. We hypothesize that an approximately homogeneous distribution of Fe I and TiO-depletion via thermal dissociation in the dayside hemisphere of the planet can explain these results. A similar situation has also emerged in our study of the atomic species in the atmosphere of the same planet in Chapter 4. In this study, our retrieval yields a slightly cooler temperature profile for V I in comparison to the profile of the other chemical species studied. This result may indicate a reduced V I concentration in the hottest part of the planetary dayside due to predominant ionization of the species. Besides our work, also in the literature chemical gradients have been invoked to explain the observed offsets in the cross-correlation peaks of different species detected in exoplanet atmospheres (e.g., Kesseli et al. 2022; Sánchez-López et al. 2022).

Different geographical longitudes of an exoplanet align with the observer's line of sight as a function of the orbital phase. The variable alignment during the orbit of an exoplanet offers the pos-

sibility to investigate the atmospheric conditions at different longitudes in planetary atmospheres. In Chapter 4, we measured a temperature decrease from the substellar point toward the nightside of WASP-33b by using a phase resolved retrieval, which confirms that the nightside of the planet has cooler temperatures than the dayside. This result shows that state-of-the-art retrieval frameworks are a powerful tool for the detailed investigation of planetary atmospheres. Recent studies have increasingly focused on measuring physical and chemical conditions at specific geographical longitudes in exoplanet atmospheres. For instance, a phase resolved retrieval has been carried out by Brogi et al. (2022) on the emission spectra of the strongly irradiated planet WASP-18b, and Gandhi et al. (2022) retrieved the conditions at the morning and evening terminators of the UHJ WASP-76b via transmission spectroscopy.

Another detectable property of gas giant exoplanet atmospheres with elevated temperatures are dayside to nightside winds, which are observed as a deviation of the spectral lines from the planetary rest frame (e.g., Alonso-Floriano et al. 2019; Sánchez-López et al. 2019). Our analyses of the emission spectra of WASP-33b and KELT-20b/MASCARA-2b in Chapters 2, 3, and 4 could not detect significant deviations from the planetary rest frame. Thus, we conclude that no strong dayside to nightside winds are present in the atmospheres of the two planets. On the other hand, we found the spectral signature of rotation and possible super-rotation based on the detection of an additional blueshift and redshift before and after the secondary eclipse of WASP-33b, respectively. Using spectral models that include the wind-induced Doppler-shifts into future studies may advance the characterization of the global circulation in exoplanet atmospheres.

5.3. Outlook

In this thesis, we observed the emission spectra of two UHJs and characterized the thermal structure, chemistry, and dynamics of their atmospheres. Our results contributed to a deeper understanding of the two investigated targets and of UHJs in general. Future research can advance our knowledge about exoplanet atmospheres and improve high-resolution spectroscopy methodologies.

In this work, we discovered the spectral signature of Si I in the atmospheres of two UHJs. Si I, Si II, and SiO are expected to account for the vast majority of Si inventory in the hot atmospheres of giant exoplanets and are important silicate cloud precursor species (Gao & Powell 2021). Thus, searching for and characterizing the spectral signatures of these Si-bearing species in the spectra of several other UHJs could progress our understanding of atmospheric silicate clouds. Recently, hints for the presence of SiO have been detected at low spectral resolution in a UHJ atmosphere (Lothringer et al. 2022), but neither Si II nor SiO has been detected at high spectral resolution in exoplanet atmospheres. The detection of Si II by either transmission or emission spectroscopy is expected to be challenging due to the relatively faint spectral lines, but the signal from SiO should have strong spectral features enabling a successful observation of the species in the near future. On the other hand, this thesis presents the detection of atomic Ti and V in the dayside atmosphere

of a strongly irradiated exoplanet. Ti- and V-bearing species are expected to be important drivers for atmospheric thermal inversions (Hubeny et al. 2003; Fortney et al. 2008), but recent investigations found the spectral signature of these species to be missing in the spectra of several UHJs (e.g., Merritt et al. 2020; Tabernero et al. 2021; Yan et al. 2022b). Consequently, analyzing the conditions for the presence of Ti and V in UHJ atmospheres could allow us to deepen our understanding of depletion mechanisms acting on these species. Future research could conduct a survey of several hot giant exoplanets to investigate the presence of Ti I, V I, Ti II, V II, TiO, and VO across a range of different planetary parameters. Such a survey could enable us to constrain the relevant physical parameters and the thresholds at which these species rain-out from the gaseous phase. The atmospheric thermal conditions are considered an important parameter in the depletion of these species. However, according to recent observations (Ishizuka et al. 2021), we expect that physical parameters other than the temperature also influence the occurrence of Ti and V in exoplanet atmospheres.

In addition, spectroscopy methodologies need to be further developed to advance the successful characterization of exoplanet atmospheres. Low-resolution spectra provide information on the spectral continuum level, while high-resolution spectra encode the properties of the individual spectral lines (Gandhi et al. 2019). Thus, retrieval frameworks that combine low- and high-resolution observations could significantly improve our abilities to extract information on exoplanet atmospheres from spectroscopic data. In this thesis, we have made a first step toward this direction by combining data from multiple high-resolution instruments covering different wavelength ranges. A promising next step could be the inclusion of low- and medium-resolution data from space-based observatories into our high-resolution retrieval framework. Spectroscopic data of several UHJs available in the *Hubble* Space Telescope data archive could be used and *James Webb* Space Telescope observations of strongly irradiated planets could be included in the near future.

Thanks to next-generation telescopes and instruments, also planets other than hot Jupiters and UHJs will become accessible for characterization via high-resolution spectroscopy in the future. In the short-term, HiRISE (Vigan et al. 2018) will come operational, which is realized by coupling the high-contrast exoplanet imager SPHERE (Beuzit et al. 2019) and the high-resolution spectrograph CRIRES+ (Dorn et al. 2016) at the Very Large Telescope. This combination will allow us to observe young giant exoplanets on wide orbits and enable their characterization for the first time via high-resolution emission spectroscopy. Currently, these planets are observed exclusively at low spectral resolution, thus revealing only unresolved spectral features. Investigation of these targets with high-resolution spectroscopy could focus on measuring the planetary rotation and atmospheric chemistry to gain insight into their evolution and formation history. In the mid-term future, ground-based telescopes with aperture sizes up to approximately 40 m will enable further advances in the study of exoplanet atmospheres. These telescopes are the Giant Magellan Telescope (Johns 2008), the Thirty Meter Telescope (Nelson & Sanders 2008), and the Extremely Large Telescope (Gilmozzi & Spyromilio 2007). The high-resolution spectrographs mounted at these telescopes will significantly increase the sample of exoplanets accessible for atmospheric

characterization, including the possible detection of features in the spectra of habitable-zone super-Earths (Madhusudhan 2019). Moreover, the atmospheric structure and dynamics of gas giant exoplanets will be characterized in unprecedented detail. The results of these analyses will lead to a deeper understanding of the physics in their atmospheres and narrow the possible scenarios of planetary formation. The emerging era of exoplanet science based on the use of extremely large telescopes will benefit from the high-resolution methodologies currently applied to the planets with the strongest signals, such as hot Jupiters and UHJs. The methods used in this thesis will therefore contribute to solving challenging tasks in future exoplanet research.

Bibliography

Allart, R., Bourrier, V., Lovis, C. et al. (2019) High-resolution confirmation of an extended helium atmosphere around WASP-107b. *A&A*, **623**, A58.

Alonso-Floriano, F. J., Sánchez-López, A., Snellen, I. A. G. et al. (2019) Multiple water band detections in the CARMENES near-infrared transmission spectrum of HD 189733 b. *A&A*, **621**, A74.

Arcangeli, J., Désert, J.-M., Line, M. R. et al. (2018) H^- Opacity and Water Dissociation in the Dayside Atmosphere of the Very Hot Gas Giant WASP-18b. *ApJ*, **855**(2), L30.

Arcangeli, J., Désert, J.-M., Parmentier, V. et al. (2019) Climate of an ultra hot Jupiter. Spectroscopic phase curve of WASP-18b with HST/WFC3. *A&A*, **625**, A136.

Ballester, G. E. & Ben-Jaffel, L. (2015) Re-visit of HST FUV Observations of the Hot-Jupiter System HD 209458: No Si III Detection and the Need for COS Transit Observations. *ApJ*, **804**(2), 116.

Batygin, K., Bodenheimer, P. H. & Laughlin, G. P. (2016) In Situ Formation and Dynamical Evolution of Hot Jupiter Systems. *ApJ*, **829**(2), 114.

Bell, T. J. & Cowan, N. B. (2018) Increased Heat Transport in Ultra-hot Jupiter Atmospheres through H_2 Dissociation and Recombination. *ApJ*, **857**(2), L20.

Bello-Arufe, A., Cabot, S. H. C., Mendonça, J. M., Buchhave, L. A. & Rathcke, A. D. (2022) Mining the Ultrahot Skies of HAT-P-70b: Detection of a Profusion of Neutral and Ionized Species. *AJ*, **163**(2), 96.

Beltz, H., Rauscher, E., Brogi, M. & Kempton, E. M. R. (2021) A Significant Increase in Detection of High-resolution Emission Spectra Using a Three-dimensional Atmospheric Model of a Hot Jupiter. *AJ*, **161**(1), 1.

Beltz, H., Rauscher, E., Kempton, E. M. R. et al. (2022) Magnetic Drag and 3D Effects in Theoretical High-resolution Emission Spectra of Ultrahot Jupiters: the Case of WASP-76b. *AJ*, **164**(4), 140.

Ben-Yami, M., Madhusudhan, N., Cabot, S. H. C. et al. (2020) Neutral Cr and V in the Atmosphere of Ultra-hot Jupiter WASP-121 b. *ApJ*, **897**(1), L5.

Bernath, P. F. (2020) MoLLIST: Molecular Line Lists, Intensities and Spectra. *J. Quant. Spec. Radiat. Transf.*, **240**, 106687.

Beuzit, J. L., Vigan, A., Mouillet, D. et al. (2019) SPHERE: the exoplanet imager for the Very Large Telescope. *A&A*, **631**, A155.

Birkby, J. L. (2018) Spectroscopic Direct Detection of Exoplanets. In *Handbook of Exoplanets*, edited by H. J. Deeg & J. A. Belmonte, p. 16.

Birkby, J. L., de Kok, R. J., Brogi, M., Schwarz, H. & Snellen, I. A. G. (2017) Discovery of Water at High Spectral Resolution in the Atmosphere of 51 Peg b. *AJ*, **153**(3), 138.

Birkby, J. L., de Kok, R. J., Brogi, M. et al. (2013) Detection of water absorption in the day side atmosphere of HD 189733 b using ground-based high-resolution spectroscopy at 3.2μm. *MNRAS*, **436**, L35–L39.

Boley, A. C., Granados Contreras, A. P. & Gladman, B. (2016) The In Situ Formation of Giant Planets at Short Orbital Periods. *ApJ*, **817**(2), L17.

Booth, R. A., Clarke, C. J., Madhusudhan, N. & Ilee, J. D. (2017) Chemical enrichment of giant planets and discs due to pebble drift. *MNRAS*, **469**(4), 3994–4011.

Borsa, F., Allart, R., Casasayas-Barris, N. et al. (2021a) Atmospheric Rossiter-McLaughlin effect and transmission spectroscopy of WASP-121b with ESPRESSO. *A&A*, **645**, A24.

Borsa, F., Fossati, L., Koskinen, T., Young, M. E. & Shulyak, D. (2021b) High-resolution detection of neutral oxygen and non-LTE effects in the atmosphere of KELT-9b. *Nature Astronomy*, **6**, 226–231.

Borsa, F., Giacobbe, P., Bonomo, A. S. et al. (2022) The GAPS Programme at TNG. XXXIII. HARPS-N detects multiple atomic species in emission from the dayside of KELT-20b. *A&A*, **663**, A141.

Borsa, F., Lanza, A. F., Raspantini, I. et al. (2021c) The GAPS Programme at TNG. XXXI. The WASP-33 system revisited with HARPS-N. *A&A*, **653**, A104.

Brogi, M., de Kok, R. J., Albrecht, S. et al. (2016) Rotation and Winds of Exoplanet HD 189733 b Measured with High-dispersion Transmission Spectroscopy. *ApJ*, **817**(2), 106.

Brogi, M., Emeka-Okafor, V., Line, M. R. et al. (2022) The Roasting Marshmallows Program with IGRINS on Gemini South I: Composition and Climate of the Ultra Hot Jupiter WASP-18 b. *arXiv e-prints*, arXiv:2209.15548.

Brogi, M., Giacobbe, P., Guilluy, G. et al. (2018) Exoplanet atmospheres with GIANO. I. Water in the transmission spectrum of HD 189 733 b. *A&A*, **615**, A16.

Brogi, M., Line, M., Bean, J., Désert, J. M. & Schwarz, H. (2017) A Framework to Combine Low- and High-resolution Spectroscopy for the Atmospheres of Transiting Exoplanets. *ApJ*, **839**(1), L2.

Brogi, M. & Line, M. R. (2019) Retrieving Temperatures and Abundances of Exoplanet Atmospheres with High-resolution Cross-correlation Spectroscopy. *AJ*, **157**(3), 114.

Brogi, M., Snellen, I. A. G., de Kok, R. J. et al. (2012) The signature of orbital motion from the dayside of the planet τ Boötis b. *Nature*, **486**(7404), 502–504.

Brogi, M., Snellen, I. A. G., de Kok, R. J. et al. (2013) Detection of Molecular Absorption in the Dayside of Exoplanet 51 Pegasi b? *ApJ*, **767**(1), 27.

Brooke, J. S. A., Bernath, P. F., Western, C. M. et al. (2016) Line strengths of rovibrational and rotational transitions in the X^2 Π ground state of OH. *J. Quant. Spec. Radiat. Transf.*, **168**, 142–157.

Brown, T. M. (2001) Transmission Spectra as Diagnostics of Extrasolar Giant Planet Atmospheres. *ApJ*, **553**(2), 1006–1026.

Butler, R. P. & Marcy, G. W. (1996) A Planet Orbiting 47 Ursae Majoris. *ApJ*, **464**, L153.

Butler, R. P., Marcy, G. W., Williams, E., Hauser, H. & Shirts, P. (1997) Three New "51 Pegasi-Type" Planets. *ApJ*, **474**(2), L115–L118.

Caballero, J. A., Guàrdia, J., López del Fresno, M. et al. (2016) CARMENES: data flow. In *Observatory Operations: Strategies, Processes, and Systems VI*, vol. 9910 of *Proc. SPIE*.

Cabot, S. H. C., Madhusudhan, N., Hawker, G. A. & Gandhi, S. (2019) On the robustness of analysis techniques for molecular detections using high-resolution exoplanet spectroscopy. *MNRAS*, **482**(4), 4422–4436.

Carolan, S., Vidotto, A. A., Hazra, G., Villarreal D'Angelo, C. & Kubyshkina, D. (2021) The effects of magnetic fields on observational signatures of atmospheric escape in exoplanets: Double tail structures. *MNRAS*, **508**(4), 6001–6012.

Casasayas-Barris, N., Orell-Miquel, J., Stangret, M. et al. (2021) CARMENES detection of the Ca II infrared triplet and possible evidence of He I in the atmosphere of WASP-76b. *A&A*, **654**, A163.

Casasayas-Barris, N., Pallé, E., Yan, F. et al. (2018) Na I and Hα absorption features in the atmosphere of MASCARA-2b/KELT-20b. *A&A*, **616**, A151.

Casasayas-Barris, N., Pallé, E., Yan, F. et al. (2019) Atmospheric characterization of the ultra-hot Jupiter MASCARA-2b/KELT-20b. Detection of CaII, FeII, NaI, and the Balmer series of H (Hα, Hβ, and Hγ) with high-dispersion transit spectroscopy. *A&A*, **628**, A9.

Cauley, P. W., Shkolnik, E. L., Ilyin, I. et al. (2019) Atmospheric Dynamics and the Variable Transit of KELT-9 b. *AJ*, **157**(2), 69.

Cauley, P. W., Wang, J., Shkolnik, E. L. et al. (2021) Time-resolved Rotational Velocities in the Upper Atmosphere of WASP-33 b. *AJ*, **161**(3), 152.

Changeat, Q. & Edwards, B. (2021) The Hubble WFC3 Emission Spectrum of the Extremely Hot Jupiter KELT-9b. *ApJ*, **907**(1), L22.

Charbonneau, D., Brown, T. M., Latham, D. W. & Mayor, M. (2000) Detection of Planetary Transits Across a Sun-like Star. *ApJ*, **529**(1), L45–L48.

Charbonneau, D., Brown, T. M., Noyes, R. W. & Gilliland, R. L. (2002) Detection of an Extrasolar Planet Atmosphere. *ApJ*, **568**(1), 377–384.

Collier Cameron, A., Guenther, E., Smalley, B. et al. (2010) Line-profile tomography of exoplanet transits - II. A gas-giant planet transiting a rapidly rotating A5 star. *MNRAS*, **407**(1), 507–514.

Cont, D., Yan, F., Reiners, A. et al. (2021) Detection of Fe and evidence for TiO in the dayside emission spectrum of WASP-33b. *A&A*, **651**, A33.

Cont, D., Yan, F., Reiners, A. et al. (2022a) Atmospheric characterization of the ultra-hot Jupiter WASP-33b. Detection of Ti and V emission lines and retrieval of a broadened line profile. *A&A*, **668**, A53.

Cont, D., Yan, F., Reiners, A. et al. (2022b) Silicon in the dayside atmospheres of two ultra-hot Jupiters. *A&A*, **657**, L2.

Cosentino, R., Lovis, C., Pepe, F. et al. (2012) Harps-N: the new planet hunter at TNG. In *Ground-based and Airborne Instrumentation for Astronomy IV*, edited by I. S. McLean, S. K. Ramsay & H. Takami, vol. 8446 of *Society of Photo-Optical Instrumentation Engineers (SPIE) Conference Series*.

Cosentino, R., Lovis, C., Pepe, F. et al. (2014) HARPS-N @ TNG, two year harvesting data: performances and results. In *Ground-based and Airborne Instrumentation for Astronomy V*, edited by S. K. Ramsay, I. S. McLean & H. Takami, vol. 9147 of *Society of Photo-Optical Instrumentation Engineers (SPIE) Conference Series*.

Cumming, A., Marcy, G. W. & Butler, R. P. (1999) The Lick Planet Search: Detectability and Mass Thresholds. *ApJ*, **526**(2), 890–915.

Czesla, S., Klocová, T., Khalafinejad, S., Wolter, U. & Schmitt, J. H. M. M. (2015) The center-to-limb variation across the Fraunhofer lines of HD 189733. Sampling the stellar spectrum using a transiting planet. *A&A*, **582**, A51.

Czesla, S., Schröter, S., Schneider, C. P. et al. (2019) PyA: Python astronomy-related packages.

Deibert, E. K., de Mooij, E. J. W., Jayawardhana, R. et al. (2021) Detection of Ionized Calcium in the Atmosphere of the Ultra-hot Jupiter WASP-76b. *ApJ*, **919**(2), L15.

Deline, A., Hooton, M. J., Lendl, M. et al. (2022) The atmosphere and architecture of WASP-189 b probed by its CHEOPS phase curve. *A&A*, **659**, A74.

Diamond-Lowe, H., Stevenson, K. B., Bean, J. L., Line, M. R. & Fortney, J. J. (2014) New Analysis Indicates No Thermal Inversion in the Atmosphere of HD 209458b. *ApJ*, **796**(1), 66.

Donati, J. F. (2003) ESPaDOnS: An Echelle SpectroPolarimetric Device for the Observation of Stars at CFHT. In *Solar Polarization*, edited by J. Trujillo-Bueno & J. Sanchez Almeida, vol. 307 of *Astronomical Society of the Pacific Conference Series*.

Donati, J. F., Semel, M., Carter, B. D., Rees, D. E. & Collier Cameron, A. (1997) Spectropolarimetric observations of active stars. *MNRAS*, **291**(4), 658–682.

Dorn, R. J., Follert, R., Bristow, P. et al. (2016) The "+" for CRIRES: enabling better science at infrared wavelength and high spectral resolution at the ESO VLT. In *Ground-based and Airborne Instrumentation for Astronomy VI*, edited by C. J. Evans, L. Simard & H. Takami, vol. 9908 of *Society of Photo-Optical Instrumentation Engineers (SPIE) Conference Series*.

Edwards, B., Changeat, Q., Baeyens, R. et al. (2020) ARES I: WASP-76 b, A Tale of Two HST Spectra. *AJ*, **160**(1), 8.

Ehrenreich, D., Lovis, C., Allart, R. et al. (2020) Nightside condensation of iron in an ultrahot giant exoplanet. *Nature*, **580**(7805), 597–601.

Espinoza, N., Rackham, B. V., Jordán, A. et al. (2019) ACCESS: a featureless optical transmission spectrum for WASP-19b from Magellan/IMACS. *MNRAS*, **482**(2), 2065–2087.

Evans, T. M., Aigrain, S., Gibson, N. et al. (2015) A uniform analysis of HD 209458b Spitzer/IRAC light curves with Gaussian process models. *MNRAS*, **451**(1), 680–694.

Evans, T. M., Sing, D. K., Kataria, T. et al. (2017) An ultrahot gas-giant exoplanet with a stratosphere. *Nature*, **548**(7665), 58–61.

Evans, T. M., Sing, D. K., Wakeford, H. R. et al. (2016) Detection of H_2O and Evidence for TiO/VO in an Ultra-hot Exoplanet Atmosphere. *ApJ*, **822**(1), L4.

Fisher, C., Hoeijmakers, H. J., Kitzmann, D. et al. (2020) Interpreting High-resolution Spectroscopy of Exoplanets using Cross-correlations and Supervised Machine Learning. *AJ*, **159**(5), 192.

Flowers, E., Brogi, M., Rauscher, E., Kempton, E. M. R. & Chiavassa, A. (2019) The High-resolution Transmission Spectrum of HD 189733b Interpreted with Atmospheric Doppler Shifts from Three-dimensional General Circulation Models. *AJ*, **157**(5), 209.

Foreman-Mackey, D., Hogg, D. W., Lang, D. & Goodman, J. (2013) emcee: The MCMC Hammer. *PASP*, **125**(925), 306.

Fortney, J. J. (2005) The effect of condensates on the characterization of transiting planet atmospheres with transmission spectroscopy. *MNRAS*, **364**(2), 649–653.

Fortney, J. J., Lodders, K., Marley, M. S. & Freedman, R. S. (2008) A Unified Theory for the Atmospheres of the Hot and Very Hot Jupiters: Two Classes of Irradiated Atmospheres. *ApJ*, **678**(2), 1419–1435.

Fossati, L., Haswell, C. A., Froning, C. S. et al. (2010) Metals in the Exosphere of the Highly Irradiated Planet WASP-12b. *ApJ*, **714**(2), L222–L227.

Fossati, L., Young, M. E., Shulyak, D. et al. (2021) Non-local thermodynamic equilibrium effects determine the upper atmospheric temperature structure of the ultra-hot Jupiter KELT-9b. *A&A*, **653**, A52.

Fu, G., Sing, D. K., Lothringer, J. D. et al. (2022) Strong H_2O and CO Emission Features in the Spectrum of KELT-20b Driven by Stellar UV Irradiation. *ApJ*, **925**(1), L3.

Fulton, B. J., Petigura, E. A., Howard, A. W. et al. (2017) The California-Kepler Survey. III. A Gap in the Radius Distribution of Small Planets. *AJ*, **154**(3), 109.

Gandhi, S., Kesseli, A., Snellen, I. et al. (2022) Spatially resolving the terminator: variation of Fe, temperature, and winds in WASP-76 b across planetary limbs and orbital phase. *MNRAS*, **515**(1), 749–766.

Gandhi, S. & Madhusudhan, N. (2019) New avenues for thermal inversions in atmospheres of hot Jupiters. *MNRAS*, **485**(4), 5817–5830.

Gandhi, S., Madhusudhan, N., Hawker, G. & Piette, A. (2019) HyDRA-H: Simultaneous Hybrid Retrieval of Exoplanetary Emission Spectra. *AJ*, **158**(6), 228.

Gao, P. & Powell, D. (2021) A Universal Cloud Composition on the Nightsides of Hot Jupiters. *ApJ*, **918**(1), L7.

Gao, P., Thorngren, D. P., Lee, E. K. H. et al. (2020) Aerosol composition of hot giant exoplanets dominated by silicates and hydrocarbon hazes. *Nature Astronomy*, **4**, 951–956.

Gao, P., Wakeford, H. R., Moran, S. E. & Parmentier, V. (2021) Aerosols in Exoplanet Atmospheres. *Journal of Geophysical Research (Planets)*, **126**(4), e06655.

García Muñoz, A. & Schneider, P. C. (2019) Rapid Escape of Ultra-hot Exoplanet Atmospheres Driven by Hydrogen Balmer Absorption. *ApJ*, **884**(2), L43.

Gargaud, M., Irvine, W. M., Amils, R. et al. (2015) *Encyclopedia of Astrobiology*.

Giacobbe, P., Brogi, M., Gandhi, S. et al. (2021) Five carbon- and nitrogen-bearing species in a hot giant planet's atmosphere. *Nature*, **592**(7853), 205–208.

Gibson, N. P., Merritt, S., Nugroho, S. K. et al. (2020) Detection of Fe I in the atmosphere of the ultra-hot Jupiter WASP-121b, and a new likelihood-based approach for Doppler-resolved spectroscopy. *MNRAS*, **493**(2), 2215–2228.

Gibson, N. P., Nugroho, S. K., Lothringer, J., Maguire, C. & Sing, D. K. (2022) Relative abundance constraints from high-resolution optical transmission spectroscopy of WASP-121b, and a fast model-filtering technique for accelerating retrievals. *MNRAS*, **512**(3), 4618–4638.

Gilmozzi, R. & Spyromilio, J. (2007) The European Extremely Large Telescope (E-ELT). *The Messenger*, **127**, 11.

Ginzburg, S., Schlichting, H. E. & Sari, R. (2018) Core-powered mass-loss and the radius distribution of small exoplanets. *MNRAS*, **476**(1), 759–765.

Gordon, I. E., Rothman, L. S., Hill, C. et al. (2017) The HITRAN2016 molecular spectroscopic database. *J. Quant. Spec. Radiat. Transf.*, **203**, 3–69.

Gupta, A. & Schlichting, H. E. (2020) Signatures of the core-powered mass-loss mechanism in the exoplanet population: dependence on stellar properties and observational predictions. *MNRAS*, **493**(1), 792–806.

Hands, T. O. & Helled, R. (2022) Super stellar abundances of alkali metals suggest significant migration for hot Jupiters. *MNRAS*, **509**(1), 894–902.

Hansen, C. J., Schwartz, J. C. & Cowan, N. B. (2014) Features in the broad-band eclipse spectra of exoplanets: signal or noise? *MNRAS*, **444**(4), 3632–3640.

Haynes, K., Mandell, A. M., Madhusudhan, N., Deming, D. & Knutson, H. (2015) Spectroscopic Evidence for a Temperature Inversion in the Dayside Atmosphere of Hot Jupiter WASP-33b. *ApJ*, **806**(2), 146.

Helled, R., Bodenheimer, P., Podolak, M. et al. (2014) Giant Planet Formation, Evolution, and Internal Structure. In *Protostars and Planets VI*, edited by H. Beuther, R. S. Klessen, C. P. Dullemond & T. Henning.

Helling, C., Gourbin, P., Woitke, P. & Parmentier, V. (2019) Sparkling nights and very hot days on WASP-18b: the formation of clouds and the emergence of an ionosphere. *A&A*, **626**, A133.

Henry, G. W., Marcy, G. W., Butler, R. P. & Vogt, S. S. (2000) A Transiting "51 Peg-like" Planet. *ApJ*, **529**(1), L41–L44.

Herman, M. K., de Mooij, E. J. W., Jayawardhana, R. & Brogi, M. (2020) Search for TiO and Optical Nightside Emission from the Exoplanet WASP-33b. *AJ*, **160**(2), 93.

Herman, M. K., de Mooij, E. J. W., Nugroho, S. K., Gibson, N. P. & Jayawardhana, R. (2022) Dayside Fe I Emission, Day-Night Brightness Contrast and Phase Offset of the Exoplanet WASP-33b. *AJ*, **163**(6), 248.

Herrero, E., Morales, J. C., Ribas, I. & Naves, R. (2011) WASP-33: the first δ Scuti exoplanet host star. *A&A*, **526**, L10.

Hoeijmakers, H. J., Cabot, S. H. C., Zhao, L. et al. (2020a) High-resolution transmission spectroscopy of MASCARA-2 b with EXPRES. *A&A*, **641**, A120.

Hoeijmakers, H. J., de Kok, R. J., Snellen, I. A. G. et al. (2015) A search for TiO in the optical high-resolution transmission spectrum of HD 209458b: Hindrance due to inaccuracies in the line database. *A&A*, **575**, A20.

Hoeijmakers, H. J., Ehrenreich, D., Heng, K. et al. (2018) Atomic iron and titanium in the atmosphere of the exoplanet KELT-9b. *Nature*, **560**(7719), 453–455.

Hoeijmakers, H. J., Ehrenreich, D., Kitzmann, D. et al. (2019) A spectral survey of an ultra-hot Jupiter. Detection of metals in the transmission spectrum of KELT-9 b. *A&A*, **627**, A165.

Hoeijmakers, H. J., Kitzmann, D., Morris, B. M. et al. (2022) The Mantis Network III: A titanium cold-trap on the ultra-hot Jupiter WASP-121 b. *arXiv e-prints*, arXiv:2210.12847.

Hoeijmakers, H. J., Seidel, J. V., Pino, L. et al. (2020b) Hot Exoplanet Atmospheres Resolved with Transit Spectroscopy (HEARTS). IV. A spectral inventory of atoms and molecules in the high-resolution transmission spectrum of WASP-121 b. *A&A*, **641**, A123.

Hubeny, I., Burrows, A. & Sudarsky, D. (2003) A Possible Bifurcation in Atmospheres of Strongly Irradiated Stars and Planets. *ApJ*, **594**(2), 1011–1018.

Huitson, C. M., Sing, D. K., Pont, F. et al. (2013) An HST optical-to-near-IR transmission spectrum of the hot Jupiter WASP-19b: detection of atmospheric water and likely absence of TiO. *MNRAS*, **434**(4), 3252–3274.

Hut, P. (1981) Tidal evolution in close binary systems. *A&A*, **99**, 126–140.

Ishizuka, M., Kawahara, H., Nugroho, S. K. et al. (2021) Neutral Metals in the Atmosphere of HD 149026b. *AJ*, **161**(4), 153.

Jensen, A. G., Cauley, P. W., Redfield, S., Cochran, W. D. & Endl, M. (2018) Hydrogen and Sodium Absorption in the Optical Transmission Spectrum of WASP-12b. *AJ*, **156**(4), 154.

Johns, M. (2008) The Giant Magellan Telescope (GMT). In *Extremely Large Telescopes: Which Wavelengths? Retirement Symposium for Arne Ardeberg*, edited by T. E. Andersen, vol. 6986 of *Society of Photo-Optical Instrumentation Engineers (SPIE) Conference Series*.

Johnson, M. C., Cochran, W. D., Collier Cameron, A. & Bayliss, D. (2015) Measurement of the Nodal Precession of WASP-33 b via Doppler Tomography. *ApJ*, **810**(2), L23.

Kasper, D., Bean, J. L., Line, M. R. et al. (2021) Confirmation of Iron Emission Lines and Nondetection of TiO on the Dayside of KELT-9b with MAROON-X. *ApJ*, **921**(1), L18.

Kesseli, A. Y. & Snellen, I. A. G. (2021) Confirmation of Asymmetric Iron Absorption in WASP-76b with HARPS. *ApJ*, **908**(1), L17.

Kesseli, A. Y., Snellen, I. A. G., Alonso-Floriano, F. J., Mollière, P. & Serindag, D. B. (2020) A Search for FeH in Hot-Jupiter Atmospheres with High-dispersion Spectroscopy. *AJ*, **160**(5), 228.

Kesseli, A. Y., Snellen, I. A. G., Casasayas-Barris, N., Mollière, P. & Sánchez-López, A. (2022) An Atomic Spectral Survey of WASP-76b: Resolving Chemical Gradients and Asymmetries. *AJ*, **163**(3), 107.

Kitzmann, D., Heng, K., Rimmer, P. B. et al. (2018) The Peculiar Atmospheric Chemistry of KELT-9b. *ApJ*, **863**(2), 183.

Knutson, H. A., Charbonneau, D., Allen, L. E., Burrows, A. & Megeath, S. T. (2008) The 3.6-8.0 μm Broadband Emission Spectrum of HD 209458b: Evidence for an Atmospheric Temperature Inversion. *ApJ*, **673**(1), 526–531.

Knutson, H. A., Charbonneau, D., Allen, L. E. et al. (2007) A map of the day-night contrast of the extrasolar planet HD 189733b. *Nature*, **447**(7141), 183–186.

Komacek, T. D. & Showman, A. P. (2016) Atmospheric Circulation of Hot Jupiters: Dayside-Nightside Temperature Differences. *ApJ*, **821**(1), 16.

Komacek, T. D. & Showman, A. P. (2020) Temporal Variability in Hot Jupiter Atmospheres. *ApJ*, **888**(1), 2.

Komacek, T. D., Showman, A. P. & Tan, X. (2017) Atmospheric Circulation of Hot Jupiters: Dayside-Nightside Temperature Differences. II. Comparison with Observations. *ApJ*, **835**(2), 198.

Komacek, T. D. & Tan, X. (2018) Effects of Dissociation/Recombination on the Day-Night Temperature Contrasts of Ultra-hot Jupiters. *Research Notes of the American Astronomical Society*, **2**(2), 36.

Kovács, G., Kovács, T., Hartman, J. D. et al. (2013) Comprehensive time series analysis of the transiting extrasolar planet WASP-33b. *A&A*, **553**, A44.

Kreidberg, L., Line, M. R., Parmentier, V. et al. (2018) Global Climate and Atmospheric Composition of the Ultra-hot Jupiter WASP-103b from HST and Spitzer Phase Curve Observations. *AJ*, **156**(1), 17.

Kurucz, R. L. (2011) Including all the lines. *Canadian Journal of Physics*, **89**, 417–428.

Kurucz, R. L. (2018) Including All the Lines: Data Releases for Spectra and Opacities through 2017. In *Workshop on Astrophysical Opacities*, vol. 515 of *Astronomical Society of the Pacific Conference Series*.

Lammer, H., Selsis, F., Ribas, I. et al. (2003) Atmospheric Loss of Exoplanets Resulting from Stellar X-Ray and Extreme-Ultraviolet Heating. *ApJ*, **598**(2), L121–L124.

Landman, R., Sánchez-López, A., Mollière, P. et al. (2021) Detection of OH in the ultra-hot Jupiter WASP-76b. *A&A*, **656**, A119.

Lehmann, H., Guenther, E., Sebastian, D. et al. (2015) Mass of WASP-33b. *A&A*, **578**, L4.

Lesjak, F., Nortmann, L. & Carmenes Consortium (2022) Characterizing the atmosphere of the warm Neptune HAT-P-11 b with high resolution spectroscopy. In *Bulletin of the American Astronomical Society*, vol. 54.

Line, M. R., Brogi, M., Bean, J. L. et al. (2021) A solar C/O and sub-solar metallicity in a hot Jupiter atmosphere. *Nature*, **598**(7882), 580–584.

Line, M. R., Marley, M. S., Liu, M. C. et al. (2017) Uniform Atmospheric Retrieval Analysis of Ultracool Dwarfs. II. Properties of 11 T dwarfs. *ApJ*, **848**(2), 83.

Linsky, J. L., Yang, H., France, K. et al. (2010) Observations of Mass Loss from the Transiting Exoplanet HD 209458b. *ApJ*, **717**(2), 1291–1299.

Lopez-Puertas, M. & Taylor, F. W. (2002) *Non-LTE radiative transfer in the atmosphere*, vol. 3.

Lothringer, J. D. & Barman, T. (2019) The Influence of Host Star Spectral Type on Ultra-hot Jupiter Atmospheres. *ApJ*, **876**(1), 69.

Lothringer, J. D., Barman, T. & Koskinen, T. (2018) Extremely Irradiated Hot Jupiters: Non-oxide Inversions, H^- Opacity, and Thermal Dissociation of Molecules. *ApJ*, **866**(1), 27.

Lothringer, J. D., Rustamkulov, Z., Sing, D. K. et al. (2021) A New Window into Planet Formation and Migration: Refractory-to-Volatile Elemental Ratios in Ultra-hot Jupiters. *ApJ*, **914**(1), 12.

Lothringer, J. D., Sing, D. K., Rustamkulov, Z. et al. (2022) UV absorption by silicate cloud precursors in ultra-hot Jupiter WASP-178b. *Nature*, **604**(7904), 49–52.

Louden, T. & Wheatley, P. J. (2015) Spatially Resolved Eastward Winds and Rotation of HD 189733b. *ApJ*, **814**(2), L24.

Lund, M. B., Rodriguez, J. E., Zhou, G. et al. (2017) KELT-20b: A Giant Planet with a Period of P ~ 3.5 days Transiting the V ~ 7.6 Early A Star HD 185603. *AJ*, **154**(5), 194.

Maciejewski, G., Fernández, M., Aceituno, F. et al. (2018) Planet-Star Interactions with Precise Transit Timing. I. The Refined Orbital Decay Rate for WASP-12 b and Initial Constraints for HAT-P-23 b, KELT-1 b, KELT-16 b, WASP-33 b and WASP-103 b. *Acta Astron.*, **68**(4), 371–401.

MacLeod, M. & Oklopčić, A. (2022) Stellar Wind Confinement of Evaporating Exoplanet Atmospheres and Its Signatures in 1083 nm Observations. *ApJ*, **926**(2), 226.

Madhusudhan, N. (2012) C/O Ratio as a Dimension for Characterizing Exoplanetary Atmospheres. *ApJ*, **758**(1), 36.

Madhusudhan, N. (2019) Exoplanetary Atmospheres: Key Insights, Challenges, and Prospects. *ARA&A*, **57**, 617–663.

Madhusudhan, N., Amin, M. A. & Kennedy, G. M. (2014a) Toward Chemical Constraints on Hot Jupiter Migration. *ApJ*, **794**(1), L12.

Madhusudhan, N., Bitsch, B., Johansen, A. & Eriksson, L. (2017) Atmospheric signatures of giant exoplanet formation by pebble accretion. *MNRAS*, **469**(4), 4102–4115.

Madhusudhan, N., Crouzet, N., McCullough, P. R., Deming, D. & Hedges, C. (2014b) H_2O Abundances in the Atmospheres of Three Hot Jupiters. *ApJ*, **791**(1), L9.

Mansfield, M., Bean, J. L., Line, M. R. et al. (2018) An HST/WFC3 Thermal Emission Spectrum of the Hot Jupiter HAT-P-7b. *AJ*, **156**(1), 10.

Mayor, M., Pepe, F., Queloz, D. et al. (2003) Setting New Standards with HARPS. *The Messenger*, **114**, 20–24.

Mayor, M. & Queloz, D. (1995) A Jupiter-mass companion to a solar-type star. *Nature*, **378**(6555), 355–359.

McCann, J., Murray-Clay, R. A., Kratter, K. & Krumholz, M. R. (2019) Morphology of Hydrodynamic Winds: A Study of Planetary Winds in Stellar Environments. *ApJ*, **873**(1), 89.

McKemmish, L. K., Masseron, T., Hoeijmakers, H. J. et al. (2019) ExoMol molecular line lists - XXXIII. The spectrum of Titanium Oxide. *MNRAS*, **488**(2), 2836–2854.

McLaughlin, D. B. (1924) Some results of a spectrographic study of the Algol system. *ApJ*, **60**, 22–31.

Merritt, S. R., Gibson, N. P., Nugroho, S. K. et al. (2020) Non-detection of TiO and VO in the atmosphere of WASP-121b using high-resolution spectroscopy. *A&A*, **636**, A117.

Mikal-Evans, T., Sing, D. K., Kataria, T. et al. (2020) Confirmation of water emission in the dayside spectrum of the ultrahot Jupiter WASP-121b. *MNRAS*, **496**(2), 1638–1644.

Miller-Ricci Kempton, E. & Rauscher, E. (2012) Constraining High-speed Winds in Exoplanet Atmospheres through Observations of Anomalous Doppler Shifts during Transit. *ApJ*, **751**(2), 117.

Molaverdikhani, K., Helling, C., Lew, B. W. P. et al. (2020) Understanding the atmospheric properties and chemical composition of the ultra-hot Jupiter HAT-P-7b. II. Mapping the effects of gas kinetics. *A&A*, **635**, A31.

Mollière, P., van Boekel, R., Bouwman, J. et al. (2017) Observing transiting planets with JWST. Prime targets and their synthetic spectral observations. *A&A*, **600**, A10.

Mollière, P., Wardenier, J. P., van Boekel, R. et al. (2019) petitRADTRANS. A Python radiative transfer package for exoplanet characterization and retrieval. *A&A*, **627**, A67.

Mordasini, C., van Boekel, R., Mollière, P., Henning, T. & Benneke, B. (2016) The Imprint of Exoplanet Formation History on Observable Present-day Spectra of Hot Jupiters. *ApJ*, **832**(1), 41.

Nelson, J. & Sanders, G. H. (2008) The status of the Thirty Meter Telescope project. In *Ground-based and Airborne Telescopes II*, edited by L. M. Stepp & R. Gilmozzi, vol. 7012 of *Society of Photo-Optical Instrumentation Engineers (SPIE) Conference Series*.

Nikolov, N., Sing, D. K., Fortney, J. J. et al. (2018) An absolute sodium abundance for a cloud-free 'hot Saturn' exoplanet. *Nature*, **557**(7706), 526–529.

Nissen, P. E. (2013) The carbon-to-oxygen ratio in stars with planets. *A&A*, **552**, A73.

Nortmann, L., Pallé, E., Salz, M. et al. (2018) Ground-based detection of an extended helium atmosphere in the Saturn-mass exoplanet WASP-69b. *Science*, **362**(6421), 1388–1391.

Nugroho, S. K., Gibson, N. P., de Mooij, E. J. W. et al. (2020a) Detection of Fe I Emission in the Dayside Spectrum of WASP-33b. *ApJ*, **898**(2), L31.

Nugroho, S. K., Gibson, N. P., de Mooij, E. J. W. et al. (2020b) Searching for thermal inversion agents in the transmission spectrum of KELT-20b/MASCARA-2b: detection of neutral iron and ionised calcium H&K lines. *MNRAS*, **496**(1), 504–522.

Nugroho, S. K., Kawahara, H., Gibson, N. P. et al. (2021) First Detection of Hydroxyl Radical Emission from an Exoplanet Atmosphere: High-dispersion Characterization of WASP-33b Using Subaru/IRD. *ApJ*, **910**(1), L9.

Nugroho, S. K., Kawahara, H., Masuda, K. et al. (2017) High-resolution Spectroscopic Detection of TiO and a Stratosphere in the Day-side of WASP-33b. *AJ*, **154**(6), 221.

Öberg, K. I., Murray-Clay, R. & Bergin, E. A. (2011) The Effects of Snowlines on C/O in Planetary Atmospheres. *ApJ*, **743**(1), L16.

Oklopčić, A. & Hirata, C. M. (2018) A New Window into Escaping Exoplanet Atmospheres: 10830 Å Line of Helium. *ApJ*, **855**(1), L11.

Owen, J. E. (2019) Atmospheric Escape and the Evolution of Close-In Exoplanets. *Annual Review of Earth and Planetary Sciences*, **47**, 67–90.

Parmentier, V., Line, M. R., Bean, J. L. et al. (2018) From thermal dissociation to condensation in the atmospheres of ultra hot Jupiters: WASP-121b in context. *A&A*, **617**, A110.

Parmentier, V., Showman, A. P. & Lian, Y. (2013) 3D mixing in hot Jupiters atmospheres. I. Application to the day/night cold trap in HD 209458b. *A&A*, **558**, A91.

Pino, L., Désert, J.-M., Brogi, M. et al. (2020) Neutral Iron Emission Lines from the Dayside of KELT-9b: The GAPS Program with HARPS-N at TNG XX. *ApJ*, **894**(2), L27.

Plez, B. (1998) A new TiO line list. *A&A*, **337**, 495–500.

Plez, B. (2012) Turbospectrum: Code for spectral synthesis.

Pollack, J. B., Hubickyj, O., Bodenheimer, P. et al. (1996) Formation of the Giant Planets by Concurrent Accretion of Solids and Gas. *Icarus*, **124**(1), 62–85.

Prinoth, B., Hoeijmakers, H. J., Kitzmann, D. et al. (2022) Titanium oxide and chemical inhomogeneity in the atmosphere of the exoplanet WASP-189 b. *Nature Astronomy*, **6**, 449–457.

Quirrenbach, A., Amado, P. J., Caballero, J. A. et al. (2014) CARMENES instrument overview. In *Ground-based and Airborne Instrumentation for Astronomy V*, edited by S. K. Ramsay, I. S. McLean & H. Takami, vol. 9147 of *Society of Photo-Optical Instrumentation Engineers (SPIE) Conference Series*.

Quirrenbach, A., Amado, P. J., Caballero, J. A. et al. (2016) CARMENES: an overview six months after first light. In *Ground-based and Airborne Instrumentation for Astronomy VI*, vol. 9908 of *Proc. SPIE*.

Quirrenbach, A., Amado, P. J., Ribas, I. et al. (2018) CARMENES: high-resolution spectra and precise radial velocities in the red and infrared. In *Ground-based and Airborne Instrumentation for Astronomy VII*, edited by C. J. Evans, L. Simard & H. Takami, vol. 10702 of *Society of Photo-Optical Instrumentation Engineers (SPIE) Conference Series*.

Quirrenbach, A., CARMENES Consortium, Amado, P. J. et al. (2020) The CARMENES M-dwarf planet survey. In *Society of Photo-Optical Instrumentation Engineers (SPIE) Conference Series*, vol. 11447 of *Society of Photo-Optical Instrumentation Engineers (SPIE) Conference Series*.

Rainer, M., Borsa, F., Pino, L. et al. (2021) The GAPS programme at TNG. XXX. Atmospheric Rossiter-McLaughlin effect and atmospheric dynamics of KELT-20b. *A&A*, **649**, A29.

Reiners, A., Zechmeister, M., Caballero, J. A. et al. (2018) The CARMENES search for exoplanets around M dwarfs. High-resolution optical and near-infrared spectroscopy of 324 survey stars. *A&A*, **612**, A49.

Rodler, F., Lopez-Morales, M. & Ribas, I. (2012) Weighing the Non-transiting Hot Jupiter τ Boo b. *ApJ*, **753**(1), L25.

Rogers, J. G., Gupta, A., Owen, J. E. & Schlichting, H. E. (2021) Photoevaporation versus core-powered mass-loss: model comparison with the 3D radius gap. *MNRAS*, **508**(4), 5886–5902.

Rossiter, R. A. (1924) On the detection of an effect of rotation during eclipse in the velocity of the brigher component of beta Lyrae, and on the constancy of velocity of this system. *ApJ*, **60**, 15–21.

Rothman, L. S., Gordon, I. E., Barber, R. J. et al. (2010) HITEMP, the high-temperature molecular spectroscopic database. *J. Quant. Spec. Radiat. Transf.*, **111**, 2139–2150.

Salz, M., Czesla, S., Schneider, P. C. et al. (2018) Detection of He I λ10830 Å absorption on HD 189733 b with CARMENES high-resolution transmission spectroscopy. *A&A*, **620**, A97.

Sánchez-López, A., Alonso-Floriano, F. J., López-Puertas, M. et al. (2019) Water vapor detection in the transmission spectra of HD 209458 b with the CARMENES NIR channel. *A&A*, **630**, A53.

Sánchez-López, A., Landman, R., Mollière, P. et al. (2022) Searching for the origin of the Ehrenreich effect in ultra-hot Jupiters. Evidence for strong C/O gradients in the atmosphere of WASP-76 b? *A&A*, **661**, A78.

Schwarz, H., Brogi, M., de Kok, R., Birkby, J. & Snellen, I. (2015) Evidence against a strong thermal inversion in HD 209458b from high-dispersion spectroscopy. *A&A*, **576**, A111.

Sedaghati, E., Boffin, H. M. J., MacDonald, R. J. et al. (2017) Detection of titanium oxide in the atmosphere of a hot Jupiter. *Nature*, **549**(7671), 238–241.

Seidel, J. V., Ehrenreich, D., Wyttenbach, A. et al. (2019) Hot Exoplanet Atmospheres Resolved with Transit Spectroscopy (HEARTS). II. A broadened sodium feature on the ultra-hot giant WASP-76b. *A&A*, **623**, A166.

Serindag, D. B., Nugroho, S. K., Mollière, P. et al. (2021) Is TiO emission present in the ultra-hot Jupiter WASP-33b? A reassessment using the improved ExoMol TOTO line list. *A&A*, **645**, A90.

Sheppard, K. B., Mandell, A. M., Tamburo, P. et al. (2017) Evidence for a Dayside Thermal Inversion and High Metallicity for the Hot Jupiter WASP-18b. *ApJ*, **850**(2), L32.

Shibata, S., Helled, R. & Ikoma, M. (2020) The origin of the high metallicity of close-in giant exoplanets. Combined effects of resonant and aerodynamic shepherding. *A&A*, **633**, A33.

Shibata, S., Helled, R. & Ikoma, M. (2022) The origin of the high metallicity of close-in giant exoplanets. II. The nature of the sweet spot for accretion. *A&A*, **659**, A28.

Showman, A. P., Fortney, J. J., Lewis, N. K. & Shabram, M. (2013) Doppler Signatures of the Atmospheric Circulation on Hot Jupiters. *ApJ*, **762**(1), 24.

Sing, D. K., Fortney, J. J., Nikolov, N. et al. (2016) A continuum from clear to cloudy hot-Jupiter exoplanets without primordial water depletion. *Nature*, **529**(7584), 59–62.

Sing, D. K., Lavvas, P., Ballester, G. E. et al. (2019) The Hubble Space Telescope PanCET Program: Exospheric Mg II and Fe II in the Near-ultraviolet Transmission Spectrum of WASP-121b Using Jitter Decorrelation. *AJ*, **158**(2), 91.

Smette, A., Sana, H., Noll, S. et al. (2015) Molecfit: A general tool for telluric absorption correction. I. Method and application to ESO instruments. *A&A*, **576**, A77.

Snellen, I., de Kok, R., Birkby, J. L. et al. (2015) Combining high-dispersion spectroscopy with high contrast imaging: Probing rocky planets around our nearest neighbors. *A&A*, **576**, A59.

Snellen, I. A. G., Brandl, B. R., de Kok, R. J. et al. (2014) Fast spin of the young extrasolar planet β Pictoris b. *Nature*, **509**(7498), 63–65.

Snellen, I. A. G., de Kok, R. J., de Mooij, E. J. W. & Albrecht, S. (2010) The orbital motion, absolute mass and high-altitude winds of exoplanet HD209458b. *Nature*, **465**, 1049–1051.

Spake, J. J., Sing, D. K., Evans, T. M. et al. (2018) Helium in the eroding atmosphere of an exoplanet. *Nature*, **557**(7703), 68–70.

Spiegel, D. S., Silverio, K. & Burrows, A. (2009) Can TiO Explain Thermal Inversions in the Upper Atmospheres of Irradiated Giant Planets? *ApJ*, **699**(2), 1487–1500.

Stangret, M., Casasayas-Barris, N., Pallé, E. et al. (2020) Detection of Fe I and Fe II in the atmosphere of MASCARA-2b using a cross-correlation method. *A&A*, **638**, A26.

Stangret, M., Casasayas-Barris, N., Pallé, E. et al. (2022) High-resolution transmission spectroscopy study of ultra-hot Jupiters HAT-P-57b, KELT-17b, KELT-21b, KELT-7b, MASCARA-1b, and WASP-189b. *A&A*, **662**, A101.

Tabernero, H. M., Zapatero Osorio, M. R., Allart, R. et al. (2021) ESPRESSO high-resolution transmission spectroscopy of WASP-76 b. *A&A*, **646**, A158.

Tala, M., Vanzi, L., Avila, G. et al. (2017) Two simple image slicers for high resolution spectroscopy. *Experimental Astronomy*, **43**(2), 167–176.

Talens, G. J. J., Justesen, A. B., Albrecht, S. et al. (2018) MASCARA-2 b. A hot Jupiter transiting the m_V = 7.6 A-star HD 185603. *A&A*, **612**, A57.

Tamuz, O., Mazeh, T. & Zucker, S. (2005) Correcting systematic effects in a large set of photometric light curves. *MNRAS*, **356**(4), 1466–1470.

Tan, X. & Komacek, T. D. (2019) The Atmospheric Circulation of Ultra-hot Jupiters. *ApJ*, **886**(1), 26.

Tennyson, J., Yurchenko, S. N., Al-Refaie, A. F. et al. (2016) The ExoMol database: Molecular line lists for exoplanet and other hot atmospheres. *Journal of Molecular Spectroscopy*, **327**, 73–94.

Tsiaras, A., Waldmann, I. P., Zingales, T. et al. (2018) A Population Study of Gaseous Exoplanets. *AJ*, **155**(4), 156.

van Sluijs, L., Birkby, J. L., Lothringer, J. et al. (2022) Carbon monoxide emission lines reveal an inverted atmosphere in the ultra hot Jupiter WASP-33 b and indicate an eastward hot spot. *arXiv e-prints*, arXiv:2203.13234.

Vidal-Madjar, A., Désert, J. M., Lecavelier des Etangs, A. et al. (2004) Detection of Oxygen and Carbon in the Hydrodynamically Escaping Atmosphere of the Extrasolar Planet HD 209458b. *ApJ*, **604**(1), L69–L72.

Vidal-Madjar, A., Huitson, C. M., Bourrier, V. et al. (2013) Magnesium in the atmosphere of the planet HD 209458 b: observations of the thermosphere-exosphere transition region. *A&A*, **560**, A54.

Vidal-Madjar, A., Lecavelier des Etangs, A., Désert, J. M. et al. (2003) An extended upper atmosphere around the extrasolar planet HD209458b. *Nature*, **422**(6928), 143–146.

Vigan, A., Otten, G. P. P. L., Muslimov, E. et al. (2018) Bringing high-spectral resolution to VLT/SPHERE with a fiber coupling to VLT/CRIRES+. In *Ground-based and Airborne Instrumentation for Astronomy VII*, edited by C. J. Evans, L. Simard & H. Takami, vol. 10702 of *Society of Photo-Optical Instrumentation Engineers (SPIE) Conference Series*.

von Essen, C., Mallonn, M., Borre, C. C. et al. (2020) TESS unveils the phase curve of WASP-33b. Characterization of the planetary atmosphere and the pulsations from the star. *A&A*, **639**, A34.

von Essen, C., Mallonn, M., Welbanks, L. et al. (2019) An optical transmission spectrum of the ultra-hot Jupiter WASP-33 b. First indication of aluminum oxide in an exoplanet. *A&A*, **622**, A71.

Waldmann, I. P., Tinetti, G., Rocchetto, M. et al. (2015) Tau-REx I: A Next Generation Retrieval Code for Exoplanetary Atmospheres. *ApJ*, **802**(2), 107.

Watanabe, N., Narita, N. & Johnson, M. C. (2020) Doppler tomographic measurement of the nodal precession of WASP-33b. *PASJ*, **72**(2), 19.

Welch, B. L. (1947) The generalization of student's' problem when several different population variances are involved. *Biometrika*, **34**(1-2), 28–35.

Wolszczan, A. & Frail, D. A. (1992) A planetary system around the millisecond pulsar PSR1257 + 12. *Nature*, **355**(6356), 145–147.

Wyttenbach, A., Mollière, P., Ehrenreich, D. et al. (2020) Mass-loss rate and local thermodynamic state of the KELT-9 b thermosphere from the hydrogen Balmer series. *A&A*, **638**, A87.

Yan, F., Casasayas-Barris, N., Molaverdikhani, K. et al. (2019) Ionized calcium in the atmospheres of two ultra-hot exoplanets WASP-33b and KELT-9b. *A&A*, **632**, A69.

Yan, F., Fosbury, R. A. E., Petr-Gotzens, M. G., Zhao, G. & Pallé, E. (2015) The centre-to-limb variations of solar Fraunhofer lines imprinted upon lunar eclipse spectra. Implications for exoplanet transit observations. *A&A*, **574**, A94.

Yan, F. & Henning, T. (2018) An extended hydrogen envelope of the extremely hot giant exoplanet KELT-9b. *Nature Astronomy*, **2**, 714–718.

Yan, F., Pallé, E., Fosbury, R. A. E., Petr-Gotzens, M. G. & Henning, T. (2017) Effect of the stellar absorption line centre-to-limb variation on exoplanet transmission spectrum observations. *A&A*, **603**, A73.

Yan, F., Pallé, E., Reiners, A. et al. (2020) A temperature inversion with atomic iron in the ultra-hot dayside atmosphere of WASP-189b. *A&A*, **640**, L5.

Yan, F., Pallé, E., Reiners, A. et al. (2022a) Detection of CO emission lines in the dayside atmospheres of WASP-33b and WASP-189b with GIANO. *A&A*, **661**, L6.

Yan, F., Reiners, A., Pallé, E. et al. (2022b) Detection of iron emission lines and a temperature inversion on the dayside of the ultra-hot Jupiter KELT-20b. *A&A*, **659**, A7.

Yan, F., Wyttenbach, A., Casasayas-Barris, N. et al. (2021) Detection of the hydrogen Balmer lines in the ultra-hot Jupiter WASP-33b. *A&A*, **645**, A22.

Yousefi, M., Bernath, P. F., Hodges, J. & Masseron, T. (2018) A new line list for the $A^2\Sigma^+$ -X^2 Π electronic transition of OH. *J. Quant. Spec. Radiat. Transf.*, **217**, 416–424.

Zechmeister, M., Anglada-Escudé, G. & Reiners, A. (2014) Flat-relative optimal extraction. A quick and efficient algorithm for stabilised spectrographs. *A&A*, **561**, A59.

Zhang, J., Kempton, E. M. R. & Rauscher, E. (2017) Constraining Hot Jupiter Atmospheric Structure and Dynamics through Doppler-shifted Emission Spectra. *ApJ*, **851**(2), 84.

Zhang, M., Knutson, H. A., Kataria, T. et al. (2018) Phase Curves of WASP-33b and HD 149026b and a New Correlation between Phase Curve Offset and Irradiation Temperature. *AJ*, **155**(2), 83.

Acknowledgements

After roughly three years of work on my PhD thesis I would like to thank everybody who supported me during this phase. In particular, I would like to thank:

- Ansgar Reiners, Fei Yan and Lisa Nortmann for being excellent supervisors and mentors. Thanks a lot for your expertise, commitment and your infinite patience. I feel that your guidance has allowed me to improve significantly in both my academic and personal skills.
- Stefan Dreizler for very helpful suggestions and discussions in the thesis advisory committee meetings.
- The members of the CARMENES consortium for their support and fruitful collaboration. Particularly, I would like to say thanks to José Caballero for the wonderful guidance throughout the publication procedures.
- My friends and colleagues who have enriched my journey through the PhD aside from the scientific work. Especially, I would like to thank Fabio Lesjak and Jessica Khaimova for many interesting discussions and ideas that contributed to this work.
- My parents Christina and Marcello, my sisters Valeria and Franziska and my wife Sabine. Thank you for your patience and support!